Time-Domain Antenna and Scattering Analysis for Micro- and Millimeter-Wave Applications

Vakili, Iman

2015

Document Version:
Publisher's PDF, also known as Version of record

Link to publication

Citation for published version (APA):
Vakili, I. (2015). *Time-Domain Antenna and Scattering Analysis for Micro- and Millimeter-Wave Applications*. [Doctoral Thesis (compilation), Department of Electrical and Information Technology].

Total number of authors:
1

LUND UNIVERSITY

PO Box 117
221 00 Lund
+46 46-222 00 00

Time-Domain Antenna and Scattering Analysis for Micro- and Millimeter-Wave Applications

Iman Vakili

Doctoral Dissertation
Electromagnetic Theory

Lund University
Lund, Sweden
2015

Doctoral dissertation which, by due permission of the Faculty of Engineering, Lund University, will be publicly defended on November 27, 2015, at 10.15 a.m. in lecture hall E:1406, John Erikssons väg 4, Lund, for the degree of Doctor of Philosophy in Engineering in Electromagnetic Theory.

Department of Electrical and Information Technology
Electromagnetic Theory Group
Lund University
P.O. Box 118, S-221 00 Lund, Sweden

Series of licentiate and doctoral theses
ISSN 1654-790X; No. 76
ISBN 978-91-7623-480-8 (print)
ISBN 978-91-7623-481-5 (digital)

Abstract

Telecommunications industries are investing tremendously to meet the ever-increasing demands for higher data rates and capacity. In particular to develop standardization for 5G, which is expected around 2020. The existing spectrum for traditional mobile networks is limited to highly occupied bands at microwave frequencies below 6 GHz. It is expected that 5G will use millimeter-waves to enable higher data rates. Even though losses at millimeter-waves are higher, higher data rates for short range applications can be achieved due to the available wide bandwidth.

The radio channel between a transmitter and a receiver has a great impact on the quality of the received signals. The channel includes everything between the transmitter and receiver that may impact the signals, such as buildings, walls, windows, etc. High data rate transmission at millimeter-wave frequencies requires size- and cost-efficient circuitry. The recent advances in nanotechnology and semiconductor devices enable the signal generation at millimeter-waves. The existence of the available extreme bandwidth at millimeter-wave frequencies enables the application of impulse radio using high frequency ultra-short pulses. Transmission of a short pulse through antennas and a free-space radio channel without significant distortion requires a wideband antenna with high fidelity.

In this thesis a time-domain antenna system with ultra-short pulse transmission and reception at millimeter-waves is presented. The antenna system consists of wideband and non-dispersive leaky lens antennas and a high frequency short pulse (wavelet) generator based on III–V technology. The time-domain system is presented in Paper I. The transmission of 100 ps long pulses at 60 GHz produced by the wavelet generator through different antennas is investigated. It is shown that the leaky lens antennas have negligible pulse distortion and preserve the shape of the generated high frequency short pulses. Further characterizations of the leaky lens antennas for the 60 GHz band, using a time-domain gating method is presented in Paper III. The results show that the antenna has a low dispersion and can thereby transmit short pulses with high fidelity.

A time-domain characterization method at millimeter-waves using the antenna system is presented in Paper II. The complex permittivity of low loss non-magnetic materials with low dispersion are estimated directly from the received time-domain pulses. The wide bandwidth of the wavelet is also used to determine the frequency dependence of dispersive materials.

Time-domain scattering analysis of periodic structures is presented in Paper IV and Paper V. A sum rule for scattering in parallel-plate waveguides based on energy conservation and the optical theorem is derived in Paper IV. A parallel-plate waveguide with wideband TEM horn antennas and a parallel-plate capacitor are used for dynamic and low frequency (static) measurements, respectively. The results show that the all waveleghts electromagnetic interaction introduced by the object is given by the static polarizability.

The broad bandwidth and high resolution of the time-domain system is uti-

lized for radar imaging application in Sec. 6 of the Research Overview. The images are obtained through gridding method which is a classical Fourier reconstruction and ℓ_1-minimization problem. It is shown that the resolution achieved by the time-domain system is similar to the frequency-domain measurements using a vector network analyzer.

Popular Science

The recent advances in wireless technology have enabled a variety of new applications. The standardization of the next generation of the mobile communications (5G) is expected to be finalized by approximately 2020. It is expected that all the electronic devices, from vacuum cleaners to coffee machines, are connected and can be controlled by smartphone apps. For everything to be connected steadily, good transmitters and receivers are required. In this thesis an antenna system operating at millimeter-waves is presented. These types of devices can be used for high speed communications. They can also be used in cars to detect the distance to nearby vehicles and pedestrians.

Operating many of these devices simultaneously, they can be used as a camera for imaging applications. This is similar to security cameras at airports. These cameras can detect hidden objects, *e.g.*, weapons, underneath clothes since textiles are transparent for millimeter-waves. High resolution images can also be captures using only one radar device and moving the radar around an object or moving an object in front of the radar. These types of imaging frameworks are known as synthetic aperture radar (SAR). The radar captures a signal for each position and combines them to make a high resolution image. These types of systems are also used to make images from landscapes when mounted on airplanes or spacecrafts.

The radio waves that are received by a cellphone are transmitted through windows and walls and affected by the electrical properties of those materials. The human body also interfere with these signals. The antenna system discussed in this thesis is used to detect the material properties of plastics and water at millimeter-waves.

Preface

This thesis summarizes my research which I have carried out at the Department of Electrical and Information Technology, Lund University, Sweden. The thesis starts with a research overview followed by the scientific papers as listed below.

List of included papers

I. I. Vakili, L. Ohlsson, M. Gustafsson and L.-E. Wernersson,
"Wideband and Non-Dispersive Wavelet Transmission using Leaky Lens Antenna"
IET Electronics Letters, Vol. 49, No. 5, pp. 321-322, 2013
Contributions of the author: The author of this thesis is the main contributor to this paper. I designed and fabricated the leaky lens antennas, performed the measurements, and wrote the paper.

II. I. Vakili, L. Ohlsson, L.-E. Wernersson and M. Gustafsson,
"Time-Domain System for Millimeter-Wave Material Characterization"
IEEE Transactions on Microwave Theory and Techniques, Vol. 63, No. 9, pp. 2915-2922, 2015
Contributions of the author: The author of this thesis is the main contributor to this paper. I designed and fabricated the antenna, performed the measurements and data analysis, and wrote the paper.

III. L. Ohlsson, I. Vakili, D. Sjöberg and L.-E. Wernersson
"Time-Domain Wavelet Characterisation With Gating Techniques Applied to Millimetre-Wave Antennas"
Submitted to: *IEEE Transactions on Antennas and Propagations*
Contributions of the author: I designed and fabricated the leaky lens antennas and helped in writing the paper.

IV. I. Vakili, M. Gustafsson, D. Sjöberg, R. Seviour, M. Nilsson, S. Nordebo,
"Sum Rules for Parallel-Plate Waveguides: Experimental Results and Theory"
IEEE Transactions on Microwave Theory and Techniques, Vol. 62, No. 11, pp. 2574-2582, 2014
Contributions of the author: The author of this thesis is the main contributor to this paper. I designed and fabricated the measurement setup, developed the sum rule for parallel-plate waveguides, performed the measurements, made the numerical analysis, and wrote the paper.

V. M. Gustafsson, I. Vakili, D. Sjöberg,
"Optical theorem and forward scattering sum rule for periodic structures"
IEEE Transactions on Antennas and Propagation, Vol. 60, No. 8, pp. 3818-3826, 2012
Contributions of the author: I designed and fabricated the measurement setup, performed the measurements, and helped in writing the paper.

Other publications by the author

The author of this dissertation is also the author or co-author of the following conference papers which are related to but not considered part of the dissertation:

VI. I. Vakili, M. Gustafsson and D. Sjöberg,
"Sum Rules for Metamaterials in Parallel Plate Waveguides"
URSI General Assembly and Scientific Symposium, Beijing, China, 2014-08-16

VII. I. Vakili, M. Gustafsson and D. Sjöberg,
"All spectrum identities for periodic metamaterials"
2013 International Symposium on Electromagnetic Theory, Hiroshima, Japan, pp. 391-392, 2013-05-20

VIII. I. Vakili, L. Ohlsson, M. Gustafsson and L.-E. Wernersson,
"Pulse transmission using leaky lens antenna and RTD-MOSFET wavelet generator"
7th European Conference on Antennas and Propagation (EuCAP 2013), Gothenburg, pp. 324-325, 2013-04-08

IX. I. Vakili, M. Gustafsson and D. Sjöberg,
"Forward scattering properties of periodic metamaterials"
6th European Conference on Antennas and Propagation (EuCAP 2012), Prague, Czech Republic, pp. 2680-2682, 2012-03-26

X. C. Larsson, S. E. Bayer Keskin, M. Gustafsson, G. Kristensson, D. Sjöberg, C. Sohl, I. Vakili,
"Scattering measurements in a parallel plate waveguide: first results"
URSI General Assembly and Scientific Symposium, Istanbul, Turkey, 2011-08-13

XI. M. Gustafsson and D. Sjöberg, I. Vakili,
"On the extraordinary transmission through sub-wavelength apertures in perfectly conducting sheets"
International Conference on Electromagnetics in Advanced Applications (ICEAA 2011), Torino, Italy, 2011-09-12

XII. D. Sjöberg, L. Ohlsson, I. Vakili, M. Gustafsson and L.-E. Wernersson,
"Impulse Based Radio Technology for Mm-Waves"
9th European Conference on Antennas and Propagation (EuCAP), Lisbon, 2015-04-13

XIII. I. Vakili, L. Ohlsson, L.-E. Wernersson, M. Gustafsson
"Complex Permittivity Extraction Using a Leaky-Lens Antenna System"
Progress in Electromagnetics Research Symposium (PIERS), Guangzhou, China, 2014-08-25

XIV. I. Vakili, L. Ohlsson, M. Gustafsson and L.-E. Wernersson
"Time Domain Material Characterizations Using Leaky Lens Antennas"
URSI General Assembly and Scientific Symposium, Beijing, China, 2014-08-16

Acknowledgments

This thesis is the outcome of a journey that started Aug. 2009 when I came to Lund University as a masters student in wireless communications. In 2010 I started to work with the electromagnetic group at the Dept. of Electrical and Information Technology and from 2011 as a PhD. student. Now after several years being in this group, I realize that without the help of many, I would not have been here. First and foremost, I would like to express my deep gratitude to my main supervisor Prof. Mats Gustafsson for his knowledge, guidance and support over all these years. I would like to thank my co-supervisor Prof. Lars-Erik Wernersson, for supporting and inspiring me with great ideas. I am grateful to Prof. Daniel Sjöberg for his positive attitude, encouragement and the invaluable discussions. I would like to thank Prof. Christer Larsson from Saab Bofors Dynamics for his great suggestions, support and guidance in measurements. Prof. Gerhard Kristensson is gratefully acknowledged for his encouragement.

I would like to thank Dr. Lars Ohlsson for the great discussions we always had in the lab and also for proof reading of my thesis. I thank Alexander Bondarik, Dr. Carl Gustafson and Sebastian Heunisch for their invaluable assistance in the measurements. I would like to thank everyone in the electromagnetic group. It was an honor working beside you all.

I gratefully acknowledge Prof. John B. Anderson, Prof. Buon Kiong Lau, Dr. Fredrik Rusek, Prof. Ove Edfors, and Prof. Fredrik Tufvesson for the guidance and the support they provided me with over the several years in Lund. I would like to thank all the colleagues and friends who provided me with energy and motivation.

Last but not the least I would like to thank my family for believing in me and always being supportive and encouraging. I am also grateful to my girlfriend for all the support and her being by my side.

Lund, November 2015

Iman Vakili

Iman Vakili

Contents

Research Overview

Iman Vakili

1 Motivation

Radio technology has grown to become a vital component in everyday life. An interruption even for a very short moment can cause irreparable damages. From mobile communications and internet of things (IoT) to airport radars and medical imaging devices, the radio transmitters and receivers are ubiquitous.

James Clerk Maxwell mathematically predicted the existence of electromagnetic waves in 1864 [90–92]. The theory was later experimentally verified by Heinrich Hertz [62]. In 1887 Hertz performed a set of experiments using a spark gap transmitter and a loop of wire for receiving electromagnetic waves at microwave frequencies [49]. He also found that these waves could be transmitted through dielectrics and reflected by objects. Guglielmo Marconi was one of the main contributors to radio technology, starting in 1894 from short distances and steadily increasing the distance up to transatlantic transmission in 1901. Marconi shared the Nobel Prize with Karl Ferdinand Braun in physics in 1909 for their contributions to the development of wireless telegraphy [88].

Christian Hülsmeyer is one of the pioneers in radio technology and radar. He developed a ship anti collision system based on echo-location of the electromagnetic waves [85]. During the 1930s the electromagnetic reflections caused by airplanes were observed by Young and Hyland. They used continuous wave measurements using multiple transmitters and receivers [139].

Nowadays, radio technologies have become more complex with more efficient circuitry as well as higher data rates. Radio systems utilize frequencies from a few MHz up to a couple of THz [23, 33, 51, 96, 113, 136]. Mobile phones, WiFi, microwave tomography, and many radar systems operate at microwave frequencies up to 30 GHz, that correspond to wavelengths down to 1 cm. New advances in semiconductor technology have enabled the development of circuitry for millimeter-wave (mm-wave) frequencies 30-300 GHz with wavelength 1-10 mm [38,51,69,95]. The existence of unlicensed bands with comparably wide bandwidth in the mm-wave spectrum enables an increased capacity of the communication channels and hence an increased data rate [1,2]. In radar and imaging systems, the short wavelength and wide bandwidth at mm-waves are directly proportional to a high resolution. An antenna with a given physical aperture has a higher gain at mm-wave frequencies compared to lower frequencies. Some applications include but are not limited to on-vehicle radars, security radars, sensor networks, and high definition (HD) video streaming [48, 59, 69, 115].

1.1 Friis' Transmission Equation

A communication link between a radio transmitter and a receiver in a downlink configuration, *i.e.*, the transmission from the base station to users, is illustrated in Fig. 1. The available power at the transmitter side, P_{t}, is delivered to an antenna with *realized gain* G_{t}. The realized gain is the antenna gain that includes losses due to the impedance mismatch at the antenna input port [10]. Assuming free-

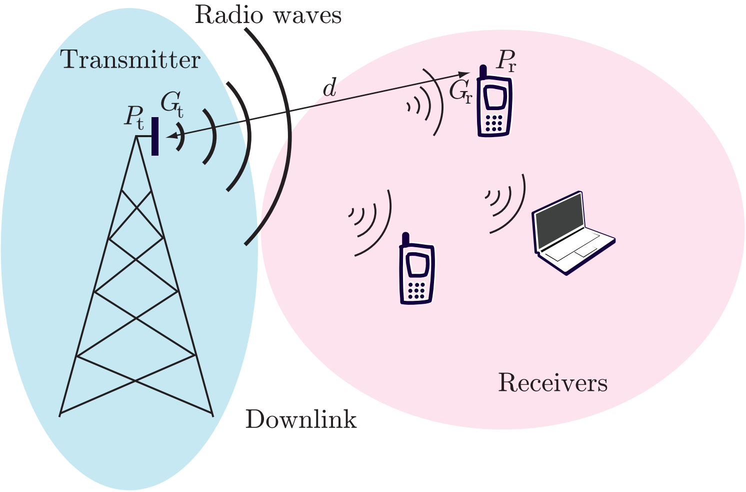

Figure 1: Radio link between a transmitting base station and multiple receivers in a downlink configuration. The power at the port of the transmitting antenna with realized gain G_t is denoted by P_t. The realized gain of the receiving antenna is G_r and the power detected at the antenna port P_r. The distance between the transmitter and a receiver is denoted by d.

space propagation with a polarization matched receiving antenna with realized gain G_r located at distance d from the transmitter, the received power at the receiver antenna port for distance d in the far-field is given by [45]

$$P_r = P_t G_t G_r \left(\frac{\lambda}{4\pi d}\right)^2, \tag{1.1}$$

where $\lambda = c_0/f$ is the free-space wavelength and $c_0 = 1/\sqrt{\epsilon_0\mu_0} \approx 3 \times 10^8$ m/s is the speed of light in vacuum, where ϵ_0 and μ_0 are the free-space permittivity and permeability, respectively. The relation in (1.1) is known as Friis' transmission equation [45, 131]. The inverse of the last term on the right hand side of (1.1) is known as the free-space path loss, $L_{\text{path}} = \left(\frac{4\pi d}{\lambda}\right)^2$ which is proportional to the square of the distance and inversely proportional to the square of the wavelength. Assuming a constant gain at the transmitting and receiving sides, the received power decreases when the frequency is increased (or the wavelength is decreased). This means that at higher frequencies the distance must be shorter to receive the same amount of power. The high propagation loss can be considered as a security benefit for short range communications since the possibility of eavesdropping and interference is smaller [112]. It should be noted that Friis' law in (1.1) is an approximated model for the far-field region and line of sight transmission. The channel models in realistic scenarios can be more complex due to the existence of multipath components [96, 121].

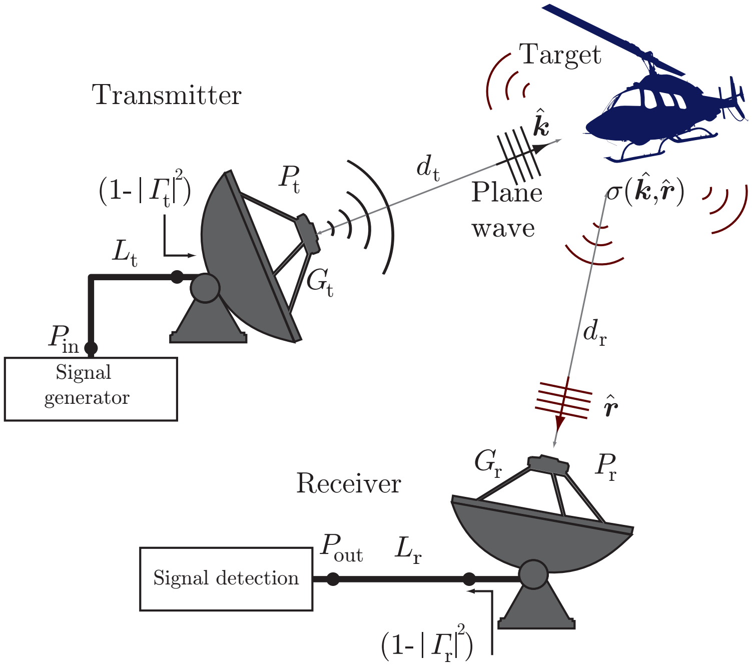

Figure 2: Bi-static radar geometry including a signal generator, transmission lines, transmitting and receiving antennas, and a signal detection unit. The propagated spherical wave front from the antenna is approximated by plane waves at the target position when the target is in the far-field region. The radar cross section is denoted $\sigma(\hat{\boldsymbol{k}}, \hat{\boldsymbol{r}})$ where $\hat{\boldsymbol{k}}$ is a unit vector in the direction of incidence and $\hat{\boldsymbol{r}}$ is a unit vector towards the observation direction.

1.2 Radar System

Radio transmitters and receivers can be used to detect reflection (or scattering) from targets. These systems are called radars (radio detection and ranging) [31, 78, 132]. Radar systems are widely used for a variety of applications from simple speed control to advanced imaging and tracking. The major parts of a simplified radar system are depicted in Fig. 2. One of the most important parts is the signal generator that produces dedicated types of signals based on the application of the radar. The generated signal is then sent to the transmitting antenna via a transmission line such as coaxial cables or waveguides. The transmission lines have finite conductivities and therefore cause losses, L_t. Due to the impedance mismatch at the interface between the transmission line and the antenna port, the radiated power by the antenna can be written [16, 132]

$$P_\mathrm{t} = P_\mathrm{in}(1 - |\mathit{\Gamma}_\mathrm{t}|^2)e_\mathrm{t,rad}/L_\mathrm{t}, \tag{1.2}$$

where $\mathit{\Gamma}_{\mathrm{t}} = (Z_{\mathrm{c}} - Z_{\mathrm{L}})/(Z_{\mathrm{c}} + Z_{\mathrm{L}})$ is the transmitting antenna reflection coefficient, Z_{c} is the input impedance of the antenna and Z_{L} is the characteristic impedance of the transmission line. The radiation efficiency, $e_{\mathrm{t,rad}}$, is used to take the ohmic losses of the antenna into account. The radiated waves can be approximated by plane waves in the far-field region, $d_{\mathrm{t}} > 2D^2/\lambda$, where D is the largest dimension of the antenna [16]. The incident power density on the target can be written $W_{\mathrm{i}} = P_{\mathrm{t}}/(4\pi d_{\mathrm{t}}^2)$.

The electromagnetic waves incident on the object are scattered. The scattered field depends on the shape, material and size of the object. A measure of the amount of scattering is the radar cross section (RCS), $\sigma(\hat{\boldsymbol{k}}, \hat{\boldsymbol{r}})\,\mathrm{m}^2$, defined as [122, 132]

$$\sigma(\hat{\boldsymbol{k}}, \hat{\boldsymbol{r}}) = 4\pi d_{\mathrm{t}}^2 \frac{W_{\mathrm{s}}}{W_{\mathrm{i}}}, \tag{1.3}$$

where W_{s} is the scattered power density and W_{i} denotes the power density incident on the target. The unit vector $\hat{\boldsymbol{k}}$ is in the direction of incidence and $\hat{\boldsymbol{r}}$ is a unit vector towards the observation direction, see Fig.2. A portion of the scattered electromagnetic fields is captured by the receiving antenna effective aperture, A_{eff}. The antenna effective aperture is related to the antenna realized gain as $A_{\mathrm{eff}} = \lambda^2 G_{\mathrm{r}}/[4\pi(1 - |\mathit{\Gamma}_{\mathrm{r}}|^2)]$ [10, 16]. Similar to the transmitting side, a fraction of the power is lost due to the antenna impedance mismatch, $\mathit{\Gamma}_{\mathrm{r}}$, and losses in the transmission line, L_{r}. The final relation between the input power, P_{in}, and the detected power in the receiver side, P_{out}, known as radar equation, becomes [109, 132]

$$\frac{P_{\mathrm{out}}}{P_{\mathrm{in}}} = \frac{\lambda^2 \sigma(\hat{\boldsymbol{k}}, \hat{\boldsymbol{r}}) G_{\mathrm{t}} G_{\mathrm{r}}}{(4\pi)^3 (d_{\mathrm{t}} d_{\mathrm{r}})^2 L_{\mathrm{t}} L_{\mathrm{r}}}. \tag{1.4}$$

2 Wideband Antennas

Wideband systems have been introduced for high data rate communication, high resolution radar imaging, localization, and resolving multipath components in fading channels [5, 32, 77, 111, 120, 124, 125, 128, 142, 149]. The large operational bandwidth introduces challenges in design and implementations of system components. Antennas are among the most challenging elements to be designed efficiently in order to transmit and receive wideband signals. The antennas that are commonly used fall into two main categories: narrowband and wideband. Narrowband antennas operate over a narrow frequency band, which makes it possible to assume constant characteristic parameters over the operating frequency band. In wideband systems, however, the antenna design and characterization is challenging due to the frequency dependent performance of the antenna [5, 40, 41, 128, 142].

Two wideband antennas are used throughout this thesis for scattering, radar and imaging applications. A wideband non-dispersive leaky lens antenna [99, 101, 145] with stable gain and radiation pattern in the frequency interval 20-67 GHz

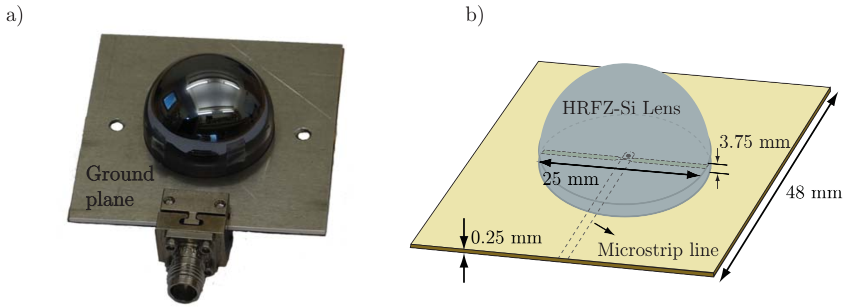

Figure 3: Leaky lens antenna for non-dispersive radiation. a) Leaky lens antenna prototype consisting of a planar feeding structure, silicon lens and a 2.4 mm end-launch connector. b) Antenna geometry and dimensions.

is presented first. The second example is a TEM horn antenna [17, 84, 127], designed for wideband measurements inside a parallel-plate waveguide operating in the 1-20 GHz interval.

2.1 Leaky Lens Antenna

Leaky lens antennas for wideband and non-dispersive radiation were introduced by Neto [99–101]. The antenna can be categorized as a travelling wave antenna that is combined with a wideband lens to direct the radiated beam. Similar to other travelling wave antennas, leaky lens antennas have a wide bandwidth. However unlike most other wideband antennas, they have a negligible phase distortion over a large operational bandwidth.

In this work, frequency-domain as well as time-domain properties of the leaky lens antenna, in Fig. 3, are presented. A leaky lens antenna has been designed and fabricated to be well matched to 50 Ω impedance at the port of the antenna and operate over the frequency interval 20-67 GHz, see [145]. The antenna consists of a planar feeding structure including a microstrip line, a narrow slot and a hemispherical silicon lens, see Fig. 3(a-b).

Consider a narrow slot located between medium 1 and medium 2 with different electrical properties as depicted in Fig. 4. The propagation in each medium is associated with its wavenumber, k_1 and k_2. For a slot width that is much smaller than the wavelength, $W_\mathrm{s} \ll \lambda_\mathrm{d}$, where λ_d is the wavelength inside the denser material, the propagation in the denser medium is in the form of a leaky wave [87, 99, 102]. Assuming that medium 2 is denser, $k_2 > k_1$, the resulting Poynting vector has an oblique direction inside medium 2. The angle inside the denser medium is known as the leaky wave angle,γ_LW, and is given by [99]

$$\gamma_\mathrm{LW} = \cos^{-1}\left(\frac{\beta}{k_2}\right) \approx \cos^{-1}\left(\sqrt{\frac{1 + k_1^2/k_2^2}{2}}\right), \tag{2.1}$$

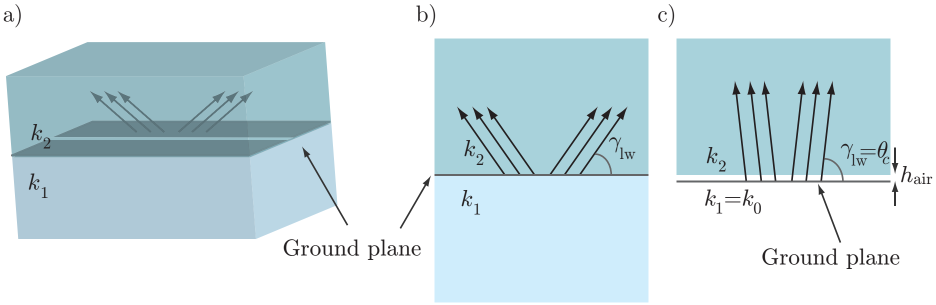

Figure 4: Leaky wave propagation produced by a narrow slot between medium 1 and medium 2. a) Perspective view. b) Side view. The leaky wave angle is denoted by γ_{LW}. c) Side view. Increased radiation angle to the critical angle, $\gamma_{\mathrm{LW}} = \theta_{\mathrm{c}}$, by introducing an airgap, $k_1 = k_0$, on top of the ground plane.

where $\beta \approx \sqrt{(k_1^2 + k_2^2)/2}$ is the propagation constant of the slot and is approximated by the quadratic average of the propagation constants in two dielectrics [22,100]. According to (2.1) the maximum angle of the leaky wave propagation is always less than 45°. By inserting a small airgap with height $h_{\mathrm{air}} \leqslant W_{\mathrm{s}}$ on top of the slot, the slot propagation constant which is the quadratic average between two materials becomes $\beta \approx k_0$, where k_0 is the free-space wavenumber, see Fig. 4(c). The resulting frequency independent leaky wave propagation angle increases as $\gamma_{\mathrm{LW}} = \cos^{-1}(k_0/k_2) \approx \cos^{-1}(1/\sqrt{\epsilon_{\mathrm{r2}}})$ [99]. This angle is similar to the critical angle of the dielectric, *i.e.*, $\gamma_{\mathrm{LW}} = \theta_{\mathrm{c}}$.

Inserting an airgap between the feeding structure and the dielectric improves the matching and reduces the sidelobe level [99]. Having a dielectric lens instead of semi-infinite medium results in a broadband and directive propagation from the antenna. The ideal lens to form a directive beam and a planar phase front is an elliptical lens with its lower focal point located at the middle of the slot [42]. Due to limitations in commercial manufacturing processes, the elliptical lens is replaced by a hemispherical lens with a cylindrical extension [64]. The eccentricity of the lens is a function of the dielectric constant and is given by $e = 1/\sqrt{\epsilon_{\mathrm{r}}}$ [61]. For a silicon lens ($\epsilon_{\mathrm{r}} \approx 11.6$) with diameter of 25 mm the extension length is 3.75 mm. The airgap inserted between the lens and the planar feeding structure is chosen to 0.25 mm to achieve the best matching in the frequency interval 20-67 GHz.

The planar feeding structure of the antenna is printed on a 250 μm thick Arlon Diclad 880 having a relative dielectric constant $\epsilon_{\mathrm{r}} = 2.2$. In order to match the antenna port to 50 Ω the width of the microstrip line is chosen to $W_\mu = 0.7$ mm. A Southwest 2.4 mm end-launch connector is used to provide coaxial interface. The microstrip line on the other side is utilized to excite the currents on the slot below the lens. The antenna feeding structure is optimized to be well matched to 50 Ω from 20 GHz to 67 GHz. The reflection coefficient of

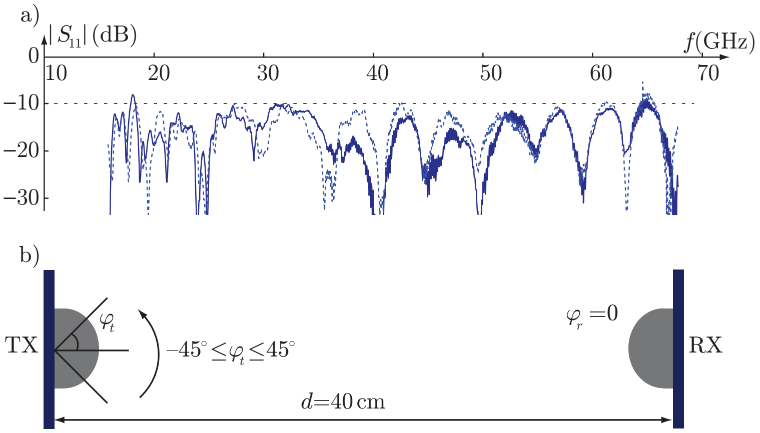

Figure 5: Leaky lens antenna characterization. a) Measured magnitude of the reflection coefficient, $|S_{11}|$, of two identical leaky lens antennas in dB scale, see Fig.3. b) Measurement configuration. The transmitting antenna is rotated over the angular range $\varphi_{\mathrm{t}} = [-45°, 45°]$ while the receiving antenna is kept at $\varphi_{\mathrm{r}} = 0$. The distance between the two antennas is $d = 40\,\mathrm{cm}$.

the two fabricated leaky lens antennas, measured by an Agilent E8361A vector network analyzer (VNA) in the 15-67 GHz interval, is shown in Fig. 5(a). The reflection coefficients of two antennas are similar and typically matched better than −10 dB. It should be noted that 2.4 mm connectors are specified up to 50 GHz. Two recently fabricated leaky lens antennas using 1.85 mm connectors specified up to 67 GHz are partially investigated in Paper III. In this thesis, however, due to the similarity in measured antenna parameters and consistency with Paper I and Paper II, the leaky lens antennas with 2.4 mm connectors are shown.

The transmission of the leaky lens antenna is characterized over a link consisting of two identical leaky lens antennas that are separated by the distance $d = 40\,\mathrm{cm}$. The transmitting antenna rotates around the center of its connector with $-45° \leqslant \varphi_{\mathrm{t}} \leqslant 45°$ in the H-plane of the antenna as shown in Fig. 5(b) and the receiving antenna angle is kept constant, $\varphi_{\mathrm{r}} = 0°$. The transfer function of the antenna, $H(\varphi, \omega)$, for a linear dominant polarization and can be found from the transmission between two identical antennas in the H-plane according to [110]

$$S_{21}(\varphi_{\mathrm{t}}, \varphi_{\mathrm{r}}, \omega) = \frac{\mathrm{j}\omega}{2\pi d c_0} H(\varphi_{\mathrm{t}}, \omega) H(\varphi_{\mathrm{r}}, \omega) \mathrm{e}^{-\mathrm{j}\omega d / c_0}, \tag{2.2}$$

where $S_{21}(\varphi_{\mathrm{t}}, \varphi_{\mathrm{r}}, \omega)$ is the transmission coefficient when the angle of departure is φ_{t} and the angle of arrival is φ_{r}, see Fig. 5(b). Note that the ratio between the transmitted power, P_{t}, and received power, P_{r}, in (1.1) is proportional to $|S_{21}|^2$.

The band limited response, $h(\varphi_{\rm t}, t)$, of the leaky lens antenna is computed by the inverse Fourier transform of the transfer function, *i.e.*, $h(t, \varphi_{\rm t}) = \mathrm{IFT}[H(\varphi_{\rm t}, \omega)]$. The envelope of the impulse response, $h_{\rm env}(t, \varphi_{\rm t})$, as a function of angle and time is shown in Fig. 6(a). The antenna impulse response shows a strong peak at 0.3 ns which stands for the time delay in the connector, microstrip line and the time delay in the lens. The second strongest peak at 0.63 ns corresponds to the first round-trip reflection inside the lens due to impedance mismatch at the lens-air interface. The flatness of the antenna impulse response over the angles $-20^\circ \leqslant \varphi_{\rm t} \leqslant 20^\circ$ indicates that the antenna group delay is almost constant in this region. In other words, the antenna phase center position can be interpreted to be approximately constant over the main beam of the antenna. At larger angles, however, the group delay is larger, one interpretation for this could be that the antenna rotation center is not positioned at the antenna phase center.

The antenna relative group delay is defined as

$$\tau_{\rm g,rel}(\varphi_{\rm t}, \varphi_{\rm r}, \omega) = \tau_{\rm g} - \langle \tau_{\rm g} \rangle \tag{2.3}$$

according to [152] where $\langle \tau_{\rm g} \rangle$ is the mean value of the antenna group delay, $\tau_{\rm g} = -\frac{\partial}{\partial \omega} \angle H(\varphi_{\rm r}, \omega)$, over the frequency band. The antenna relative group delay for the dominant polarization of the antenna, the angles $-45^\circ \leqslant \varphi_{\rm t} \leqslant 45^\circ$, and having $\langle \tau_{\rm g} \rangle \approx 0.3$ ns, is illustrated in Fig. 6(b). As can be seen in the figure, the relative group delay is slowly varying from 20 GHz to 67 GHz especially around 0° which is the direction of the main beam of the antenna. The variations of the group delay are mainly due to the mismatch at the lens-air interface and can be reduced by using an optimized wideband matching layer to taper the impedance transition from silicon to air [99]. The group delay in Fig. 6(c) is obtained by gating out everything but the main peak of the impulse response using a 400 ps time window around the main peak. This shows that the variations in antenna group delay can be mitigated by improving the impedance mismatch at the lens-air interface.

The realized gain of the antenna, $G(\varphi, \omega)$, for two identical antennas and the dominant polarization can be estimated from the obtained transfer function according to [152] as

$$G(\varphi, \omega) = \frac{\omega^2}{\pi c_0^2} |H(\theta, \varphi, \omega)|^2, \tag{2.4}$$

which is similar to Friis transmission equation in (1.1). The realized gain of the leaky lens antenna from 20 GHz to 67 GHz and for $-45^\circ \leqslant \varphi_{\rm t} \leqslant 45^\circ$ which corresponds to the H-plane of the antenna is depicted in Fig. 6(d). As can be seen, the antenna is directional and the gain increases slowly with frequency and is almost constant from 30 GHz to 67 GHz. Similar to the group delay, the gain of the antenna is also affected by the multiple reflections inside the lens. The HPBW of the antenna over a range of frequencies is listed in Table 1. The leaky lens antenna is also simulated using the time-domain solver in CST Microwave Studio and the resulting realized gain in the forward direction is compared to

Table 1: Measured half power beam width (HPBW) of the leaky lens antenna.

Frequency (GHz)	20	30	40	50	60
HPBW (°)	26	18	13	13	11

the measured realized gain in Fig. 6(e). The measured values agree with the simulation results and the fluctuations in the measurement results are mainly due to the mismatch at the connector as well as the soldering of the via on the ground plane.

One way to evaluate the pulse fidelity of the antenna is to compare the output pulse from the antenna with a reference non-distorted pulse through the fidelity factor [81, 93, 110, 120]. The fidelity factor for an antenna in a certain direction, φ_t, for the H-plane of the antenna is defined as $F(\varphi_\mathrm{t}) = \max_\tau [F_\tau(\varphi_\mathrm{t}, \tau)]$ where

$$F_\tau(\varphi_\mathrm{t}, \tau) = \frac{\int_{-\infty}^{\infty} S_{21}(\varphi_\mathrm{t}, t-\tau) S_{21,\mathrm{ref}}(t)\,\mathrm{d}t}{\sqrt{\int_{-\infty}^{\infty} |S_{21}(\varphi_\mathrm{t}, \tau)|^2\,\mathrm{d}\tau \int_{-\infty}^{\infty} |S_{21,\mathrm{ref}}(\tau)|^2\,\mathrm{d}\tau}} \tag{2.5}$$

and $S_{21}(t)$ is the inverse Fourier transform of $S_{21}(\omega)$. In this case the reference signal is measured when two ports of the VNA are connected via a cable. This corresponds to a sinc function since $S_{21,\mathrm{ref}}(\omega)$ is constant (a rectangular spectrum) over the measurement bandwidth. The resulting fidelity factor is illustrated in Fig. 6(f). The fidelity factor has its highest value, $F(\varphi_\mathrm{t} = 0) \approx 0.98$, around the main beam of the antenna and reduces with increasing departure angle.

The narrow impulse response, slowly varying group delay, almost constant gain and high fidelity factor of the antenna indicate a promising time-domain behavior for impulse radiation. In addition to this, the circular symmetry of the lens leads to a stable radiation pattern in the E- and H-planes over a wide range of frequencies [101]. The antenna behavior in a time-domain system is investigated in Sec. 3.

2.2 TEM Horn Antenna

The second wideband antenna discussed in the thesis is a wideband transverse electromagnetic (TEM) horn antenna [18, 41, 71, 127] which is used for exciting propagating waves in a parallel-plate waveguide, see Fig. 7. The antenna is designed for broadband scattering measurements with the requirement of having a sufficiently flat phase front at a short distance from the antenna. The TEM horn antenna can be categorized as a travelling wave antenna with a broadband impedance matching and short transient response [127]. These antennas are widely used in impulse radar, ground penetrating radar [46], electromagnetic compatibly (EMC) tests [68], and wideband scattering measurements [7].

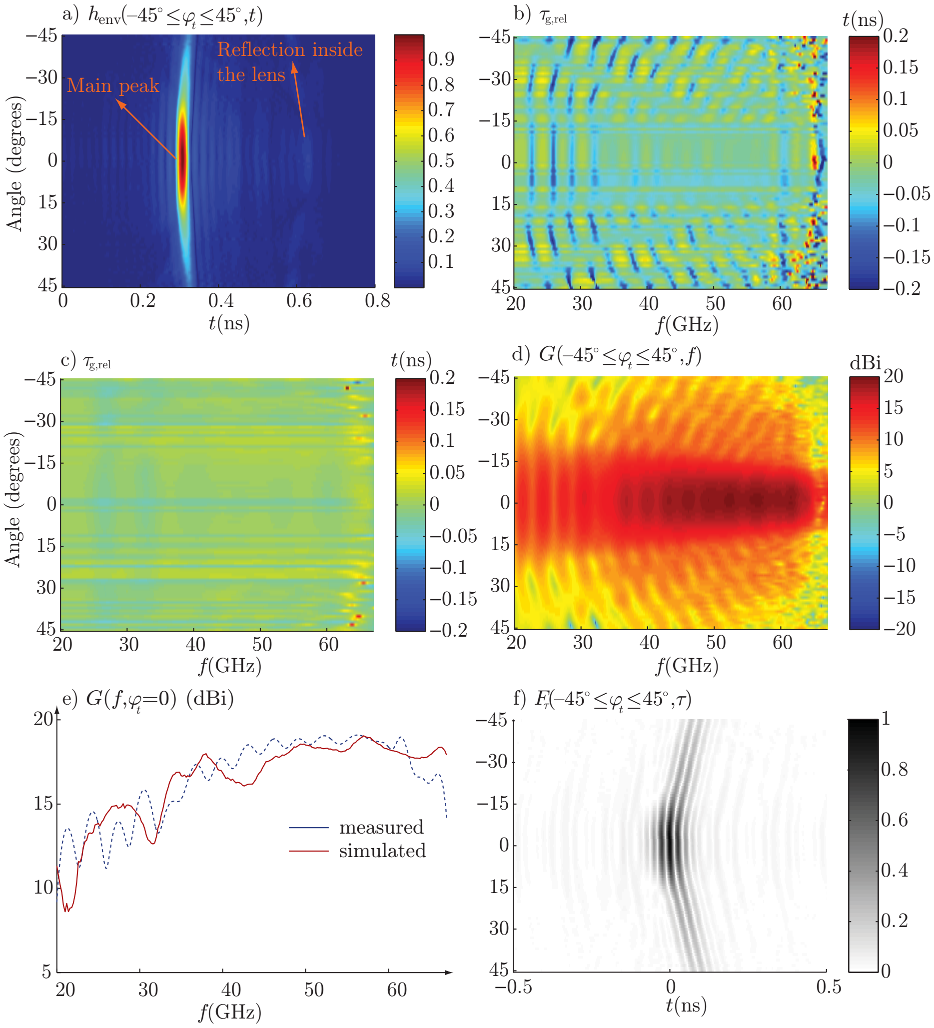

Figure 6: Measured time-domain properties of the leaky lens antenna in ±45° scan around the main beam of the antenna, see Fig 5. a) Envelope of the band limited impulse response (20-67 GHz). b) Relative group delay of the leaky lens antenna, $\tau_{\mathrm{g,rel}}$, in (2.3). c) Relative group delay of the antenna by gating 400 ps around the main peak of the received signal. d) Gain of the leaky lens antenna from 20 GHz to 67 GHz in dB scale. e) Simulated (solid) and measured (dashed) antenna gain in the forward direction. f) Angular dependent fidelity factor of the antenna defined in (2.5).

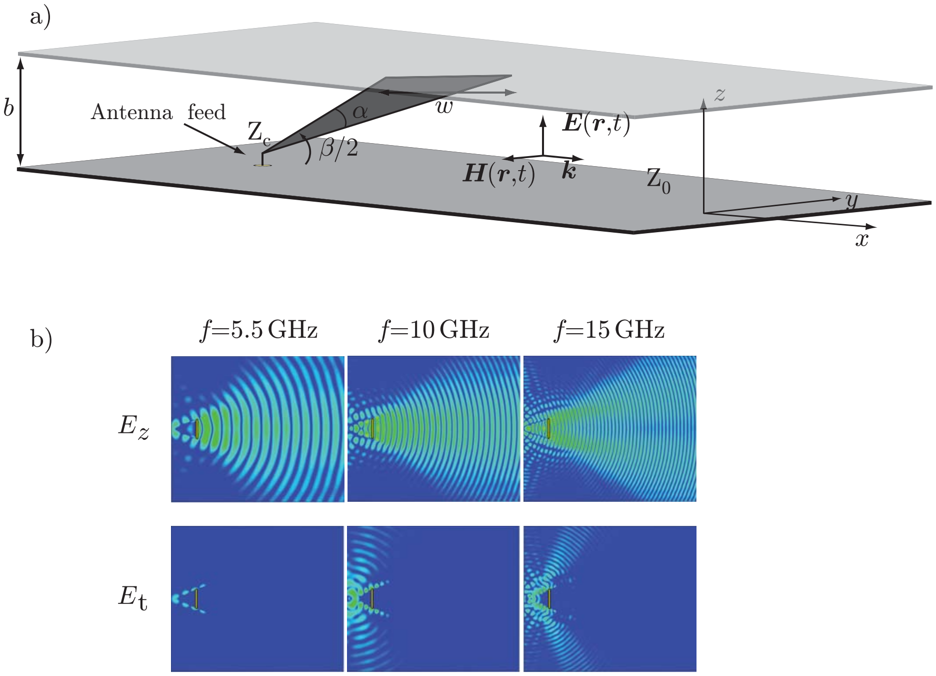

Figure 7: TEM horn antenna and field propagation. a) TEM horn antenna with aperture width $w = 120\,\mathrm{mm}$ inside the parallel-plate waveguide with the height $b = 20\,\mathrm{mm}$, the angle at the apex, α, and the separation angle between the antenna and its image, β. The electric field is $\boldsymbol{E}(\boldsymbol{r}, t)$, the magnetic field is denoted by $\boldsymbol{H}(\boldsymbol{r}, t)$ and $\boldsymbol{k}$ is the wavenumber in the direction of propagation. b) Normal component, E_z, and tangential component, E_t, of the electric field at height $z = b/2$. The first cutoff for TM_1 and TE_1 is at 7.5 GHz and the second one for TM_2 and TE_2 at 15 GHz.

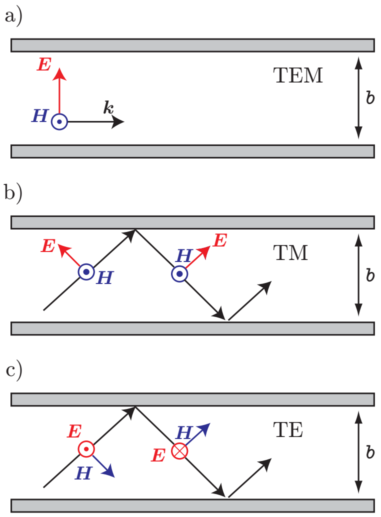

Figure 8: Propagating modes in a parallel-plate waveguide. a) Transverse electric and magnetic (TEM) modes. b) Transverse magnetic (TM_m) modes ($m = 0, 1, 2, \ldots$). c) Transverse electric (TE_m) modes ($m = 1, 2, \ldots$).

The field propagation mechanism of a TEM horn antenna is very similar to that of a parallel-plate waveguide. In both cases the electric field is uniform transverse to the direction of propagation and generated by the voltage difference between the two plates and the magnetic field is produced by the current flow on the plates [117]. The fundamental propagating mode inside a parallel-plate waveguide is a TEM mode, which has the electric and magnetic fields perpendicular to the direction of propagation, see Fig. 8(a). The field propagation inside a parallel-plate waveguide is also decomposed to transverse electric (TE) and transverse magnetic (TM) modes as shown in Fig. 8(b-c). TE_m and TM_m modes have the same cutoff frequencies and are given by [117]

$$f_{\mathrm{cm}} = \frac{mc_0}{2b\sqrt{\mu_{\mathrm{r}}\epsilon_{\mathrm{r}}}}, \tag{2.6}$$

where $m = 0, 1, 2, \ldots$ for TM and $m = 1, 2, \ldots$ for TE modes, is the index for the waveguide modes, and μ_{r} and ϵ_{r} are the relative permeability and permittivity, respectively, of the medium inside the parallel-plate waveguide. It should be noted that the TM_0 mode is the same as the TEM mode. The details of the waveguide modes and the expansion of the fields in cylindrical modes are *e.g.*, given in [143]. The TEM horn antenna designed for a parallel-plate waveguide should be characterized with respect to the higher order waveguide modes. The antenna geometry is defined by the angle at the apex, α, and the separation angle between the antenna and its image, β, as depicted in Fig. 7. The metallic plate of the antenna can be divided into many microstrip line segments with the height from the ground plane, b, and the width, w, such that

$$\alpha = 2 \arctan \left[\frac{w}{2b} \sin(\beta/2) \right]. \tag{2.7}$$

The characteristic impedance of each microstrip line segment is related to the height and the width of the lines. Krause [79] proposed a model to calculate the impedance of a microstrip line as

$$Z = \frac{\eta_0}{\sqrt{\epsilon_r} \left[\left(\frac{w}{b} \right) + 2 \right]}, \tag{2.8}$$

where $\eta_0 \approx 120\pi\,\Omega$ is the intrinsic impedance of free space, ϵ_{r} is the relative dielectric constant of the material between the microstrip line and the ground plane. The antenna is designed and optimized according to (2.8) to give the best matching inside the parallel-plate waveguide and yet easy to fabricate. The separation between the plates was chosen to $b = 20\,\mathrm{mm}$, however due to manufacturing inaccuracies the final height $b = 21.3$ mm. The heights of the antennas were also adjusted to 21.3 mm. The height of the waveguide determines the propagating modes inside the waveguide. Above the first cutoff frequency, $f = 7\,\mathrm{GHz}$, the TE_1 and TM_1 modes can propagate; above second cutoff frequency, $f = 14\,\mathrm{GHz}$, the TE_2 and TM_2 modes can propagate; and so on. The normal and tangential components of the electric field generated by the antenna at different frequencies are illustrated in Fig.7(b). The effect of the higher order modes is small for forward scattering measurements presented in Paper IV and Paper V; since measured forward scattering in (4.9) is weighted by the inverse of the wavenumber squared which reduces the unwanted effects at higher frequencies.

The measured reflection coefficient of the antenna inside the parallel-plate waveguide is shown in Fig. 9(a) by solid blue lines. The antenna is well matched for the intended application from 1 GHz to 20 GHz and the oscillations are due to the impedance mismatch at the aperture of the antenna. By inserting a microwave absorber on top of the antenna, these oscillations can be reduced. This is similar to the time gating of the main reflection of the signal due to the antenna mismatch at the port of the antenna and ignoring the aperture mismatch. The numerical time gated reflection coefficient is shown in Fig. 9 by the green curves and the reduced reflection coefficient using a microwave absorber is illustrated by the red curves. The prototype of the TEM horn antenna is depicted in Fig. 9(b).

The time-domain characterization method based on (2.2) and [40, 110] can be applied to 3D antennas in free-space. The derivation in [40] is based on the 3D potential vector and separating the input currents and the impulse response of the antenna. In 2D problems, however, defining an impulse response is a more demanding task due to the complications in separating the terms in the electric field [86, 147]. In order to simplify the problem, the path loss model for two

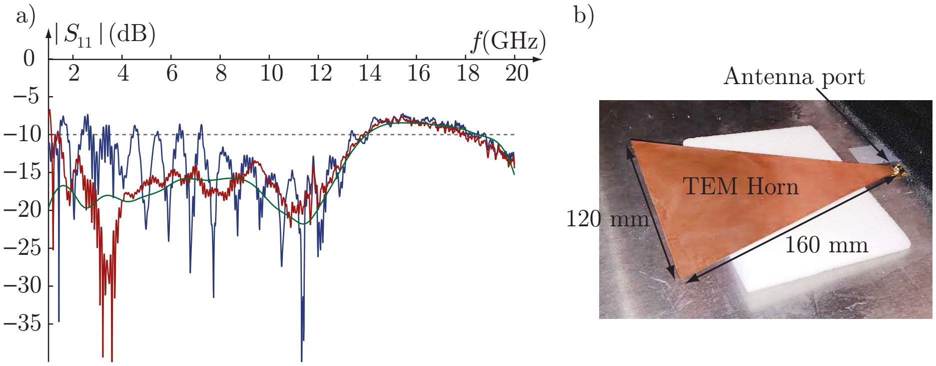

Figure 9: TEM horn antenna. a) Magnitude of the reflection coefficient (blue curves). The reflection coefficient of the antenna when isolating the aperture reflection using absorbing material (red curves) and reflection coefficient by gating the blue curves to remove the aperture reflection (green curves). b) The prototype of the antenna.

dimensional antennas is approximated by

$$S_{21} = H^2(\varphi, \omega)\sqrt{\frac{c_0}{\pi \omega d}}\,\mathrm{e}^{\frac{-\mathrm{j}\omega d}{c_0}}\,\mathrm{e}^{-\alpha_{\mathrm{c}} d}, \tag{2.9}$$

wherein it is assumed that the transmission is between two identical antennas with transfer function, $H(\omega, \varphi)$, and distance $d = 0.98\,\mathrm{cm}$ is used in Fig. 10. The power density averaged over the height of the waveguide (W/m) is proportional to $(2\pi d)^{-1}$, and the antenna effective aperture is approximated by $\lambda/(2\pi)$. The loss due to the finite conductivity in the plates of the parallel-plate waveguide is denoted by α_{c}. The conductor loss can be ignored for short distances, *i.e.*, $\alpha_{\mathrm{c}} d \approx 0$. Note that the decay factor inside a parallel-plate waveguide for TEM mode propagation is inversely proportional to the square root of the distance similar to the two dimensional problems [147]. The impulse response of the antenna, $h(t, \varphi = 0)$, can then be estimated by the inverse Fourier transform of the transfer function. The band-limited response of the antenna in the forward direction is shown in Fig. 10(a). The main peak of the impulse response at 0.52 ns represents the direct path from the antenna port to the aperture. The second highest peak approximately 1 ns after the first peak represents the reflection from the aperture of the antenna due to a small mismatch between the antenna and the parallel-plate waveguide.

The relative group delay of the antenna estimated from (2.3) and using a 5 ns time window around the main peak of the antenna is shown in Fig. 10(b) over the frequency range 1 to 20 GHz. The fluctuations of the antenna group delay of the antenna are due to the reflection from the aperture of the antenna. To verify this, the group delay of the antenna using a narrower time window, 2 ns, and removing the reflection from the antenna aperture is shown in Fig. 10(b) by red curves.

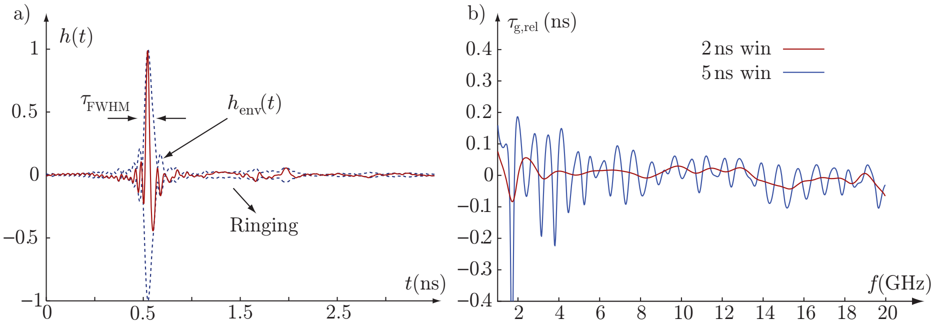

Figure 10: Measured time-domain properties of the TEM horn antenna. a) Band limited impulse response of the TEM horn antenna in the forward direction, $h(t)$ (solid lines) and its envelope, $h_{\mathrm{env}}(t)$ (dashed-lines). b) Relative group delay of the transfer function of the antenna, $\tau_{\mathrm{g,rel}}$, in (2.3).

3 Time-Domain System

Impulse radiation at mm-wave frequencies is beneficial in several applications. In radar and imaging systems, the use of high frequency short pulses increases the accuracy and resolution [109, 132]. In wireless systems and sensor networks this can be utilized to produce high or energy-efficient low data rate communications [106]. This thesis presents a time-domain system consisting of a wavelet generator and non-dispersive antennas. The leaky lens antennas, in Sec. 2.1, with stable radiation properties and promising time-domain behavior together with RTD-MOSFET wavelet generators that produce short pulses at mm-wave frequencies are utilized for impulse applications.

3.1 Mm-Wave Wavelet Generator

There are a variety of methods to generate ultra-wideband (UWB) short pulses at different frequencies [11,38,47,66,118,125]. The application of commercialized wideband systems have been initiated mainly from 2002 when the Federal Communication Commission (FCC) introduced an unlicensed band from 3.1 GHz to 10.6 GHz [34]. The use of UWB technology at mm-wave frequencies for different applications are discussed in [9, 13, 112, 116]. Short pulse generators, in general, fall into four main categories [12]: 1) signal multipliers [11], 2) digital generators [47], 3) impulse filter response [66], and 4) pulse oscillators [13, 38, 114]. The impulse radio UWB (IR-UWB) circuit used in this thesis is based on a novel $\mathrm{In}_{0.53}\mathrm{Ga}_{0.47}\mathrm{As}$ RTD-MOSFET short pulse generator [38]. These short mm-wave pulses are also known as wavelets [38].

These devices are fabricated based on III–V compound semiconductors that compared to silicon technology allow higher operation frequencies [70]. Negative differential conductance of the RTD is used to generate oscillations. It should be

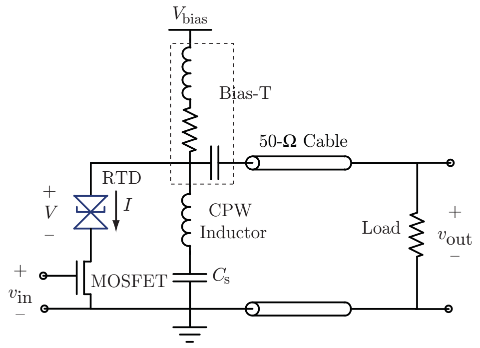

Figure 11: Circuit model of the wavelet generator consisting of a fast switching MOSFET in series with an RTD. It should be noted that in some cases the load (antenna) is directly connected to the output of the bias-T, see Fig. 13.

noted that negative differential conductance, in contrary to practice, causes decreasing current for increasing voltage. A short baseband pulse on the MOSFET gate can thereby be used to switch in or disconnect the RTD. This generates a mm-wave pulse. The oscillation frequency of the generated pulse depends on the RTD capacitance and the on-chip resonant circuit [38]. A wavelet generator that generates 100 ps pulses at 60 GHz is shown in Fig. 12. An input baseband 100 ps rectangular pulse is shown in Fig. 12(a). The input pulse is transmitted to the gate of the MOSFET as shown in Fig. 12(b). The generated mm-wave 100 ps pulse is then taken from the output of the circuit and is illustrated in Fig. 12(c). The pulse is centered at 60 GHz and has a main lobe width of 20 GHz and 10 dB bandwidth of 14 GHz. The power spectral density of the generated signal is shown in Fig. 12(d).

3.2 Leaky Lens Antenna System

In order to validate the time-domain properties of the aforementioned antenna system, transmission of a wavelet is tested over a link consisting of antennas and the wavelet generator, see Fig.13. An Agilent N4906B is used to produce 100 ps baseband rectangular pulses. The pulses are then fed to the wavelet generator, which is typically biased at 1-2 V. The circuit generates a mm-wave short pulse which is then transferred to the transmitting antenna via a bias-T. The transmitting antenna converts the voltage delivered at the antenna port to electromagnetic waves with high fidelity. The radiated signal is then received by an identical antenna and captured by a LeCroy 100H oscilloscope with a 100 GHz sampling head. Three cases are tested: 1) the output of the wavelet generator is connected directly to the sampling oscilloscope via a cable (reference). 2) The leaky lens antennas are connected at the transmitting and receiving sides. 3) Standard V-band (50-75 GHz) gain horn antennas are connected at the transmit-

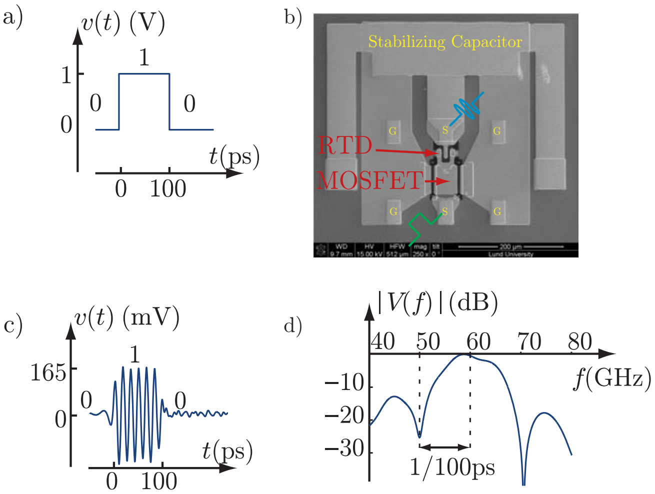

Figure 12: Mm-wave wavelet generator. a) Baseband 100 ps pulse. b) Prototype of an RTD-MOSFET wavelet generator c) The out pulse by the wavelet generator. d) Normalized power spectral density of the generated pulse.

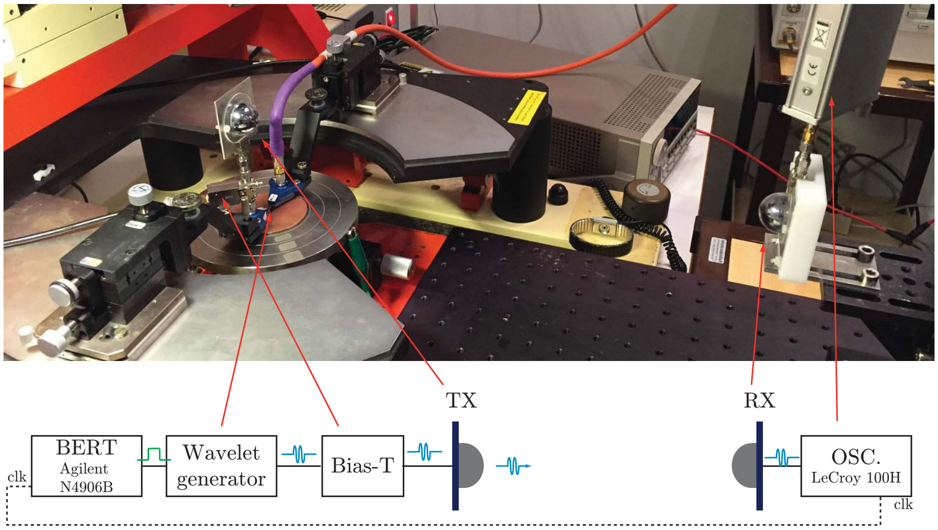

Figure 13: Experimental time-domain setup consisting of a wavelet generator connected to the leaky lens antenna on the transmitting side and a leaky lens antenna connected to the sampling head of a LeCroy 100H oscilloscope on the receiving side. Baseband pulses are 100 ps long and are generated by a BERT Agilent N4906B.

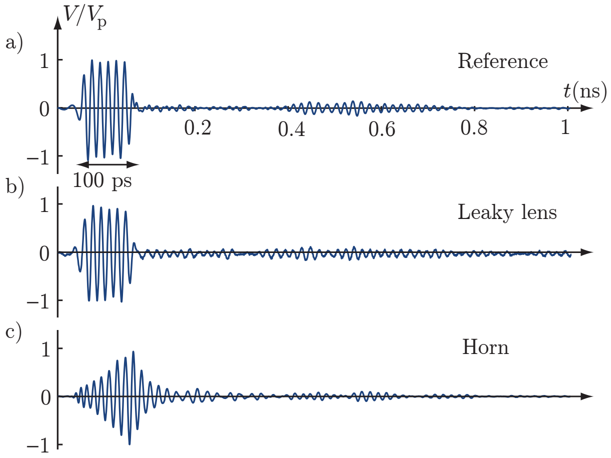

Figure 14: Received pulses normalized with their maximum amplitude, V_P. a) Reference pulse that is measured by connecting the output of the wavelet generator to the sampling head of the oscilloscope. b) The received pulse when the output of the wavelet generator is connected to a leaky lens antenna and an identical antenna is used on the receiving side. c) Received pulse with horn antennas in the transmitting and receiving sides.

ting and receiving sides. The reference signal, which is a 100 ps wavelet centered at 60 GHz is shown in Fig.14(a). The transmission through the leaky lens antennas and horn antennas are shown in Fig.14(b-c), respectively. As is shown, the time-domain signal of the lens antennas is similar to the reference signal as the pulse shape is preserved. For horn antennas, however, the pulse is distorted and widened. Due to the waveguide interfaces of the standard gain horn antennas, the pulse shape is affected by the waveguide dispersion.

4 Wideband Metamaterial Characterization

Metamaterials are synthesized materials that are artificially designed and fabricated with properties that are not found in nature [6, 25, 27, 39, 97]. One of the first metamaterial investigation was the focusing using left handed [21, 28] planar lens by V.G. Veselago in 1967 [150]. One way to realize metamaterials is to use periodic structures with electrically small (sub wavelength) unit cells. In some applications, these uncommon scattering properties are required to be valid over a wide range of frequencies; however this is not always achievable.

The forward scattering sum rule and the optical theorem can be used to determine physical bounds on periodic structures. The forward scattering sum rule is related to the total (extinction) cross section of scatterers through the optical theorem [65, 103, 138]. The forward scattering sum rule is an identity indicating that the all wavelength electromagnetic interactions of the total cross section of an object are given by the static polarizability of the object that can be found by solving a relatively simple problem. Purcell was the first to discuss this effect on dielectric spheroids [119]. Forward scattering sum rule is, in recent years, generalized to arbitrary objects [52, 134], antennas [53–55, 133], and metamaterials [56, 135].

In this work the optical theorem and the forward scattering sum rule is investigated for parallel-plate waveguides. Theoretical values are verified by measuring the forward scattering in a parallel-plate waveguide and capacitance change in a parallel-plate capacitor.

4.1 Optical Theorem for Bounded Scatterer

Consider a TEM mode with linearly polarized plane wave, $\boldsymbol{E}_\mathrm{i}(\boldsymbol{r}) = \hat{\boldsymbol{z}} E_0 \mathrm{e}^{-\mathrm{j}kx}$ incident on a scatterer confined between the plates of a parallel-plate waveguide. $\hat{\boldsymbol{z}}$ is the polarization vector and k is the wavenumber. The scatterer is enclosed by an imaginary surface S that is defined by the outward pointing normal unit vector $\hat{\boldsymbol{n}} = \hat{\boldsymbol{\varrho}} = \hat{\boldsymbol{x}} \cos\varphi + \hat{\boldsymbol{y}} \sin\varphi$, see Fig. 1. If the object is dissipative, a fraction of power is absorbed by the object, P_a, and the rest is scattered, P_s. The total power is the sum of the outward-going scattering Poynting vector and the inwardly directed component of the total field Poynting vector [65, p. 501]

$$\begin{aligned} P_\mathrm{tot} = P_\mathrm{a} + P_\mathrm{s} &= \frac{1}{2} \mathrm{Re} \int_S \hat{\boldsymbol{n}} \cdot \big(\boldsymbol{E}_\mathrm{s} \times \boldsymbol{H}_\mathrm{s}^* - (\boldsymbol{E}_\mathrm{i} + \boldsymbol{E}_\mathrm{s}) \times (\boldsymbol{H}_\mathrm{i} + \boldsymbol{H}_\mathrm{s})^* \big) \,\mathrm{dS} \\ &= -\frac{1}{2} \mathrm{Re} \int_S \hat{\boldsymbol{n}} \cdot (\boldsymbol{E}_\mathrm{s} \times \boldsymbol{H}_\mathrm{i}^* + \boldsymbol{E}_\mathrm{i} \times \boldsymbol{H}_\mathrm{s}^*) \,\mathrm{dS}, \end{aligned} \tag{4.1}$$

where $\boldsymbol{E}_\mathrm{s} = \boldsymbol{E} - \boldsymbol{E}_\mathrm{i}$ and $\boldsymbol{H}_\mathrm{s} = \boldsymbol{H} - \boldsymbol{H}_\mathrm{i}$ denote the scattered electric and magnetic fields, receptively. It should be noted that the surface S does not include the metallic plates at $z = 0$ and $z = b$. With some rearrangements and inserting the incident field, $\boldsymbol{E}_\mathrm{i}(\boldsymbol{r}) = \hat{\boldsymbol{z}} E_0 \mathrm{e}^{-\mathrm{j}kx}$, the total power can be expressed as

$$P_\mathrm{tot} = \frac{-b}{2\eta_0} \mathrm{Re} \int_0^{2\pi} E_0^* \mathrm{e}^{\mathrm{j}kx} \hat{\boldsymbol{z}} \cdot \langle \boldsymbol{E}_\mathrm{s} (\hat{\boldsymbol{n}} \cdot \hat{\boldsymbol{x}}) + \eta_0 \boldsymbol{H}_\mathrm{s} \times \hat{\boldsymbol{n}} \rangle \rho \,\mathrm{d}\varphi, \tag{4.2}$$

where $\langle . \rangle$ denotes the mean value of the fields over the height of the waveguide. The total cross section, defined as the total power normalized by the incident power flux density, $P_\mathrm{i} = |E_0|^2 / 2\eta_0$, takes the form,

$$\sigma_\mathrm{tot} = -\mathrm{Re} \Big\{ \frac{b}{E_0} \int_0^{2\pi} \mathrm{e}^{\mathrm{j}kx} \hat{\boldsymbol{z}} \cdot \langle \boldsymbol{E}_\mathrm{s} (\hat{\boldsymbol{n}} \cdot \hat{\boldsymbol{x}}) + \eta_0 \boldsymbol{H}_\mathrm{s} \times \hat{\boldsymbol{n}} \rangle \rho \,\mathrm{d}\varphi \Big\}. \tag{4.3}$$

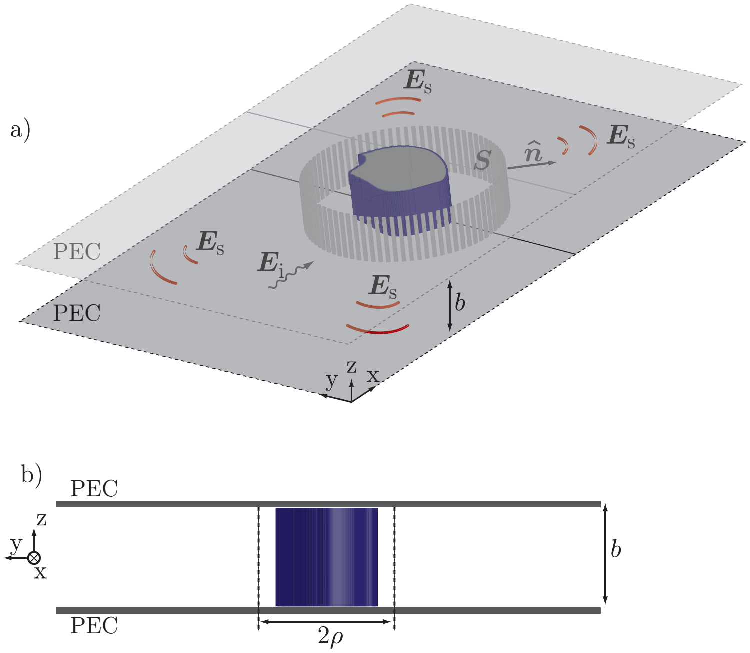

Figure 15: Scattering geometry for a bounded scatterer inside the parallel-plate waveguide. a) Perspective view. $\boldsymbol{E}_\mathrm{i}$ is the incident field and $\boldsymbol{E}_\mathrm{s}$ is the resulting scattered field. b) Front view. The scatterer is enclosed by an imaginary surface S of radius ρ and normal vector $\hat{\boldsymbol{n}}$.

The integral in (4.3) is the two-dimensional far-field amplitude, f_s, and by inserting this into (4.3) the total cross section can be simplified to [147]

$$\sigma_\mathrm{tot} = -4b\,\mathrm{Re}\left\{\frac{f_\mathrm{s}}{\mathrm{j}kE_0}\right\}. \tag{4.4}$$

The resulting total cross section is similar to the two-dimensional total cross section and the only difference is the height of the waveguide, b, in (4.4). It is possible to conclude that the parallel-plate waveguide can be considered as a quasi 2-D measurement setup for the TEM mode.

4.2 Forward Scattering Sum Rules

The forward scattering sum rule is an identity stating that the total cross section of an object integrated over the entire spectrum is given by its (static) polarizability [19, 58, 144]. Holomorphic functions such as positive real (PR) functions or Herglotz (Nevalinna) functions are used to derive the forward scattering sum rules [19, 57, 60, 105]. This gives an upper bound on the total interaction between the fields and the object. The PR function, $\mathscr{P}(\kappa)$, is given by the forward

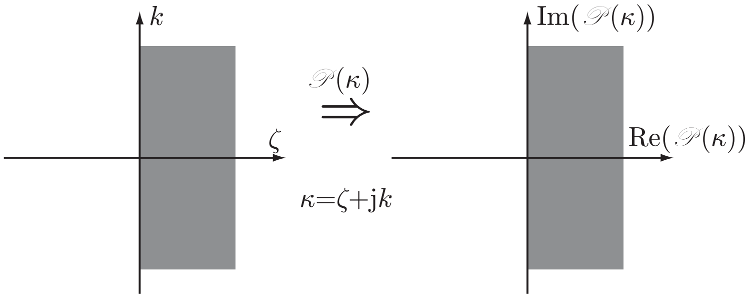

Figure 16: Positive real function, $\mathscr{P}(\kappa)$ for $\kappa = \zeta + \mathrm{j}k$, is holomorphic and maps the right half plane to the right half plane, *i.e.*, $\mathrm{Re}\{\mathscr{P}(\kappa)\} \geqslant 0$ for $\mathrm{Re}\{\kappa\} > 0$.

scattering amplitude in (4.4) as

$$\mathscr{P}(\kappa) = -\frac{4b}{\kappa E_0} f_{\mathrm{s}}(\kappa), \tag{4.5}$$

where $\kappa = \zeta + \mathrm{j}k$ and $\mathrm{Re}\{\mathscr{P}(\kappa)\} \geqslant 0$ for $\mathrm{Re}\{\kappa\} > 0$ and $\mathscr{P}(\kappa)$ is holomorphic in the right half plane, see Fig.16 [58]. Comparing (4.4) and (4.5), we can rewrite the expression of the total cross section as

$$\sigma_{\mathrm{tot}} = \mathrm{Re}\{\mathscr{P}(\kappa)\}. \tag{4.6}$$

This shows that the total cross section is related to a PR function, $\mathscr{P}(\kappa)$. The function $\mathscr{P}(\kappa)$ has a low frequency asymptotic expansion that is proportional to the polarizability of the object as

$$\mathscr{P}(\kappa) = \kappa\big(\hat{\boldsymbol{z}} \cdot \boldsymbol{\gamma}_{\mathrm{e}} \cdot \hat{\boldsymbol{z}} + \hat{\boldsymbol{y}} \cdot \boldsymbol{\gamma}_{\mathrm{m}} \cdot \hat{\boldsymbol{y}}\big) + o(\kappa) \quad \text{as } \kappa \to 0, \tag{4.7}$$

where $\boldsymbol{\gamma}_{\mathrm{e}}$ and $\boldsymbol{\gamma}_{\mathrm{m}}$ are the electric and magnetic polarizability dyadics, respectively. At the low frequency limit ($k \to 0$) the parallel-plate waveguide is equivalent to a parallel-plate capacitor with the electric field, $\boldsymbol{E}_0$, uniformly distributed between the plates, as shown in Fig. 17. Using image theory the problem in Fig. 17(a) is equivalent to Fig. 17(b) and it means that the polarizability $\boldsymbol{\gamma}_{\mathrm{e}}$ equals half of the polarizability found from the image problem with height $2b$. It is observed that Fig. 17(b) and Fig. 17(c) which is a periodic structure are identical and methods used in [58, 129] to determine the polarizability for periodic structures can be used. In this case the electric polarizability using the static electric field, $\boldsymbol{E}(\boldsymbol{r}, 0)$, and permittivity dyadics, $\boldsymbol{\epsilon}(\boldsymbol{r}, 0)$, over the unit cell volume V is found as [134, 135]

$$\hat{\boldsymbol{z}} \cdot \boldsymbol{\gamma}_{\mathrm{e}} \cdot \hat{\boldsymbol{z}} = \frac{1}{E_0} \int\limits_V \hat{\boldsymbol{z}} \cdot (\boldsymbol{\epsilon}(\boldsymbol{r}, 0)/\epsilon_0 - \mathbf{I}) \cdot \boldsymbol{E}(\boldsymbol{r}, 0)\, \mathrm{d}V, \tag{4.8}$$

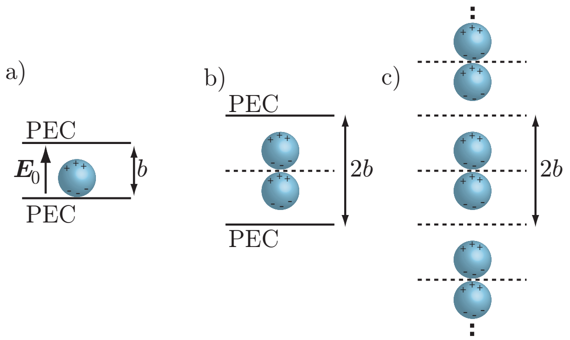

Figure 17: Periodic equivalent problem. a) An object is placed in an arbitrary position between the plates of a capacitor. b) An equivalent problem for part-a by placing the object and its image at the midpoint between two plates. c) The equivalent periodic problem.

where $\mathbf{I}$ is the 3×3 identity matrix and ϵ_0 denotes the permittivity of vacuum. The resulting polarizability gives an upper bound on the total cross section weighted by the inverse of the wavenumber square integrated over all spectrum and is the forward scattering sum rule [19] as

$$\frac{2}{\pi}\int_0^\infty \frac{\sigma_{\text{tot}}(\hat{\boldsymbol{x}},\hat{\boldsymbol{z}},k)}{k^2}\,\mathrm{d}k = \hat{\boldsymbol{z}}\cdot\boldsymbol{\gamma}_{\mathrm{e}}\cdot\hat{\boldsymbol{z}} + \hat{\boldsymbol{y}}\cdot\boldsymbol{\gamma}_{\mathrm{m}}\cdot\hat{\boldsymbol{y}}. \tag{4.9}$$

This can be simplified by interchanging the wavenumber with wavelength, $\lambda = 2\pi/k$, and assuming a non-magnetic object, *i.e.*, $\mu=\mu_0$ and hence $\boldsymbol{\gamma}_{\mathrm{m}}=0$ giving

$$\frac{1}{\pi^2}\int_0^\infty \sigma_{\text{tot}}(\lambda)\,\mathrm{d}\lambda = \hat{\boldsymbol{z}}\cdot\boldsymbol{\gamma}_{\mathrm{e}}\cdot\hat{\boldsymbol{z}} = \gamma, \tag{4.10}$$

where γ is the co-polarized electric polarizability.

4.3 System Identification

Utilizing causality, passivity and the properties of PR functions and separating the real part from the imaginary part of the PR function, the forward scattering in (4.5) satisfies the dispersion relation

$$\operatorname{Im}\mathscr{P}(\mathrm{j}k) = b_1 k + \frac{1}{\pi}\int_{-\infty}^{\infty}\frac{1}{\xi-k}\operatorname{Re}\mathscr{P}(\mathrm{j}\xi)\,\mathrm{d}\xi, \tag{4.11}$$

where b_1 is a non-negative real valued constant. The integral is a Hilbert transform [75, 76] and relates the imaginary part of the forward scattering to its real part. This property gives the possibility to estimate the imaginary part of $\mathscr{P}(\mathrm{j}k)$ from its real part which might be less affected by noise or easier to model. On the other hand the forward scattering sum rule in (4.9) states that the total cross section, $\sigma_{\mathrm{tot}} = \operatorname{Re}\mathscr{P}(\mathrm{j}k)$, integrated over all frequencies is given by the polarizability of the scatterer. These two conditions together with the passivity condition of the PR function, *i.e.*, $\operatorname{Re}\mathscr{P}(\mathrm{j}k) \geqslant 0$, can be used to construct a convex optimization problem as [20]

$$\begin{aligned} &\text{minimize} && \left\| \mathscr{P}(\mathrm{j}k) - \mathscr{P}^{(\mathrm{M})}(\mathrm{j}k) \right\| \\ &\text{subject to} && \operatorname{Re}\mathscr{P}(\mathrm{j}k) \geqslant 0,\ k \in [k_0, k_3], \\ & && \frac{2}{\pi}\int\limits_{k_0}^{k_3} \frac{\operatorname{Re}\mathscr{P}(\mathrm{j}k)}{k^2}\,\mathrm{d}k \leqslant \gamma_{\mathrm{u}}, \end{aligned} \tag{4.12}$$

where $\mathscr{P}^{(\mathrm{M})}(\mathrm{j}k)$ denotes the noisy measurement values and $\mathscr{P}(\mathrm{j}k)$ is the closest PR function to the measurement values that satisfies the passivity, dispersion relation and the forward scattering sum rule. The modeling interval is $k_0 < k < k_3$ and γ_u is the upper bound on the polarizability.

4.4 Methodology and Results

The forward scattering sum rule of a periodic structure over a wide range of frequencies can be measured by realizing the periodic structure from a bounded scatterer using a parallel-plate waveguide. The static polarizability of the object can also be measured using a parallel-plate capacitor which is a relatively simple setup.

The parallel-plate waveguide, as shown in Fig. 18, consists of two $1 \times 1.5\,\mathrm{m}^2$ Aluminum plates and two broadband in-house fabricated TEM horn antennas, discussed in Sec. 2.2. Microwave absorbers are used to reduce the reflection at the side walls in the dynamic measurements. The TEM horn antennas are fed via coaxial transitions through the bottom plate of the waveguide and they are placed at a distance of $d = 98\,\mathrm{cm}$ from each other. The object to be characterized is inserted inside the waveguide and placed at the midpoint between the two antennas, see Fig. 18(a). The forward scattering is normalized by the height of the waveguide, *i.e.*, $\mathscr{P}_b = \mathscr{P}/b$, according to (4.4) for a scatterer, located at the distance $d_1 = 49\,\mathrm{cm}$ from the transmitting antenna, and takes the form

$$\mathscr{P}_b(\mathrm{j}k) = \frac{-4f_{\mathrm{s}}}{\mathrm{j}kE_0} \approx \frac{4}{\mathrm{j}k}\left(1 - \frac{S_{21,\mathrm{obj}}}{S_{21,\mathrm{emp}}}\right)\sqrt{\frac{\pi\mathrm{j}kd_1(d-d_1)}{2d}}, \tag{4.13}$$

where $S_{21,\mathrm{obj}}$ and $S_{21,\mathrm{emp}}$ are the measured S-parameters in the presence and the absence of the scatterer, respectively. The ratio between the measured values in the absence and presence of the object presents the calibration process which

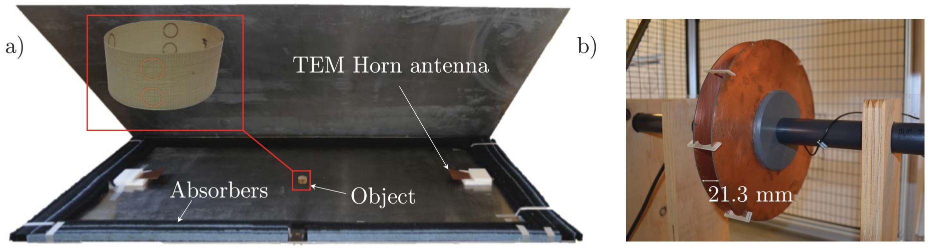

Figure 18: Parallel-plate waveguide and parallel-plate capacitor to estimate the left-side and right hand side of (4.9). a) The parallel-plate waveguide setup consists of two TEM horn antennas and microwave flat absorbers. The distance between the antennas is 98 cm and the object is placed at the midpoint between the antennas. The two plates are 150 × 100 cm^2 and separated by 21.3 mm. b) The parallel-plate capacitor setup consists of two circular copper plates held by plastic arms. The distance between the plates is 21.3 mm and is fixed by plastic distance supports.

removes unwanted effects and setup inaccuracies. The S-parameters are recorded using an HP 8720 VNA.

The polarizability of the object is measured inside a parallel-plate capacitor, see Fig. 18(b). The parallel-plate capacitor is similar to a parallel-plate waveguide at low frequencies (static). By inserting an object between the plates, the capacitance changes depending on the material of the scatterer and the induced charges of the metallic parts in the object. The polarizabilty of the object is proportional to the amount of capacitance change and can be written as [80]

$$\gamma_{\mathrm{e}} = \hat{\boldsymbol{z}} \cdot \boldsymbol{\gamma}_{\mathrm{e}} \cdot \hat{\boldsymbol{z}} = \frac{\Delta C d^2}{\epsilon_0}, \tag{4.14}$$

for periodic structures. In order to experimentally illustrate the forward scattering sum rule and the convex optimization problem to predict the all spectrum electromagnetic interactions, an example of a bounded scatterer inside the waveguide is considered. The object is a cylindrical shaped split ring resonators (SRRs) printed on 18 μm thick Arlon Diclad880 with relative permittivity $\epsilon_{\mathrm{r}} = 2.17$. The split ring resonators, as shown in Fig. 19, are designed to be resonant at 5.5 GHz. The polarizability of the object inside the parallel-plate capacitor is estimated to $\gamma_{\mathrm{e}} = 3.65 \pm 0.04\,\mathrm{cm}^3$. The changes of the capacitance are measured using an Agilent 4294A precision impedance analyzer.

The dynamic properties of the scatterer are measured inside the parallel-plate waveguide from 1 to 20 GHz. The averaged forward scattering, $\mathscr{P}_b$, over 10 measurements is shown in Fig. 19 by the solid curves. The real part of the forward scattering which is the total cross section of the object shows a strong blockage at the resonance frequency. Note that the peak value is approximately 3 times larger than the diameter of the object. The amount of the total cross section of

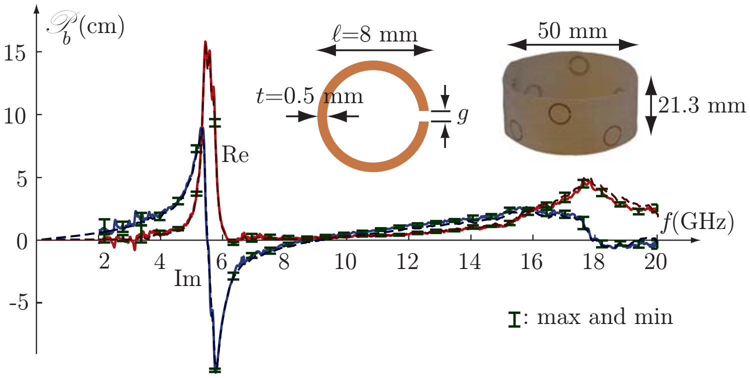

Figure 19: Average of the 10 measurements (solid curves) and the optimal solution (dashed curves) for the forward scattering for an array of circular split rings. Maximum and minimum values over the 10 measurements are illustrated by the bars.

a perfectly conducting (PEC) cylinder with the same diameter as of the object is about 12.5 cm which is less than that of a few SRRs printed on a thin substrate with low permittivity. The bars in Fig. 19 show the maximum and minimum of the forward scattering over the 10 measurements. The measurement setup shows a stable performance, except for the low frequencies where the scatterer is in near field of the antennas and the amount of interference and noise is higher. The total cross section integrated from 2 to 20 GHz on the left hand side of the sum rule (4.9) is estimated to 2.75 cm^2. This value gives a lower bound on the polarizability since the measurement is performed over a finite range of frequencies instead of 0 to ∞.

The value of the polarizability estimated from the dynamic measurement is affected by noise producing negative unphysical values of the total cross section. The convex optimization problem (4.12) using passivity and sum rule constraints is formulated in order to improve the estimate and mitigate the spurious resonances. It also gives an all spectrum representation of the total cross section. The solution of the convex optimization problem using the Matlab software for disciplined convex programming (CVX) [50] is shown by dashed lines in Fig. 19. As can be seen from the figure, it removes the negative values and gives a better estimate for lower frequencies. The value of the upper bound γ_{u} is found from a Pareto search [123] over a range of possible solutions. The region between the dynamic and static measurement should be a subset of the search range, shown as the shaded region in Fig.20. In this example the optimum lower bound $\gamma_{\mathrm{e}}^{\mathrm{olb}} = 3.4\,\mathrm{cm}^3$ is chosen as the upper bound of (4.12). The total cross section found by the convex optimization solution integrated from 0 to 20 GHz is 2.87 cm^3 which is 84% of the optimal lower bound, $\gamma_{\mathrm{e}}^{\mathrm{olb}}$. The optimal lower bound is the lowest possible polarizability found from the measurements and the actual value can be greater.

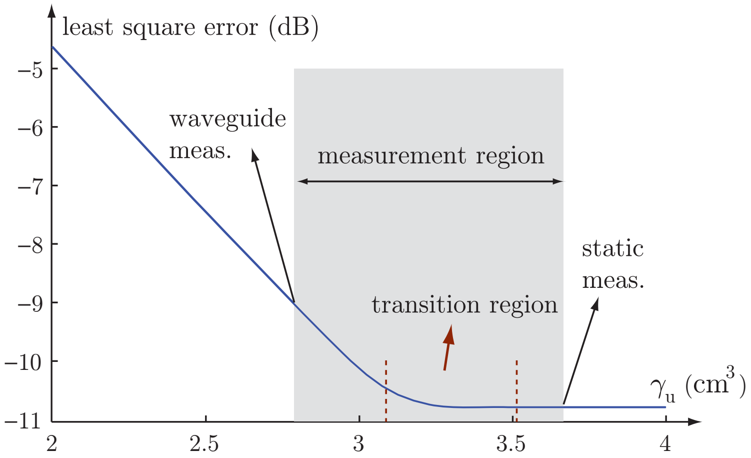

Figure 20: Optimal value of $\left\|\mathscr{P}(\mathrm{j}k) - \mathscr{P}^{(\mathrm{M})}(\mathrm{j}k)\right\|$ (in dB) as a function of the sum rule constraint over the range $\gamma_{\mathrm{u}} = [2,4]\,\mathrm{cm}^3$. The smallest range for search has to be in a region that is obtained from measurements in the quasi-static (right hand side of sum rule in (4.9)) as well as the waveguide measurement (left hand side of sum rule in (4.9)).

5 Time-Domain Material Characterization

Electromagnetic fields in a propagation channel between a transmitter and a receiver are affected by the materials and objects in between. Knowledge about the electrical properties of the materials are needed in order to optimize a wireless link or determine the shape and position of a target in imaging systems. There are a variety of methods for material characterizations, see *e.g.*, [3, 14, 15, 29, 83, 104, 130, 140]. In many cases these properties are determined over a narrow frequency band for a specific application. The extracted parameters are not necessarily valid for other frequency bands and the extraction needs to be done for each specific frequency region. Broadband and time-domain material measurements were first introduced by Nicolson [104]. One of the broadband characterization method is the free-space method [63, 148] where the material under test is placed at some distance from the transmitting and receiving antennas that are usually directive. In Sec. 4 a broadband scattering characterization method for parallel-plate waveguides is presented. In this section a time-domain material characterization method using the time-domain system in Sec. 3 is investigated. Short pulses at mm-wave frequencies are generated using the RTD-MOSFET wavelet generator and transmitted and received by broadband and non-dispersive leaky lens antennas.

5.1 Dielectric Properties

The charges in materials interact with propagating electromagnetic waves. They produce currents and affect the electromagnetic field propagation. At a macroscopic scale, there are relations that relate the fields in free space and the fields that are affected by the material. These relations are known as constitutive relations [65, 72, 82, 108] and $\epsilon(t)$ and $\mu(t)$ are the convolution kernels of constitutive parameters also known as permittivity and permeability kernels, respectively. For time varying fields propagating in isotropic and homogenous dielectric and magnetic materials, the relations are given by [72, 108]

$$\begin{aligned} \boldsymbol{D}(\boldsymbol{r},t) &= \epsilon(t) * \boldsymbol{E}(\boldsymbol{r},t) = \int\limits_{-\infty}^{t} \epsilon(t-t')\boldsymbol{E}(\boldsymbol{r},t')\,\mathrm{d}t' \\ \boldsymbol{B}(\boldsymbol{r},t) &= \mu(t) * \boldsymbol{H}(\boldsymbol{r},t) = \int\limits_{-\infty}^{t} \mu(t-t')\boldsymbol{H}(\boldsymbol{r},t')\,\mathrm{d}t' \end{aligned} \tag{5.1}$$

where $\boldsymbol{D}$ and $\boldsymbol{B}$ are the electric and magnetic flux densities and $\boldsymbol{E}$ and $\boldsymbol{H}$ are the electric and magnetic field intensities, respectively, in the time-domain. In free-space, the permittivity kernel is $\epsilon(t) = \delta(t)\epsilon_0$ where $\epsilon_0 = 8.84 \times 10^{-12}\,\mathrm{F/m}$ and permeability kernel is $\mu(t) = \delta(t)\mu_0$ where $\mu_0 = 4\pi \times 10^{-7}\,\mathrm{H/m}$. In the frequency-domain this relation becomes multiplicative as

$$\begin{aligned} \boldsymbol{D}(\boldsymbol{r},\omega) &= \epsilon(\omega)\boldsymbol{E}(\boldsymbol{r},\omega) \\ \boldsymbol{B}(\boldsymbol{r},\omega) &= \mu(\omega)\boldsymbol{H}(\boldsymbol{r},\omega) \end{aligned} \tag{5.2}$$

There are a variety of material models to model the frequency dependence of the constitutive parameters such as the Debye and Lorentz models [36, 108]. The electric permittivity is a complex number and is expressed as $\epsilon(\omega) = \epsilon_0\epsilon_\mathrm{r}(\omega)$ where $\epsilon_\mathrm{r}(\omega) = \epsilon_\mathrm{r,r}(\omega) + \mathrm{i}\epsilon_\mathrm{r,i}(\omega)$ is the relative permittivity. It should be noted that in this section, similar to Paper II, the time conversion $\mathrm{e}^{-\mathrm{i}\omega t}$ with $\mathrm{i} = -\mathrm{j}$ is used. A propagating electric field in a medium with permittivity $\epsilon(\omega)$ and permeability $\mu(\omega)$ at position $\boldsymbol{r}$ can be expressed as $\boldsymbol{E}(\boldsymbol{r}) = \hat{\boldsymbol{e}}E_0\mathrm{e}^{\mathrm{i}k_\mathrm{c}\hat{\boldsymbol{k}}\cdot\boldsymbol{r}}$, where $\hat{\boldsymbol{e}}$ is a unit vector in the polarization direction, $\hat{\boldsymbol{k}}$ denotes the propagation direction and k_c is the complex wavenumber and can be written as

$$k_\mathrm{c} = \beta + \mathrm{i}\alpha = k_0 n, \tag{5.3}$$

wherein β is the phase constant, α denotes the attenuation constant, $k_0 = \omega/c_0$ is the free-space wavenumber, and $n(\omega) = \sqrt{\mu_\mathrm{r}(\omega)\epsilon_\mathrm{r}(\omega)}$ is the complex refractive index. The real part of the refractive index stands for phase shifts and refraction in the material and the imaginary part represents the decay due to absorption or loss in the material. The expression for the electric field shows that an electromagnetic propagating wave through a dielectric is attenuated and the phase of the signal is shifted based on the electric and magnetic properties of the material. The phase shift in the frequency-domain corresponds to a delay in the time-domain.

5.2 Transmission Through Multilayer Structures

In this section electromagnetic wave propagation through a medium including one or more layers with different electrical properties is investigated [108]. The electric and magnetic field propagation in a medium can be decomposed into forward and backward propagating electric fields as

$$\begin{aligned} E(x) &= E^{+}(x) + E^{-}(x) \\ H(x) &= \frac{1}{\eta}(E^{+}(x) + E^{-}(x)), \end{aligned} \tag{5.4}$$

where $E^{+}(x) = E_0^{+}\mathrm{e}^{\mathrm{i}kx}$ and $E^{-}(x) = E_0^{-}\mathrm{e}^{-\mathrm{i}kx}$ are the forward and backward propagating fields. Due to the boundary conditions the total electric and magnetic fields are continuous for normal incidence, since the field components are tangential. Consider an air-dielectric interface where the fields in the dielectric are $E'(x)$ and $H'(x)$. Using the boundary conditions at the interface we have $E(x) = E'(x)$ and $H(x) = H'(x)$, and therefore the forward and backward radiating fields are related as $E^{+} + E^{-} = E'^{+} + E'^{-}$ and $E^{+} - E^{-} = (E'^{+} - E'^{-})n$, where n is the refractive index of the medium. This can be summarized in a matrix form known as matching matrix [108]:

$$\begin{bmatrix} E^{+} \\ E^{-} \end{bmatrix} = \frac{1}{\tau} \begin{bmatrix} 1 & \rho \\ \rho & 1 \end{bmatrix} \begin{bmatrix} E'^{+} \\ E'^{-} \end{bmatrix}, \tag{5.5}$$

where $\rho = (1-n)/(1+n)$ is the reflection coefficient at the air-dielectric interface and $\tau = 1+\rho$ is the transmission coefficient. Consider the multilayer structure in Fig. 21 with M dielectrics and $M+1$ interfaces. The length of the i^{th} dielectric slab is ℓ_i and has a refractive index n_i. At each interface the fields are transferred through the matching matrix and are phase shifted and attenuated from the left interface to the right interface in each layer. The relation between the fields from the left interface of the layer i to the left interface of the layer $i+1$ is given by

$$\begin{bmatrix} E_{\mathrm{i}}^{+} \\ E_{\mathrm{i}}^{-} \end{bmatrix} = \frac{1}{\tau_i} \begin{bmatrix} \mathrm{e}^{-\mathrm{i}k_i\ell_i} & \rho_i \mathrm{e}^{\mathrm{i}k_i\ell_i} \\ \rho_i \mathrm{e}^{-\mathrm{i}k_i\ell_i} & \mathrm{e}^{\mathrm{i}k_i\ell_i} \end{bmatrix} \begin{bmatrix} E_{\mathrm{i+1}}^{+} \\ E_{\mathrm{i+1}}^{-} \end{bmatrix} \tag{5.6}$$

where the matrix in the middle is the multiplication result of the propagation and matching matrices for layer i. The field passing through the most right interface of the multilayer structure is solely affected by the matching matrix as

$$\begin{bmatrix} E_{\mathrm{M+1}}^{+} \\ E_{\mathrm{M+1}}^{-} \end{bmatrix} = \frac{1}{\tau_{M+1}} \begin{bmatrix} 1 & \rho_{M+1} \\ \rho_{M+1} & 1 \end{bmatrix} \begin{bmatrix} E'^{+}_{\mathrm{M+1}} \\ 0 \end{bmatrix} \tag{5.7}$$

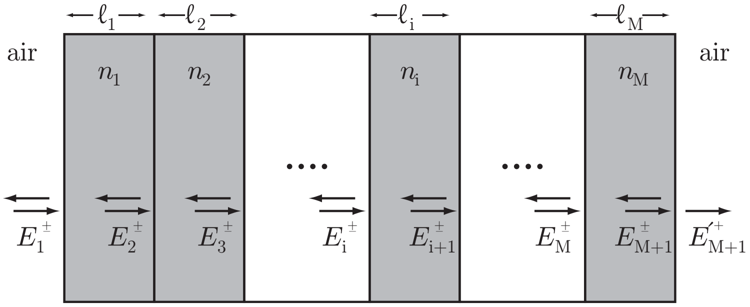

Figure 21: Multilayer structure consisting of M dielectrics with permittivities ϵ_1, $\epsilon_2,\ldots,\epsilon_{\mathrm{M}}$ and refractive indexes n_1, $n_2,\ldots,n_{\mathrm{M}}$ in otherwise free space with $M+1$ interfaces.

The complete propagation from the most left interface, *i.e.*, incident field, to the field transmitted from the most right interface can be expressed as

$$\begin{bmatrix} E_1^+ \\ E_1^- \end{bmatrix} = \frac{1}{\prod\limits_{i=1}^{M+1} \tau_i} \begin{bmatrix} \mathrm{e}^{-\mathrm{i}k_1\ell_1} & \rho_1 \mathrm{e}^{\mathrm{i}k_1\ell_1} \\ \rho_1 \mathrm{e}^{-\mathrm{i}k_1\ell_1} & \mathrm{e}^{\mathrm{i}k_1\ell_1} \end{bmatrix} \begin{bmatrix} \mathrm{e}^{-\mathrm{i}k_2\ell_2} & \rho_2 \mathrm{e}^{\mathrm{i}k_2\ell_2} \\ \rho_2 \mathrm{e}^{-\mathrm{i}k_2\ell_2} & \mathrm{e}^{\mathrm{i}k_2\ell_2} \end{bmatrix} \cdots$$
$$\begin{bmatrix} \mathrm{e}^{-\mathrm{i}k_M\ell_M} & \rho_M \mathrm{e}^{\mathrm{i}k_M\ell_M} \\ \rho_M \mathrm{e}^{-\mathrm{i}k_M\ell_M} & \mathrm{e}^{\mathrm{i}k_M\ell_M} \end{bmatrix} \begin{bmatrix} 1 & \rho_{M+1} \\ \rho_{M+1} & 1 \end{bmatrix} \begin{bmatrix} E_{\mathrm{M+1}}^{\prime +} \\ 0 \end{bmatrix}. \quad (5.8)$$

The ratio between the reflected field and the incident field is the reflection coefficient, $\mathit{\Gamma} = E_1^-/E_1^+$, and the ratio between the transmitted field, $E_{\mathrm{M+1}}^{\prime +}$, and the incident field is the transmission coefficient, $\mathcal{T} = E_{\mathrm{M+1}}^{\prime +}/E_1^+$. For a single layer dielectric slab with length ℓ and refractive index n placed in an otherwise free space the transmission and reflection coefficients are given by [108]

$$\begin{aligned} \mathcal{T}(\omega) &= \frac{(1-\rho^2)\mathrm{e}^{\mathrm{i}k_0 n\ell}}{1-\rho^2\mathrm{e}^{2\mathrm{i}k_0 n\ell}} \\ \mathit{\Gamma}(\omega) &= \frac{\rho(1-\mathrm{e}^{2\mathrm{i}k_0 n\ell})}{1-\rho^2\mathrm{e}^{2\mathrm{i}k_0 n\ell}}, \end{aligned} \quad (5.9)$$

where $n\ell$ is the optical length of the slab and k_0 is the free-space wavenumber.

5.3 Direct Method

A simple time-domain method to extract the material parameters for non-magnetic, low loss and low dispersive materials is developed. Since the complex permittivity of the material is found directly from the received time-domain signal, the method is called a direct method of extraction in this thesis. The time-domain transmission response can be found by expressing (5.9) in the z-transform and expanding

$\mathcal{T}(z)$ in power series of z^{-1} [108]. The time-domain transmission coefficient from a wavelet, $v(t)$, modulated at the carrier frequency, f_0, and for a single layer material with thickness, d, and complex refractive index $n(f_0) = n_\mathrm{r} + \mathrm{i}n_\mathrm{i}$ can be approximated as [108]

$$\mathcal{T}(t) \approx \sum_{m=0}^{\infty} \frac{4n_\mathrm{r}(n_\mathrm{r}-1)^{2m}}{(n_\mathrm{r}+1)^{2m+2}} v(t - mT - T/2)\mathrm{e}^{-(2m+1)\alpha_{k_0} d}\ , \ m{=}0,1,2,\ldots \tag{5.10}$$

where $T = 2dn_\mathrm{r}/c_0$ is the two way travel time inside the slab and $mT + T/2$ denotes the time delay for each transmitted term. As is illustrated in Fig. 22, the term $m = 0$ is the main transmission over the slab whereas $m \geqslant 1$ denotes the higher order terms that are caused by multiple reflections in the material. The amplitude of the transmitted signal is affected by the losses inside the dielectric slab and decreases exponentially with respect to the distance, *i.e.*, $\exp(-(2m+1)\alpha_{k_0} d)$. Here $\alpha_{k_0} = k_0 n_\mathrm{i}$ denotes the attenuation constant at the carrier frequency, f_0.

An example of a dielectric slab, shown in Fig. 22, with thickness d and relative dielectric constant $\epsilon_\mathrm{r} = 4{+}\mathrm{i}0.01$ is considered. The incident signal on the material interface is an 80 ps long pulse centered around $f_0 = 50$ GHz with amplitude 1 V. The solid curves are simulated received signals in the absence of the object and the dashed lines are the simulated received signals affected by the material. For the material in Fig. 22(a) with thickness $d = 20$ mm the first transmitted term with amplitude V_1 is attenuated because of the impedance mismatch at the interfaces and delayed due to the real part of the refractive index. The second term with amplitude V_2 is well separated from the first term since the slab is electrically thick compared to the pulse width ($T > t_\mathrm{p}$). The real part of the refractive index is estimated using the time delay t_d, between the reference signal and the signal affected by the slab. The imaginary part, n_i, can be determined using the ratio between two signals, $\varDelta$, as

$$\begin{cases} n_\mathrm{r} = \frac{c_0 t_\mathrm{d}}{d} + 1 \approx 2, & \text{with } t_\mathrm{d}{=}66.7\,\text{ps} \\ n_\mathrm{i} = \frac{1}{k_0 d} \ln\left(\frac{\varDelta(n(f_0)+1)^2}{4n(f_0)}\right) = 2.5\times10^{-3}, & \text{with } \varDelta = 0.8434. \end{cases} \tag{5.11}$$

The resulting complex permittivity becomes $\epsilon_\mathrm{r} = 4 + \mathrm{i}0.01$ which is, not surprisingly, the same as the starting value. In the second case with an electrically thin dielectric sample, see Fig. 22(b), the first and second terms of the transmission coefficient overlap and finding the ratio, $\varDelta$, between two signals is more challenging. In order to overcome this effect, the first T part of the signal which only includes the first term, $m = 0$, is utilized. The rest of the signal, shown as the shadowed region in Fig. 22, is affected by the multiple reflections inside the material and is ignored. The value of T is calculated based on the real part of the refractive index which is basically the delay introduced by the sample. The useful peak of the signal in the presence of the object is indicated by $\circ$ in Fig. 22(b) and can be used to estimate the complex permittivity according to (5.11). The resulting

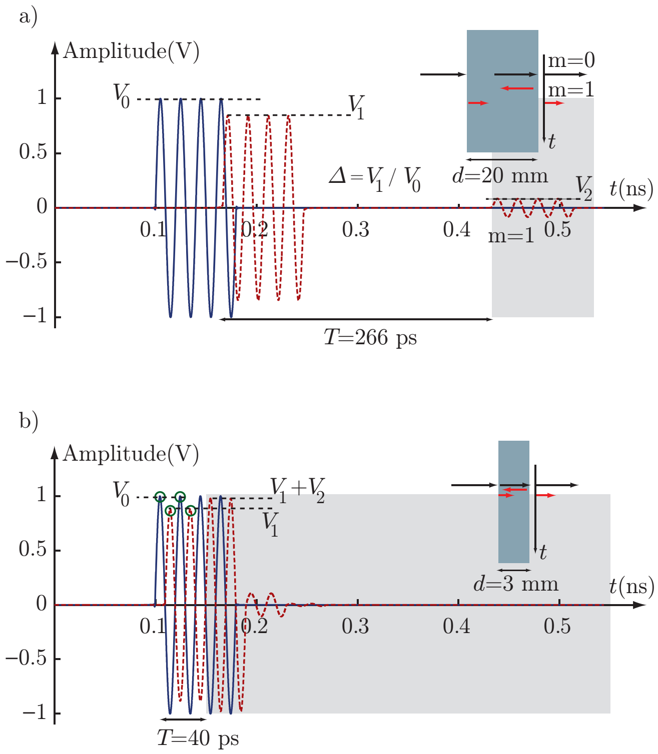

Figure 22: Transmitted signals in the absence (solid) and the presence (dashed) of the materials with thickness 20 mm (a) and 3 mm (b) and relative permittivity $\epsilon_\mathrm{r} = 4+\mathrm{i}0.01$. V_0 is the amplitude of the received signal in the absence of the sample, V_1 denotes the amplitude of the first term in (5.10) and V_2 is the amplitude of the second term. The ratio between V_1 and V_0 is denoted by $\Delta = V_1/V_0$.

complex permittivity from the direct method is valid at the carrier frequency of the signal, however, in dielectrics with negligible dispersion, the obtained value is approximate the same over a large bandwidth.

5.4 Broadband Characterization

The broad bandwidth of a short pulse can be utilized to characterize the frequency dependence of materials. Similar to time-domain spectroscopy [4, 24, 67], a short pulse is generated and transmitted through a propagation channel including the material under test. The detected signal is the Fourier transform for frequency-domain characterizations. The frequency-domain transmission coefficient for a single dielectric slab, with complex refractive index, n, and thickness, d, according to (5.9) is given by

$$\mathcal{T}(\omega) = \frac{4n(\omega)}{(n(\omega)+1)^2} \mathrm{e}^{\mathrm{i}(n(\omega)-1)k_0 d} \left(1 - \big(\frac{n(\omega)-1}{n(\omega)+1}\big)^2 \mathrm{e}^{2\mathrm{i}n(\omega)k_0 d}\right)^{-1}. \tag{5.12}$$

The frequency-domain transmission coefficient, $\mathcal{T}(\omega)$, is estimated as the ratio between the Fourier transform of the received signal in presence of the object and the Fourier transform of the received signal in the absence of the object, *i.e.*, $\mathcal{T}_{\text{meas}}(\omega) = V_{\text{sample}}(\omega)/V_{\text{ref}}(\omega)$. Since the measurement is in a transmission configuration and the reflection is not measured, the final permittivity is not unique. The simplest way to estimate the refractive index is to minimize the difference between the modeled values and the measured transmission coefficient, *i.e.*, $\mathcal{T} - \mathcal{T}_{\text{meas}}$, for a range of refractive indexes. The real part of the refractive index can always be found simply through the direct method. In the minimization problem, this value is used to restrict the real part to a neighborhood of the estimated value. The resulting refractive index is still not very accurate since brute force search is very sensitive to noise and the parts of the signal spectrum with low amplitude.

For passive material, we can define a symmetric Herglotz function [19] $h = \omega\epsilon$, where h is holomorphic and $\operatorname{Im} h(\omega) \geqslant 0$ for $\operatorname{Im}\omega > 0$. Similar to positive real functions in (4.11), the real part and imaginary part of h are related by

$$\operatorname{Re} h(\omega) = \epsilon_\infty \omega + \frac{1}{\pi} \int_{-\infty}^{\infty} \frac{1}{\zeta - \omega} \operatorname{Im} h(\zeta) \mathrm{d}\zeta, \tag{5.13}$$

where $\epsilon_\infty > 0$ is the the high frequency permittivity. A convex optimization formulation can be used to find the most similar Herglotz function to the measured values, as

$$\begin{aligned} \text{minimize} \quad & \left\| h(\omega) - h^{(\mathrm{M})}(\omega) \right\| \\ \text{subject to} \quad & \operatorname{Im} h(\omega) \geqslant 0 \\ & \epsilon_\infty \geqslant 0 \\ & \operatorname{Re} h(\omega) = \epsilon_\infty \omega + \frac{1}{\pi} \int_{\omega_0}^{\omega_3} \frac{1}{\zeta - \omega} \operatorname{Im} h(\zeta) \mathrm{d}\zeta \\ & \left\| \frac{1}{\omega} \frac{\partial h}{\partial \omega} \right\|_\infty < \frac{0.01}{\Delta\omega} \end{aligned} \tag{5.14}$$

where $[\omega_0, \omega_3]$ is the range of the modeled data and $[\omega_1, \omega_2]$ is the measurement interval as $\omega_0 < \omega_1 < \omega_2 < \omega_3$. The optimization solution has the advantage of removing non-physical values of the permittivity using the passivity constraint. In most cases the imaginary part is more sensitive to noise and the Kramers-Kronig [65, 76, 82] condition improves the accuracy of the estimation. The third condition has smoothing effects and is enforced to remove spikes between two adjacent frequency points which is usually due to the poor signal amplitude.

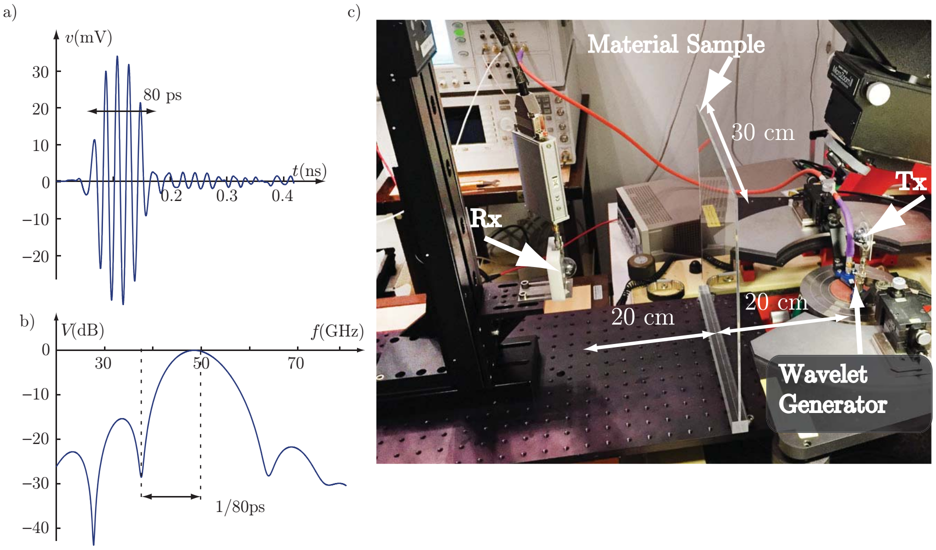

Figure 23: Time-domain system for material characterization. a) 80 ps pulse modulated at 50 GHz and received in the absence of the object. b) The power spectral density of the received signal. c) Transmission measurement in the presence of a 3 mm sample [146].

5.5 Measurement Examples

The time-domain antenna system in Sec. 3 is used to generate 80 ps pulses with carrier frequency at 50 GHz. The generated pulse and its power spectral density are shown in Fig. 23(a) and (b). The antennas are separated by 40 cm facing each other, see Fig. 23(c) and two materials are tested. In both cases the material under test is placed at the midpoint between two antennas and the signal is recorded in the presence and the absence of the object. The first example is a poly methyl methacrylate (PMMA) dielectric which has a relatively low dispersion and the second example is distilled water (dH_2O) which is highly dispersive and lossy at mm-wave frequencies [94].

5.5.1 Poly Methyl Methacrylate (PMMA)

A dielectric slab made of PMMA with dimensions of $30 \times 30 \times 2\,\text{cm}^3$ is characterized using the time-domain system consisting the leaky lens antennas and RTD-MOSFET wavelet generator, as discussed in Sec. 3. The recorded reference signal and the received signal in the presence of the object are shown in Fig. 24(a) by solid- and dashed-lines, respectively. The delay caused by the dielectric is estimated to $t_\text{d} = 39.5\,\text{ps}$. The first step in the direct method is to determine the value of T to find the region that the peak detection is allowed.

By using the real part of the refractive index the double travel time is estimated to $T = 2dn_\mathrm{r}/c_0 = 212\,\mathrm{ps}$. This means that the signal in the shadowed region includes multiple scattering and peak values for refractive index estimation in (5.11) should be taken from the first T part of the signal. Taking the peak with maximum amplitude of the reference signal and the corresponding peak of the signal in the presence of the object, as shown in Fig. 24(a), the ratio between the amplitudes of two signal becomes $\varDelta = 0.881$. By applying the obtained ratio and the real part of the refractive index in (5.11), the imaginary part of the refractive index is determined to $n_\mathrm{i} = 0.003$ and the resulting permittivity becomes $\epsilon_\mathrm{r,r} = 2.532 \pm 0.005$ and the imaginary part $\epsilon_\mathrm{r,i} = 0.009 \pm 0.002$. The uncertainty levels are found by repeating the measurement 10 times.

As mentioned in Sec. 5.4, the broad bandwidth of the wavelets can be utilized to determine the frequency dependence of the objects. Using the frequency-domain transmission coefficient the estimated results of extracted permittivity of the PMMA sample is shown in Fig.24(b) utilizing brute-force search (dashed-lines) and convex optimization solution (dashed-dotted lines). The bars show the maximum and minimum values of the convex optimization solution over 10 measurements. The deviation from the mean value is small over the frequency region where the power spectral density of the signal has its highest values, *i.e.*, $50 \pm 12.5\,\mathrm{GHz}$.

The direct method solution follows the broadband extraction result based on the convex optimization problem at the carrier frequency $f_0 = 50\,\mathrm{GHz}$. The previously reported works are shown by ($*$) and ($\diamond$) in the Fig. 24. The measurement from the time-domain system have also been verified by measuring the same sample from 20 to 67 GHz using an Agilent E8361A the VNA and leaky lens antennas. The resulting complex permittivity is shown by solid lines and is estimated using the brute-force search explained in Sec. 5.4. More examples of low dispersive materials can be found in [146].

5.5.2 Distilled Water ($\mathbf{dH_2O}$)

In order to show the wideband performance of the system, distilled water ($\mathrm{dH_2O}$) which is a dispersive material, is characterized. Due to the high losses inside the water at mm-wave frequencies, the permittivity extraction is challenging. The electric properties of dispersive materials with high losses are usually measured in reflection configuration.

A layer of $\mathrm{dH_2O}$ is inserted between two 20 mm PMMA samples and the separation is fixed to 1 mm. The sample is located between the antennas and an 80 ps wavelet at 60 GHz is generated and propagated through the sample. The reference signal in the absence of the object is shown in Fig. 25(a) and the received signal in the presence of the sample is depicted in Fig. 25(b). The strong peak in the received signal arrives approximately 90 ps later than the reference signal, which is related to the delay inside the PMMA samples (79.2 ps) and the delay inside $\mathrm{dH_2O}$ layer (11.5 ps) at 60 GHz.

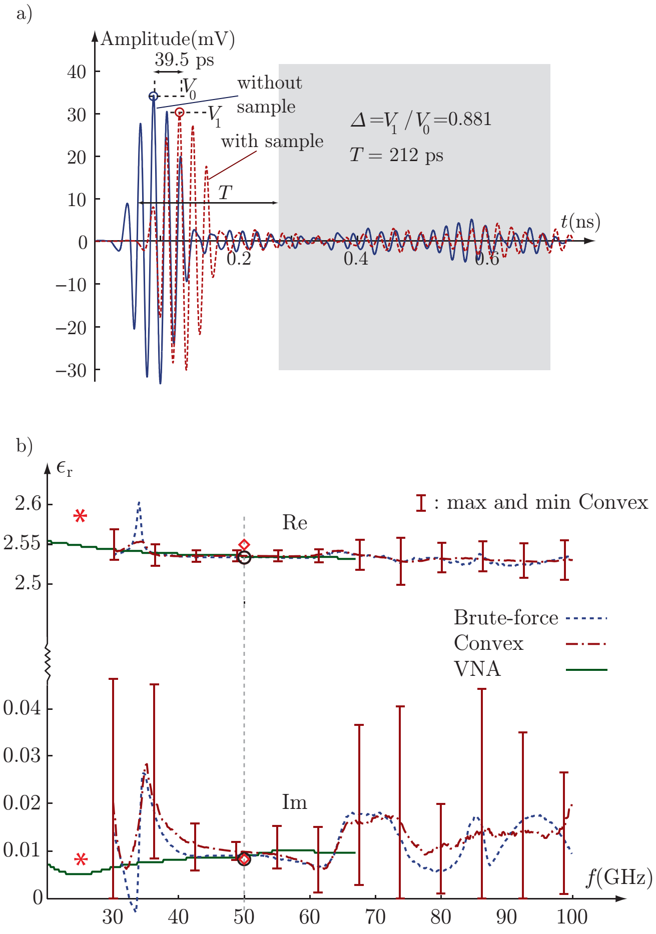

Figure 24: Time- and frequency-domain characterizations of a 20 mm PMMA sample. a) Transmitted signal in the absence (solid) and the presence (dashed) of a PMMA material with thickness 20 mm. The transmitted signal through the material is delayed by 39.5 ps and attenuated by a factor of $\varDelta = 0.881$. The shadowed region shows the part of the signal that is affected by the multiple scattering inside the material and is discarded in the direct method. b) Complex permittivity of a 20 mm PMMA sample estimated from time-domain measurement using the direct method ($\circ$) in (5.11), using the brute-force search in (5.12) (dashed lines), convex optimization solution in (4.12) (dashed-dotted lines) and from the frequency-domain measurements using network analyzer (solid lines). The previously reported works are denoted by ($\diamond$) for the values found from [35] and ($*$) for [151]. Bars indicate the maximum and minimum values over the 10 measurements using convex optimization solution.

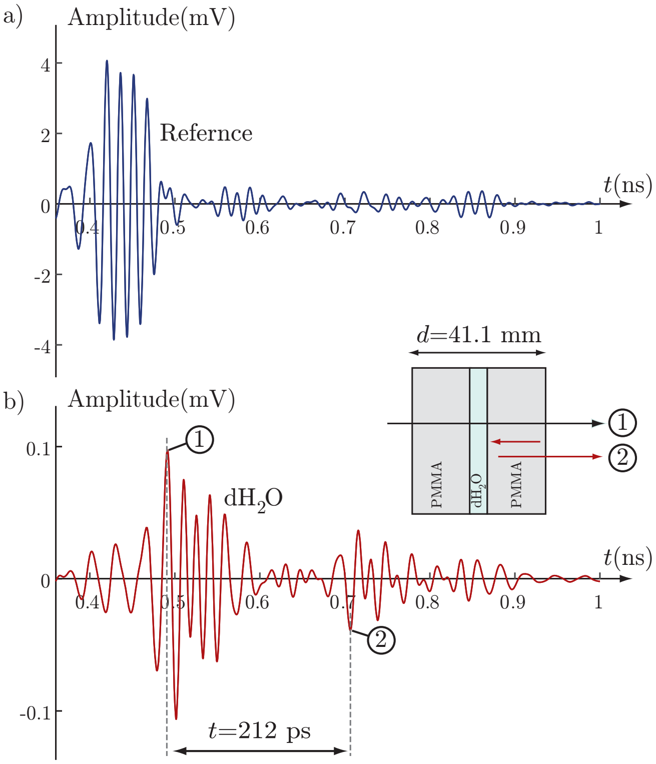

Figure 25: Generated 80 ps wavelet with center frequency at 60 GHz for distilled water characterization. a) Reference signal that is received in the absence of the object. b) Received signal in the presence of 1 mm of distilled water confined between two 20 mm samples of PMMA.

Due to the frequency dispersion of water and the small thickness of the sample, the time-domain signal is highly distorted and affected by the frequency dependent multiple scattering. The second strongest peak denoted by ② in Fig. 25(b) arrives 212 ps after the peak ①. The phase of the signal is shifted 180° due to the internal reflection at the PMMA-dH_2O interface. The time-domain analysis using the direct method is not valid here and needs some modifications. However, the broad bandwidth of the pulse make it possible to extract the frequency dependence of the dH_2O sample.

Characterizing the constitutive parameters of liquids in a free-space measurement configuration is always challenging and since the liquid should be inside a container, we usually face a multilayer problem instead of a single layer one, see Sec. 5.5.1. As mentioned in Sec. 5.2, the total transmission coefficient of the sample can be represented by propagation and matching matrices. For a three layer structure there exist four interfaces and the transmission coefficient can be

Table 2: Debye relaxation parameters for distilled water at 25°.

Parameter	value
ϵ_{s}	78.4
ϵ_1	2.54
ϵ_∞	4.33
ν_1	19.1 GHz
ν_2	215.6 GHz

found by (5.8) and $\mathcal{T} = E'^{+}_{\mathrm{M}+1}/E^{+}_{1}$. In this problem, the properties of the first and last PMMA layer are known and the only unknown is the refractive index of the water. The thickness of the water sample is approximately 1.1 ± 0.05 mm. Using (5.8), brute force search method and convex optimization the complex dielectric constant of water is extracted and shown in Fig. 26. Due to the high losses inside the water ($\approx$ 30 dB/mm at 60 GHz) and a limiting transmitting power, the received signal to noise ratio is relatively, low. As shown in Fig. 26, the convex optimization solution reduces the amount of oscillations and improves the estimations, especially at frequencies where the power is relatively low, such as in nulls in the power spectral density.

A double Debye relaxation model is used to verify the measured values as [36]

$$\epsilon_{\mathrm{r}}(f) = \epsilon_\infty + \frac{\epsilon_{\mathrm{s}} - \epsilon_1}{1 - \mathrm{i}\frac{f}{\nu_1}} + \frac{\epsilon_1 - \epsilon_\infty}{1 - \mathrm{i}\frac{f}{\nu_2}} + \mathrm{i}\frac{\sigma}{2\pi f \epsilon_0}, \tag{5.15}$$

where ϵ_{s} is the static dielectric constant and ν_1 and ν_2 are the relaxation frequencies. The conductivity of distilled water in the frequency range 30 GHz to 75 GHz is assumed to be negligible, *i.e.*, $\sigma = 0$. The Debye relaxation parameters for 25°, and using the temperature and conductivity model presented in [94] are summarized in Table. 2. The obtained results show that over the frequency range that the power spectral density of the signal is high, the estimation is closer to the values predicted in (5.15). The oscillation of the permittivity is mainly due to the time gating of the received reference pulse and other interferences.

6 High Resolution Imaging

The time-domain system in Sec. 3 can be utilized in radar and imaging applications. The high frequency and wide bandwidth of the mm-wave short pulses can provide high resolution images. The time-domain system consists of non-dispersive and wideband leaky lens antennas and an RTD-MOSFET wavelet generator that produces mm-wave short pulses [145]. In this section a radar

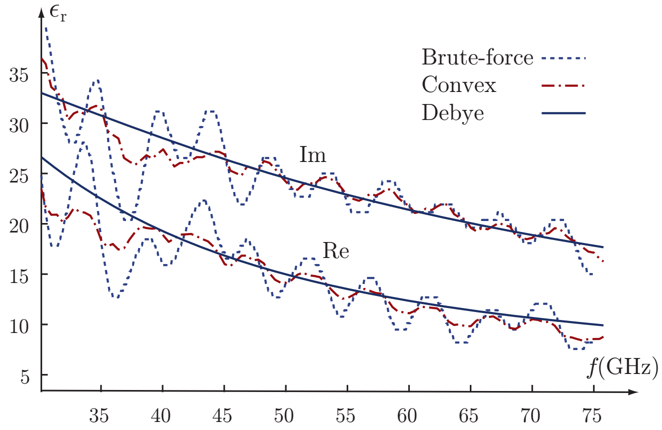

Figure 26: Real and imaginary part of the complex permittivity for distilled water from 30 to 75 GHz found from brute-force search(dashed-curves), convex optimization solution (dashed-dotted curves) and the equivalent Debye model using the parameters introduced in [94].

imaging application based on circular inverse synthetic aperture radar (C-ISAR) is presented and preliminary results are illustrated. The image reconstruction based on the gridding method (GM) and ℓ_1-optimization is investigated.

6.1 ISAR Basics

Synthetic aperture radar is one among the most popular imaging methods in airborne and spaceborne applications [30,44,109,132,137]. The synthetic aperture refers to an aperture that is synthesized from smaller antenna apertures. The SAR image is formed from the recorded reflections by a moving radar, as shown in Fig. 27. Inverse SAR (ISAR) refers to the case when the target is moving instead of the radar. Two main ISAR configurations are stripmap and spotlight. In stripmap configuration the target moves along the radar and the reflected waves are recorded for a predefined path. In spotlight mode the radar focuses on a particular region or a turn table. The spotlight mode, in some cases, results in a better resolution that the stripmap mode. In this thesis circular ISAR (C-ISAR) which is in spotlight mode is considered. The target is positioned on a turntable and is assumed to be illuminated uniformly by the antennas.

6.2 Circular ISAR Image Reconstruction

In this section image reconstruction in C-ISAR configuration based on the gridding method is investigated [8, 98]. In C-ISAR the object can be rotated 360° in a spotlight radar configuration, which results in a high resolution image that

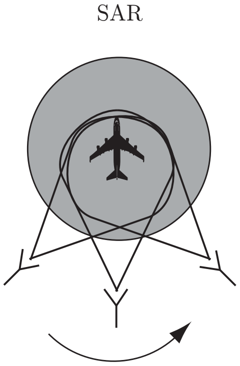

Figure 27: Spotlight mode imaging radar. In SAR the radar moves and the target is stationary whereas in ISAR the target moves and the radar is stationary.

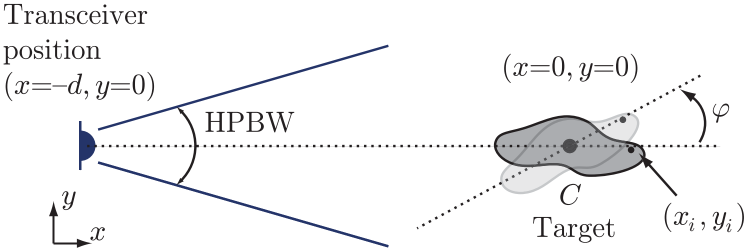

Figure 28: System configuration in C-ISAR mode. The angle of rotation is denoted by φ with the center of rotation at the origin. The target is at distance d from the antennas and is located in the HPBW of the antennas.

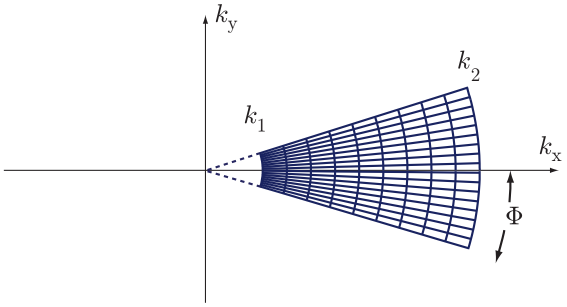

Figure 29: Data collection manifold of the reflectivity function, $\rho(x, y)$, with radar illumination angle 2Φ and the bandwidth, $B = c_0(k_2 - k_1)/4\pi$.

includes many details of the object. The C-ISAR configuration is illustrated in Fig. 28. The target rotates around the point $(x = 0, y = 0)$ with rotation angle φ from the x-axis. The recorded range profile in two-dimensions and for Dirac Delta function, $\delta(t)$, transmitted signals can be written as [8, 137]

$$s(\varphi, t) = \int_{-Y_{\max}/2}^{Y_{\max}/2} \int_{-X_{\max}/2}^{X_{\max}/2} \rho(x, y)\delta\left(t - \frac{2}{c_0}\sqrt{(x + d\cos\varphi)^2 + (y + d\sin\varphi)^2}\right) \mathrm{d}x\,\mathrm{d}y \tag{6.1}$$

where $\rho(x, y)$ is the reflectivity function and $X_{\max}$ and $Y_{\max}$ are the largest extents of the radar illumination region in x- and y-directions, respectively. The corresponding measured signal in the frequency-domain is related to the spatial Fourier transform of the reflectivity function, $\rho(\tilde{\boldsymbol{k}})$, as

$$s(\varphi, \omega) = \rho(\tilde{\boldsymbol{k}}), \tag{6.2}$$

where $\tilde{\boldsymbol{k}} = k_x\hat{\boldsymbol{x}} + k_y\hat{\boldsymbol{y}} = 2k(\cos\varphi\hat{\boldsymbol{x}} + \sin\varphi\hat{\boldsymbol{y}})$ is the spatial frequency and $k = \omega/c_0$ is the wavenumber. Assume that the radar signal has non-zero power spectral density over the wavenumber range $k = [k_1, k_2]$ and the scan angle is Φ. The support of the reflectivity function, also known as data collection manifold [30], in the frequency-domain is shown in Fig. 29. The image, $\rho(x, y)$, can then be reconstructed as

$$\rho(x, y) = \frac{1}{4\pi^2}\int_{k_x}\int_{k_y} \rho(k_x, k_y)\mathrm{e}^{\mathrm{j}(k_x x + k_y y)}\,\mathrm{d}k_x\,\mathrm{d}k_y, \tag{6.3}$$

which is the two dimensional inverse Fourier transform of $\rho(k_x, k_y)$. Note that $\rho(x, y)$ is the reflectivity function in the time-domain and $\rho(k_x, k_y)$ in the spatial frequency-domain.

There are a variety of methods to reconstruct the image such as: filtered backprojection algorithms, Fourier reconstructions and iterative methods [98, 109, 137]. The wide aperture angle in the present case limits the choice of the reconstruction algorithm. In some algorithms similar to polar formatting, on the other hand, the illumination angle is required to be $\Phi \leqslant \pi/2$. The gridding method (GM), on the other hand, is robust for wide angle SAR and ISAR image reconstruction based on two-dimensional Fourier transforms [8, 73, 98]. Even though this method is not computationally efficient, as compared to the classical methods, modern computational resources operate sufficiently fast for the cases in this thesis.

The resolution in a conventional radar with bandwidth, B, and small illumination angle, Φ, can be written as [109, 137]

$$\Delta x = \frac{c_0}{2B} \quad \text{and} \quad \Delta y = \frac{\lambda}{2\sin(2\Phi)}, \tag{6.4}$$

where Δx is the resolution in the x-direction in Fig. 28, also known as down-range resolution. The resolution along the y-direction is denoted by Δy, also known as cross-range resolution. In a 2π scan, however, the cross range resolution is the same as the down range resolution, *i.e.*, $\Delta x = \Delta y = \frac{c_0}{2B}$ [30].

6.3 Imaging System and Examples

Here, the time-domain system in Sec. 3 is utilized for ISAR measurements and the results are compared to measurements using a VNA. In the imaging system, as shown in Fig. 30, a SHF827 broadband power amplifier (PA) with approximately 10 dB gain is used. The transmitting and receiving antennas are located next to each other in a quasi-monostatic configuration. The metallic target is positioned on a CR1-Z7 platform and is rotated 360° around its center. Each measurement is coherently averaged over 1024 pulses to increase the SNR using a 70 GHz Agilent 86100D sampling oscilloscope. The generated pulses are 80 ps long and centered at 50 GHz. The period of the generated signal is set to $T_{\mathrm{PR}} = 10\,\mathrm{ns}$ which increases the ambiguous range to $R_{\max} = c_0 T_{\mathrm{PR}}/2 = 1.5\,\mathrm{m}$. In order to acquire reliable data up to 70 GHz according to the Nyquist-Shanon sampling theorem [107, 137], the sampling rate of the oscilloscope is set to $f_{\mathrm{s}} = 140\,\mathrm{GHz}$ ($f_{\mathrm{s}} \geqslant 2f_{\max}$). It is assumed that the object is located in the HPBW of the antennas and the illumination on the target is uniform. The reflection from the target is recorded from $-180°$ to $180°$ with $1°$ sample spacing due to the slow-time Nyquist criteria [137].

An example of a metallic target with $2 \times 2\,\mathrm{cm}^2$ cross section area is used in this section to illustrate the time-domain imaging system in Fig. 30. The reflection from a $30 \times 30\,\mathrm{cm}^2$ flat metallic sheet facing the antennas and placed at the rotation center, denoted $p(t)$, is used to calibrate the distance as well as matched-filtering the received signal. The frequency-domain received signal after matched-filter, which is an optimum receiver, can be written as [137]

$$s_{\mathrm{M}}(\varphi, \omega) = s(\varphi, \omega) p^*(\omega). \tag{6.5}$$

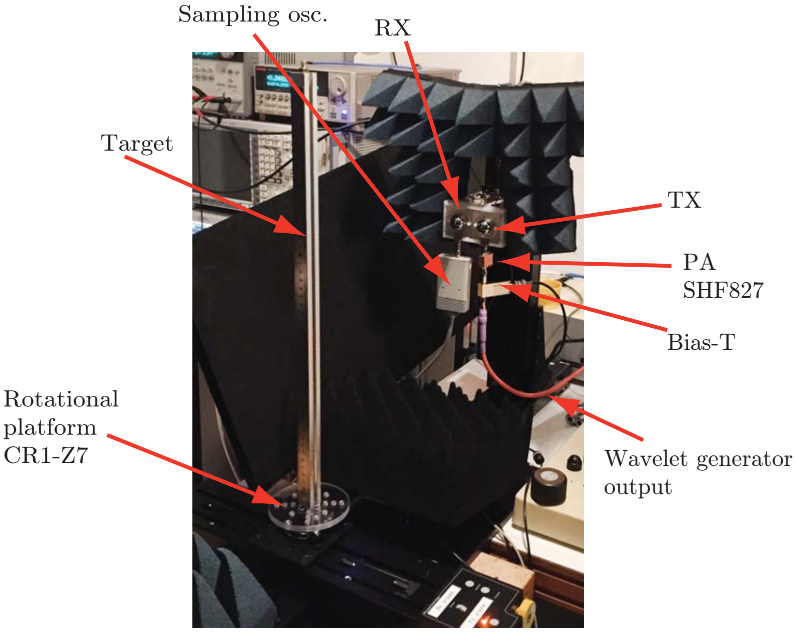

Figure 30: Time-domain imaging system setup consisting of a wavelet generator and leaky lens antennas as the transmitter and receiver antennas. The target is located at $d = 40\,\text{cm}$ from the antennas and is rotated 360° with 1° steps.

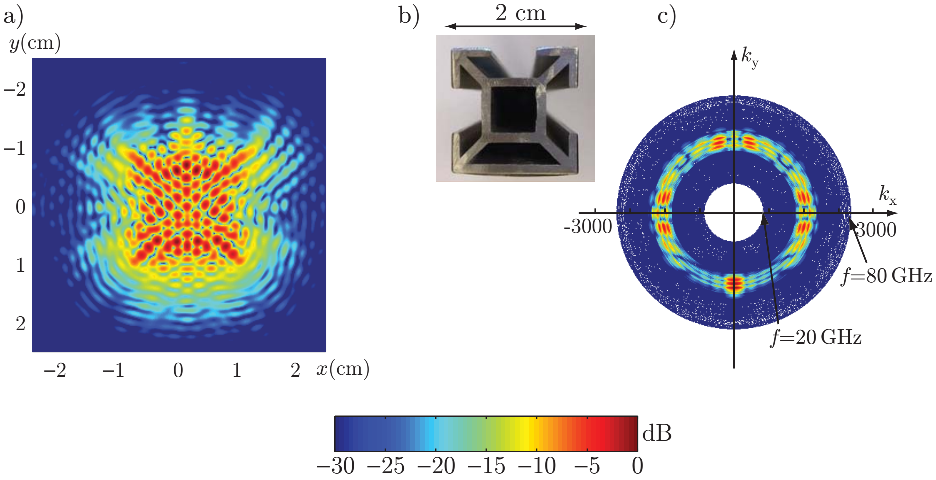

Figure 31: C-ISAR image reconstruction. a) Reconstructed image using the matched-filter in (6.5) and gridding method in [8]. b) The cross section of the actual object. c) The data collection manifold shows that the bandwidth of the signal is limited by the main lobe of the power spectral density of the wavelet.

This corresponds to a cross correlation between the received signal and the reference signal in the time-domain. By inserting $s_\mathrm{M}(\varphi,\omega)$ in (6.2) instead of $s(\varphi,\omega)$ and using (6.3) and the gridding method in [8,98], the estimated image can be reconstructed. The image, data collection manifold, and the cross section of the actual target are illustrated in Fig. 31. The target region with slightly larger cross section can be seen whereas the details of the object are not visible. The corresponding manifold shows that the measured values in the main lobe of the power spectral density are dominant and hence the resolution is poor. One way to equalize the signal is through zero-forcing equalization [74]. The received signal after matched-filter can be written as

$$s_\mathrm{M}(\varphi,\omega) = \frac{s(\varphi,\omega)p^*(\omega)}{|p(\omega)|^2}, \tag{6.6}$$

where the denominator is the power spectral density of the reference time-domain signal and is similar to the signal in Fig. 12(d). This introduces artifacts and enhances the noise due to the low power in the nulls of the signal spectrum. One way to mitigate this problem, is to regularize the problem by adding a positive coefficient to the denominator, similar to minimum mean square error (MMSE) [74] as

$$s_\mathrm{M}(\varphi,\omega) = \frac{s(\varphi,\omega)p^*(\omega)}{|p(\omega)|^2+\varepsilon}, \tag{6.7}$$

where $\varepsilon = \alpha\langle|p(\omega)|^2\rangle$ and the value of α is smaller for signals with sufficiently high SNR. The value of $\alpha = 0.1$ is chosen in the examples illustrated in this section.

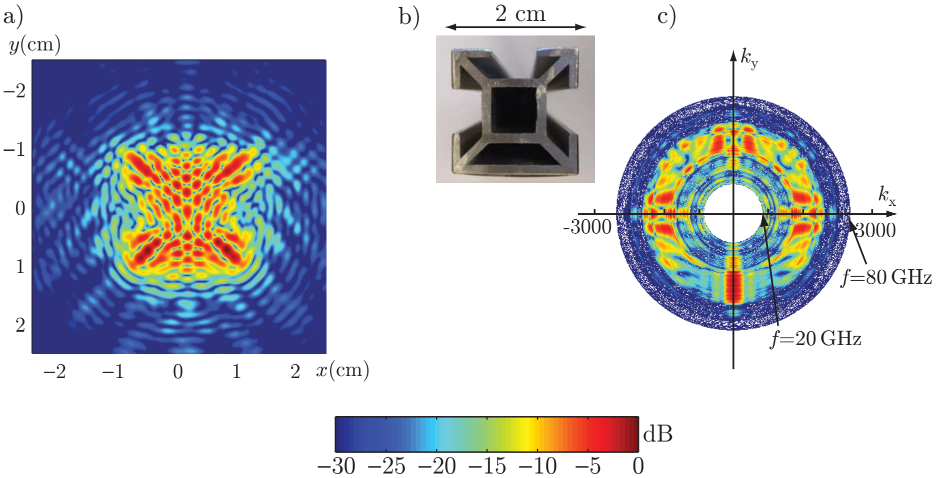

Figure 32: C-ISAR image reconstruction. a) Reconstructed image using the matched-filter, zero-forcing equalization in (6.7) and gridding method in [8]. b) The cross section of the actual object. c) The data collection manifold shows that the bandwidth of the measurement is wider when the zero-forcing is applied. The image has also higher resolution compared to the matched-filter results in Fig. 31.

The reconstructed image based on the MMSE equalization technique is shown in Fig. 32. The image has a higher resolution and the data collection manifold shows that more of the spectrum is utilized. Due to the wideband nature of the time-domain signals, using an appropriate equalization method to *e.g.*, boost up the power at the sildelobes of the power spectral density, can improve the resolution. It should be noted that some of the deconvolution methods such as zero-forcing and MMSE suffer from noise enhancements and use of these methods have to be avoided when the SNR is low.

In order to verify the time-domain imaging system and the obtained results, the same sample is measured in the frequency-domain using an Agilent E8361A VNA from 20 GHz to 67 GHz. The leaky lens antennas and SHF827 broadband PA were used to resemble the time-domain setup. The reflected signal from the target, $s(\varphi, \omega)$ is recorded for each angular step and the gridding method is applied to reconstruct the images. The reconstructed image as well as the data collection manifold are shown in Fig. 33. The wide bandwidth of the VNA with approximately constant power level at all frequencies results in a high resolution image, *i.e.*, $\Delta x = \Delta y \approx 3\,\text{mm}$ according to (6.4).

6.4 Compressive sensing and ℓ_1-minimization

Radar is mostly used to detect objects with sufficiently high RCS in a region where limited amount of scatterers exist, *e.g.*, detecting an airplane in the sky.

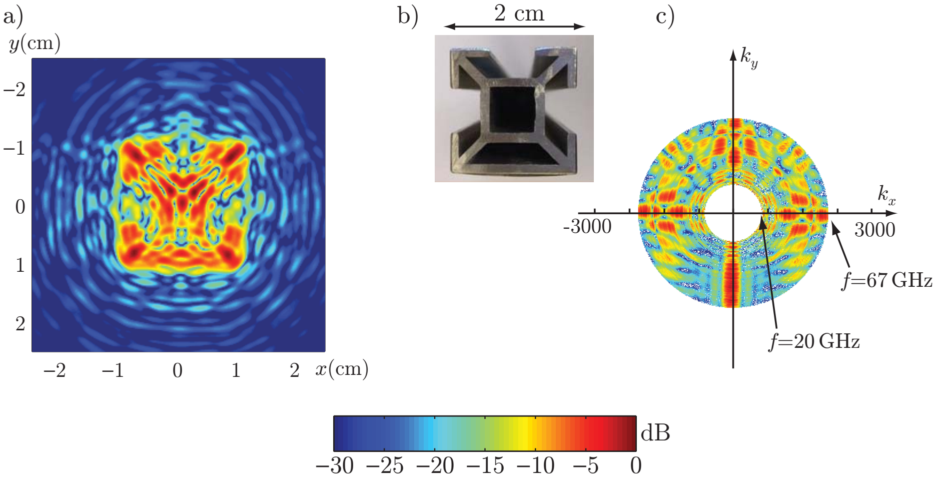

Figure 33: C-ISAR image reconstruction. a) Reconstructed image using the VNA measurement and gridding method in [8]. b) The cross section of the actual object. c) The data collection manifold is similar to Fig 32 which verifies the zero-forcing method to equalize measurements and hence increasing the bandwidth. The frequency range of the measurement is $f = [20, 67]$ GHz.

In these cases the radar images are sparse [89]. There are a variety of methods to reduce the number of measurements and yet reconstruct the image with reasonable resolution [37, 43, 126]. One of the popular frameworks over the recent years is the compressive sensing that utilizes sparse sampling [37, 89]. The estimated image, $\hat{\boldsymbol{x}}$, in a noisy case can be reconstructed through an ℓ_1-minimization problem, as

$$\hat{\boldsymbol{x}} = \text{argmin}\{||\mathbf{A}\boldsymbol{x} - \mathbf{b}||_2^2 + \mu||\boldsymbol{x}||_1\}, \tag{6.8}$$

where $\mathbf{A}_{M\times N}$ is the measurement matrix including the sensing matrix as well as the representation basis with $M \leqslant N$ and $b_{M\times 1}$ is the measurement vector. The original image is transformed into a vector denoted by $\boldsymbol{x}_{N\times 1}$. The regularization parameter, also known as least absolute shrinkage and selection operator (LASSO) [141], denoted μ and $\mathbf{b}$ is a $1 \times N$ vector representing the measurement values [8]. It should be noted that the optimization problem in (6.8) can be solved using a variety formulations, *e.g.*, see [26, 37, 89]. Here in this thesis, $\mathbf{A}$, represents the Fourier transform. The preliminary results of ℓ_1-minimization problem using the iterative method given in [8] and $\mu = 10^{-5}$ for two different targets are compared with the gridding method in Fig. 34 and Fig. 35.

It is seen that the ℓ_1-minimization problem improves the detection and the object looks sharper. It should be noted that the effectiveness of the ℓ_1-minimization problem is higher for sparse temporal or spatial data sets. The reconstructed image using the gridding method is shown in Fig. 34(a) and the corresponding

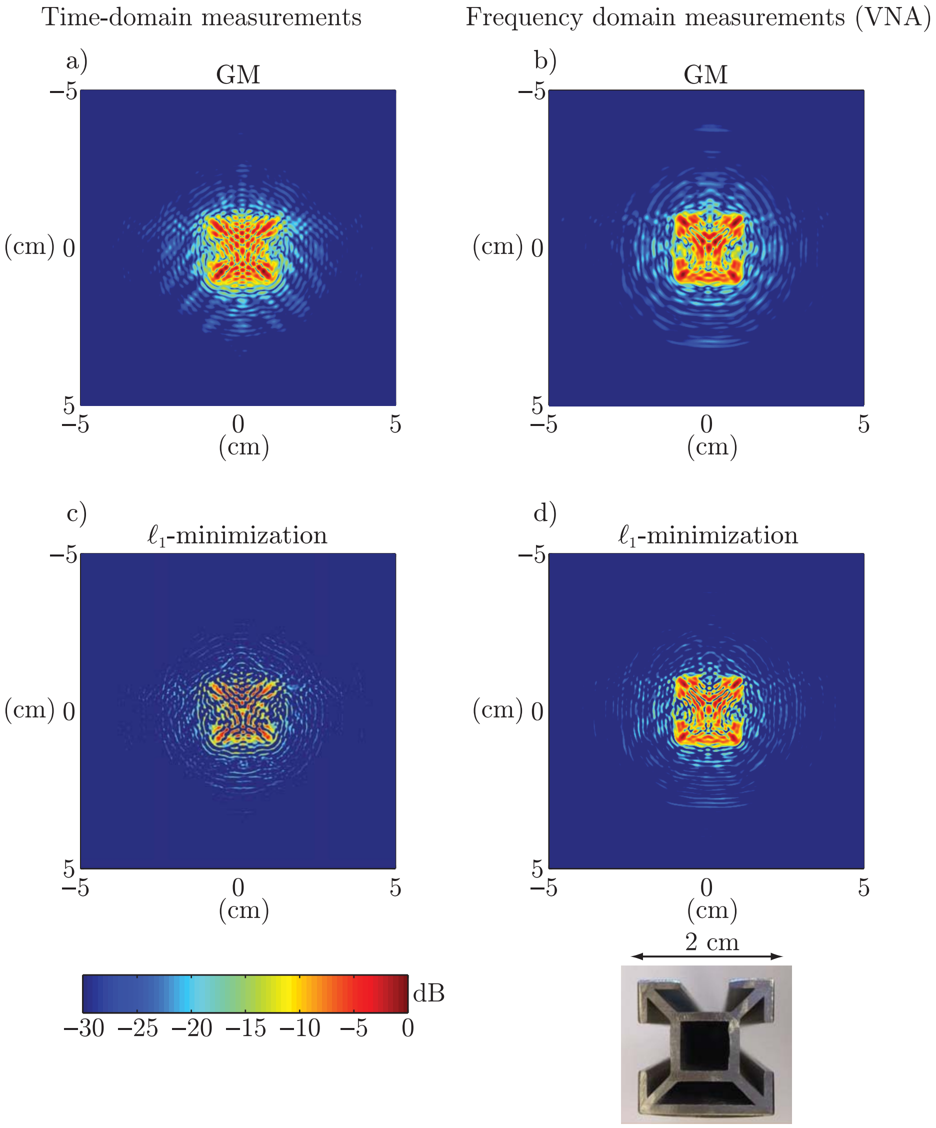

Figure 34: Image reconstruction based on the gridding method (GM) using a) time-domain system and b) VNA and ℓ_1-minimization problem using c) time-domain system and d) VNA. The cross section of the target and the dynamic range of the images are shown at the bottom.

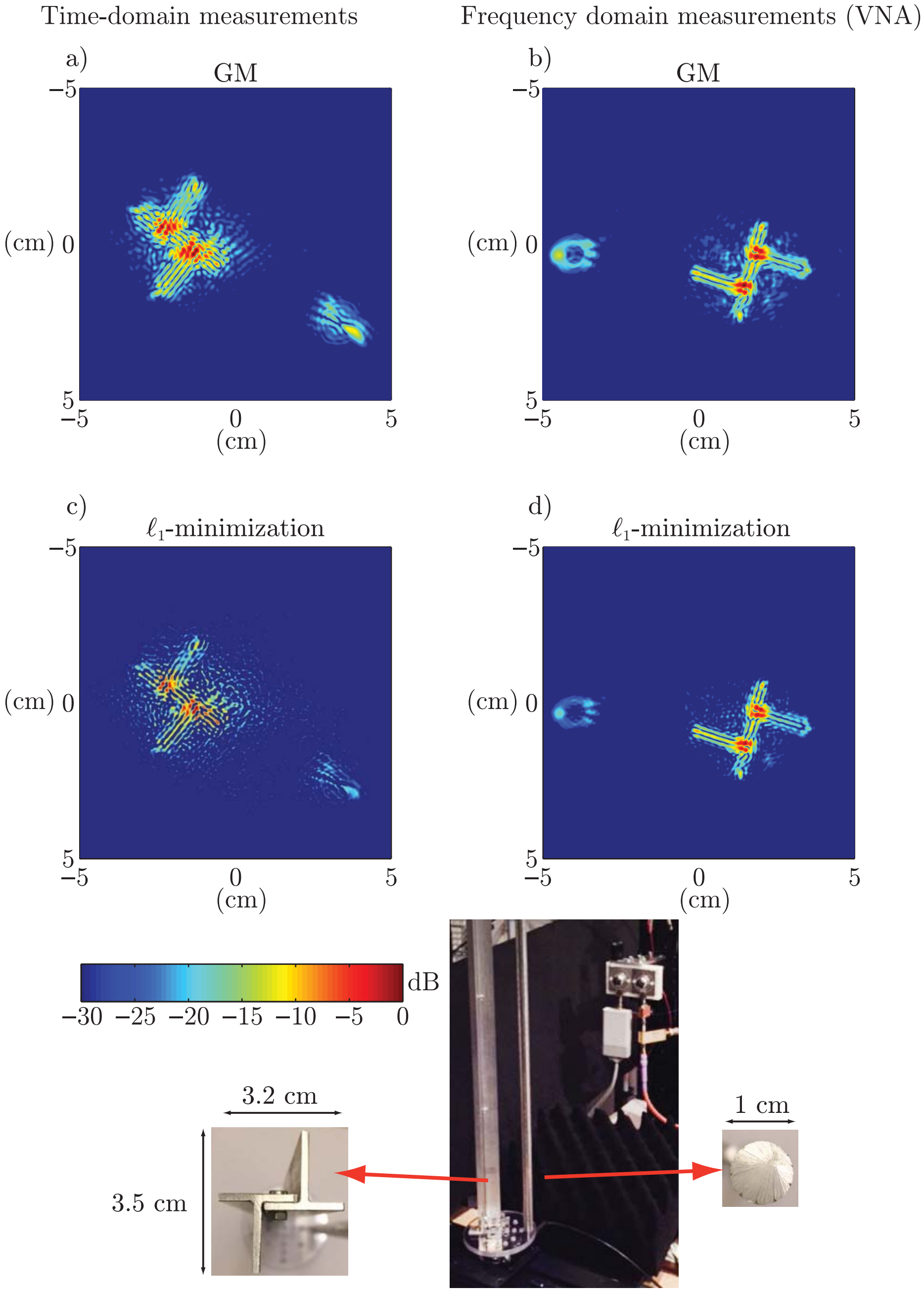

Figure 35: Image reconstruction based on the gridding method (GM) with a) time-domain system and b) VNA and ℓ_1-monimization problem with c) time-domain system and d) VNA. The cross section of the targets, the measurement configuration and the dynamic range of the images are shown at the bottom.

ℓ_1-minimization solution is depicted in Fig. 34(b). The optimization solution is sharper at the edges and the image broadening seems to be smaller. The reconstructed image using the frequency-domain setup is shown in Fig. 34(c) and the optimization solution in Fig. 34(d). Another target, as shown in Fig. 35, is also used for C-ISAR image reconstruction. The target consists of a metallic cylinder with diameter 1 cm and a metallic object with the cross section $3.2 \times 3.5\ \text{cm}^2$. The two objects were put together on the rotational stage. It should be noted that different positions in time-domain and frequency-domain measurement were used. The reconstructed image using ℓ_1-minimization in Fig. 35(b) shows more details from the object and is similar to the frequency-domain measurements with large bandwidth in Figs 35(b) and (d).

7 Conclusions

A time-domain system consisting of leaky lens antennas and an RTD-MOSFET wavelet generator is investigated. The wavelet generator produces coherent high frequency short pulses that are transmitted using the non-dispersive and wideband lens antennas. A wideband material characterization method is developed to extract the complex permittivity of dielectrics from time-domain measurements. The wide bandwidth of the wavelets is used to describe the frequency dependency of the materials over a large bandwidth.

The time-domain antenna system is utilized for high resolution mm-wave imaging, where the wideband wavelets allow high resolution. The performance of the system is compared to standard wideband frequency-domain VNA measurements for different targets. The gridding method based on a Fourier reconstruction method is compared to the ℓ_1-optimization.

A forward scattering sum rule for parallel-plate waveguides is derived. It is shown that the total electromagnetic interaction introduced by a low pass structure is given by the static polarizability. A parallel-plate waveguide fed by wideband TEM horn antennas is utilized for dynamic measurements and a parallel-plate capacitor for static measurements. The results for a bounded scatterer and periodic structure verify the theoretical findings.

8 Future Work

The leaky lens antennas and the RTD-MOSFET wavelet generator are connected via intermediate devices such as adapters and cables. Therefore ohmic loss and mismatch degrade the performance. By integrating the wavelet generator on the antenna ground plane underneath the lens, losses in the microstrip line as well as any mismatch can be reduced. Furthermore, an integrated receiver on another leaky lens antenna could provide a more efficient system for real-time imaging applications. Using multiple transmitters and receivers as well as fast algorithms such as compressive sensing and sparsity assumptions, it will possible to provide real-time high resolution images. An example is to make real-time high resolution images from chemical processes with a relatively simple setup. Another application of such systems is in real time material characterizations. The large bandwidth of the system can also be utilized to extract the electrical properties of dispersive materials.

References

[1] European Telecommunications Standards Institute. *EN 302 264-1.* Electromagnetic Compatibility and Radio Spectrum.

[2] Federal Communications Commission, FCC. pages 11–79, May 2011.

[3] M. N. Afsar, J. R. Birch, R. N. Clarke, and G. W. Chantry. The measurement of the properties of material. *Proc. IEEE*, **74**(1), 183–199, January 1986.

[4] M. N. Afsar and K. J. Button. Millimeter-wave dielectric measurement of materials. *Proc. IEEE*, **73**(1), January 1985.

[5] O. E. Allen, D. Hill, A. R. Ondrejka, et al. Time-domain antenna characterizations. *IEEE Trans. Electromagn. Compat.*, **35**(3), 339–346, 1993.

[6] A. Alù, M. G. Silveirinha, A. Salandrino, and N. Engheta. Epsilon-near-zero metamaterials and electromagnetic sources: Tailoring the radiation phase pattern. *Physical Review B*, **75**(15), 155410, 2007.

[7] R. K. Amineh, M. Ravan, A. Trehan, and N. K. Nikolova. Near-field microwave imaging based on aperture raster scanning with TEM horn antennas. *IEEE Trans. Antennas Propag.*, **59**(3), 928–940, 2011.

[8] F. Andersson, R. Moses, and F. Natterer. Fast fourier methods for synthetic aperture radar imaging. *IEEE Trans. Aerosp. Electron. Syst.*, **48**(1), 215–229, 2012.

[9] J. R. Andrews. UWB signal sources, antennas and propagation. In *Wireless Communication Technology, 2003. IEEE Topical Conference on*, pages 439–440. IEEE, 2003.

[10] Antenna Standards Committee of the IEEE Antennas and Propagation Society. IEEE Standard Definitions of Terms for Antennas, 1993. IEEE Std 145-1993.

[11] A. Arbabian, S. Callender, S. Kang, B. Afshar, J.-C. Chien, and A. M. Niknejad. A 90 GHz hybrid switching pulsed-transmitter for medical imaging. *IEEE Journal of Solid-State Circuits*, **45**(12), 2667–2681, December 2010.

[12] M. Ärlelid. *Milimeter-Wave Impulse Radio.* PhD thesis, Lund Institute of Technology, Department of Electroscience, Lund Institute of Technology, P.O. Box 118, S-221 00 Lund, Sweden, 2012. ISSN 1654–790X, No. 42.

[13] M. Ärlelid, M. Egard, E. Lind, and L.-E. Wernersson. Coherent V-band pulse generator for impulse radio BPSK. *IEEE Microw. Compon. Lett*, **20**(7), 414–416, 2010.

[14] S. Arslanagic, T. V. Hansen, N. A. Mortensen, A. H. Gregersen, O. Sigmund, R. W. Ziolkowski, and O. Breinbjerg. A review of the scattering-parameter extraction method with clarification of ambiguity issues in relation to metamaterial homogenization. *IEEE Antennas Propag. Mag.*, **55**(2), 91–106, 2013.

[15] J. Baker-Jarvis, E. J. Vanzura, and W. A. Kissick. Improved technique for determining complex permittivity with the transmission/reflection method. *IEEE Trans. Microwave Theory Tech.*, **38**(8), 1096–1103, August 1990.

[16] C. A. Balanis. *Antenna Theory.* John Wiley & Sons, New York, second edition, 1997.

[17] S. Bassam and J. Rashed-Mohassel. A chebyshev tapered TEM horn antenna. *PIRES Online*, **2**(6), 706–709, 2006.

[18] C. E. Baum and E. G. Farr. Impulse radiating antennas. In *Ultra-wideband, short-pulse electromagnetics*, pages 139–147. Springer, 1993.

[19] A. Bernland, A. Luger, and M. Gustafsson. Sum rules and constraints on passive systems. *J. Phys. A: Math. Theor.*, **44**(14), 145205, 2011.

[20] S. P. Boyd and L. Vandenberghe. *Convex Optimization.* Cambridge Univ Pr, 2004.

[21] L. Brillouin. *Wave propagation in periodic structures.* Dover Publications, New York, 1953.

[22] S. Bruni, A. Neto, and F. Marliani. The ultrawideband leaky lens antenna. *IEEE Trans. Antennas Propag.*, **55**(10), 2642–2653, 2007.

[23] K. G. Budden. *The propagation of radio waves.* Cambridge University Press, Cambridge, U.K., 1985.

[24] J. D. Buron, F. Pizzocchero, B. S. Jessen, T. J. Booth, P. F. Nielsen, O. Hansen, M. Hilke, E. Whiteway, P. U. Jepsen, P. Boggild, and D. H. Petersen. Electrically continuous graphene from single crystal copper verified by terahertz conductance spectroscopy and micro four-point probe. *ACS Nano lett.*, **14**(11), 6348–6355, October 2014.

[25] C. Caloz. Metamaterial dispersion engineering concepts and applications. *Proceedings of the IEEE*, **99**(10), 1711–1719, 2011.

[26] E. J. Candès. Compressive sampling. In *Proceedings of the international congress of mathematicians*, volume 3, pages 1433–1452. Madrid, Spain, 2006.

[27] F. Capolino. *Metamaterials handbook*. CRC, 2009.

[28] F. Capolino, editor. *Theory and Phenomena of Metamaterials*. CRC Press, 2009.

[29] L. F. Chen, C. K. Ong, C. P. Neo, V. V. Varadan, and V. K. Varadan. *Microwave electronics: Measurement and materials characterisation*. John Wiley & Sons, New York, 2004.

[30] M. Cheney and B. Borden. *Fundamentals of radar imaging*, volume 79. Society for Industrial Mathematics, 2009.

[31] F. L. Chevalier. *Principles of Radar and Sonar Signal Processing*. Artech House, Boston, London, 2002.

[32] Y. J. Cho, K. H. Kim, D. H. Choi, S. S. Lee, and S.-O. Park. A miniature UWB planar monopole antenna with 5-GHz band-rejection filter and the time-domain characteristics. *IEEE Trans. Antennas Propag.*, **54**(5), 1453–1460, 2006.

[33] R. E. Collin. *Antennas and Radiowave Propagation*. McGraw-Hill, New York, 1985.

[34] F. C. Commission et al. Revision of part 15 of the commission's rules regarding ultra-wideband transmission systems,first report and order, FCC 02. *V48, April*, 2002.

[35] W. Culshaw and M. Anderson. Measurement of permittivity and dielectric loss with a millimetre-wave Fabry-Perôt interferometer. *IEE Proc.-G Electronic Circuits and Systems*, **109**(23), 820–826, 1962.

[36] P. J. W. Debye. *Polar molecules*. Chemical Catalog Company, Incorporated, 1929.

[37] D. L. Donoho. Compressed sensing. *IEEE Trans. Inf. Theory*, **52**(4), 1289–1306, 2006.

[38] M. Egard, M. Ärlelid, L. Ohlsson, B. M. Borg, E. Lind, and L.-E. Wernersson. $\mathrm{In}_{0.53}\mathrm{Ga}_{0.47}\mathrm{As}$ RTD-MOSFET millimeter-wave wavelet generator. *Electron Device Letters, IEEE*, **33**(7), 970–972, 2012.

[39] N. Engheta and R. W. Ziolkowski. *Metamaterials: physics and engineering explorations.* John Wiley & Sons, 2006.

[40] E. G. Farr and C. E. Baum. Extending the definitions of antenna gain and radiation pattern into the time domain. *Sensor and Simulation Notes*, **350**, 1992.

[41] E. G. Farr and C. E. Baum. Time domain characterization of antennas with TEM feeds. Technical report, Citeseer, 1998.

[42] D. F. Filipovic, S. S. Gearhart, and G. M. Rebeiz. Double-slot antennas on extended hemispherical and elliptical silicon dielectric lenses. *IEEE Trans. Microw. Theory Techn.*, **41**(10), 1738–1749, 1993.

[43] E. Fishler, A. Haimovich, R. Blum, D. Chizhik, L. Cimini, and R. Valenzuela. MIMO radar: an idea whose time has come. In *Radar Conference, 2004. Proceedings of the IEEE*, pages 71–78. IEEE, 2004.

[44] G. Franceschetti and R. Lanari. *Synthetic Aperture Radar Processing.* CRC Press, Boca Raton, 1999.

[45] H. T. Friis. A note on a simple transmission formula. *proc. IRE*, **34**(5), 254–256, 1946.

[46] G. G. Gentili and U. Spagnolini. Electromagnetic inversion in monostatic ground penetrating radar: TEM horn calibration and application. *IEEE Trans. Geosci. Remote Sens.*, **38**(4), 1936–1946, Jul 2000.

[47] A. Gerosa, S. Soldà, A. Bevilacqua, D. Vogrig, and A. Neviani. A digitally programmable ring oscillator in the UWB range. In *Circuits and Systems (ISCAS), Proceedings of 2010 IEEE International Symposium on*, pages 1101–1104. IEEE, 2010.

[48] V. Giannini, D. Guermandi, Q. Shi, K. Vaesen, B. Parvais, W. V. Thillo, A. Bourdoux, C. Soens, J. Craninckx, and P. tWambacq. 14.2 a 79 GHz phase-modulated 4GHz-BW CW radar TX in 28nm CMOS. In *Solid-State Circuits Conference Digest of Technical Papers (ISSCC), 2014 IEEE International*, pages 250–251. IEEE, 2014.

[49] W. Gordy. Millimeter and submillimeter waves in physics. In *Proc. Symp. Millimeter Waves*, pages 1–23, 1959.

[50] M. Grant and S. Boyd. Graph implementations for nonsmooth convex programs. In V. Blondel, S. Boyd, and H. Kimura, editors, *Recent Advances in Learning and Control*, Lecture Notes in Control and Information Sciences, pages 95–110. Springer-Verlag Limited, 2008.

[51] N. Guo, R. C. Qiu, S. S. Mo, and K. Takahashi. 60-GHz millimeter-wave radio: Principle, technology, and new results. *EURASIP Journal on Wireless Communications and Networking*, **2007**(1), 48–48, 2007.

[52] M. Gustafsson. Time-domain approach to the forward scattering sum rule. *Proc. R. Soc. A*, **466**, 3579–3592, 2010.

[53] M. Gustafsson, M. Cismasu, and S. Nordebo. Absorption efficiency and physical bounds on antennas. *International Journal of Antennas and Propagation*, **2010**(Article ID 946746), 1–7, 2010.

[54] M. Gustafsson, C. Sohl, and G. Kristensson. Physical limitations on antennas of arbitrary shape. *Proc. R. Soc. A*, **463**, 2589–2607, 2007.

[55] M. Gustafsson, C. Sohl, and G. Kristensson. Illustrations of new physical bounds on linearly polarized antennas. *IEEE Trans. Antennas Propagat.*, **57**(5), 1319–1327, May 2009.

[56] M. Gustafsson. Sum rule for the transmission cross section of apertures in thin opaque screens. *Opt. Lett.*, **34**(13), 2003–2005, 2009.

[57] M. Gustafsson and D. Sjöberg. Physical bounds and sum rules for high-impedance surfaces. *IEEE Trans. Antennas Propagat.*, **59**(6), 2196–2204, 2011.

[58] M. Gustafsson, I. Vakili, S. E. B. Keskin, D. Sjöberg, and C. Larsson. Optical theorem and forward scattering sum rule for periodic structures. *IEEE Trans. Antennas Propagat.*, **60**(8), 3818–3826, 2012.

[59] J. Hasch, E. Topak, R. Schnabel, T. Zwick, R. Weigel, and C. Waldschmidt. Millimeter-wave technology for automotive radar sensors in the 77 GHz frequency band. *IEEE Trans. Microwave Theory Tech.*, **60**(3), 845–860, 2012.

[60] S. Hassi and A. Luger. Generalized zeros and poles of $\mathcal{N}_\kappa$-functions: On the underlying spectral structure. *Methods of Functional Analysis and Topology*, **12**(2), 131–150, 2006.

[61] E. Hecht. *Optics*. Addison-Wesley, Reading, MA, USA, second edition, 1987.

[62] H. Hertz. *Electric waves: being researches on the propagation of electric action with finite velocity through space*. Dover Publications, 1893.

[63] R. D. Hollinger, K. J. A. Tellakula, V. Varadan, and V. Varadan. Microwave characterization of dielectric materials from 8 to 110 ghz using a free-space setup. *Microwave and Optical Technology Letters*, **26**(2), 100–105, 2000.

[64] Y. Huo, G. W. Taylor, and R. Bansal. Planar log-periodic antennas on extended hemishperical silicon lenses for millimeter/submillimeter wave detection applications. *International Journal of Infrared and Millimeter Waves*, **23**(6), 819–839, 2002.

[65] J. D. Jackson. *Classical Electrodynamics.* John Wiley & Sons, New York, third edition, 1999.

[66] Y. Jeong, S. Jung, and J. Liu. A CMOS impulse generator for UWB wireless communication systems. In *Circuits and Systems, 2004. ISCAS'04. Proceedings of the 2004 International Symposium on*, volume 4, pages IV–129. IEEE, 2004.

[67] P. U. Jepsen, D. G. Cooke, and M. Koch. Terahertz spectroscopy and imaging–modern techniques and applications. *Laser & Photonics Reviews*, **5**(1), 124–166, October 2011.

[68] R. T. Johnk, D. R. Novotny, C. M. Weil, M. Taylor, and T. J. Hara. Efficient and accurate testing of an EMC compliance chamber using an ultra-wideband measurement system. In *Electromagnetic Compatibility, 2001. EMC. 2001 IEEE International Symposium on*, volume 1, pages 302–307. IEEE, 2001.

[69] I. Kallfass, A. Tessmann, H. Massler, D. Lopez-Diaz, A. Leuther, M. Schlechtweg, and O. Ambacher. A 300 GHz active frequency-doubler and integrated resistive mixer MMIC. In *Microwave Integrated Circuits Conference, 2009. EuMIC 2009. European*, pages 200–203. IEEE, 2009.

[70] H. Kanaya, H. Shibayama, S. Suzuki, and M. Asada. Fundamental oscillation up to 1.31 THz in thin-well resonant tunneling diodes. In *24th IEEE Int. Conf. Indium Phosphide and Related Materials (IPRM 2012)*, pages 106–109, August 27-30, 2012.

[71] M. Kanda. Time domain sensors for radiated impulsive measurements. *IEEE Trans. Antennas Propag.*, **31**(3), 438–444, 1983.

[72] A. Karlsson and G. Kristensson. Constitutive relations, dissipation and reciprocity for the Maxwell equations in the time domain. *J. Electro. Waves Applic.*, **6**(5/6), 537–551, 1992.

[73] M. Kaveh and M. Soumekh. Computer-assisted diffraction tomography. *Image recovery: theory and application*, pages 369–413, 1987.

[74] S. M. Kay. *Fundamentals of Statistical Signal Processing, Estimation Theory.* Prentice-Hall, Inc., NJ, 1993.

[75] F. W. King. *Hilbert Transforms, Volume 1.* Cambridge University Press, 2009.

[76] F. W. King. *Hilbert Transforms, Volume 2.* Cambridge University Press, 2009.

[77] M. Klemm and G. Troester. Textile UWB antennas for wireless body area networks. *IEEE Trans. Antennas Propag.*, **54**(11), 3192–3197, 2006.

[78] E. F. Knott, J. F. Shaeffer, and M. T. Tuley. *Radar Cross Section.* SciTech Publishing Inc., 5601 N. Hawthorne Way, Raleigh, NC 27613, 2004.

[79] J. D. Kraus. *Antennas.* McGraw-Hill, New York, second edition, 1988.

[80] G. Kristensson. The polarizability and the capacitance change of a bounded object in a parallel plate capacitor. *Physica Scripta*, **86**(3), 035405, 2012.

[81] D. Lamensdorf and L. Susman. Baseband-pulse-antenna techniques. *IEEE Antennas Propag. Mag.*, **36**(1), 20–30, Feb 1994.

[82] L. D. Landau and E. M. Lifshitz. *Electrodynamics of Continuous Media.* Pergamon, Oxford, first edition, 1960.

[83] C. Larsson, D. Sjöberg, and L. Elmkvist. Waveguide measurements of the permittivity and permeability at temperatures up to 1000 °C. *IEEE Trans. Instrumentation and Measurement*, 2011. Accepted for publication.

[84] R. T. Lee and G. S. Smith. A design study for the basic TEM horn antenna. *IEEE Antennas Propag. Mag.*, **46**(1), 86–92, 2004.

[85] B. V. Loon. Radar 101: Celebrating 101 years of development. *Proc. IEEE*, **93**(4), 844–846, 2005.

[86] R. Luebbers, D. Ryan, and J. Beggs. A two-dimensional time-domain near-zone to far-zone transformation. *IEEE Trans. Antennas Propag.*, **40**(7), 848–851, 1992.

[87] S. Maci and A. Neto. Green's function of an infinite slot printed between two homogeneous dielectrics-Part II: uniform asymptotic solution. *IEEE Trans. Antennas Propag.*, **52**(3), 666–676, 2004.

[88] G. Marconi. Wireless telegraphic communication. *Nobel Lecture, December*, **11**, 1909.

[89] A. Massa, P. Rocca, and G. Oliveri. Compressive sensing in electromagnetics-a review. *IEEE Antennas and Propagation Magazine*, **57**(1), 224–238, 2015.

[90] J. C. Maxwell. A dynamical theory of the electromagnetic field. *Phil. Trans. Royal Soc. London*, **155**, pp. 459–512, 1865.

[91] J. C. Maxwell. *A Treatise on Electricity and Magnetism*, volume 1. Dover Publications, New York, 1954.

[92] J. C. Maxwell. *A Treatise on Electricity and Magnetism*, volume 2. Dover Publications, New York, 1954.

[93] A. Mehdipour, K. Mohammadpour-Aghdamand, and R. Faraji-Dana. Complete dispersion analysis of vivaldi antenna for ultra wideband applications. *Progress in Electromagnetics Research*, **77**, 85–96, 2007.

[94] T. Meissner and F. J. Wentz. The complex dielectric constant of pure and sea water from microwave satellite observations. *IEEE Trans. Geosci. Remote Sens.*, **42**(9), 1836–1849, 2004.

[95] T. Mitomo, N. Ono, H. Hoshino, Y. Yoshihara, O. Watanabe, and I. Seto. A 77 GHz 90 nm CMOS transceiver for FMCW radar applications. *IEEE J. Solid-State Circuits*, **45**(4), 928–937, 2010.

[96] A. F. Molisch. *Wireless Communications.* John Wiley & Sons, New York, second edition, 2011.

[97] B. Munk. *Metamaterials: Critique and Alternatives.* John Wiley & Sons, New York, 2009.

[98] F. Natterer. *Mathematical methods in image reconstruction.* Siam, 2001.

[99] A. Neto. UWB, non dispersive radiation from the planarly fed leaky lens antenna-part I: Theory and design. *IEEE Trans. Antennas Propagat.*, **58**(7), 2238–2247, 2010.

[100] A. Neto, S. Bruni, G. Gerini, and M. Sabbadini. The leaky lens: a broadband fixed-beam leaky-wave antenna. *IEEE Trans. Antennas Propagat.*, **53**(10), 3240–3246, 2005.

[101] A. Neto, S. Monni, and F. Nennie. UWB, non dispersive radiation from the planarly fed leaky lens antenna-part II: Demonstrators and measurements. *IEEE Trans. Antennas Propagat.*, **58**(7), 2248–2258, 2010.

[102] A. Neto and S. Maci. Green's function for an infinite slot printed between two homogeneous dielectrics-Part I: Magnetic currents. *IEEE Trans. Antennas Propag.*, **51**(7), 1572–1581, 2003.

[103] R. Newton. Optical theorem and beyond. *Am. J. Phys*, **44**, 639–642, 1976.

[104] A. M. Nicolson. Broad-band microwave transmission characteristics from a single measurement of the transient response. *IEEE Trans. Instrumentation and Measurement*, **17**(4), 395–402, December 1968.

[105] H. M. Nussenzveig. *Causality and dispersion relations.* Academic Press, London, 1972.

[106] L. Ohlsson and L.-E. Wernersson. A 15-Gb/s wireless on-off keying link. *IEEE Access*, **2**(1), 1307–1313, October 2014.

[107] A. V. Oppenheim and R. W. Schafer. *Digital Signal Processing.* Prentice-Hall, Inc., Englewood Cliffs, New Jersey, 1975.

[108] S. J. Orfanidis. *Electromagnetic waves and antennas.* Rutgers University New Brunswick, NJ, 2002.

[109] C. Özdemir. *Inverse synthetic aperture radar imaging with MATLAB algorithms*, volume 210. John Wiley & Sons, 2012.

[110] E. Pancera, T. Zwick, and W. Wiesbeck. Spherical fidelity patterns of UWB antennas. *IEEE Trans. Antennas Propag.*, **59**(6), 2111–2119, June 2011.

[111] S. Paquelet, L.-M. Aubert, and B. Uguen. An impulse radio asynchronous transceiver for high data rates. In *Ultra Wideband Systems, 2004. Joint with Conference on Ultrawideband Systems and Technologies. Joint UWBST & IWUWBS. 2004 International Workshop on*, pages 1–5. IEEE, 2004.

[112] C. Park and T. S. Rappaport. Short-range wireless communications for next-generation networks: UWB, 60 GHz millimeter-wave WPAN, and ZigBee. *Wireless Commun.*, **14**(4), 70–78, 2007.

[113] A. Paulraj, R. Nabar, and D. Gore. *Introduction to Space-Time Wireless Communications.* Cambridge University Press, Cambridge, U.K., 2003.

[114] T.-A. Phan, J. Lee, V. Krizhanovskii, S.-K. Han, and S.-G. Lee. A 18-pj/pulse OOK CMOS transmitter for multiband UWB impulse radio. *IEEE Microw. Compon. Lett*, **17**(9), 688–690, 2007.

[115] Z. Pi and F. Khan. An introduction to millimeter-wave mobile broadband systems. *IEEE Commun. Mag.*, **49**(6), 101–107, 2011.

[116] S. Pinel, S. Sarkar, P. Sen, B. Perumana, D. Y. David, D. Dawn, and J. Laskar. A 90nm CMOS 60GHz radio. In *Solid-State Circuits Conference, 2008. ISSCC 2008. Digest of Technical Papers. IEEE International*, pages 130–601. IEEE, 2008.

[117] D. M. Pozar. *Microwave Engineering.* John Wiley & Sons, New York, third edition, 2005.

[118] W. D. Prather, C. E. Baum, J. M. Lehr, J. P. Loughlin, S. Tyo, J. S. Schoenberg, R. J. Torres, T. C. Tran, D. W. Scholfield, and J. Gaudet. Ultra-wideband source and antenna research. *IEEE Trans. Plasma Sci.*, **28**(5), 1624–1630, 2000.

[119] E. M. Purcell. On the absorption and emission of light by interstellar grains. *J. Astrophys.*, **158**, 433–440, 1969.

[120] G. Quintero, J.-F. Zurcher, and A. K. Skrivervik. System fidelity factor: A new method for comparing UWB antennas. *IEEE Trans. Antennas Propag.*, **59**(7), 2502–2512, 2011.

[121] T. S. Rappaport. *Wireless communications: principles and practice*, volume 2. prentice hall PTR New Jersey, 1996.

[122] G. T. Ruck, D. E. Barrick, W. D. Stuart, and C. K. Krichbaum. *Radar Cross-Section Handbook*, volume 1 and 2. Plenum Press, New York, 1970.

[123] Y. Sawaragi, H. Nakayama, and T. Tanino. *Theory of Multiobjective Optimization.* Elsevier Science & Technology Books, 1985.

[124] H. Schantz. *The Art and Science of Ultrawideband Antennas.* Artech House, Boston, London, 2005.

[125] J. S. Schoenberg, J. W. Burger, J. S. Tyo, M. D. Abdalla, M. C. Skipper, and W. R. Buchwald. Ultra-wideband source using gallium arsenide photoconductive semiconductor switches. *IEEE Trans. Plasma Sci.*, **25**(2), 327–334, 1997.

[126] J. L. Schwartz and B. D. Steinberg. Ultrasparse, ultrawideband arrays. *IEEE Trans. Ultrason., Ferroelect., Freq. Control*, **45**(2), 376–393, 1998.

[127] K. L. Shlager, G. S. Smith, and J. G. Maloney. Accurate analysis of TEM horn antennas for pulse radiation. *IEEE Trans. Electromagn. Compat.*, **38**(3), 414–423, 1996.

[128] A. Shlivinski, E. Heyman, and R. Kastner. Antenna characterization in the time domain. *IEEE Trans. Antennas Propag.*, **45**(7), 1140–1149, 1997.

[129] D. Sjöberg. Low frequency scattering by passive periodic structures for oblique incidence: low pass case. *J. Phys. A: Math. Theor.*, **42**, 385402, 2009.

[130] D. Sjberg and C. Larsson. Material characterization in partially filled waveguides using inverse scattering and multiple sample orientations. *Radio Science*, **50**(6), 554–561, 2015.

[131] M. I. Skolnick. Nonuniform arrays. In R. E. Collin and F. J. Zucker, editors, *Antenna theory, part 1*, pages 207–234. McGraw-Hill, New York, 1969.

[132] M. I. Skolnik. *Introduction to radar systems.* McGraw-Hill, Boston, 3rd edition, 2001.

[133] C. Sohl and M. Gustafsson. A priori estimates on the partial realized gain of Ultra-Wideband (UWB) antennas. *Quart. J. Mech. Appl. Math.*, **61**(3), 415–430, 2008.

[134] C. Sohl, M. Gustafsson, and G. Kristensson. Physical limitations on broadband scattering by heterogeneous obstacles. *J. Phys. A: Math. Theor.*, **40**, 11165–11182, 2007.

[135] C. Sohl, C. Larsson, M. Gustafsson, and G. Kristensson. A scattering and absorption identity for metamaterials: experimental results and comparison with theory. *J. Appl. Phys.*, **103**(5), 054906, 2008.

[136] H.-J. Song and T. Nagatsuma. Present and future of terahertz communications. *IEEE Trans. THz Sci. Technol*, **1**(1), 256–263, 2011.

[137] M. Soumekh. *Synthetic Aperture Radar Signal Processing with MATLAB Algorithms.* John Wiley & Sons, New York, 1999.

[138] J. W. Strutt. On the light from the sky, its polarization and colour. *Phil. Mag.*, **41**, 107–120 and 274–279, April 1871. Also published in Lord Rayleigh, Scientific Papers, volume I, Cambridge University Press, Cambridge, 1899.

[139] A. H. Taylor, L. C. Young, and L. A. Hyland. System for detecting objects by radio, 13 1933. US Patent 1,981,884.

[140] O. V. Tereshchenko, F. J. K. Buesink, and F. B. J. Leferink. An overview of the techniques for measuring the dielectric properties of materials. In *XXXth URSI Symp. General Assembly and Scientific (URSI GASS 2011)*, pages 1–4, August 2011.

[141] R. Tibshirani. Regression shrinkage and selection via the lasso. *Journal of the Royal Statistical Society. Series B (Methodological)*, pages 267–288, 1996.

[142] J. S. Tyo. Optimization of the TEM feed structure for four-arm reflector impulse radiating antennas. *IEEE Trans. Antennas Propag.*, **49**(4), 607–614, 2001.

[143] I. Vakili, M. Gustafsson, D. Sjöberg, R. Seviour, M. Nilsson, and S. Nordebo. Sum rules for parallel plate waveguides: Experimental results and theory. Technical Report LUTEDX/(TEAT-7229)/1–20/(2014), Lund University, Department of Electrical and Information Technology, P.O. Box 118, S-221 00 Lund, Sweden, 2014. http://lup.lub.lu.se.

[144] I. Vakili, M. Gustafsson, D. Sjoberg, R. Seviour, M. Nilsson, and S. Nordebo. Sum rules for parallel-plate waveguides: Experimental results and theory. *IEEE Trans. Microw. Theory Techn.*, **62**(11), 2574–2582, 2014.

[145] I. Vakili, L. Ohlsson, M. Gustafsson, and L.-E. Wernersson. Wideband and non-dispersive wavelet transmission using leaky lens antenna. *Electronic Letters*, **49**(5), 321–322, 2013.

[146] I. Vakili, L. Ohlsson, L.-E. Wernersson, and M. Gustafsson. Time-domain system for millimeter-wave material characterization. *IEEE Trans. Microw. Theory Techn.*, **63**(9), 2915 – 2922, 2015.

[147] J. G. Van Bladel. *Electromagnetic Fields.* IEEE Press, Piscataway, NJ, second edition, 2007.

[148] V. V. Varadan, R. D. Hollinger, D. K. Ghodgaonkar, and V. K. Varadan. Free-space, broadband measurements of high-temperature, complex dielectric properties at microwave frequencies. *IEEE Trans. Instrumentation and Measurement*, **40**(5), 842–846, 1991.

[149] V. Venkatasubramanian and H. Leung. A novel chaos-based high-resolution imaging technique and its application to through-the-wall imaging. *IEEE Signal Process. Lett.*, **12**(7), 528–531, 2005.

[150] V. G. Veselago. The electrodynamics of substances with simultaneously negative values of ϵ and μ. *Sov. Phys. Usp.*, **10**(4), 509–514, 1968.

[151] A. von Hippel. *Dielectric Materials and Applications.* Artech House, Boston, London, 1954.

[152] W. Wiesbeck, G. Adamiuk, and C. Sturm. Basic properties and design principles of UWB antennas. *Proc. IEEE*, **97**(2), 372–385, Feb 2009.

Wideband and Non-Dispersive Wavelet Transmission using Leaky Lens Antenna

Paper I

Iman Vakili, Lars Ohlsson, Mats Gustafsson and Lars-Erik Wernersson

---

Published as: I. Vakili, L. Ohlsson, M. Gustafsson and L.-E. Wernersson, Wideband and Non-Dispersive Wavelet Transmission using Leaky Lens Antenna, *Electronics Letters*, Vol. 49, No. 5, pp. 321-322, 2013.

Abstract

An ultra-wideband, non dispersive leaky lens antenna system for impulse applications is designed, fabricated and characterized. An in-house wavelet generator is connected to the antenna to transmit 100 ps long square pulses with center frequencies at 45, 60 and 75 GHz. It is shown that the leaky lens antenna has negligible distortion and preserves the pulse shape generated by the mm-wave pulse generator.

1 Introduction

Short pulse radiation is a growing demand in many applications such as imaging, radars, and high data rate wireless communications. These applications require antenna phase linearity over a wide bandwidth of operation. TEM horn [11], Vivaldi, and spiral [4] antennas are examples that show relatively low-dispersive radiation over a wide bandwidth. However, in TEM horn antennas the phase center moves along the longitudinal axis and in spirals, non-linear phase variations gives pulse distortion and degrades the performance. A combination of leaky wave radiation and a dielectric lens has been proposed for very low-dispersive radiation over a wide bandwidth [9]. An octave bandwidth with excellent pulse preservation is demonstrated in [8,10]. This is done using a planar fed leaky lens antenna that has been characterized using a frequency domain system.

In this work, the leaky lens antenna has been modified and tested by both frequency-domain and time-domain systems. Its reflection coefficient was characterized by a network analyzer, while its transient characteristics were investigated through transmission of 100 ps long pulses realized by a wavelet generator [3]. Wavelet generators are used in short range ultra-wideband applications, such as radars and high data rate communications [1,6]. The wavelet generator presented here consists of a fast switching metal-oxide-semiconductor field-effect-transistor (MOSFET) in series with a resonant tunneling diode (RTD) which generates short high-frequency pulses. The wavelet generator delivers pulses to one transmitting lens antenna and another is used as a receiver. It is demonstrated that the antenna preserves the pulse shape, *i.e.*, the pulse distortion is negligible.

2 Antenna Design

The antenna consists of a synthesized hemi-sphere High Resistivity Float Zone-Silicon (HRFZ-Si) lens with relative permittivity $\epsilon_{\mathrm{r}} = 11.67$ integrated to a planar feeding structure. In order to achieve a fixed phase center, the shape of the lens has to be elliptical, but fabricating an elliptical lens has difficulties. Instead, a synthesized hemispherical silicon lens with a cylindrical extension at its fictitious focal point may be used as a good approximation of an ellipsoid [5]. In Fig. 1a, the lens together with the slot feeding structure is depicted and Fig. 1b shows the manufactured lens antenna. The feed is placed at the focal point of the lens.

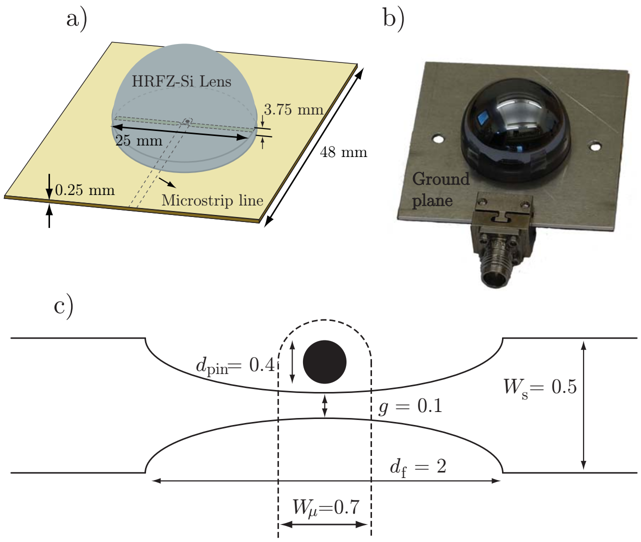

Figure 1: Geometry of the leaky wave lens antenna with all the dimensions in mm. a) 3-D view of the lens antenna. b) Leaky lens antenna prototype. c) Microstrip to slot transition details.

The radius of the lens is $a = 12.5\,\text{mm}$ and the eccentricity is $e = 1/\sqrt{\epsilon_{\text{r}}}$ [7], which gives the height of the extension, $h = 3.75\,\text{mm}$. An air gap of 0.25 mm is introduced between the antenna and the planar structure to reduce the sidelobes. This air gap gives an upper bound to leaky wave propagation direction and is equal to the critical angle of the dielectric ($\theta_c \approx 73°$) [2]. The resulting radiation is directive and frequency independent [8, 10].

In order to match the antenna to $50\,\Omega$, the microstrip width $W_\mu = 0.7\,\text{mm}$ has been chosen. This microstrip line feeds the slot through a metallic via etched in a $250\,\mu\text{m}$ substrate of Arlon Diclad 880 with permittivity $\epsilon_{\text{r}} = 2.2$. Figure 1c shows the microstrip to slot connection, which has been optimized to achieve a very low reflection over the frequency range [15, 65] GHz. CST Microwave studio has been used to design and simulate the antenna.

3 Frequency-domain measurements

The frequency domain performance of the antenna has been verified by an Agilent E8361A PNA from 15 GHz to 67 GHz. A SouthWest Microwave 2.40 mm end launch connector has been used to connect the manufactured antenna to a 1.85 mm MegaPhase cable. Two antenna prototypes have been manufactured and their reflection coefficients are shown in Fig. 2. It is obvious that the antenna is well matched over the targeted frequency band. This is achieved without use

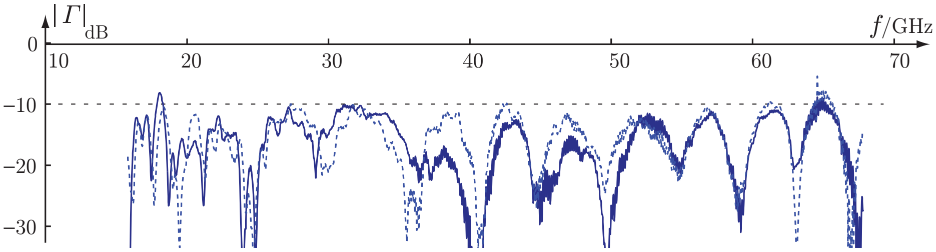

Figure 2: Reflection coefficients of two leaky lens antenna prototypes with the same dimensions.

of any matching layers, which are difficult to fabricate at higher frequencies. The main reflection is from the lens-air interface and can be reduced using matching layers [8].

4 Time-domain measurements

To verify the non-distorting pulsed operation of the lens antenna, it was tested together with an in-house fabricated RTD-MOSFET wavelet generator [3]. The wavelet generator is implemented fully on-chip and it consists of an InGaAs RTD, *i.e.*, a negative differential conductance device, connected in series with a $\text{In}_{0.53}\text{Ga}_{0.47}\text{As}$ MOSFET operated as a switch. When switching the generator input gate to a high state, the total conductance in the circuit becomes negative and an oscillation builds up. In this state, as the MOSFET channel is open, the drive voltage falls primarily over the RTD. The frequency of oscillation is controlled by an on-chip resonance circuit and the RTD capacitance, which is dependent on the drive voltage. When the voltage on the gate is returned to a low state, charge transport through the MOSFET is impeded. This turns the total conductance in the circuit positive and the oscillation is quenched, see [3] for details.

During the measurements, a probe station with 100 μm pitch GSG Cascade Infinity Probes was used to access both the MOSFET gate input and the output taken over the on-chip resonance circuit. An Agilent N4906B Serial BERT was used to generate 100 ps long baseband pulses, with a periodic repetition every 10 ns. These pulses were transferred to the input of the RTD-based wavelet generator, switching the output between oscillating and non-oscillating states. The transmitting (Tx) antenna was connected to the isolated port of a bias-T. The receiving (Rx) antenna was connected to the sampling head of a LeCroy WaveExpert 100H sampling oscilloscope via a 30 inch MegaPhase cable with 1.85 mm interfaces. The Tx and Rx antennas depicted in Fig. 4 are separated by 30 cm, measured between the ground planes. Reference measurements were also made using the cable to connect the bias-T and sampling head directly.

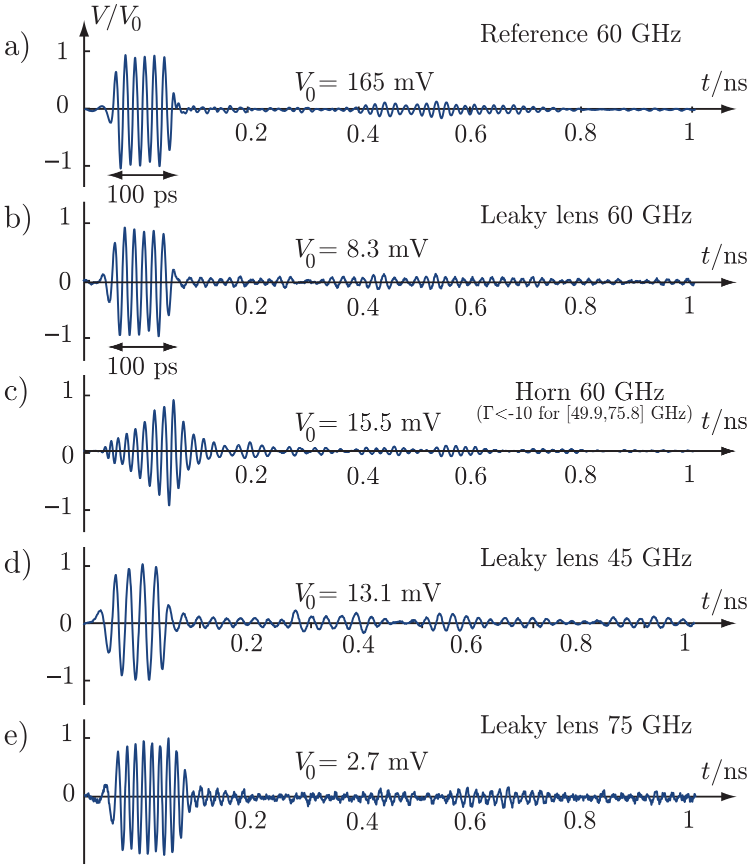

Figure 3: Received voltage normalized by the maximum received pulse amplitude, V_0. The transmitted pulse is 100 ps long. a) Reference pulse ($f_\mathrm{c} = 60\,\mathrm{GHz}$). b) Lens antenna ($f_\mathrm{c} = 60\,\mathrm{GHz}$). c) Horn antenna ($f_\mathrm{c} = 60\,\mathrm{GHz}$) which is well matched over the frequency range $[45, 75.8]\,\mathrm{GHz}$ d) Lens antenna ($f_\mathrm{c} = 45\,\mathrm{GHz}$). e) Lens antenna ($f_\mathrm{c} = 75\,\mathrm{GHz}$).

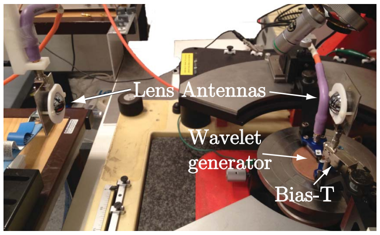

Figure 4: Time domain measurement setup using an in-house fabricated wavelet generator.

Three wavelet generators with center frequencies, $f_\mathrm{c} = 45$, 60 and 75 GHz were used. In Fig. 3a, the 100 ps long reference pulse with $f_\mathrm{c} = 60\,\mathrm{GHz}$ is shown. The amplitude of the pulse is normalized to its maximum value, $V_0 = 165\,\mathrm{mV}$. Figure 3b-c show the lens to lens transmission and the horn to horn transmission, respectively. It is seen that the pulse width in the leaky lens case remains almost the same as the reference pulse, and the rectangular pulse shape is preserved. The maximum value of the received pulse in the lens to lens configuration is $V_0 = 8.3\,\mathrm{mV}$ and considering the path loss at 60 GHz, the gain of the antenna is found to be 15.3 dB. In horn to horn configuration the amplitude of the received signal is $V_0 = 15.5\,\mathrm{mV}$, which corresponds to 19.1 dB gain, in agreement with 19.48 dBi in the manufacturer specification.

In order to verify the UWB performance of the antenna system, two additional wavelet generators with 100 ps long pulses at $f_\mathrm{c} = 45\,\mathrm{GHz}$ and 75 GHz were used. The measured lens to lens transmission voltages with 100 ps long pulses at $f_\mathrm{c} = 45\,\mathrm{GHz}$ and $f_\mathrm{c} = 75\,\mathrm{GHz}$ are depicted in Fig. 3d and e, respectively. Considering the path loss and the reference voltages $V_0 = 186\,\mathrm{mV}$ at $f_\mathrm{c} = 45\,\mathrm{GHz}$ and $V_0 = 76.4\,\mathrm{mV}$ at $f_\mathrm{c} = 75\,\mathrm{GHz}$ the corresponding approximate gains are 15.5 dB and 14.8 dB, respectively. These figures further verify the ultra-wideband gain property and non-dispersiveness of the leaky lens antenna.

5 Conclusions

A leaky lens antenna has been designed and fabricated. The antenna has been verified by frequency- and time-domain measurements. The frequency-domain results show that the antenna is well matched over the frequency band $[15, 67]$ GHz which is an advantage in adaptive systems. The antenna has been tested using in-house wavelet generators at different frequencies. The results demonstrate pulse radiation through a millimeter-wave radio channel with negligible pulse distortion.

References

[1] M. Ärlelid, M. Egard, L. Ohlsson, E. Lind, and L.-E. Wernersson. Impulsed-based 4 Gbit/s radio link at 60 GHz. *Electronic Letters*, **47**(7), 467–468, 2011.

[2] M. Born and E. Wolf. *Principles of Optics.* Cambridge University Press, Cambridge, U.K., seventh edition, 1999.

[3] M. Egard, M. Ärlelid, L. Ohlsson, B. M. Borg, E. Lind, and L.-E. Wernersson. $In_{0.53}Ga_{0.47}As$ RTD-MOSFET millimeter-wave wavelet generator. *Electron Device Letters, IEEE*, **33**(7), 970–972, 2012.

[4] M. A. Elmansouri and D. S. Filipovic. Low-dispersion spiral antennas. *IEEE Trans. Antennas Propag.*, **60**(12), 5522–5530, 2012.

[5] D. F. Filipovic, S. S. Gearhart, and G. M. Rebeiz. Double-slot antennas on extended hemispherical and elliptical silicon dielectric lenses. *IEEE Trans. Microw. Theory Techn.*, **41**(10), 1738–1749, 1993.

[6] I. Gresham, A. Jenkins, R. Egri, N. C. Eswarappa mand Kinayman, N. Jain, R. Anderson, F. Kolak, R. Wohlert, S. Bawell, J. Bennett, and J.-P. Lanteri. Ultra-wideband radar sensors for short-range vehicular applications. *IEEE Trans. Microwave Theory and Techniques*, **52**(9), 2105–2122, 2004.

[7] E. Hecht. *Optics.* Addison-Wesley, Reading, MA, USA, second edition, 1987.

[8] A. Neto. UWB, non dispersive radiation from the planarly fed leaky lens antenna-part I: Theory and design. *IEEE Trans. Antennas Propagat.*, **58**(7), 2238–2247, 2010.

[9] A. Neto, S. Bruni, G. Gerini, and M. Sabbadini. The leaky lens: a broadband fixed-beam leaky-wave antenna. *IEEE Trans. Antennas Propagat.*, **53**(10), 3240–3246, 2005.

[10] A. Neto, S. Monni, and F. Nennie. UWB, non dispersive radiation from the planarly fed leaky lens antenna-part II: Demonstrators and measurements. *IEEE Trans. Antennas Propagat.*, **58**(7), 2248–2258, 2010.

[11] K. L. Shlager, G. S. Smith, and J. G. Maloney. Accurate analysis of TEM horn antennas for pulse radiation. *IEEE Trans. Electromagn. Compat.*, **38**(3), 414–423, 1996.

Time-Domain System for Millimeter-Wave Material Characterization

Paper II

Iman Vakili, Lars Ohlsson, Lars-Erik Wernersson and Mats Gustafsson

---

Published as: I. Vakili, L. Ohlsson, L.-E. Wernersson and M. Gustafsson , Time-Domain System for Millimeter-Wave Material Characterization, *IEEE Transactions on Microwave Theory and Techniques*, Vol. 63, No. 9, pp. 2915-2922, 2015.

Abstract

Time-domain material characterization using a leaky lens antenna and an in-house fabricated millimeter-wave wavelet generator using III–V technology is investigated. The wavelet generator produces short high-frequency pulses and is connected to a wideband and non-dispersive leaky lens antenna. A purely time-domain methodology is used to extract the complex permittivity of non-dispersive and non-magnetic materials. The permittivity is found from the phase delay and the amplitude mismatch introduced by the object at the carrier frequency of the pulse. The wide bandwidth of the wavelet is used to investigate frequency dependent material properties. Measurement results from two dielectric slabs are illustrated. The time-domain methodology is verified by frequency-domain measurements and analysis.

1 Introduction

In recent years, there has been an increasing interest in applications at millimeter-wave (mm-wave) frequencies due to the existence of unlicensed bands for a variety of applications in radars, imaging, medical, and wireless communications [12, 18, 26]. From tomography in medical applications to channel modeling in wireless communications, the knowledge about material properties is essential. Broadband measurements of material properties at microwave frequencies were introduced by Nicolson [24, 25]. The measurements have been scaled up in frequency using spectroscopy technique at millimeter-wave frequencies [2].

A variety of methods have been applied for material characterizations [1,6,29], such as: 1) Parallel plate capacitor method [3], where the material is inserted between two metallic plates of the capacitor and the permittivity is estimated from the change in the capacitance. 2) Resonant cavity technique [5, 21], where the material parameters are estimated from the resonance frequency. In the resonant cavity model, the size of the object has to be smaller than the operating wavelength which results in inaccuracies at mm-wave frequencies. 3) The transmission line techniques using open ended coaxial probes [4] or rectangular waveguides [13], wherein the contact between the transmission line and the material under test has to be done in a precise way. 4) Free-space method [32] using directive antennas. The free-space method has the advantage of making accurate wideband indirect measurements with a relatively simple setup. In the time-domain, the most common measurement systems are time-domain reflectometry (TDR) [10] and time-domain spectroscopy (TDS) [2, 9, 20]. Free-space measurements can be performed in transmission and/or reflection configurations.

In this paper, we demonstrate a relatively simple time-domain free-space transmission methodology for extraction of the electromagnetic properties of materials. The system consists of a wideband non-dispersive leaky lens antenna [22, 23, 31] and an in-house fabricated wavelet generator [14]. Leaky wave propagation together with a silicon hemispherical lens give wideband and non-dispersive radiation properties. The circular symmetry of the lens produces a symmetrical stable radiation pattern over the operating frequency band. The wavelet generator produces short pulses at mm-wave frequencies using a resonant tunneling diode (RTD) in series with a surface channel metal-oxide-semiconductor field-effect-transistor (MOSFET). The antenna system transmits short pulses and are received by an identical lens antenna to assure that the pulse shape is preserved.

The pulse is recorded in the absence and presence of an object and the distortions of the signal determines the material properties. Both amplitude changes and time delay of the signal are measured and utilized to extract the relative permittivity and loss of the material. A purely time-domain technique is established for time-domain characterization. The method has the advantage of simplicity and reliability for detecting the material properties, especially the losses in materials. It has high accuracy at the carrier frequency of the wavelet but the wide signal bandwidth also yields broadband estimations due to the short mm-wave pulse length. A time-domain method for lossless and electrically thick materials is outlined in [31]. The system has a small size and low technical complexity, as compared to existing mm-wave time-domain setups [1]. Other time-domain techniques are operating mainly either at frequencies lower than 20 GHz [28] or higher than 300 GHz with THz-based technologies.

The methodology is used to characterize electrically thick and thin samples of poly methyl methacrylate (PMMA) and poly vinyl chloride (PVC)-based materials. The wide bandwidth of the time-domain pulse is utilized to determine frequency dependent material properties. The results are verified by frequency-domain measurements using a network analyzer and compared to previously reported works on similar materials.

The remainder of the paper is structured as follows. The time-domain system is presented in Section 2. A time-domain direct technique to extract the dielectric constant is reported in Section 3. The experimental results are presented in Section 4. The frequency-domain analysis is discussed in Section 5, and the paper is concluded in Section 6.

2 Time-domain system

A time-domain system based on a mm-wave RTD-MOSFET wavelet generator [14] connected to a non-dispersive and wideband leaky lens antenna [22,23,31] is investigated for material characterization.

2.1 Leaky lens antenna

The leaky lens antenna is considered a non-dispersive wideband antenna that can be used for transmission of short high-frequency pulses. This antenna, as shown in Fig. 1, consists of a planar feeding structure and a hemispherical silicon lens with relative permittivity of 11.67. The feeding structure consists of a 25 mm long

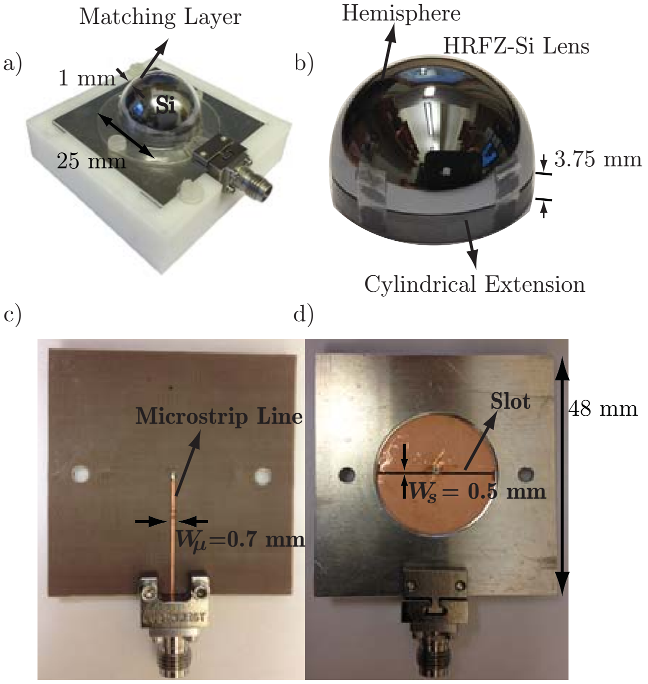

Figure 1: The leaky lens antenna prototype. a) Leaky lens antenna with 1 mm thick PMMA matching layer. b) Synthesized lens using a hemispherical silicon and a cylindrical extension. The diameter of the lens is 25 mm and the extension height is 3.75 mm. c) Microstrip feed line. The width of the microstrip line is $W_\mu = 0.7\,\mathrm{mm}$. d) Front view of the feeding structure. A metallic support is placed on the substrate to introduce a 0.25 mm air gap between the slot and the silicon lens. The feeding structure is $48 \times 48\,\mathrm{mm}^2$ and the width of the slot is $W_\mathrm{s} = 0.5\,\mathrm{mm}$.

slot etched in the ground plane of the antenna and is fed from a $50\,\Omega$ microstrip line through a metalized via. The substrate is a $250\,\mu$m thick Arlon Diclad 880 with relative permittivity of 2.2. The $W_\mu = 0.7\,\mathrm{mm}$ microstrip line is fed by a SouthWest Microwave 2.40 mm end-launch coaxial to microstrip connector.

The lens is integrated to the feeding structure and located on top of the slot, in a way that the focal point of the lens is in the same position as the middle of the slot. The resulting radiation between the feeding structure and the silicon lens is a leaky wave propagation for a small slot width, $W_\mathrm{s} \ll \lambda_\mathrm{d}$, where λ_d is the wavelength inside the dielectric [22]. A 0.25 mm air gap is inserted between the antenna and the feeding structure in order to suppress the side lobe level, improve the matching, and stabilize the leaky wave radiation angle over a wide frequency range. The angle of the leaky wave radiation has a maximum in $\theta_\mathrm{LW} \approx 73°$ which is similar to the direction of the critical angle. To simplify the fabrication, the elliptical lens is synthesized using a hemispherical lens with a cylindrical extension. The radius of the hemisphere is $r = 12.5\,\mathrm{mm}$ and the extension length is chosen to $h = 3.75\,\mathrm{mm}$ using the eccentricity of the lens $e = 1/\sqrt{\epsilon_{\mathrm{r,lens}}}$, where $\epsilon_{\mathrm{r,lens}}$ denotes the relative permittivity of the lens material [19]. The circular symmetry of the lens results in a directive and symmetric radiation pattern. Measurements show that the antenna is well matched to $50\,\Omega$ from 15 to at least 67 GHz [31]. One issue in lens antennas is multiple reflections inside the lens caused by the impedance mismatch at the lens-air interface. A matching layer made of PMMA has been added on top of the lens to reduce the reflections and at the same time improve the transmission, as indicated in Fig. 1a. The gain of the antenna is 18 dBi at 50 GHz and the half-power beam width is approximately 13°. It should be noted that the gain and the beamwidth of the leaky lens antenna remains almost constant from 30 to 67 GHz.

2.2 Wavelet generator

A wavelet generator fabricated in III–V compound semiconductor technology, as shown in Fig. 2, is used to produce 80 ps long pulses with 50 GHz carrier frequency. The wavelet generator consists of an RTD as a negative differential conductive device in series with a III–V MOSFET switch [14]. This circuit presents negative differential conductance when biased and the switch is on. As a result the circuit produces oscillations with a center frequency around 50 GHz given by the RTD capacitance and the on-chip resonance circuit. The input on the MOSFET gate and the output over the resonance circuit are interfaced by Cascade i67 probes. The input baseband signal is generated by an Agilent N4906B that generates a programmable pulse pattern with an 80 ps time-base. The baseband pulses are then transformed into 50 GHz oscillations by the wavelet generator circuit. The transmitting antenna is connected to the output via the isolated port of a bias-T.

The leaky lens antenna transmits the generated ultra-short pulses with negligible distortion. These signals propagate through the radio channel and are received by an identical antenna. A LeCroy 100H oscilloscope is used to sample the signals. The measured signal in the presence of the antennas and the link in between is illustrated in Fig. 2a and the power spectral density of the pulse is shown in Fig. 2b. The pulse shape preservation of the antenna is demonstrated in [31]. The bandwidth of the pulse is 25 GHz, however, in an optimized measurement system the power in the rest of the spectrum, *e.g.*, 30–100 GHz, can also be used for wideband measurements, see Fig. 2b.

3 Direct time-domain extraction method

In this section, the definition of the transmission coefficient in the time-domain is used to introduce a method for material characterization. Consider a wavelet, $v(t)$, with the carrier frequency f_0 and pulse duration t_{p}, cf. Fig. 2, incident on

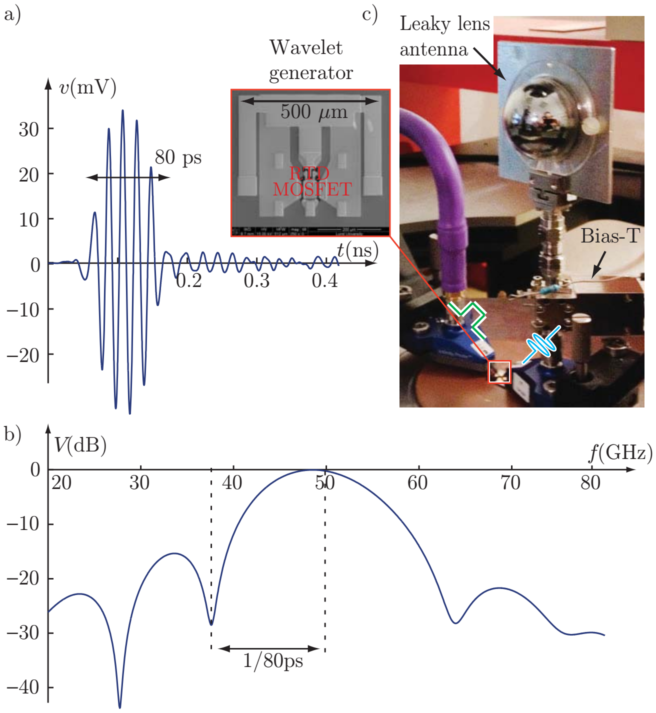

Figure 2: The wavelet generator transforms baseband pulses to high frequency oscillations. a) The received signal using leaky lens antennas in transmission over a free-space channel. b) Normalized power spectral density of the signal. c) Probed transmitter setup when the wavelet generator transforms baseband pulses to millimeter wave wavelets.

a single dielectric slab with thickness d and refractive index $n(f_0) = n_\mathrm{r} + \mathrm{i}n_\mathrm{i}$. The refractive index for non-magnetic materials is defined as $n = \sqrt{\epsilon_\mathrm{r}}$, where $\epsilon_\mathrm{r}(f) = \epsilon_\mathrm{r,r}(f) + \mathrm{i}\epsilon_\mathrm{r,i}(f)$ is the relative permittivity and describes how an electric field is affected by a medium. Here, the time convention $\mathrm{e}^{-\mathrm{i}2\pi f t}$ with $\mathrm{i}^2 = -1$ is used.

The transmission impulse response, which is the transmission response from a Dirac delta function, $\delta(t)$, as defined in [27], is used to estimate the transmission response to the wavelet generated by the system. The time-domain transmission response to the input $v(t)$ is then approximately given by

$$\mathcal{T}(t) \approx \sum_{m=0}^{\infty} \frac{4n_\mathrm{r}(n_\mathrm{r}-1)^{2m}}{(n_\mathrm{r}+1)^{2m+2}} v(t - mT - T/2)\mathrm{e}^{-(2m+1)\alpha d}, \tag{3.1}$$

where $m+1$ denotes the number of reflections from the material that are delayed by mT and $T = 2dn_\mathrm{r}/c_0$ is the two way travel time delay through the material. Also, the attenuation constants within the material is denoted $\alpha = k_0 n_\mathrm{i}$ where $k_0 = 2\pi f_0/c_0$ is the wavenumber in free space and $c_0 \approx 3 \times 10^8$ m/s is the speed of light in vacuum. The first term, $m = 0$, is the immediate transmitted signal while the $m \geqslant 1$ terms represent multiple reflections inside the material.

Consider an example with an 80 ps long square pulse modulated at $f_0 =$ 50 GHz with amplitude 1 V as shown in Fig. 3. The signal strikes the left interface of a non-magnetic and non-dispersive homogeneous material with thickness d and relative permittivity $\epsilon_\mathrm{r} = 4 + \mathrm{i}0.01$. The transmitted signal at the right interface of the sample is shown as the dashed curves in Fig. 3 for different thicknesses of the sample and the solid lines illustrate the reference signal in the absence of the material. The thickness d is set to 20 mm in Fig. 3a and to 3 mm in Fig. 3b. In both cases, in the presence of the object, the starting point of the transmitted signal is delayed and its amplitude is affected by the losses inside the media as well as the impedance mismatch at the air-dielectric and dielectric-air interfaces. As shown in Fig. 3, the amplitude of the signal when $d = 20$ mm is attenuated and the second term of the transmitted field, *i.e.*, $m = 1$ in (3.1), is well separated from the first term. The time delay, t_d, is defined as the time difference between the received signals in the presence and the absence of the object. For this sample $t_\mathrm{d} = 66.7$ ps and determines the real part of the refractive index as

$$n_\mathrm{r} = \frac{c_0 t_\mathrm{d}}{d} + 1 \approx 2. \tag{3.2}$$

The ratio between the amplitudes of the signals, solid- and dashed-lines in Fig. 3, is $\mathit{\Delta} = 0.8434$ and estimates the attenuation constant of the material. Using the attenuation constant and $\alpha = k_0 n_\mathrm{i}$ the imaginary part of the refractive index is estimated to

$$n_\mathrm{i} = \frac{1}{k_0 d} \ln\left(\frac{\mathit{\Delta}(n(f_0)+1)^2}{4n(f_0)}\right) = 2.5 \times 10^{-3}, \tag{3.3}$$

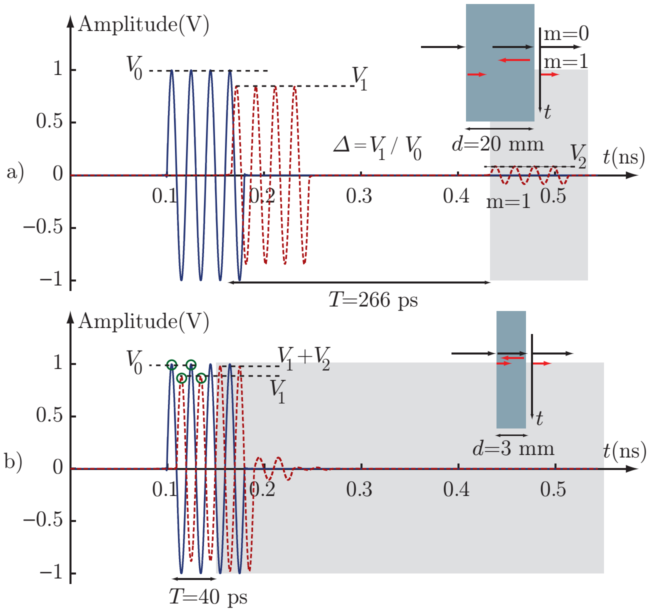

Figure 3: Transmitted signals in the absence (solid) and the presence (dashed) of the materials with thickness a) 20 mm and b) 3 mm and relative permittivity $\epsilon_\mathrm{r} = 4 + \mathrm{i}0.01$. V_0 is the amplitude of the received signal in the absence of the sample, V_1 denotes the amplitude of the first term in (3.1) and V_2 is the amplitude of the second term. The ratio between V_1 and V_0 is denoted by $\Delta = V_1/V_0$.

where the refractive index in (3.3) is approximated as $n(f_0) \approx n_\mathrm{r}$ for low-loss materials. The resulting permittivity is $\epsilon_\mathrm{r} = (n_\mathrm{r} + \mathrm{i}n_\mathrm{i})^2 = 4 + \mathrm{i}0.01$, which is, as expected, the same as the permittivity assigned to the material.

The same method can be applied to electrically thin materials, *i.e.*, $T < t_\mathrm{p}$, however, the higher orders of the transmitted field in (3.1) are combined in the received signal. In order to mitigate this effect, the signal at the right interface is divided into two regions: 1) the first T part of the signal and 2) the rest of the signal which is affected by the multiple scattering inside the media. The signal peaks in the first region are detected, as shown by ($\circ$) in Fig. 3b, and using the corresponding peaks in the reference signal and the expressions (3.2) and (3.3) we get the same results as in the previous example.

The method presented above is called a direct method (DM) in this paper, since the complex permittivity is estimated directly from the time-domain signals. The method is an efficient and simple way of estimating the complex permittivity for low loss materials. In dispersive materials the resulting permittivity is valid at f_0 where the power spectral density of the signal is maximum, cf. Fig. 2b. However, in materials with negligible dispersion the obtained value is approximately valid over a wide range of frequencies since the difference between the

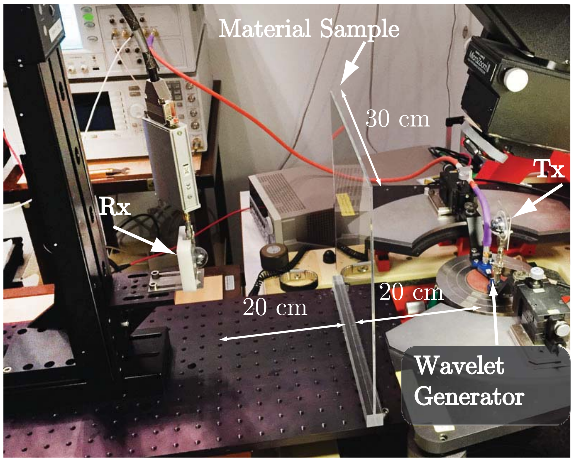

Figure 4: Time-domain material measurement setup consisting of two leaky lens antennas at a distance of 40 cm facing each other. The material sample is placed at the midpoint between the two antennas.

static permittivity, ϵ_s, and permittivity at high frequency limit, ϵ_∞, is very small.

In a system implementation, the real part of the refractive index, n_r, can be found from a cross correlation between the transmitted signals in the presence and the absence of the material. The imaginary part, n_i, is estimated using the ratio between the amplitudes of two signals that can be implemented using an envelope detector. In next section we show how to extract material properties of thin and thick samples.

4 Measurement examples

In this section, the properties of three dielectric samples with different thicknesses are investigated. The samples are placed at the midpoint between two antennas as shown in Fig. 4. The antenna system at the transmitting side (Tx) generates 80 ps long pulses with the center frequency at $f_0 = 50\,\mathrm{GHz}$. The generated pulses are received by an identical leaky lens antenna (Rx) at a distance of 40 cm from the transmitting antenna. The received signal is then recorded in the absence and the presence of the object. In each case, an averaging of 100 pulses, which takes about 8 s, is applied with the oscilloscope to increase the speed of the measurements and prevent possible instabilities in the equipment over time. Electrically thick and thin PMMA samples and an electrically thin PVC sample are characterized. In each case the measurement is repeated 10 times to estimate the uncertainties.

Table 1: Dielectric constant of PMMA

Method	f(GHz)	$\epsilon_{\mathrm{r,r}}$	$\epsilon_{\mathrm{r,i}}$	d(mm)
DM[a]	50	2.532 ± 0.005	0.009 ± 0.002	20
DM[a]	50	2.561 ± 0.030	0.010 ± 0.033	2.9
FPI[b][11]	50	2.557 ± 0.026	0.0083 ± 0.0007	23.5

[a] Direct method

[b] Fabry-Pérot Interferometer

4.1 Poly methyl methacrylate (PMMA)

A dielectric poly methyl methacrylate (PMMA) material with dimensions $30 \times 30 \times 2\,\mathrm{cm}^3$ is placed at the midpoint between the transmitting and the receiving antennas. The signal in the absence of the object is depicted by solid line in Fig. 5 and the dashed line illustrates the received signal when the object is inserted between the two antennas. The first term of the transmitted signal ($m = 0$) is received temporally separated from the higher orders ($m \geqslant 1$). These trailing signals are buried in noise and ringings caused by the circuit as well as the multiple reflections inside the lens and cannot readily be utilized. As shown in Fig. 5, the first $T = 212\,\mathrm{ps}$ part of the signal consists of the first transmission and all the higher order transmissions occur after time T. The direct method in Section 3 can be applied to the first part of the signal and the shadowed part in Fig. 5 is discarded.

Here the third peak of each signal, as shown in Fig. 5, is chosen to make the calculations. The time delay introduced by the object is $t_{\mathrm{d}} = 39.5\,\mathrm{ps}$ and the resulting real part of the refractive index using (3.2) is estimated to $n_{\mathrm{r}} = 1.592$. The amplitude ratio between the signals in the presence and the absence of the object is $\mathit{\Delta} = 0.881$. Using the real part of the refractive index as well as the ratio between the two signals in (3.3) the imaginary part of the refractive index becomes $n_{\mathrm{i}} = 0.003$ and the resulting complex relative permittivity is estimated to $\epsilon_{\mathrm{r}} = 2.534 + \mathrm{i}0.009$. The measurements were repeated 10 times and the uncertainties are reported in Table 1. The averaged real part of permittivity is $\epsilon_{\mathrm{r,r}} = 2.532 \pm 0.005$ and the imaginary part $\epsilon_{\mathrm{r,i}} = 0.009 \pm 0.002$. In [11] the permittivity of a 23.5 mm thick PMMA measured at 50 GHz is $\epsilon_{\mathrm{r}} = 2.557 + \mathrm{i}0.0083$ using Fabry-Pérot Interferometer (FPI) method, where the permittivity is deduced from the quality factor, Q, and changes in the resonant frequency.

An electrically thin PMMA sample with dimensions of $30 \times 30 \times 0.29\,\mathrm{cm}^3$ has also been measured and the complex permittivity using the direct method in Section 3 is extracted. The transmitted signals in the absence and the presence of the object are shown in Fig. 6 with solid and dashed lines, respectively. The time difference between the signals is estimated to 5.875 ps. The dispersion inside the material is negligible, since the shape of the pulse is not affected by the material and is the same as the original signal in the absence of the object. Using the delay

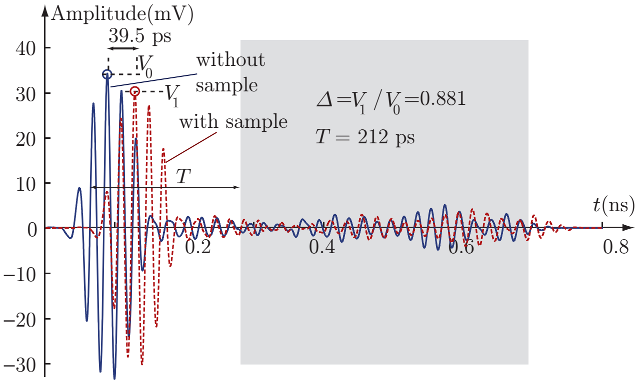

Figure 5: Transmitted signal in the absence (solid) and the presence (dashed) of a PMMA material with thickness 20 mm. The transmitted signal through the material is delayed by 39.5 ps and attenuated by a factor of $\Delta = 0.881$. The shadowed region shows the part of the signal that is affected by the multiple scattering inside the material and is discarded in the direct method.

between the signals, the real part of the refractive index is estimated to $n_\mathrm{r} = 1.597$ and the time delay $T = 2dn_\mathrm{r}/c_0 = 31.43\,\mathrm{ps}$. The first T part of the signal as is shown in Fig. 6 is not affected by the higher orders of the transmission ($m \geqslant 1$) and can be used in order to apply the direct method. The shadowed part of Fig. 6 shows the transmitted signal in the presence of the multiple scatterings inside the material and is discarded. The first part of the signal is used to estimate the coefficient Δ in (3.3) which is the ratio between the amplitude of the two signals when $m = 0$. In this case, the peaks in the negative part of the signal, illustrated with circles, are used and the ratio is estimated to $\Delta = 0.926$ and consequently the imaginary part of the refractive index becomes $n_\mathrm{i} = 0.007$. The complex relative permittivity is then estimated to $\epsilon_\mathrm{r} = (n_\mathrm{r} + \mathrm{i}n_\mathrm{i})^2 = 2.550 + \mathrm{i}0.023$. The real part and imaginary part of the permittivity averaged over 10 measurements, as reported in Table 1 and are $\epsilon_\mathrm{r,r} = 2.561 \pm 0.030$ and $\epsilon_\mathrm{r,i} = 0.010 \pm 0.033$, respectively. As is shown in Table 1, the estimation of the real part of the permittivity for an electrically thin sample is more sensitive and this can be due to the fact that misalignments have higher impacts on electrically thin materials than the electrically thick ones. It should also be noted that the results are more susceptible to jitter for electrically thin samples as the corresponding delay introduced by the sample is relatively small.

4.2 Poly vinyl chloride (PVC)

A dielectric poly vinyl chloride (PVC)-based sample with the dimensions of $30 \times 30 \times 0.3\,\mathrm{cm}^3$ has been characterized using the direct method in Section 3. The material is located between the transmitting and the receiving antennas. The

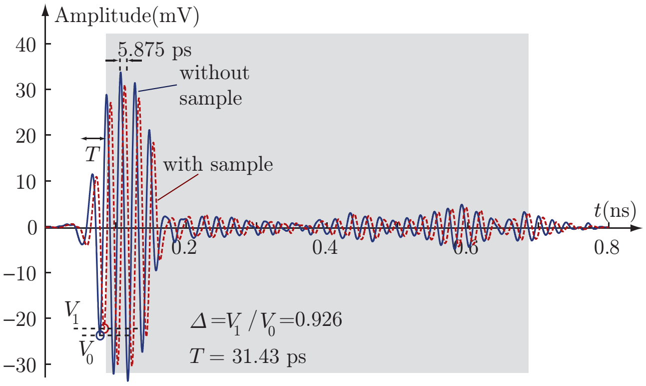

Figure 6: Transmitted signal in the absence (solid) and the presence (dashed) of a PMMA material with thickness 2.9 mm. The transmitted signal through the material is delayed by 5.875 ps and attenuated by a factor of $\mathit{\Delta} = 0.926$. The shadowed region shows the part of the signal that is affected by the multiple scattering inside the material and is discarded in the direct method.

Table 2: Dielectric constant of PVC

Method	f(GHz)	$\epsilon_{\mathrm{r,r}}$	$\epsilon_{\mathrm{r,i}}$	d(mm)
DM[a]	50	2.952 ± 0.043	0.014 ± 0.016	3
FSM[b][16]	76.5	2.74 ± 0.005	0.025 ± 0.001	5.05
FSM[b][15]	85	2.878	0.316	

[a] Direct method

[b] Free-sapce method

received signals in the absence and the presence of the object are shown in Fig. 7 with solid- and dashed-lines, respectively. The time difference between the signals is estimated to 7.12 ps which results in $n_{\mathrm{r}} = 1.712$ and $T = 2dn_{\mathrm{r}}/c_0 = 34.2$ ps. Using the first T part of the signal and discarding the shadow part that includes the multiple terms, the ratio is estimated to $\mathit{\Delta} = 0.906$ and consequently the imaginary part of the refractive index becomes $n_{\mathrm{i}} = 0.008$. The complex relative permittivity is then estimated to $\epsilon_{\mathrm{r}} = (n_{\mathrm{r}} + \mathrm{i}n_{\mathrm{i}})^2 = 2.931 + \mathrm{i}0.029$. The resulting permittivity averaged over 10 measurements is $\epsilon_{\mathrm{r,r}} = 2.952 \pm 0.043$ and $\epsilon_{\mathrm{r,i}} = 0.014 \pm 0.016$. As stated in Table 2 the previously reported relative permittivities of PVC are $\epsilon_{\mathrm{r}} = 2.74 + \mathrm{i}0.025$ in [16] at 76.5 GHz, and $\epsilon_{\mathrm{r}} = 2.88 + \mathrm{i}0.031$ in [15] at 85 GHz. In both cases the free space method in W-band is utilized to characterize polymer materials. To the best of our knowledge, PVC has not been characterized at 50 GHz before. The relatively small difference between the two reference values given and the similar value found here indicate a weak frequency dependence.

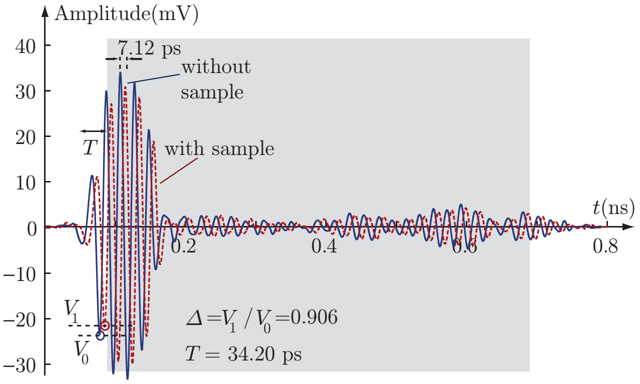

Figure 7: Transmitted signal in the absence (solid) and the presence (dashed) of a PVC material with thickness 3 mm. The transmitted signal through the material is delayed by 7.12 ps and attenuated by a factor of $\mathit{\Delta} = 0.906$. The shadowed region shows the part of the signal that is affected by the multiple scattering inside the material.

5 Broadband material characterization

In this part, a frequency-domain representation of the time-domain system is investigated. The direct method in Section 3 is a simple method to identify the dielectric properties at mm-wave frequencies for non-dispersive materials. However, for dispersive materials we need to determine the properties over a wide frequency band. Since the signal is a short pulse in the time-domain, the resulting frequency-domain spectrum is wideband. This is similar to time-domain spectroscopy [9], where the Fourier transform of the time-domain signal is used to determine the frequency dependence of the material. The transmission coefficient, $\mathcal{T}(\omega)$, as a function of frequency is represented as

$$\mathcal{T}(\omega) = \frac{4n(\omega)}{(n(\omega)+1)^2} \mathrm{e}^{\mathrm{i}(n(\omega)-1)k_0 d} \mathrm{FP}(\omega), \tag{5.1}$$

where $\omega = 2\pi f$, and $\mathrm{FP}(\omega)$ (Fabry-Pérot effect) represents multiple reflections inside the material. It is given by

$$\mathrm{FP}(\omega) = \left(1 - \Big(\frac{n(\omega)-1}{n(\omega)+1}\Big)^2 \mathrm{e}^{2\mathrm{i}n(\omega)k_0 d}\right)^{-1}, \tag{5.2}$$

and can be neglected ($\mathrm{FP} = 1$) for a thick material by applying time gating to the signal. The measured transmission coefficient of the material represents the ratio between the Fourier transforms of the received signals in the presence, V_{sample}, and the absence, V_{ref}, of the object and is given by

$$\mathcal{T}_{\text{meas}}(\omega) = \frac{V_{\text{sample}}(\omega)}{V_{\text{ref}}(\omega)}. \tag{5.3}$$

By minimizing the difference between the measured and analytic values of the transmission coefficient, *i.e.*, $\mathcal{T} - \mathcal{T}_{\text{meas}}$, using a brute-force search (fitting) over a range of the refractive indexes, the minimum is found for a certain value, n. It should be noted that the range is chosen in a neighborhood of the refractive index found from the direct method and is narrowed down to achieve more accurate results. Since the obtained values from this method are non-unique and the measured values at the frequencies where the spectrum of the pulse has low amplitude are inaccurate, the method needs to be improved.

Using the passivity of the material, the function $h = \omega\epsilon$ is identified as a symmetric Herglotz function [7], where h is holomorphic, *i.e.*, infinitely differentiable complex valued function, and $\operatorname{Im} h(\omega) \geqslant 0$ for $\operatorname{Im} \omega \geqslant 0$. The Herglotz function, h, can be represented as [7]

$$\operatorname{Re} h(\omega) = \epsilon_\infty \omega + \frac{1}{\pi} \int\limits_{-\infty}^{\infty} \frac{1}{\zeta - \omega} \operatorname{Im} h(\zeta) \mathrm{d}\zeta, \tag{5.4}$$

where $\epsilon_\infty > 0$ and denotes the permittivity at the high frequency limit. The relation (5.4) is similar to the Hilbert transform and the Kramers-Kronig relations. Convex optimization [8] can be used by representing the data by triangular pulses and based on (5.4) to identify the most similar Hergoltz function to the measured values. The details of the optimization steps are explained in [30]. The optimization problem is expressed as

$$\begin{aligned}
\text{minimize} \quad & \left\| h(\omega) - h^{(\mathrm{M})}(\omega) \right\| \\
\text{subject to} \quad & \operatorname{Im} h(\omega) \geqslant 0 \\
& \epsilon_\infty \geqslant 0 \\
& \operatorname{Re} h(\omega) = \epsilon_\infty \omega + \frac{1}{\pi} \int_{\omega_0}^{\omega_3} \frac{1}{\zeta - \omega} \operatorname{Im} h(\zeta) \mathrm{d}\zeta \\
& \left\| \frac{1}{\omega} \frac{\partial h}{\partial \omega} \right\|_\infty < \frac{0.01}{\Delta\omega}
\end{aligned} \tag{5.5}$$

where $||.||$ is the L^2-norm, $h(\omega)$ is the modeled Herglotz function, and $h^{(\mathrm{M})}(\omega)$ denotes the measured values for $\omega \in [\omega_1, \omega_2]$ that is included inside the modeling interval $\omega_0 < \omega_1 < \omega_2 < \omega_3$. Note that the dimension of $h = \omega\epsilon$ is rad/s.

The relative permittivity of the PMMA sample in Section 4.1 is found from the aforementioned frequency-domain method. The time-domain signals acquired over 10 measurements in the presence and absence of the sample are time gated with a 300 ps long Hanning window. The resulting relative permittivity using the brute-force search with FP = 1 in (5.1) and averaged over 10 measurements is shown in Fig. 8 with dashed lines. Considering the values on the y-axis, the results from this method are sufficiently accurate for some applications. The small jump at $f \approx 36\,\text{GHz}$ on the real and imaginary parts of the relative permittivity is due

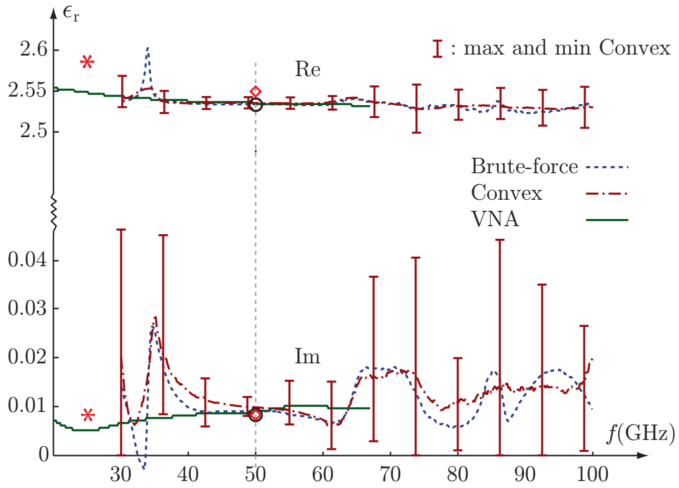

Figure 8: Complex permittivity of a 20 mm PMMA sample estimated from time-domain measurement using the direct method (∘) in (3.2) and (3.3) , using the brute-force search in (5.1)-(5.3) (dashed lines), convex optimization solution in (5.5) (dashed-dotted lines) and from the frequency-domain measurements using network analyzer (solid lines). The previously reported works are denoted by (◇) for the values found from [11] and (∗) for [33]. Bars indicate the maximum and minimum values over the 10 measurements using convex optimization solution.

to the weakness of the input power spectral density, as shown in Fig. 2b, at this frequency.

In order to improve the estimation, the convex optimization in (5.5) using the passivity, *i.e.*, $\operatorname{Im} h(\omega) \geqslant 0$, Kramers-Kronig relation, and smoothness constraints is applied to each measurement. The optimization problem is solved using Matlab Software for Disciplined Convex Programming (CVX) [17], and the solution averaged over 10 measurements is shown by dashed-dotted curves in Fig. 8. The bars indicate the maximum and minimum values of the real and imaginary parts of the permittivity obtained by convex optimization solution. The relative uncertainty over the imaginary part is higher, especially over the bands where the power spectral density of the signal is low, but this can be improved by amplifying the signal. The convex optimization solution has the advantage of removing the spurious resonances mainly due to the nulls in the power spectral density of the signal. In addition, the results from a time-domain pulse with the bandwidth of 25 GHz is represented over an extremely wide range of frequencies, *i.e.*, 30–100 GHz. It should be noted that the modeling interval is from $\omega_0 = 29\,\text{GHz}$ to $\omega_3 = 105\,\text{GHz}$.

The material has also been characterized in the frequency-domain using an Agilent E8361A PNA and leaky lens antennas over the frequency band 20–67 GHz. Due to the wide bandwidth of the antenna the material is characterized over a wide range of frequencies and the result is shown in Fig. 8 with solid lines. The free-space transmission method and brute-force search were used to estimate the complex permittivity. As illustrated in Fig. 8, the values are in good agreement especially over the band where the power spectral density is high, *i.e.*, 40–60 GHz.

The permittivity value found from the direct method using the delay and the attenuation of the time-domain signal at 50 GHz is shown by circles on the real and imaginary part curves. The achieved result using a relatively simple approach is on top of the frequency-domain results and as seen in Fig. 8, for a non-dispersive material, the values at 50 GHz are approximately valid for other frequencies.

6 Conclusions

A simple time-domain approach to extract the complex permittivity of non-magnetic materials is investigated. A novel time-domain system consisting of an in-house wavelet generator and a non-dispersive and wideband leaky lens antenna is used. The methodology is demonstrated using examples of electrically thick and thin materials. Measuring thin materials is difficult with narrowband systems in the frequency-domain and requires post processing and optimization methods, however, using the direct method in the time-domain it can be simplified substantially. The wide bandwidth of the pulse can also be used to investigate the dispersive behaviors of the materials. The results show good agreement with previously reported measurement results from similar materials.

References

[1] M. N. Afsar, J. R. Birch, R. N. Clarke, and G. W. Chantry. The measurement of the properties of material. *Proc. IEEE*, **74**(1), 183–199, January 1986.

[2] M. N. Afsar and K. J. Button. Millimeter-wave dielectric measurement of materials. *Proc. IEEE*, **73**(1), January 1985.

[3] I. Al-Qadi, O. Hazim, W. Su, and S. Riad. Dielectric properties of portland cement concrete at low radio frequencies. *Journal of materials in Civil Engineering*, **7**(3), 192–198, August 1995.

[4] M. Arai, J. G. P. Binner, and T. E. Cross. Correction of errors due to airgaps for microwave complex permittivity measurement using a coaxial line. *Electronics Letters*, **31**(2), 114–115, 1995.

[5] J. Baker-Jarvis, R. G. Geyer, J. John H. Grosvenor, M. D. Janezic, C. A. Jones, B. Riddle, and C. M. Weil. Dielectric characterization of low-loss materials: A comparison of techniques. *IEEE Transactions on Dielectrics and Electrical Insulation*, **5**(4), 571–577, August 1998.

[6] J. Baker-Jarvis, E. J. Vanzura, and W. A. Kissick. Improved technique for determining complex permittivity with the transmission/reflection method. *IEEE Trans. Microwave Theory Tech.*, **38**(8), 1096–1103, August 1990.

[7] A. Bernland, A. Luger, and M. Gustafsson. Sum rules and constraints on passive systems. *J. Phys. A: Math. Theor.*, **44**(14), 145205, 2011.

[8] S. P. Boyd and L. Vandenberghe. *Convex Optimization.* Cambridge Univ Pr, 2004.

[9] J. D. Buron, F. Pizzocchero, B. S. Jessen, T. J. Booth, P. F. Nielsen, O. Hansen, M. Hilke, E. Whiteway, P. U. Jepsen, P. Boggild, and D. H. Petersen. Electrically continuous graphene from single crystal copper verified by terahertz conductance spectroscopy and micro four-point probe. *ACS Nano lett.*, **14**(11), 6348–6355, October 2014.

[10] R. H. Cole. Time domain reflectometry. *Annual review of physical chemistry*, **28**, 283–300, 1977.

[11] W. Culshaw and M. Anderson. Measurement of permittivity and dielectric loss with a millimetre-wave Fabry-Perôt interferometer. *IEE Proc.-G Electronic Circuits and Systems*, **109**(23), 820–826, 1962.

[12] R. C. Daniels and R. W. Heath. 60 GHz wireless communications: emerging requirements and design recommendations. *IEEE Veh. Technol. Mag.*, **2**(3), 41–50, September 2007.

[13] M. D. Deshpande, C. J. Reddy, P. I. Tiemsin, and R. Cravey. A new approach to estimate complex permittivity of dielectric materials at microwave frequencies using waveguide measurements. *IEEE Trans. Microwave Theory Tech.*, **45**(3), 359–366, March 1997.

[14] M. Egard, M. Ärlelid, L. Ohlsson, B. M. Borg, E. Lind, and L.-E. Wernersson. $In_{0.53}Ga_{0.47}As$ RTD-MOSFET millimeter-wave wavelet generator. *Electron Device Letters, IEEE*, **33**(7), 970–972, 2012.

[15] A. Elhawil, L. Zhang, J. Stiens, C. De Tandt, N. Gotzen, G. Assche, and R. Vounckx. A quasi-optical free-space method for dielectric constant characterization of polymer materials in mm-wave band. In *Proc. Symp. IEEE/LEOS Benelux Chapter Brussels*, pages 187–190, dec 2007.

[16] G. L. Friedsam and E. Biebl. Precision free-space measurements of complex permittivity of polymers in the W-band. In *IEEE MTT-S Int. Microwave Symp. Digest*, volume 3, pages 1351–1354, June 1997.

[17] M. Grant and S. Boyd. Graph implementations for nonsmooth convex programs. In V. Blondel, S. Boyd, and H. Kimura, editors, *Recent Advances in Learning and Control*, Lecture Notes in Control and Information Sciences, pages 95–110. Springer-Verlag Limited, 2008.

[18] F. Gumbmann and L. Schmidt. Millimeter-wave imaging with optimized sparse periodic array for short-range applications. *IEEE Trans. Geosci. Remote Sens.*, **49**(10), 3629–3638, September 2011.

[19] E. Hecht. *Optics*. Addison-Wesley, Reading, MA, USA, second edition, 1987.

[20] P. U. Jepsen, D. G. Cooke, and M. Koch. Terahertz spectroscopy and imaging–modern techniques and applications. *Laser & Photonics Reviews*, **5**(1), 124–166, October 2011.

[21] R. G. Jones. Precise dielectric measurements at 35 GHz using an open microwave resonator. *IEE Proceedings*, **123**(4), 285–290, April 1976.

[22] A. Neto. UWB, non dispersive radiation from the planarly fed leaky lens antenna-part I: Theory and design. *IEEE Trans. Antennas Propagat.*, **58**(7), 2238–2247, 2010.

[23] A. Neto, S. Monni, and F. Nennie. UWB, non dispersive radiation from the planarly fed leaky lens antenna-part II: Demonstrators and measurements. *IEEE Trans. Antennas Propagat.*, **58**(7), 2248–2258, 2010.

[24] A. M. Nicolson. Broad-band microwave transmission characteristics from a single measurement of the transient response. *IEEE Trans. Instrumentation and Measurement*, **17**(4), 395–402, December 1968.

[25] A. M. Nicolson and G. F. Ross. Measurement of the intrinsic properties of materials by time-domain techniques. *IEEE Trans. Instrumentation and Measurement*, **19**, 377–382, 1970.

[26] L. Ohlsson and L.-E. Wernersson. A 15-Gb/s wireless on-off keying link. *IEEE Access*, **2**(1), 1307–1313, October 2014.

[27] S. J. Orfanidis. *Electromagnetic waves and antennas.* Rutgers University New Brunswick, NJ, 2002.

[28] B. T. Perry, E. J. Rothwell, and L. C. Kempel. A comparison of the measured pulse response of layered materials using time-and frequency-domain systems. *IEEE Antennas Propag. Mag.*, **49**(5), 117–123, October 2007.

[29] O. V. Tereshchenko, F. J. K. Buesink, and F. B. J. Leferink. An overview of the techniques for measuring the dielectric properties of materials. In *XXXth URSI Symp. General Assembly and Scientific (URSI GASS 2011)*, pages 1–4, August 2011.

[30] I. Vakili, M. Gustafsson, D. Sjoberg, R. Seviour, M. Nilsson, and S. Nordebo. Sum rules for parallel-plate waveguides: Experimental results and theory. *IEEE Trans. Microw. Theory Techn.*, **62**(11), 2574–2582, 2014.

[31] I. Vakili, L. Ohlsson, M. Gustafsson, and L.-E. Wernersson. Wideband and non-dispersive wavelet transmission using leaky lens antenna. *Electronic Letters*, **49**(5), 321–322, 2013.

[32] V. V. Varadan, R. D. Hollinger, D. K. Ghodgaonkar, and V. K. Varadan. Free-space, broadband measurements of high-temperature, complex dielectric properties at microwave frequencies. *IEEE Trans. Instrumentation and Measurement*, **40**(5), 842–846, 1991.

[33] A. von Hippel. *Dielectric Materials and Applications.* Artech House, Boston, London, 1954.

Time-Domain Wavelet Characterisation With Gating Techniques Applied to Millimetre-Wave Antennas

Paper III

Lars Ohlsson, Iman Vakili, Daniel Sjöberg, Lars-Erik Wernersson

---

Submitted: L. Ohlsson, I. Vakili, D. Sjöberg, , L.-E. Wernersson, Time-Domain Wavelet Characterisation With Gating Techniques Applied to Millimetre-Wave Antennas.

Abstract

A time-domain characterisation method that utilises wideband signals from a monolithic wavelet generator is presented and applied to millimetre-wave antennas. It also utilises gating techniques in time- and frequency-domain to relax the calibration effort for device characterisation, in this case only a thru reference is used. This method is applied to V-band horn, leaky-lens, and dielectric resonator antenna links, demonstrating various gain, dispersion, and bandwidth combinations. The results are compared to those from conventional vector network analysis. Deliberate gating allows for selective removal of known device artefacts from either time- or frequency-domain measurements, such as channel reflections. This time-domain characterisation technique can also be applied towards terahertz frequencies by generator tuning.

1 Introduction

Time-domain metrics describe performance of for systems that utilise ultra-short symbols, e.g. high-resolution radar [1] and multi-Gb/s wireless communication [2]. Devices in such millimetre-wave (mmW) systems must transfer various wavelets with high fidelity [3], intrinsically or collectively by use of signal predistortion [4]. It is thereby important that characterisation methods can provide a direct measure of time-domain performance metrics.

Frequency-domain vector network analysers (VNAs) are typically used for mmW characterisation. For some devices under test (DUTs), however, the desired reference ports may be embedded in a test assembly or waveguide fixture. This requires custom calibration standards, e.g. realising a TRL correction [5], what not always is practical. Further, some DUTs must also be analysed in an intermediate medium, e.g. antennas interfacing a radio channel. This channel must be idealised in an anechoic chamber for stand-alone antenna analysis.

Time-domain gating techniques can be utilised to virtually idealise a measurement [6, 7], instead of custom calibration and physical idealisation of any intermediate medium. This demands for short symbols to minimise temporal overlap between desired and parasitic signal components. One alternative is to transform VNA measurements, forming a band-limited impulse excitation [8]. Time-domain characterisation is also possible, e.g. using step excitations [9, 10]. Further, periodic waveforms can be transformed and processed in frequency-domain calibration algorithms [11–13]. Optical pulse-shaping can produce short microwave wavelets, with the benefit of centring the power density at the desired spectral region [14]. Femtosecond optical pulses also allow photo-conductive excitation/sampling, as used in free-space terahertz applications [15, 16], but the corresponding measurement setup is typically bulky.

As a complement to the above implementations, coherent electronic wavelet generators can be of interest, e.g. for future instrument implementations. Recent advances in monolithic technology provide ultra-short mmW wavelets at about

+10 dBm peak power [17–19]. As compared to optically pulsed terahertz sources, electronic generators are energy efficient, portable, and can operate without use of any mechanical delay stages. As an extension of initial waveform distortion studies published previously [20], a full analysis of time-domain wavelet transients is targeted to quantify device characteristics.

In this paper, a novel analysis method based on coherent time-domain wavelets and gating techniques is described. Wideband 60 GHz signals from a coherent mmW III–V wavelet generator are fed through different DUTs and captured in a sampling oscilloscope. With only one reference measurement, the DUT transfer-function is approximated. Conventional VNA measurements are performed for comparison, and the gating techniques are also shown useful for noise and artefact rejection in frequency-domain results. Various mmW antennas are characterised to verify the method, providing realistic noise and scattering limited scenarios. The antennas under test are off-the-shelf pyramidal V-band horn, wideband leaky-lens [20], and physically small dielectric resonator antenna (DRA) [21].

This paper is organised as follows. In Section 2, the wideband time-domain method is defined. Measurement procedures are described in Section 3. In Section 4, the signal processing is summarised, while results are discussed in Section 5. Conclusions are presented in Section 6.

2 Method

We use an ultra-short mmW wavelet to excite the input of a DUT and define a method for quantification of its transfer characteristics. The output departing DUT signal, u_2^-, and the corresponding input impinging excitation, u_1^+, can be sampled with an oscilloscope, the latter via a thru reference. The impulse-response, h, of the DUT can ideally be found by de-convolving the input from the output signal. This, however, requires noise-free measurements and a perfect (zero-delay unit-transfer) thru reference. The corresponding transfer-function, $H = S_{2,1}$, is the quotient of output departing and input impinging signal spectra, U_2^- and U_1^+, respectively, where $S_{2,1}$ denotes the scattering parameter from input port 1 to output port 2.

2.1 Overview and Motivation

An approximately rectangular wavelet measured in a repeated $T = 20$ ns period is depicted in Fig. 1. This signal was captured in a thru reference measurement and has a 60 GHz carrier frequency and approximately $t_\mathrm{p} = 80$ ps pulse-length. Signal components from setup non-idealities, however, are seen trailing the wavelet signal generated by an in-house fabricated quenchable oscillator circuit. The artefacts consist of various round-trip propagation components from the output probe and bias-T utilised. The result is a fine structure on the wideband power spectral density (PSD) of the wavelet. Similar non-ideal features can be produced

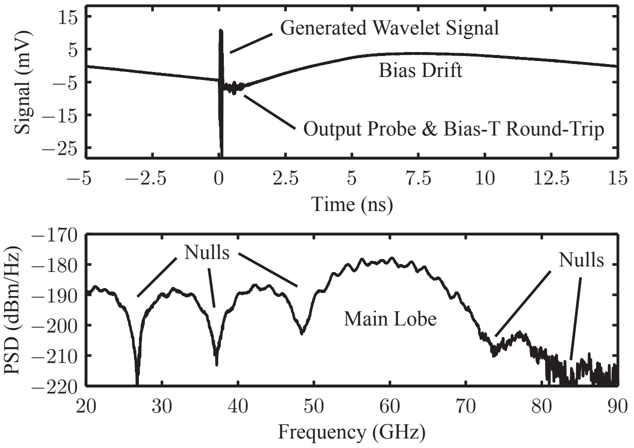

Figure 1: Signal and PSD from an in-house wavelet generator circuit measured in time-domain via a thru reference; a zoomed version is found in Fig. 4.

by high-order interaction between the DUT and the measurements setup. This will produce uncertainty in the characterisation procedure unless the corresponding response features are rejected. Further, this rectangular-envelope signal has a $2/t_\mathrm{p} = 25$ GHz main lobe bandwidth and $1/t_\mathrm{p}$-periodic nulls, about which the PSD is dominated by noise, cf. Fig. 1. Significant artefacts will be generated at any noise-dominated spectral region if a direct de-convolution is attempted [22].

Utilising an input spectrum with nulls and only a thru reference, estimation of the DUT characteristics will require both frequency- and time-domain gating. The one to suppress regions with poor signal-to-noise ratio (SNR) in the spectral domain, and the other to remove setup related signal artefacts and excess temporal noise. It must be stressed that any gating procedures require awareness of the signal properties and setup geometry, but can in ideal cases be complementary to full standard calibration procedures. This is especially useful for antenna measurements because temporal gating can be used to cancel most artefacts caused by interaction with a non-ideal radio channel. It also provides a means to cancel inter-antenna round-trip reflections, thereby offering a simple method to convert non-ideal antenna measurements to virtual free-space conditions. Symmetric antenna-link pairs realised using the antennas in Fig. 2(a) were utilised as DUTs in this study, as schematically illustrated in Fig. 2(b).

2.2 Wideband Time-Domain Method

A novel wideband time-domain analysis method that is compatible with mmW devices is outlined below. It utilises deliberate gating techniques and domain transitions to reduce noise and isolate the characteristics of the device under test

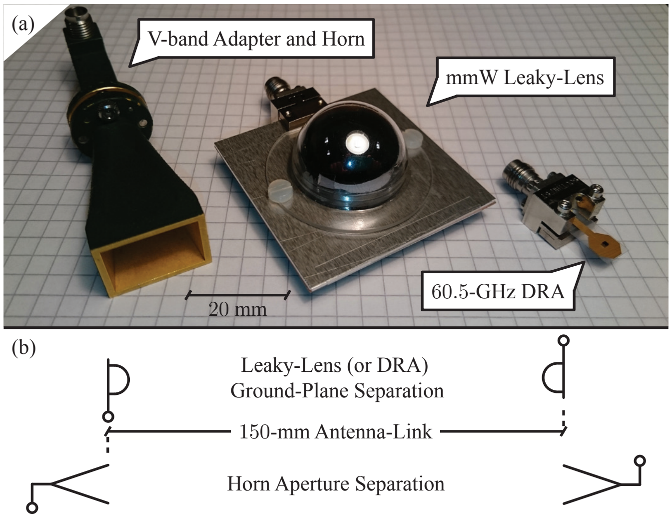

Figure 2: (a) Photograph of the tested antennas. (b) Schematic of geometrically inverted antenna-link two-port DUTs, where the horns are measured in boresight while the leaky-lenses and DRAs are measured in broadside.

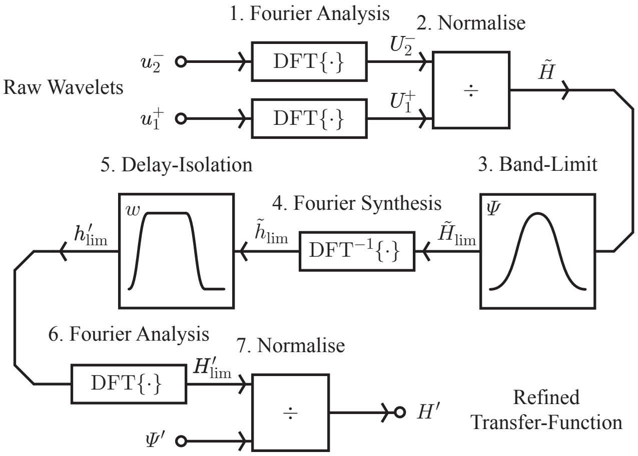

Figure 3: Flow-chart illustrating the signal processing algorithm used to isolate the band-limited noise-rejected transfer-functions of the measured DUTs.

(DUT) in the target bandwidth. This signal processing algorithm is also illustrated schematically in Fig. 3. Discrete Fourier analysis and synthesis, $\mathrm{DFT}\left\{\cdot\right\}$ and $\mathrm{DFT}^{-1}\left\{\cdot\right\}$, respectively, is used to perform the domain transformations. To verify the method, the wavelet in Fig. 1 was used as input excitation and the corresponding output signal from the DUTs were captured, u_1^+ and u_2^-, respectively. Strictly, these captured signals are noise-added linear transformations of the targeted reference port signals. To isolate the DUT transfer-function from these two measurements, the following signal processing algorithm is proposed:

1. Analyse the frequency-domain phasors of the sampled input and output transient signals, $U_1^+ = \mathrm{DFT}\left\{u_1^+\right\}$ and $U_2^- = \mathrm{DFT}\left\{u_2^-\right\}$, respectively.

2. By normalising the output over the input, calculate the raw transfer-function, $\tilde{H} = U_2^- / U_1^+$.

3. Impose a band-limiting gate, $\mathit{\Psi}$, on the raw transfer-function, $\tilde{H}_{\mathrm{lim}} = \mathit{\Psi}\tilde{H}$, excluding poor SNR.

4. Synthesise the corresponding band-limited time-domain response, $\tilde{h}_{\mathrm{lim}} = \mathrm{DFT}^{-1}\left\{\tilde{H}_{\mathrm{lim}}\right\}$.

5. Multiply the band-limited response with a gate, w, isolating signal components which are caused by the direct excitation, $h'_{\mathrm{lim}} = w\tilde{h}_{\mathrm{lim}}$.

6. Analyse the corresponding isolated band-limited transfer-function, $H'_{\mathrm{lim}} = \mathrm{DFT}\left\{h'_{\mathrm{lim}}\right\}$.

7. Revert the weight of the band-limiting gate to produce the refined transfer-function, $H' = H'_{\mathrm{lim}}/\mathit{\Psi}'$, where $\mathit{\Psi}' = \mathrm{DFT}\left\{w\,\mathrm{DFT}^{-1}\left\{\mathit{\Psi}\right\}\right\}$ is a copy of the band-limiting gate that has undergone the time-domain gating.

As the above method includes gating in both time- and frequency-domain, the choices of gate windows are critical. Improper gate selections will distort the data and complicate its interpretation in the transformed domain. For gating in the frequency-domain, let $\mathit{\Psi}$ denote a minimum 3-term Blackman-Harris window, which has a processing gain of 0.42 [23]. This generates negligible temporal envelope ringing, but the trade-off in relation to a sharper window is that it widens the time-domain response. This ideally allows the band-limited impulse-response to show only one feature per transfer event. For gating in time-domain, let w_α denote an α-Tukey window, where α is its cosine roll-off factor [23]. This window can be adjusted from a rectangular, $w_{\alpha=0}$, to a Hann window, $w_{\alpha=1}$, by scaling of this relative taper parameter. In between, its flat-top shape with tapered edges makes the Tukey window suitable for isolation of relatively temporally confined signals in a noisy or interfering environment.

Table 1: Direct Metrics of the Antenna Two-Ports

Quantity	Symbol	Horn[a]	Lens[a]	DRA[a]	Thru[b]
Fidelity	F (%)	87	96	46	100
Pulse-Length	t_p (ps)	73	97	164	93
Rise-Time	t_r (ps)	52	46	119	48
Fall-Time	t_f (ps)	44	19	159	17

Time-domain metrics of the measured signals in Fig. 4. To alleviate this parameter extraction, a 80 GHz wide 12.5%-Tukey gate was applied in the frequency-domain, removing bias variations and excess sampling-noise.

[a] Antenna two-port link measurement, including probe, bias-T, and 48-in coaxial cable at transmitter and another 48-in coaxial cable at receiver.

[b] Reference measurement, replacing the antenna link with a 1.85-mm coaxial adapter.

2.3 Direct Time-Domain Metrics

Time-domain wavelet measurements provide raw waveforms, as shown in Fig. 4, with distortion effects from the DUTs inflicted on the excitation signal. Directly analysing such transient signals, neglecting the method outlined above, this also allows for identification of basic waveform metrics. The fidelity factor, F, is a figure-of-merit for time-domain comparison of two signals, defined as the maximum value of the normalised cross-correlation between the signals [24]. Further, the analytic envelope of a signal can be evaluated via its Hilbert transform [8]. This alleviates the evaluation of envelope properties such as rise- and fall-time between 10% and 90% of the envelope peak, t_r and t_f, respectively, and full width at half maximum pulse-length, t_p. These metrics are illustrated on one of the DUT signals in Fig. 4, and quantified in Table 1. As the input signal is not an ideal impulse, these direct metrics are the combined effect of input shape and DUT characteristics.

3 Measurement Techniques

The proposed wideband time-domain method was verified for symmetric transmit-to-receive antenna-link two-ports, cf. Fig. 2. This is defined here as antenna pairs operating over a far-field free-space line-of-sight channel. Such a two-port network is reciprocal. The symmetry criterion enforces identical antennas with equivalent directions of departure and arrival, and implicitly that the antennas face each other in inverted geometrical configuration.

The mmW antennas of the antenna-link two-port DUTs investigated in this

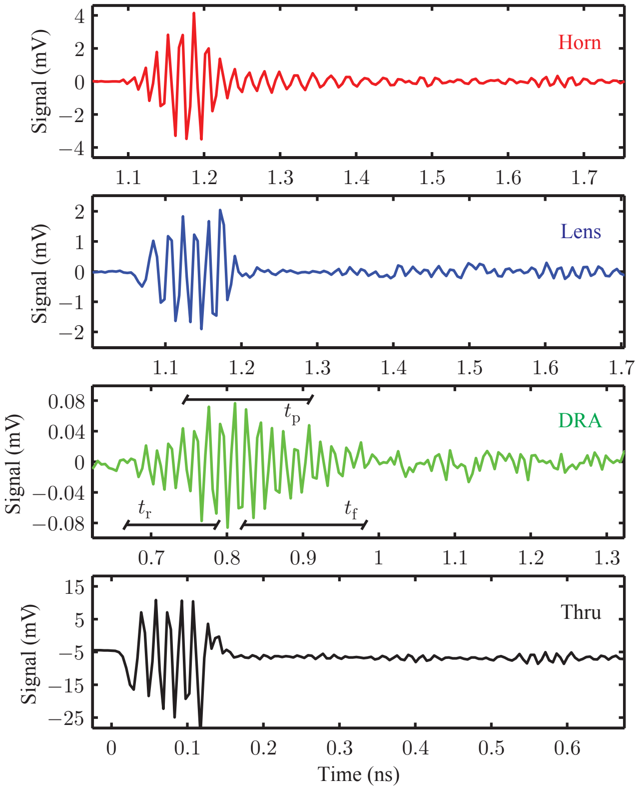

Figure 4: Measured wavelets after their passage through different antenna two-port links, and the thru reference. This thru measurement was captured by rewiring via a coaxial andapter to bypass the antennas. An overlay indicating the envelope rise-, pulse-, and fall-times, t_{r}, t_{r}, and t_{f}, respectively, is shown on one of the signals.

paper were of fundamentally different types and are shown in Fig. 2(a). On the one hand, off-the-shelf 19.5-dBi gain Flann 25240 pyramidal horn antennas with WR-15 waveguide interfaces were used. This included the corresponding Flann 25093 adapters to 1.85-mm coaxial interface, with 1 dB nominal insertion loss. On the other hand, in-house lens-augmented leaky-wave slot antennas [20], and 60.5-GHz slot-coupled dielectric resonator antennas [21] were also characterised. Both in-house antennas utilised a 1.85-mm Southwest end-launch connector. The investigated antennas thereby span various form factors and sizes but also have different radiation mechanisms. The experimental study in this paper was, except from the symmetry criterion defined previously, limited to broadside or boresight conditions, depending on the antenna geometry, as illustrated in Fig. 2(b), at a fixed 150 mm channel-distance.

3.1 Frequency-Domain Setup

Frequency-domain measurements were performed as a baseline for the proposed time-domain method. An Agilent E8361A VNA was used to capture the scattering matrix, i.e. transfer-functions and reflection coefficients, of symmetric antenna-link two-ports, cf. Fig. 2. The reference ports were defined at the tips of two 48-in MegaPhase coaxial cables by a 1.85-mm N4694A electronic calibration kit, utilising parts of the setup shown in Fig. 5(a-b). The DUT transfer-functions were measured in a 10-GHz span centred on 60 GHz, with a 50 MHz sampling-step, for a source power of -6 dBm and receiver bandwidth of 1 Hz. The measured raw transfer-functions are shown in Fig. 6. The raw phase-information in the VNA measurement is seen to be severely distorted, not allowing any detailed study of the DUT group-delay, τ_{g}. This is attributed to various minor reflections in and about the antenna DUTs, producing a multitude of interference effects. The reflections that are related to channel scattering must be cancelled for a study of the free-space antenna characteristics. The latter steps, **3**–**7**, of the analysis method outlined in Section 2.2 are utilised for this purpose.

3.2 Time-Domain Setup

Time-domain measurements were performed as follows, schematically illustrated in Fig. 5(a). An Agilent N4906B was used to generate 80 ps long baseband pulses with a repetition period of $T = 20$ ns. A coaxial cable was used to feed this periodic pulse-train to a Cascade i67 probe. The input of an on-chip probed mmW wavelet generator was thereby repeatedly pulsed from -0.45 to $+0.45$ V at 0.4% duty-cycle. This resulted in the generation of approximately $t_{\mathrm{p}} = 80$ ps square-envelope wavelets with a carrier-frequency of 60 GHz at a repetition rate of $1/T = 50$ Mpulses/s. The full signal period and its PSD is shown in Fig. 1, and a zoomed version of the transient is found in Fig. 4.

The coherent monolithic mmW wavelet generator was implemented in III–V technology and has been reported in detail elsewhere [19]. In summary, it consists

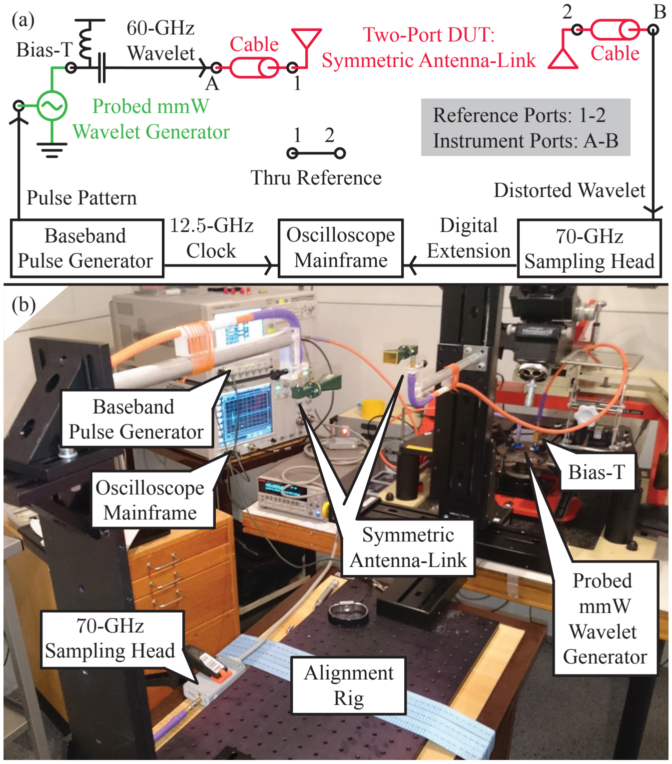

Figure 5: (a) Schematic illustration of the symmetric two-port antenna-link, or thru reference, connected to the reference ports of cables that interface the utilised time-domain setup. The instrument ports are connected to the bias-T on the probed mmW wavelet generator and the sampling head of an oscilloscope, respectively. In frequency-domain measurements, the cable instrument ports are rewired to a VNA and the reference ports are calibrated. (b) Photograph of the time-domain measurements setup, utilising a probed mmW wavelet generator that produces 80-ps 60-GHz wavelets.

of a minimalistic resonant tunnelling diode oscillator circuit operated in pulsed mode, on average consuming 3.2 mA at 1.35 V. It is controlled via a transistor switch directly connected to the baseband input signal. As this switch is integrated in series with the diode and the circuit has an on-chip bias reservoir, rapid and reproducible start-up and quench of the oscillator is possible, generating coherent wavelets. Similar diode oscillators have demonstrated continuous-wave oscillations at frequencies in excess of 1.3 THz [25]. Conceptually, the wavelet generator technology should be scalable and heterodyne detection can provide the required intermediate step for electronic time-domain terahertz sampling.

The output of the circuit was probed with another i67 probe, with 1 dB nominal insertion loss. This probe fed the additive port of a Anritsu V255 bias-T, with 1.5 dB nominal insertion loss. A 48-in MegaPhase coaxial cable with 1.85-mm interfaces and 9 dB nominal insertion loss was used to feed the wavelet from the coupled port of the bias-T, as shown in Fig. 5(a-b), its far end realised the transmit reference port. A transmit antenna and an equivalent receiving antenna were positioned at 150 mm channel-distance from each-other, as illustrated in Fig. 2(b), and connected to the respective reference ports. Another 48-in cable formed the receive reference port and fed the distorted and attenuated signal to an 86118A sampling head of an Agilent 86100D oscilloscope. To suppress noise and visualise the coherent wavelet signal, 8, 192 traces with an approximate 4.88-ps sampling-step were averaged for the horn and lens antennas. The low directivity of the DRA, as compared to the other antennas, required 32, 768 averages to moderately resolve its signal.

The signals transmitted through the antenna two-ports and the corresponding thru reference are shown in Fig. 4. The thru reference signal was captured from the wavelet generator by connecting the reference ports via a standard 1.85-mm adapter, realising a thru with a flat 53.5 ps group-delay.

4 Signal Processing

The captured time-domain transients and frequency-domain scattering parameters were processed as follows, applying the method proposed in Section 2.2.

4.1 Direct Wavelet Distortion

The direct wavelet distortion was quantified from the time-domain signals of the DUTs, shown in Fig. 4. To cancel excess sampling-noise and periodic bias drift [26], the latter seen in Fig. 1, the wavelets were transferred to the frequency-domain and gated with a 80-GHz 12.5%-Tukey window centred about 60 GHz. The signals were then returned to the time-domain and their fidelity factors with respect to the thru reference were evaluated. Also, the signal pulse-lengths, rise-, and fall-times were then characterised directly from their analytic envelopes. These direct distortion parameters are summarised for comparison in Table 1.

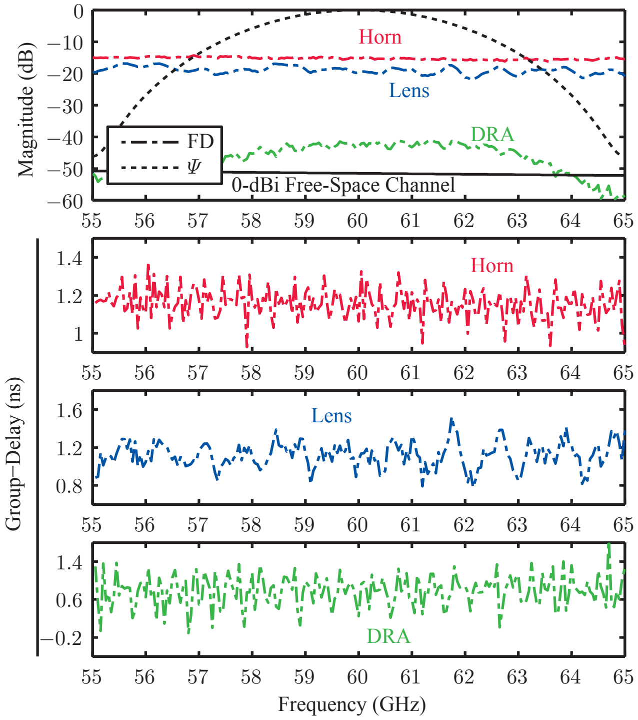

Figure 6: Raw antenna two-port transfer-functions, $\tilde{H} = S_{2,1}$, measured using a VNA. Also shown in the magnitude plot is the band-limiting Blackman-Harris gate, Ψ, defining the responses shown in Fig. 8.

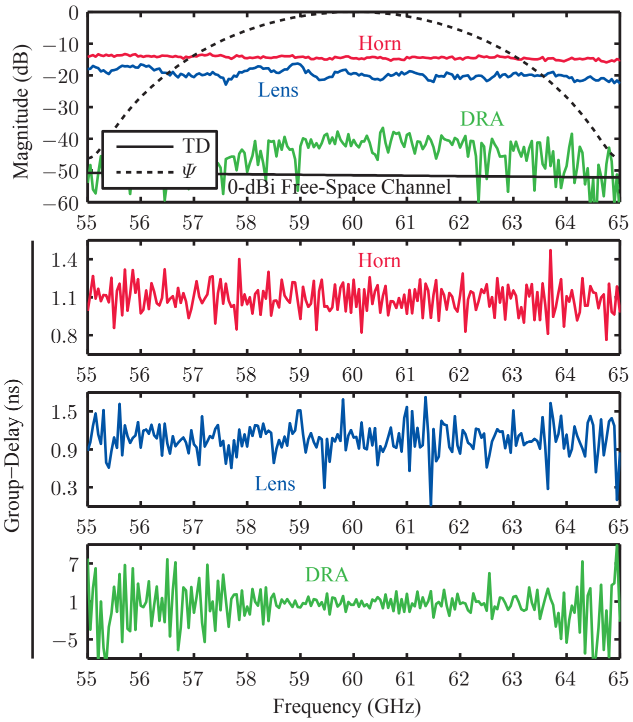

Figure 7: Raw antenna two-port transfer-functions, $\tilde{H}$, from time-domain measurements, in the target band about the 60 GHz carrier frequency of the exciting rectangular wavelet depicted in Fig. 1. The band-limiting gate, Ψ, is overlay plotted on the magnitude, defining the responses shown in Fig. 8.

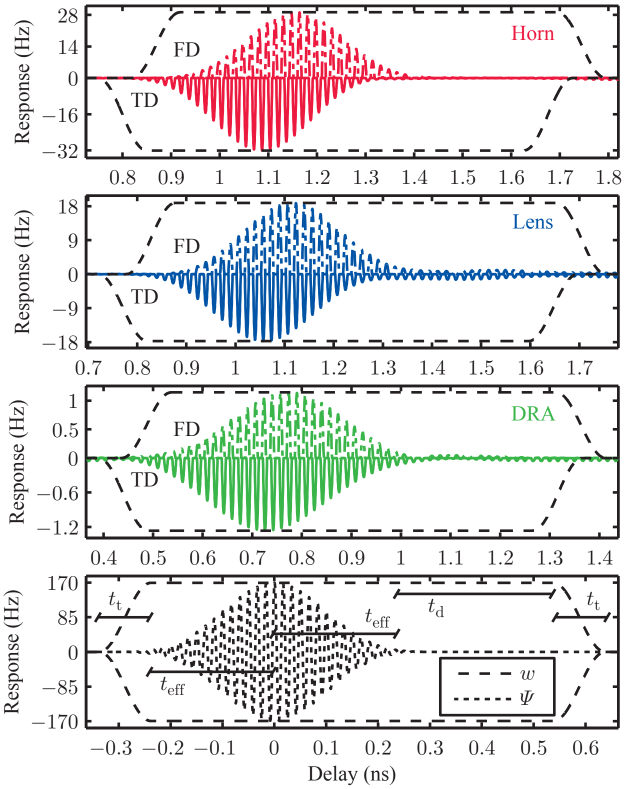

Figure 8: Band-limited responses, $\tilde{h}_{\mathrm{lim}}$, of the antenna two-ports, synthesised from the transfer-functions in Fig. 6 (FD) and Fig. 7 (TD). For ease of comparison, the upper half-planes correspond to data from frequency-domain measurements (FD) while the lower half-planes show responses from time-domain measurements (TD). The bottom plot illustrates the sole response from the band-limiting gate, Ψ. The delay-selective Tukey gate, w, is shown relatively in overlay on the responses.

4.2 Transfer-Function and Impulse-Response Refinement

For the data measured using the VNA, which is referred to as that from the frequency-domain method, the transfer scattering parameters estimate the raw transfer-functions, shown in Fig. 6. The phasor normalisation in step **1** and **2**, of the analysis algorithm defined in Section 2.2, is thereby not needed for the VNA data. For the data measured using the wavelet generator and the oscilloscope, which is referred to as that from the time-domain method, discrete Fourier analysis and normalisation to the thru reference signal is performed. The resulting raw transfer-functions from the time-domain measurements are shown in Fig. 7. The data from both methods were then padded with zeros to span from 0 to 1.64 THz. This corresponds to an interpolation in the time-domain and is only a cosmetic feature.

The remainder of the analysis algorithm is the same for both of the data sets, captured using the time- and frequency-domain methods. Performing step **3**, a band-limiting Blackman-Harris gate was defined over a $B = 10$ GHz bandwidth centred on 60 GHz, which is also shown in Fig. 6 and Fig. 7. The effective 3-term Blackman-Harris gate bandwidth, $B_{\mathrm{eff}} = 0.42B = 4.2$ GHz, is the product of its processing gain and absolute bandwidth [23].

In step **4**, the band-limited time-domain responses were synthesised from the corresponding gated transfer-functions, shown in Fig. 8. Also shown is the stand alone response of the band-limiting gate. The DUT characteristics in the other responses are embedded in any deviation from this ideal response. Note that the delay at the peak value corresponds to the propagation delay between the reference ports at 60 GHz. Also, the 53.5-ps delay of the thru utilised to normalise the signals in the time-domain method offset the corresponding impulse-responses in relation to those from the calibrated frequency-domain method. Due to the different feed structures of the antennas, the delays exceed the approximately 500 ps propagation delay over the 150-mm channel.

Implementing step **5**, a delay-selective gate was used to remove channel reflections and excess temporal noise. The main transmission responses were isolated using a Tukey window with a $t_{\mathrm{t}} = 100$-ps roll-off transition region at each edge; it thereby spans a handful of carrier cycles. To account for the delay ambiguity caused by the previously used band-limiting gate, the flat-top region was extended by the inverse of the effective gate bandwidth, i.e. $t_{\mathrm{eff}} = 1/B_{\mathrm{eff}} = 238$ ps, in each direction about the response peak. An additional $t_{\mathrm{d}} = 300$-ps flat-top region was added in the forward direction to accommodate for any DUT dispersion, but short enough to exclude any inter-antenna round-trip reflections. The final 976-ps 20.5%-Tukey gate, i.e. $\alpha = 2t_{\mathrm{t}}/(t_{\mathrm{d}} + 2t_{\mathrm{eff}} + 2t_{\mathrm{t}}) = 20.5\%$ roll-off factor [23], is shown in overlay on the responses in Fig. 8; it features a 776-ps unit-valued flat-top.

Via transformation and normalisation, step **6** and **7**, the delay-isolated band-limited transfer-functions were found, as shown in Fig. 9. These refined transfer-functions provide a much improved group-delay fidelity and a more smooth am-

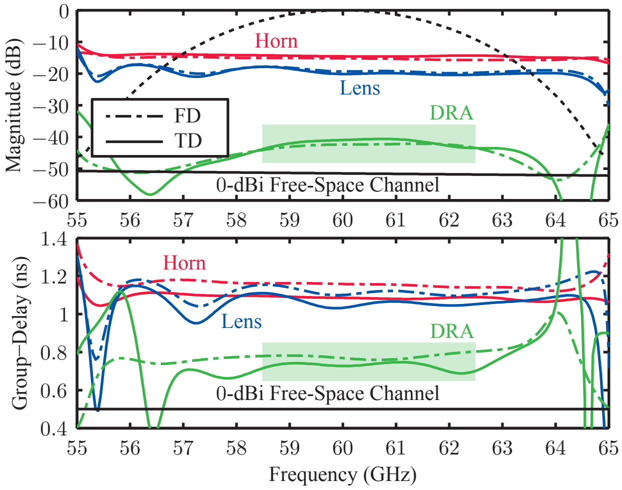

Figure 9: Refined transfer-function magnitudes and group-delays of the antenna two-ports, from time- (TD) and frequency-domain (FD) measurement methods. The green boxes indicate the approximate 4-GHz DRA bandwidth.

Table 2: 60 GHz Single Antenna Characteristics

Quantity (Method)	Symbol	Horn	Lens	DRA
Realised Gain (FD)[a]	G_{A} (dBi)	18.2	16.1	4.7
Realised Gain (TD)[a]	G_{A} (dBi)	18.5	15.7	5.3
Dispersion (FD)[b]	$\hat{\partial}_f \tau_{\mathrm{g,A}}$ (ps/GHz)	−2.5	1.1	5.3[c]
Dispersion (TD)[b]	$\hat{\partial}_f \tau_{\mathrm{g,A}}$ (ps/GHz)	−1.7	0.6	8.1[c]

Characteristics estimated from the refined transfer-functions in Fig. 9, that inherently correspond to two antennas over a free-space link.

[a] Realised gain found by de-embedding a 51.6-dB free-space loss.

[b] Effective group-delay dispersion found by taking a Hann-weighted average of this gradient over the 10 GHz gate bandwidth about 60 GHz.

[c] Range exceeds the antenna bandwidth.

plitude response, as compared to the raw data in Fig. 6 and Fig. 7. We attribute this change to removal of channel reflections and excess temporal noise. Inherently from the gating analysis utilised, the refined transfer-functions in Fig. 9 primarily describe the main transmission responses of the DUTs. Further, set by the inverse effective delay-width of the α-Tukey gate, an effective DUT dispersion bandwidth resolution, $B_{\mathrm{d}} = 1/(t_{\mathrm{d}} + 2t_{\mathrm{eff}} + t_{\mathrm{t}}) = 1.3$ GHz, is imposed. Thereby, the frequency- and time-domain gates utilised limit the possible features of the refined DUT transfer-function.

Antenna characteristics can be estimated from the refined two-port transfer-functions of the symmetric DUTs. The 51.6-dB free-space loss found from Friis' transmission equation over 150 mm at 60 GHz and the group-delay gradient, $\partial_f \tau_{\mathrm{g}}$, are utilised. The average realised antenna gain, G_{A}, and the effective dispersion, $\hat{\partial}_f \tau_{\mathrm{g,A}}$, of the antennas in the DUTs are quantified in Table 2. Here, to provide a meaningful figure-of-merit for the comparison within the target bandwidth, the effective dispersion operator, $\hat{\partial}_f$, has the meaning Hann weighted average of the gradient taken over the target bandwidth.

5 Discussion

Time-domain characterisation and gating techniques were proposed and used in this paper, based on a rectangular mmW wavelet excitation. For reference, frequency-domain characterisation using a calibrated VNA provides a comparison baseline. The same signal processing algorithm is applied for both measurements. Operation frequency limitations of the utilised components restricted the target bandwidth to 10 GHz, since 60-GHz centred time-domain measurements were used. These techniques and measurement results are compared in the following.

5.1 Time- and Frequency-Domain Systems

A measurements setup where instruments could be interchanged between a VNA or a wavelet generator and an oscilloscope, cf. Fig. 5, was used. Cables were utilised to interface the instruments and extend the reference ports. It should be noted that the timing of high-order setup reflections are shifted by insertion of these transmission lines at the reference ports of the DUT [9]. The millimetre-wave cables also provide significant insertion loss that act multiple times on any round-trip signal components. This helps to idealise the raw time- and frequency-domain measurements setup.

The VNA provides a high-intensity excitation of each frequency component within the bandwidth, resulting in a relatively clean raw transfer-function magnitude in Fig. 6. By comparison, the wideband low-intensity excitation provided by the 80-ps wavelet, cf. Fig. 1, provides less overall margin to the noise-floor. This is seen to greatly influence the quality of the DRA measurement in Fig. 7, since the limited DUT gain towards the edges of the target bandwidth causes signal loss. Any bandwidth limitation of the gating methods and noise-dominated spectral nulls of the wavelet, however, can be circumvented by superimposing measurements taken at shifted carrier frequencies.

Another significant difference between the frequency- and time-domain methods is related to calibration. A standard full calibration was performed on the VNA, making use of its specialised port transceivers. A full wavelet calibration was not possible here as it requires receiver circuits that can discern between impinging and departing port signal components.

In summary, it is shown here that mmW time-domain measurements can be directly applied to a measurements setup equivalent to that used for frequency-domain network analysis. It is further determined that the measurement results are reproduced for both methods, which demonstrates a potential for future time-domain instrument implementations.

5.2 Gating Techniques

The raw transfer-functions of the antenna-link two-port DUTs from the time- and freqency-domain methods are influenced by noise and various channel reflections. Time-domain results can also contain artefacts from high-order setup interaction. This is most apparent in the erratic behaviour of the antenna two-port group-delay in Fig. 6 and Fig. 7. Instead of un-physical fitting or smoothing, gating techniques were used to idealise the measurements setup. It was shown here to be a powerful tool in anaysis and refinement of VNA measurements of scattering-rich devices, e.g. mmW antennas, not just limited to time-domain measurements.

Gating affects the reciprocal domain and deliberate choices of windows and their alignment was thereby used. The band-limiting 3-term Blackman-Harris window ensures that every component in the corresponding band-limited response produces just one temporally confined feature. A flat-top delay-isolation gate with extension in the forward direction is then required to not apply any relative weight on the various components. The use of a Tukey window is a compromise to avoid a sharp edge. Within the spectral gate bandwidth and temporal gate delay width, the DUT transfer-functions were refined in Fig. 9. The resulting group-delays are seen to be relatively well-behaved and the magnitudes are smoothed due to interference rejection. It can further be observed that the time-domain method closely reproduces both the magnitude and group-delay found in the frequency-domain method. One difference, however, is a static group-delay offset due to the finite delay of the utilised thru reference. Also, the gating techniques produce minor artefacts that grow significant towards the edges of the target bandwidth.

Here, the proposed band-limiting gate is real-valued and thereby provides a non-causal response. If desired, a causal minimum-phase response can be produced for any stable band-limiting gate window via cepstral processing [27].

5.3 Millimetre-Wave Antenna Characterisation

Direct effects of the mmW antenna two-port DUTs on a rectangular wavelet were shown in Fig. 4, and quantified in Table 1. The lens antenna two-port provides a high, 96%, fidelity link, closely reproducing the wired thru reference signal. Although the 87% fidelity of the horn antenna two-port is only a few units of percent lower, its nearly triangular envelope visualises the crude relation between fidelity factor and signal shape. The DRA two-port spreads the wavelet transitions in approximate proportion to its inverse bandwidth. Bandwidth limitation, combined with a low-gain noise-limited measurement, causes the low, 46%, fidelity factor. All fidelity factor results are partially limited by setup artefacts and noise levels as the overall temporal distribution of sampled signals is evaluated, not the specific likenesses of the wavelets.

Comparison of signal rise- and fall times, as well as the pulse-lengths, are alternative forms of expressing the signal distortion inflicted by the DUTs. Extended transition times, in relation to the reference, are the combined effect from transfer-function bandwidth limitation and group-delay dispersion. In terms of qualitative pulse distortion, the compact DRA compares reasonably well to the much larger horn antenna, although with a lower antenna gain. The leaky-lens antenna is, as expected, found to provide non-dispersive pulse transmission and also has a moderately high antenna gain.

The refined transfer-function results in Fig. 9 allow an estimation of the 60-GHz realised antenna gain and effective group-delay dispersion; quantified in Table 2. The time- and frequency-domain methods are seen to produce similar values for all antennas over both characteristics. The determined realised gain of the horn antenna also corresponds well to the 19.5-dBi specified value when the utilised waveguide adapter insertion loss is taken into account. The horn antenna results thereby indicate that the proposed time-domain method can have an accuracy similar to VNA measurements. Further, the group-delay of the horn antenna and waveguide adapter is found to have an effective gradient of approximately -2 ps/GHz. This explains the signal dispersion in Fig. 4 and corresponds well to that found from analytic waveguide analysis [28]; the horn antenna can be approximated as a non-uniform transmission line. It must, however, be stressed that the feed waveguides of the utilised adapters provide the majority of the dispersion. The group-delay dispersion of the leaky-lens antenna is found to be approximately 0.9 ps/GHz but the variation in Fig. 9, that we attribute to internal reflections, complicates the interpretation of the effective dispersion. One of the signal components can be seen at approximately 400 ps delay after the main peak in the band-limited response, cf. Fig. 8. To facilitate further analysis, gating of shorter sections of the responses can be implemented. While the effective group-delay dispersion value is high, a very approximate saddle-point is found for the DRA two-port group-delay about its bandwidth, indicated by the box in Fig. 9, which is expected for a simple resonant device.

6 Conclusion

In conclusion, a characterisation method based on wideband time-domain wavelets has been presented. It utilises gating techniques in both time- and frequency-domain, which also were shown to refine measured results from a VNA. Testing the time-domain method, different mmW antenna two-ports were measured, which allowed for quantification of band-limited delay-isolated device characteristics. Overall, the proposed thru normalised time-domain method delivers results that are similar to those from the calibrated VNA. This indicates the future feasibility to utilise mmW wavelet generators as sources in test instruments. Shorter wavelets can provide improved bandwidth, while scaling towards terahertz frequencies can realise accurate characterisation at less accessible frequency bands.

References

[1] T. Fukuda, N. Negoro, S. Ujita, S. Nagai, M. Nishijima, H. Sakai, T. Tanaka, and D. Ueda, "A 26 GHz short-range UWB vehicular-radar using 2.5 Gcps spread spectrum modulation," in *2007 IEEE MTT-S Int. Symp. Microwave*, Jun. 3-8, 2007, pp. 1311–1314.

[2] L. Ohlsson and L.-E. Wernersson, "A 15-Gb/s wireless ON-OFF keying link," *IEEE Access*, vol. 2, pp. 1307–1313, Oct. 2014.

[3] E. Pancera, T. Zwick, and W. Wiesbeck, "Spherical fidelity patterns of UWB antennas," *IEEE Trans. Antennas Propag.*, vol. 59, no. 6, pp. 2111–2119, Jun. 2011.

[4] D. M. Pozar, "Waveform optimizations for ultrawideband radio systems," *IEEE Trans. Antennas Propag.*, vol. 51, no. 9, pp. 2335–2345, Sep. 2003.

[5] R. B. Marks, "A multiline method of network analyzer calibration," *IEEE Trans. Microw. Theory Techn.*, vol. 39, no. 7, pp. 1205–1215, Jul. 1991.

[6] G. Gronau and I. Wolff, "A simple broad-band device de-embedding method using an automatic network analyzer with time-domain option," *IEEE Trans. Microw. Theory Techn.*, vol. 37, no. 3, pp. 479–483, Mar. 1989.

[7] K. Lu and T. J. Brazil, "A systematic error analysis of HP 8510 time-domain gating techniques with experimental verification," in *1993 IEEE MTT-S Int. Symp. Microwave Dig.*, vol. 3, Jun. 14-18, 1993, pp. 1259–1262.

[8] W. Wiesbeck, G. Adamiuk, and C. Sturm, "Basic properties and design principles of UWB antennas," *Proc. IEEE*, vol. 97, no. 2, pp. 372–385, Feb. 2009.

[9] A. M. Nicolson, “Broad-band microwave transmission characteristics from a single measurement of the transient response,” *IEEE Trans. Instrum. Meas.*, vol. 17, no. 4, pp. 395–402, Dec. 1968.

[10] Y. Konishi, M. Kamegawa, M. Case, R. Yu, M. J. Rodwell, R. A. York, and D. Rutledge, “Picosecond electrical spectroscopy using monolithic GaAs circuits,” *AIP Appl. Phys. Lett.*, vol. 61, no. 23, pp. 2829–2831, Dec. 1992.

[11] M. Sipilä, K. Lehtinen, and V. Porra, “High-frequency periodic time-domain waveform measurement system,” *IEEE Trans. Microw. Theory Techn.*, vol. 36, no. 10, pp. 1397–1405, Oct. 1988.

[12] L. A. Hayden and V. K. Tripathi, “Calibration methods for time domain network analysis,” *IEEE Trans. Microw. Theory Techn.*, vol. 41, no. 3, pp. 415–420, Mar. 1993.

[13] R. B. Marks, L. A. Hayden, J. A. Jargon, and F. Williams, “Time domain network analysis using the multiline TRL calibration,” in *44th ARFTG Conf. Dig.-Fall*, vol. 26, Dec. 1994, pp. 47–55.

[14] J. D. McKinney, D. Peroulis, and A. M. Weiner, “Time-domain measurement of the frequency-dependent delay of broadband antennas,” *IEEE Trans. Antennas Propag.*, vol. 56, no. 1, pp. 39–47, Jan. 2008.

[15] H. Lee, J. Lee, and J. Kim, “Picosecond-domain radiation pattern measurement using fiber-coupled photoconductive antenna,” *IEEE J. Sel. Topics Quantum Electron.*, vol. 7, no. 4, pp. 667–673, Jul. 2001.

[16] H. Zhong, J. Xu, X. Xie, T. Yuan, R. Reightler, E. Madaras, and X.-C. Zhang, “Nondestructive defect identification with terahertz time-of-flight tomography,” *IEEE Sensors J.*, vol. 5, no. 2, pp. 203–208, Apr. 2005.

[17] Y. Nakasha, Y. Kawano, T. Suzuki, T. Ohki, T. Takahashi, K. Makiyama, T. Hirose, and N. Hara, “A W-band wavelet generator using 0.13-μm InP HEMTs for multi-gigabit communications based on ultra-wideband impulse radio,” in *2008 IEEE MTT-S Int. Symp. Microwave Dig.*, Jun. 15-20, 2008, pp. 109–112.

[18] N. Deparis, A. Siligaris, P. Vincent, and N. Rolland, “A 2 pJ/bit pulsed ILO UWB transmitter at 60 GHz in 65-nm CMOS-SOI,” in *2009 IEEE Int. Conf. Ultra-Wideband (ICUWB)*, Sep. 9-11, 2009, pp. 113–117.

[19] M. Egard, M. Ärlelid, L. Ohlsson, B. M. Borg, E. Lind, and L.-E. Wernersson, “$In_{0.53}Ga_{0.47}As$ RTD-MOSFET millimeter-wave wavelet generator,” *IEEE Electron Device Lett.*, vol. 33, no. 7, pp. 970–972, Jul. 2012.

[20] I. Vakili, L. Ohlsson, M. Gustafsson, and L.-E. Wernersson, “Wideband and non-dispersive wavelet transmission using leaky lens antenna,” *IET Electron. Lett.*, vol. 49, no. 5, pp. 321–322, Feb. 2013.

[21] L. Ohlsson, T. Bryllert, C. Gustafson, D. Sjöberg, M. Egard, M. Ärlelid, and L. Wernersson, "Slot-coupled millimeter-wave dielectric resonator antenna for high-efficiency monolithic integration," *IEEE Trans. Antennas Propag.*, vol. 61, no. 4, pp. 1599–1607, Apr. 2013.

[22] S. M. Riad, "The deconvolution problem: An overview," *Proc. IEEE*, vol. 74, no. 1, pp. 82–85, Jan. 1986.

[23] F. J. Harris, "On the use of windows for harmonic analysis with the discrete fourier transform," *Proc. IEEE*, vol. 66, no. 1, pp. 51–83, Jan. 1978.

[24] D. Lamensdorf and L. Susman, "Baseband-pulse-antenna techniques," *IEEE Antenna Propag. Mag.*, vol. 36, no. 1, pp. 20–30, Feb. 1994.

[25] H. Kanaya, H. Shibayama, S. Suzuki, and M. Asada, "Fundamental oscillation up to 1.31 THz in thin-well resonant tunneling diodes," in *24th IEEE Int. Conf. Indium Phosphide and Related Materials (IPRM 2012)*, Aug. 27-30, 2012, pp. 106–109.

[26] M. Egard, M. Ärlelid, E. Lind, and L.-E. Wernersson, "Bias stabilization of negative differential conductance oscillators operated in pulsed mode," *IEEE Trans. Microw. Theory Techn.*, vol. 59, no. 3, pp. 672–677, Mar. 2011.

[27] S.-C. Pei and H.-S. Lin, "Minimum-phase FIR filter design using real cepstrum," *IEEE Trans. Circuits Syst. II, Exp. Briefs*, vol. 53, no. 10, pp. 1113–1117, Oct. 2006.

[28] D. M. Pozar, *Microwave Engineering*, 4th ed. Wiley, 2012.

Sum Rules for Parallel Plate Waveguides: Experimental Results and Theory

Iman Vakili, Mats Gustafsson,
Daniel Sjöberg, Rebecca Seviour, Martin Nilsson, Sven Nordebo

Paper IV

Published as: I. Vakili, M. Gustafsson, D. Sjöberg, R. Seviour, M. Nilsson, S. Nordebo, Sum Rules for Parallel Plate Waveguides: Experimental Results and Theory, *IEEE Transactions on Microwave Theory and Techniques*, Vol. 62, No. 11, pp. 2574-2582, 2014.

Abstract

An experimental approach to investigate the forward scattering sum rule for periodic structures is presented. This approach allows an upper bound on the total cross section integrated over a bandwidth from a simple static problem to be found. Based on energy conservation, the optical theorem is used to construct a relation between the total cross section and the forward scattering of periodic structures as well as single scatterers inside a parallel plate waveguide. Dynamic measurements are performed using a parallel plate waveguide and a parallel plate capacitor is utilized to find the static polarizability. Convex optimization is introduced to identify the total cross section in the dynamic measurements and estimate an optimal lower bound on the polarizability for objects. The results show that the interactions between the electromagnetic field and an object over all wavelength are given by the static polarizability of the object.

1 Introduction

Scattering properties of periodic structures have been a research topic for over a century, used to study a diverse range of systems from, electron transport in nanostrutures to electromagnetic (EM) wave propagation. Determining the dynamic properties of an object using experimental scattering techniques can be very problematic, especially when the phase of the wave has to be accurately measured. In this paper we present a relative scattering technique for EM wave interactions with an arbitrary object, which enables insight into the objects dynamic properties, without the need for difficult phase calibrations. In terms of forward scattering, the optical theorem relates the real part of the forward scattering amplitude to the total cross section of any scatterer [11, 16, 25]. The forward scattering sum rule shows that the all wavelengths integration of the total cross section of an object is given by the static polarizability of the object. This simple relation offers an understanding of the total interaction between the EM field and an object over the entire spectrum. This was first discussed by Purcell for dielectric spheroids [18], then generalized to arbitrary objects in [4, 23]. The sum rule has in recent years been used to introduce bounds on antennas [5–7, 22], metamaterials [24], and extraordinary transmission [8].

The optical theorem and the forward scattering sum rule have recently been generalized to 1D and 2D periodic structures in [10]. Moreover the scattered and absorbed power from an incident plane wave is known to be proportional to $\operatorname{Im} h(k)$, where $h(k) = \mathrm{j}2(1 - T(k))A$ is a Herglotz function [1, 10, 17] (or a positive real function [30]), where $\mathrm{j}^2 = -1$. Here, k denotes the wavenumber, A is the cross sectional area of the unit cell and T is the co-polarized part of the fundamental mode transmission coefficient.

In this paper, the optical theorem and the related forward scattering sum rule are extended to the case of parallel plate waveguides. The waveguide is used for wide-band scattering characterization of materials [26]. We show that this set-up can be used as a quasi-2D experimental methodology to find the scattering properties of one-dimensional periodic structures. Properties of the positive real functions, together with convex optimization [2] are utilized to combat the noise level in the system.

The low-frequency asymptotic expansion of the positive real function [9] (similar to Herglotz and Nevanlinna functions [1]) gives the relationship between the dynamic measurements and the static polarizability. In order to measure the static properties, a basic measurement set-up consisting of a parallel plate capacitor is used. The static polarizability is deduced from the small difference of the capacitance when the object is inserted in the capacitor [13].

The results show that the entire spectrum interaction between the electromagnetic field and the periodic structure in a parallel plate waveguide is proportional to the static polarizability that can be found from a parallel plate capacitor, regardless of shape and resonant behavior. This simple approach provides physical insight into the total cross section integrated over the bandwidth of any scatterer. The method is applicable for frequency selective structures [15], metamaterials [3, 21], and electromagnetic band gap structures [29].

The remainder of the paper is structured as follows. The optical theorem for periodic structures as well as single scatterer in a parallel plate waveguide are presented in Section 2. Forward scattering sum rules are discussed in Section 3. In Section 4, we report a passive system identification using convex optimization. The experimental methodology is presented in Section 5, and numerical examples are illustrated in Section 6. The paper is concluded in Section 7.

2 Optical theorem in a parallel plate waveguide

In this section optical theorems for a parallel plate waveguide are presented. As shown in Fig. 1, the optical theorem is calculated for a one-dimensional periodic structure in Section 2.1, and for finite objects inside an imaginary cylinder in Section 2.2, see Fig. 2.

2.1 Periodic structures

We consider a one-dimensional planar periodic structure inserted inside a parallel plate waveguide. The structure has infinite periodicity in the y-direction and is oriented in the yz-plane (see Fig. 1). A linearly polarized time harmonic TEM mode, $\boldsymbol{E}_{\mathrm{i}}(\boldsymbol{r}) = \hat{\boldsymbol{z}}E_0\mathrm{e}^{-\mathrm{j}kx}$, impinges upon the periodic structure at normal incidence, where the time convention $\mathrm{e}^{\mathrm{j}\omega t}$ is used. The transmitted and the reflected fields are denoted $\boldsymbol{E}_{\mathrm{t}}$ and $\boldsymbol{E}_{\mathrm{r}}$, respectively.

The transverse components of the transmitted field, denoted by $\boldsymbol{E}_{\mathrm{t}}^{\mathrm{yz}}$ below, are expanded in a combination of waveguide and Floquet modes (the normal components can be derived from the transverse components and do not provide additional degrees of freedom). Taking the periodicity in y-direction and the elec-

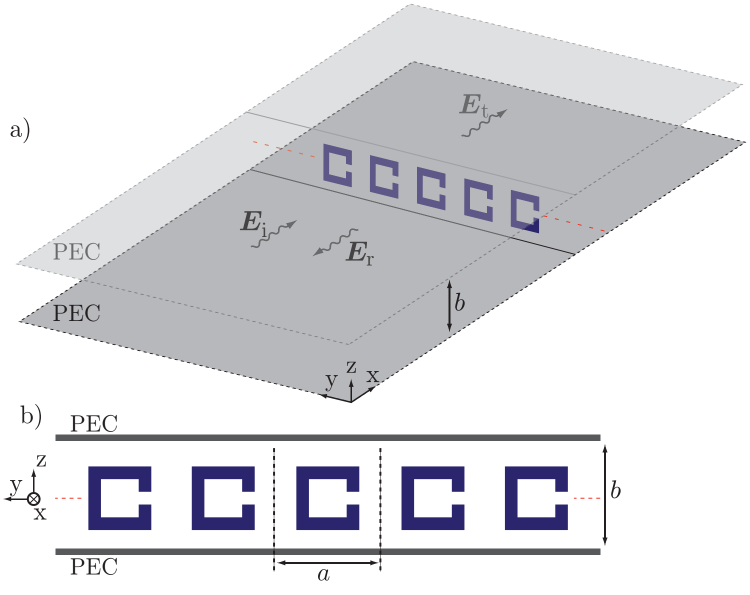

Figure 1: Scattering geometry for one dimensional periodic objects with periodicity a inside the parallel plate waveguide with the height b. a) perspective view. $\boldsymbol{E}_{\mathrm{i}}$ is the incident field, $\boldsymbol{E}_{\mathrm{t}}$ the transmitted field, and $\boldsymbol{E}_{\mathrm{r}}$ denotes the reflected field. The arrows show the direction of the propagation. b) Front view.

tric boundary conditions in z-direction into account, the transverse components can be written as

$$\boldsymbol{E}_{\mathrm{t}}^{\mathrm{yz}}(k;\boldsymbol{r}) = \sum_{m=-\infty}^{\infty}\sum_{n=0}^{\infty}\sum_{\nu=\mathrm{TE},\mathrm{TM}} E_{mn\nu}(k)\boldsymbol{E}_{\mathrm{t}n\nu}^{\mathrm{yz}}(z)\mathrm{e}^{-\mathrm{j}(k_x x + m2\pi y/a)}, \tag{2.1}$$

where $k_x = \sqrt{k^2 - (m2\pi/a)^2 - (n\pi/b)^2}$, a is the length of the unit cell in the y-direction and b is the height of the waveguide, see Fig. 1b. Note the extra factor of 2 in the term $m2\pi/a$ compared to $n\pi/b$. When m is large enough, the corresponding modes are evanescent. Here, $\boldsymbol{E}_{\mathrm{t}n\nu}^{\mathrm{yz}}$ denotes the transverse components of the vector basis functions for waveguide modes, which are $\boldsymbol{E}_{\mathrm{t}n\nu}^{\mathrm{yz}} = \sqrt{\epsilon_n}\cos(\frac{n\pi z}{b})\hat{\boldsymbol{z}}$ for $\nu = \mathrm{TM}$ (where $\epsilon_n = 1$ for $n = 0$ and $\epsilon_n = 2$ for $n \neq 0$), and $\boldsymbol{E}_{\mathrm{t}n\nu}^{\mathrm{yz}} = \sqrt{2}\sin(\frac{n\pi z}{b})\hat{\boldsymbol{y}}$ for $\nu = \mathrm{TE}$ and $n > 0$, see [14, p. 64] for details. The expansion coefficients behind the structure are,

$$E_{mn\nu} = \frac{1}{ab}\int_0^b\int_0^a \boldsymbol{E}_{\mathrm{t}}^{\mathrm{yz}}(k;0,y,z)\cdot\boldsymbol{E}_{\mathrm{t}n\nu}^{\mathrm{yz}*}(z)\mathrm{e}^{\mathrm{j}m2\pi y/a}\,\mathrm{d}y\,\mathrm{d}z, \tag{2.2}$$

where, the subscript $(*)$ denotes the complex conjugate. A general incident field can be expanded in the corresponding modes, which are related to the modes of the transmitted field by a linear mapping quantified by the transmission coefficient $T_{mn\nu,m'n'\nu'}$. In our case, we consider an incident field consisting of only the TEM mode ($m' = 0$, $n' = 0$, and $\nu' = \mathrm{TM}$), and study the corresponding transmitted mode ($m = 0$, $n = 0$, and $\nu = \mathrm{TM}$) and define the co-polarized transmission coefficient as $T = T_{00\mathrm{TM},00\mathrm{TM}}$.

The optical theorem for periodic structures is based on energy conservation and relates the forward scattered field to the total cross section [10]. The incident power per unit cell is denoted by P_i. The transmitted power is $P_\mathrm{t} = |T|^2 P_\mathrm{i} + P_\mathrm{t1}$. Here, $|T|^2 P_\mathrm{i}$ is the co-polarized transmitted power in the TEM mode and P_t1 is the transmitted power for the remaining modes. The difference between the incident and the sum of the reflected and transmitted power is the absorbed power, $P_\mathrm{a} = P_\mathrm{i} - P_\mathrm{r} - |T|^2 P_\mathrm{i} - P_\mathrm{t1}$, and the sum of the reflected power and the power in the scattered part of the transmitted field is the scattered power, $P_\mathrm{s} = P_\mathrm{r} + |1 - T|^2 P_\mathrm{i} + P_\mathrm{t1}$. The total power is the sum of the absorbed and scattered power and can be expressed as

$$P_\mathrm{tot} = P_\mathrm{a} + P_\mathrm{s} = 2\,\mathrm{Re}\{1 - T(k)\} P_\mathrm{i}. \tag{2.3}$$

By considering the incident power per unit cell, $P_\mathrm{i} = A|E_0|^2/(2\eta_0)$ and normalizing both sides of (2.3) by the incident power flux, $|E_0|^2/2\eta_0$, the total (extinction) cross section becomes

$$\sigma_\mathrm{tot} = \sigma_\mathrm{a} + \sigma_\mathrm{s} = 2\,\mathrm{Re}\{1 - T(k)\} A, \tag{2.4}$$

where $A = ab$. The optical theorem for periodic objects in a parallel plate waveguide shows that the total cross section is related to the transmission coefficient.

2.2 Bounded scatterer

In this subsection, the optical theorem is investigated for a non-periodic structure bounded by an imaginary cylinder. Assume an incident wave propagating in the positive x-direction, linearly polarized in the z-direction $\boldsymbol{E}_\mathrm{i} = \hat{\boldsymbol{z}} E_0 \mathrm{e}^{-\mathrm{j}kx}$. A scatterer of arbitrary shape and material is placed inside the parallel plate waveguide. Following [11, p. 501], the sum of the absorbed and scattered power, here denoted the total power is

$$\begin{aligned} P_\mathrm{tot} = P_\mathrm{a} + P_\mathrm{s} &= \frac{1}{2}\,\mathrm{Re} \int_S \hat{\boldsymbol{n}} \cdot \big(\boldsymbol{E}_\mathrm{s} \times \boldsymbol{H}_\mathrm{s}^* - (\boldsymbol{E}_\mathrm{i} + \boldsymbol{E}_\mathrm{s}) \times (\boldsymbol{H}_\mathrm{i} + \boldsymbol{H}_\mathrm{s})^*\big)\,\mathrm{dS} \\ &= -\frac{1}{2}\,\mathrm{Re} \int_S \hat{\boldsymbol{n}} \cdot (\boldsymbol{E}_\mathrm{s} \times \boldsymbol{H}_\mathrm{i}^* + \boldsymbol{E}_\mathrm{i} \times \boldsymbol{H}_\mathrm{s}^*)\,\mathrm{dS}, \end{aligned} \tag{2.5}$$

where the surface S encloses the scatterer and $\hat{\boldsymbol{n}} = \hat{\boldsymbol{\varrho}} = \hat{\boldsymbol{x}} \sin\phi + \hat{\boldsymbol{y}} \cos\phi$ is the outward pointing normal vector (see Fig. 2). The subscript s stands for the

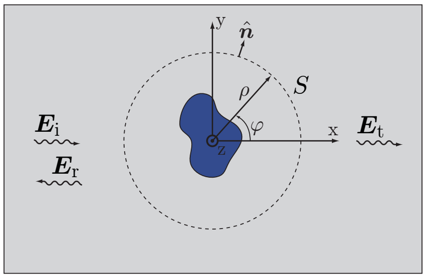

Figure 2: Top view of the parallel plate waveguide. The imaginary surface S is a cylinder of radius ρ and normal vector $\hat{\boldsymbol{n}}$, that encloses the object. The arrows show the direction of the propagation.

scattered fields that represent the difference between the fields in the presence and absence of the object, *i.e.*, $\boldsymbol{E}_{\rm s} = \boldsymbol{E} - \boldsymbol{E}_{\rm i}$. The surface S does not include the metal boundaries at $z = 0$ and $z = b$, since the power flux is zero through these boundaries. Using the real part to shift the last complex conjugate from $\boldsymbol{H}_{\rm s}^*$ to $\boldsymbol{E}_{\rm i}$, $\hat{\boldsymbol{y}} = \hat{\boldsymbol{z}} \times \hat{\boldsymbol{x}}$, and inserting the expression for the incident field, we get

$$\begin{aligned} P_{\rm tot} &= -\frac{1}{2} \operatorname{Re} \int\limits_S E_0^* \mathrm{e}^{\mathrm{j}kx} \hat{\boldsymbol{n}} \cdot (-\boldsymbol{E}_{\rm s} \times \hat{\boldsymbol{y}} \eta_0^{-1} + \hat{\boldsymbol{z}} \times \boldsymbol{H}_{\rm s}) \,\mathrm{dS} \\ &= \frac{-1}{2\eta_0} \operatorname{Re} \int\limits_0^b \int\limits_0^{2\pi} E_0^* \mathrm{e}^{\mathrm{j}kx} \hat{\boldsymbol{z}} \cdot (\boldsymbol{E}_{\rm s}(\hat{\boldsymbol{n}} \cdot \hat{\boldsymbol{x}}) + \eta_0 \boldsymbol{H}_{\rm s} \times \hat{\boldsymbol{n}}) \rho \,\mathrm{d}\phi \,\mathrm{d}z \\ &= \frac{-b}{2\eta_0} \operatorname{Re} \int\limits_0^{2\pi} E_0^* \mathrm{e}^{\mathrm{j}kx} \hat{\boldsymbol{z}} \cdot \langle \boldsymbol{E}_{\rm s}(\hat{\boldsymbol{n}} \cdot \hat{\boldsymbol{x}}) + \eta_0 \boldsymbol{H}_{\rm s} \times \hat{\boldsymbol{n}} \rangle \rho \,\mathrm{d}\phi, \end{aligned} \tag{2.6}$$

where $\langle . \rangle$ denotes the mean value of the fields over the height of the waveguide. The scattered field can be expanded in cylindrical modes, see [27]. There, it is shown that the mean value in (2.6) is nonzero only for the zeroth order mode, which is co-polarized to the incident plane wave.

By normalizing the total power with the incident power flux, $|E_0|^2/2\eta_0$, the total cross section becomes

$$\sigma_{\rm tot} = -\operatorname{Re} \Big\{ \frac{b}{E_0} \int\limits_0^{2\pi} \mathrm{e}^{\mathrm{j}kx} \hat{\boldsymbol{z}} \cdot \langle \boldsymbol{E}_{\rm s}(\hat{\boldsymbol{n}} \cdot \hat{\boldsymbol{x}}) + \eta_0 \boldsymbol{H}_{\rm s} \times \hat{\boldsymbol{n}} \rangle \rho \,\mathrm{d}\phi \Big\}, \tag{2.7}$$

where the integral in (2.7) is similar to the far-field amplitude, $f_{\rm s}$, in two dimensions which is given by [28]

$$f_{\mathrm{s}}(k) = \frac{\mathrm{j}k}{4}\int_{0}^{2\pi} \mathrm{e}^{\mathrm{j}kx}\hat{\boldsymbol{z}}\cdot\langle \boldsymbol{E}_{\mathrm{s}}(\hat{\boldsymbol{n}}\cdot\hat{\boldsymbol{x}}) + \eta_0 \boldsymbol{H}_{\mathrm{s}}\times\hat{\boldsymbol{n}}\rangle \rho \,\mathrm{d}\phi. \tag{2.8}$$

Here the co-polarized two-dimensional scattered far field $\boldsymbol{E}_{\mathrm{s}} \sim \hat{\boldsymbol{z}} f_{\mathrm{s}}\sqrt{\frac{2}{\pi \mathrm{j}k\rho}}\mathrm{e}^{-\mathrm{j}k\rho}$ and therefore, the total cross section can be written as

$$\sigma_{\mathrm{tot}} = -4b\,\mathrm{Re}\left\{\frac{f_{\mathrm{s}}(k)}{\mathrm{j}kE_0}\right\}. \tag{2.9}$$

The normalization by the height of the waveguide gives the two-dimensional total cross section.

3 Forward scattering sum rules

The forward scattering sum rule is used to find an upper bound on the total cross section of any scatterer. Identities stating that the integral (sum) of a variable has a certain value are categorized as sum rules and are mostly derived using holomorphic functions such as positive real or Herglotz (Nevanlinna) functions [1, 9,17]. In this paper the positive real (PR) function, $\mathscr{P}(\kappa)$, is given by the forward scattering amplitude derived in (2.4) and (2.9), where $\kappa = \zeta + \mathrm{j}k$. In both cases the PR function is holomorphic and $\mathrm{Re}\{\mathscr{P}(\kappa)\} \geqslant 0$ for $\mathrm{Re}\{\kappa\} > 0$ [10] and is given by

$$\mathscr{P}(\kappa) = \begin{cases} 2(1-T(\kappa))A & \text{for a periodic structure} \\ -\frac{4b}{\kappa E_0} f_{\mathrm{s}}(\kappa) & \text{for a single scatterer} \end{cases} \tag{3.1}$$

where the total cross section $\sigma_{\mathrm{tot}} = \mathrm{Re}\{\mathscr{P}(\kappa)\}$.

The low-frequency asymptotic expansion is obtained from Maxwell equations by an expansion in the fields [20], giving

$$\mathscr{P}(\kappa) = \kappa\big(\hat{\boldsymbol{z}}\cdot\boldsymbol{\gamma}_{\mathrm{e}}\cdot\hat{\boldsymbol{z}} + \hat{\boldsymbol{y}}\cdot\boldsymbol{\gamma}_{\mathrm{m}}\cdot\hat{\boldsymbol{y}}\big) + o(\kappa) \tag{3.2}$$

as $\kappa \hat{\to} 0$, where $\hat{\to}$ is the limit inside the right half plane and $|\arg(\kappa)| < \frac{\pi}{2} - \delta$ for a small positive δ, and $\boldsymbol{\gamma}_{\mathrm{e}}$ and $\boldsymbol{\gamma}_{\mathrm{m}}$ are the electric and magnetic static polarizability dyadics, respectively. The parallel plate waveguide in the static limit, $k \to 0$, is equivalent to a parallel plate capacitor with a uniform field distribution, $\boldsymbol{E}_0$, as shown in Fig. 3a. Here, $\boldsymbol{\gamma}_{\mathrm{e}}$ and $\boldsymbol{\gamma}_{\mathrm{m}}$ are identified as the polarizabilities of an object in the presence of the metal plates (in the periodic case this is understood as the polarizability per unit cell). The polarizability can be computed directly using proper boundary conditions in the finite element method, or the corresponding Green's function in the method of moments. The methods for periodic structures in [10,20] can also be used, since $\boldsymbol{\gamma}_{\mathrm{e}}$ equals half the polarizability of a mirror-symmetric, periodic structure with unit cell of length $2b$,

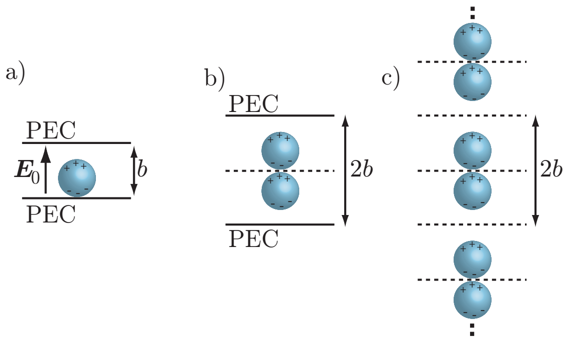

Figure 3: Periodic equivalence problem. a) An object is placed in an arbitrary position between the plates of a capacitor. b) An equivalent problem for part-a by placing the object and its image at the midpoint between two plates. c) The equivalent periodic problem.

as seen in Fig. 3bc. In either cases the static electric polarizability can be found using zero-frequency electric field computed by any of the numerical methods mentioned above, $\boldsymbol{E}(0;\boldsymbol{r})$, and the static permittivity dyadic, $\boldsymbol{\epsilon}(0;\boldsymbol{r})$, as [23, 24]

$$\hat{\boldsymbol{z}}\cdot\boldsymbol{\gamma}_{\mathrm{e}}\cdot\hat{\boldsymbol{z}} = \frac{1}{E_0}\int\limits_V \hat{\boldsymbol{z}}\cdot(\boldsymbol{\epsilon}(0;\boldsymbol{r})/\epsilon_0 - \mathbf{I})\cdot\boldsymbol{E}(0;\boldsymbol{r})\,\mathrm{d}V, \tag{3.3}$$

where ϵ_0 is the free space permittivity, $\mathbf{I}$ is an identity matrix, and V is the volume of the integration which encloses a unit cell.

The relation in (3.2) also shows that the forward scattering weighted by the frequency, $\mathscr{P}(\mathrm{j}k)/\mathrm{j}k$, gives the static polarizabilities as $k \to 0$. This can be used, as explained in Section 6, to estimate the static polarizability of an object using measurements at frequencies greater than the static limit with the requirement that the wavelength has to be longer than the size of the object.

The sum rule relates the total cross section over all wavelengths to the static polarizability and is given by [1]

$$\frac{2}{\pi}\int\limits_0^\infty \frac{\sigma_{\mathrm{tot}}(k;\hat{\boldsymbol{x}},\hat{\boldsymbol{z}})}{k^2}\,\mathrm{d}k = \hat{\boldsymbol{z}}\cdot\boldsymbol{\gamma}_{\mathrm{e}}\cdot\hat{\boldsymbol{z}} + \hat{\boldsymbol{y}}\cdot\boldsymbol{\gamma}_{\mathrm{m}}\cdot\hat{\boldsymbol{y}}. \tag{3.4}$$

The integration on the left hand side determines the dynamic behavior of the scatterer and the right hand side can be found from the static properties. The sum rule is used to derive an upper bound on the total cross section integrated over a bandwidth [1].

In this paper we use a parallel plate waveguide to determine the integral value on the left hand side and a parallel plate capacitor to measure the static polarizability on the right hand side of (3.4). The sum rule is valid for passive structures that do not support currents in the low frequency limit, *i.e.*, that do not short circuit the plates.

4 Passive system identification using convex optimization

Convex optimization [2] together with the properties of positive real functions are used to identify the measured passive system. A symmetric PR function can be represented as

$$\mathscr{P}(\kappa) = b_1\kappa + \int_{-\infty}^{\infty} \frac{\kappa}{\xi^2 + \kappa^2}\,\mathrm{d}G(\xi), \tag{4.1}$$

for $\operatorname{Re}\kappa > 0$, where b_1 is a real valued and non-negative constant, $\kappa = \zeta + \mathrm{j}k$ is the Laplace parameter, and $G(\xi)$ is a positive and finite measure such that $\int_{\mathbb{R}} \mathrm{d}G(\xi)/(1+\xi^2) < \infty$. The spectral function $G(\xi)$ is uniquely defined as [30]

$$G(\xi) = \frac{1}{\pi}\lim_{\zeta\to 0^+} \int_0^{\xi} \operatorname{Re}\mathscr{P}(\zeta + \mathrm{j}k)\,\mathrm{d}k. \tag{4.2}$$

Using the low/high-frequency asymptotic expansions of $\mathscr{P}(\kappa)$ based on the representation (4.1) in the limit $\zeta \to 0^+$, and considering the even measure of $G(-\xi) = G(\xi)$, we can write the first integral identity as [9]

$$\frac{2}{\pi}\int_0^{\infty} \frac{\operatorname{Re}\mathscr{P}(\mathrm{j}k)}{k^2}\,\mathrm{d}k = a_1 - b_1, \tag{4.3}$$

where the low frequency asymptotic of $\mathscr{P}(\kappa)$ is $a_1\kappa + o(\kappa)$ and the high frequency asymptotic is $b_1\kappa + o(\kappa)$. Here, a_1 and b_1 are real valued and non-negative constants. Assuming that the positive real function $\mathscr{P}(\kappa)$ is sufficiently regular on the frequency axis $\kappa = \mathrm{j}k$, its imaginary part is given by

$$\operatorname{Im}\mathscr{P}(\mathrm{j}k) = b_1 k + \frac{1}{\pi}\int_{-\infty}^{\infty} \frac{k}{\xi^2 - k^2}\operatorname{Re}\mathscr{P}(\mathrm{j}\xi)\,\mathrm{d}\xi = b_1 k + \frac{1}{\pi}\int_{-\infty}^{\infty} \frac{1}{\xi - k}\operatorname{Re}\mathscr{P}(\mathrm{j}\xi)\,\mathrm{d}\xi, \tag{4.4}$$

where the integral is identified as the Hilbert transform. The second equality is known as the Plemelj formula [17], it should be noted that the imaginary part of $\mathscr{P}(\mathrm{j}k)$ is odd symmetric with $\operatorname{Im}\mathscr{P}(-\mathrm{j}k) = -\operatorname{Im}\mathscr{P}(\mathrm{j}k)$. The linear transform in (4.4) acts as a linear operator on the real response $\operatorname{Re}\mathscr{P}(\mathrm{j}k)$ to yield the imaginary part $\operatorname{Im}\mathscr{P}(\mathrm{j}k)$ of the passive system. This can be treated as a convex optimization problem with constraints on the unknown quantities $b_1 \geqslant 0$ and $\operatorname{Re}\mathscr{P}(\mathrm{j}k) \geqslant 0$. As a finite-dimensional approximation, the positive and symmetric measure $\operatorname{Re}\mathscr{P}(\mathrm{j}k)$ is modeled here by

$$\operatorname{Re}\mathscr{P}(\mathrm{j}k) = \sum_{n=0}^{N-1} x_n[p(k-(n+n_0)\Delta k) + p(k+(n+n_0)\Delta k)], \tag{4.5}$$

where x_n is a non-negative real valued variable, Δk is the frequency step, n_0 is an offset parameter, $p(k)$ is a triangular pulse-shape ($p(k) = 1-|k|/\Delta k$ for $|k| \leqslant \Delta k$ and 0 otherwise), and N is the number of pulses. By inserting the approximated $\operatorname{Re}\mathscr{P}(\mathrm{j}k)$ in (4.4) the imaginary part becomes

$$\operatorname{Im}\mathscr{P}(\mathrm{j}k) = b_1 k + \sum_{n=0}^{N-1} x_n[\tilde{p}(k-(n+n_0)\Delta k) + \tilde{p}(k+(n+n_0)\Delta k)], \tag{4.6}$$

where $\tilde{p}(k)$ is the Hilbert transform of the pulse shape $p(k)$ given by

$$\begin{aligned}\tilde{p}(k) &= \frac{1}{\pi}\int_{-\infty}^{\infty} \frac{1}{\xi - k} p(\xi)\,\mathrm{d}\xi \\ &= \frac{2k\ln|k| - (k-\Delta k)\ln|k-\Delta k| - (k+\Delta k)\ln|k+\Delta k|}{\pi\Delta k}\end{aligned} \tag{4.7}$$

with $\tilde{p}(\pm\Delta k) = \mp(2\ln 2)/\pi$ and $\tilde{p}(0) = 0$. By applying the finite-dimensional approximation the sum rule in (4.3) can be represented as

$$\frac{1}{\pi\Delta k}\sum_{n=0}^{N-1} x_n \ln\frac{(n+n_0)^2}{(n+n_0-1)(n+n_0+1)} = a_1 - b_1. \tag{4.8}$$

Considering the real and imaginary responses of $\mathscr{P}(\mathrm{j}k)$, and also the sum rule in (3.4), we define the convex optimization problem

$$\begin{aligned} &\text{minimize} && \left\|\mathscr{P}(\mathrm{j}k) - \mathscr{P}^{(\mathrm{M})}(\mathrm{j}k)\right\| \\ &\text{subject to} && \operatorname{Re}\mathscr{P}(\mathrm{j}k) \geqslant 0,\ k \in [k_0, k_3], \\ &&& \frac{2}{\pi}\int_{k_0}^{k_3} \frac{\operatorname{Re}\mathscr{P}(\mathrm{j}k)}{k^2}\,\mathrm{d}k \leqslant \gamma_{\mathrm{u}}, \end{aligned} \tag{4.9}$$

where $\mathscr{P}^{(\mathrm{M})}(\mathrm{j}k)$ is the measured forward scattering for $k \in [k_1, k_2]$ which is inside the modeling interval $k_0 < k_1 < k_2 < k_3$ and γ_{u} is an upper bound on the sum rule. The norm is defined as

$$\left\|\mathscr{P}(\mathrm{j}k) - \mathscr{P}^{(\mathrm{M})}(\mathrm{j}k)\right\|^2 = \int_{k_1}^{k_2} w(k)|\mathscr{P}(\mathrm{j}k) - \mathscr{P}^{(\mathrm{M})}(\mathrm{j}k)|^2\,\mathrm{d}k, \tag{4.10}$$

where $w(k)$ is a positive weighting function.

Consider the measurement model as $\mathscr{P}(\mathrm{j}k) = f(k)+g(k)n(k)$, where $f(k)$ and $g(k)$ are given, and $n(k)$ is uncorrelated complex Gaussian noise with variance σ_n^2. Hence, the variance of the uncorrelated measurement noise is $|g(k)|^2\sigma_n^2$ and the proper weighting function in a Maximum Likelihood estimation [12] is $w(k) = |g(k)|^{-2}$, and particularly, in the methodology of this paper we find that

$$w(k) = |g(k)|^{-2} = \frac{k|S_{21,\mathrm{emp}}|^2}{4\pi d}, \tag{4.11}$$

where $S_{21,\mathrm{emp}}$ is the scattering parameter for the empty setup (see Section 5.1 for more details).

5 Experimental Methodology

The methodology used to illustrate the sum rule is presented in this section. A parallel plate waveguide is used to investigate the dynamic properties, and a parallel plate capacitor is used to determine the static properties of an object.

5.1 Parallel plate waveguide

A parallel plate waveguide is used to test the scattering properties of different objects. Two in-house fabricated wide-band TEM horn antennas are placed inside the waveguide and are fed via the lower plate as shown in Fig. 4. The object is located in the middle of the waveguide and the antennas are separated by a distance of 0.98 m.

The TEM horn antennas are supported by a piece of Rohacell material with relative permittivity, $\epsilon_\mathrm{r} \approx 1$. Microwave flat absorbers are placed around the waveguide to reduce the internal reflections and external interferences. The separation between two plates is 21.3 mm, which gives the first higher order mode at $f \approx 7\,\mathrm{GHz}$.

In order to measure the forward scattering, the scattered field, $\boldsymbol{E}_\mathrm{s}$, is determined from the difference between the fields in the presence and the absence of the object. We consider a plane wave incidence, $\boldsymbol{E}_\mathrm{i}(\boldsymbol{r}) = \hat{\boldsymbol{z}}E_0\mathrm{e}^{-\mathrm{j}k_\mathrm{x}x}$, to an object confined between the plates. The co-polarized scattered field in the far-field region can be expressed as

$$\hat{\boldsymbol{z}}\cdot\boldsymbol{E}_\mathrm{s} \sim f_\mathrm{s}\sqrt{\frac{2}{\pi\mathrm{j}k\rho}}\mathrm{e}^{-\mathrm{j}k\rho}. \tag{5.1}$$

The distance between two antennas is denoted by d and the separation between the object and the transmitting antenna is d_1. The scattered field received by the antenna in the absence of the object is

$$E_{r,0} = f_0\sqrt{\frac{2}{\pi\mathrm{j}kd}}\mathrm{e}^{-\mathrm{j}kd}, \tag{5.2}$$

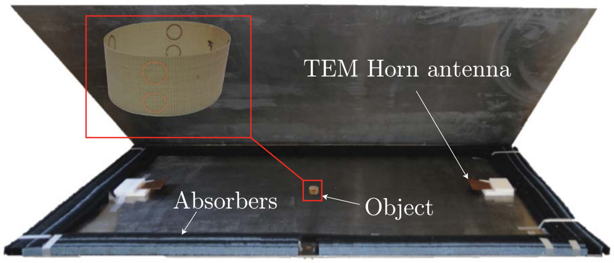

Figure 4: The parallel plate waveguide setup consists of two TEM horn antennas and microwave flat absorbers. The distance between the antennas is 98 cm and the object is placed at the midpoint between the antennas. The two plates are $150 \times 100\,\mathrm{cm}^2$ and separated by 21.3 mm.

where f_0 is the far-field amplitude generated by the transmitting antenna. The object is assumed to be in the far-field of the antenna and thus the far-field amplitude at the object is also f_0.

The incident field on the object is given by

$$E_0 = f_0\sqrt{\frac{2}{\pi \mathrm{j}kd_1}}\mathrm{e}^{-\mathrm{j}kd_1}. \tag{5.3}$$

This electric field induces currents on the object and the object scatters. The resulting electric field on the receiving antenna in the presence of the object is denoted by $E_{\mathrm{r,s}}$ and thus the scattered field of the object itself can be written as $E_{\mathrm{s}} = E_{\mathrm{r,s}} - E_{\mathrm{r,0}}$. According to (2.9), the positive real function is defined as

$$\mathscr{P}_b(\mathrm{j}k) = \frac{-4f_{\mathrm{s}}}{\mathrm{j}kE_0} = \frac{4}{\mathrm{j}k}\left(1 - \frac{E_{r,s}}{E_{r,0}}\right)\sqrt{\frac{\pi \mathrm{j}kd_1(d-d_1)}{2d}}, \tag{5.4}$$

where $\mathscr{P}_b$ denotes the PR defined in (3.1) normalized with the height of the waveguide, *i.e.*, $\mathscr{P}_b = \mathscr{P}/b$, and this can be approximated by:

$$\mathscr{P}_b(\mathrm{j}k) = \frac{-4f_{\mathrm{s}}}{\mathrm{j}kE_0} = \frac{4}{\mathrm{j}k}\left(1 - \frac{S_{21,\mathrm{obj}}}{S_{21,\mathrm{emp}}}\right)\sqrt{\frac{\pi \mathrm{j}kd_1(d-d_1)}{2d}}, \tag{5.5}$$

where $S_{21,\mathrm{obj}}$ is the ratio between the out-coming wave at the port of the receiving antenna and the incident wave at the port of the transmitting antenna in the presence of the object. For the periodic structures discussed in 2.1, we use the top equation in (3.1) to find the forward scattering, $\mathscr{P}$, where the transmission coefficient is defined as $T = S_{21,\mathrm{obj}}/S_{21,\mathrm{emp}}$. The S-parameters are extracted using an HP 8720 Vector Network Analyzer.

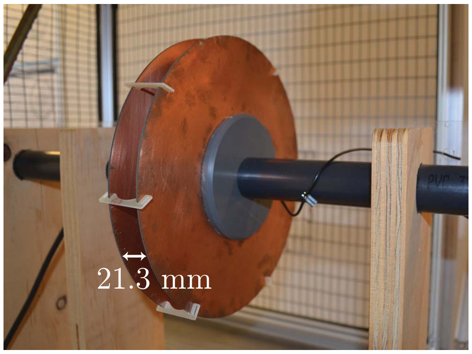

Figure 5: The parallel plate capacitor setup consists of two circular copper plates held by plastic arms. The distance between the plates is 21.3 mm and is fixed by plastic distance supports.

5.2 Parallel plate capacitor

A parallel plate capacitor is used to determine the polarizability (see Fig. 5). The capacitor consists of two circular shaped copper sheets that each of them is printed on an FR4 substrate with relative dielectric constant, $\epsilon_{\mathrm{r}} \approx 4.4$. A Faraday cage, and a ground plane, are used to mitigate interference and current flows between different grounds in the system. An Agilent 4294A Precision Impedance Analyzer is used to measure the capacitance at $f = 1\,\mathrm{MHz}$.

The relation between the capacitance change and the polarizability of a bounded object inside the parallel plate capacitor is given by [13]

$$\gamma_{\mathrm{e}} = \hat{\boldsymbol{z}} \cdot \boldsymbol{\gamma}_{\mathrm{e}} \cdot \hat{\boldsymbol{z}} = \frac{\Delta C d^2}{\epsilon_0}, \tag{5.6}$$

where $\Delta C = C_{\mathrm{obj}} - C_{\mathrm{emp}}$ is the difference between the capacitance in presence, C_{obj}, and the absence, C_{emp}, of the object, d is the separation between the two plates and ϵ_0 is the vacuum permittivity. For each sample the measurement was repeated 10 times to mitigate the possible positioning and distance errors. As seen in Fig. 5, six plastic distance precisions are placed on the edges of the plates to keep the distance constant in different measurements. The separation distance, $d = 21.3\,\mathrm{mm}$, is the same as the height of the parallel plate waveguide and the objects (more details in Section 6).

6 Experimental results

In this section, two different scattering objects are considered to illustrate the forward scattering sum rule. In each case, the static measurement of the object inside the parallel plate capacitor (Fig. 5) is illustrated. The static polarizability is determined by the variations of the capacitance between the absence and the presence of the object placed in the middle of the plates. Then the dynamic measurement in the parallel plate waveguide (Fig. 4) is shown and is used to estimate the left hand side of the sum rule (3.4). The dynamic measurements are wide band and hence affected by the noise in the system, and the quasi-static measurements are very sensitive to the placement and the distance between the plates. Using the obtained values from measurements, and in order to estimate an all-spectrum representation of the forward scattering we apply a convex optimization method in each example using passivity and sum rule constraints.

6.1 Cylindrical SRR

A cylinder of split ring resonators (SRR) composed of 16 SRRs etched in $18\,\mu$m copper and supported by a $21 \times 160\,\mathrm{mm}^2$ and $127\,\mu$m thick Arlon Diclad880 with relative permittivity, $\epsilon_\mathrm{r} = 2.17$, is used. The C-shaped unit element has the outer diameter $\ell = 8\,\mathrm{mm}$, the strip width $t = 0.5\,\mathrm{mm}$, and the gap distance $g = 0.7\,\mathrm{mm}$. The unit element is designed to be resonant at 5.5 GHz.

The parallel plate capacitor in Fig. 5 is used to measure the static polarizability of the object. The polarizability is estimated by the changes in the capacitance (5.6) and the resulting value averaged over 10 measurements with standard deviation $0.04\,\mathrm{cm}^3$, is estimated to $\gamma_\mathrm{e} = 3.65\,\mathrm{cm}^3$. This value obtained from a quasi-static measurement is an upper bound on the total cross section integrated over the entire spectrum on the left hand side of the sum rule in (3.4).

In order to investigate the dynamic properties of this sample, the forward scattering, $\mathscr{P}_b$ in (5.5), of this object is measured inside the parallel plate waveguide over the frequency range $[2-20]\,\mathrm{GHz}$ with 1601 frequency points. Solid lines in Fig. 6 show the measured values averaged over 10 measurements to reduce the noise level, whereas the error level is illustrated with bars. Averaging has the advantage of reducing the unwanted measurement errors especially at low frequencies, which have the highest impact on determining the low frequency limit on the right hand side of the sum rule (3.4). Except for the frequencies below 3 GHz, the set-up is considered to be stable over different measurements and as seen from Fig. 6 the experimental errors are small. The real part of the forward scattering denotes the object's total (or extinction) cross section, σ_tot. As is shown in the figure, the total cross section is very large compared to the size of the object at the resonance frequency ($\sigma_\mathrm{tot}/b \approx 15\,\mathrm{cm}$) and smaller at lower and higher frequencies. The total cross section per unit length of a perfectly conducting cylinder with the same diameter as this object is 12.5 cm. This shows the blocking effect of the split ring resonators at the resonance frequency. Using the measured values of σ_tot, the integral on the left hand side of the sum rule (3.4) is estimated to $2.75\,\mathrm{cm}^3$. This value is a lower bound on the polarizability since the integration on the left hand side of (3.4) is over a finite range of frequencies instead of the entire spectrum.

Convex optimization in (5.5) is used to compute an all-spectrum representation of the measured values by identifying the passive system and estimating an optimal lower bound on the polarizability according to Section 4. The dashed curves in Fig. 6 show the real and the imaginary part of the forward scattering predicted by the convex optimization problem. The number of triangles in (4.5) is set to $N = 996$. Since the imaginary part approaches $f = 0\,\mathrm{Hz}$ linearly, it can be used to estimate the low frequency limit in (3.2) accurately. The best fitting to the forward scattering that has the passivity constraint is achieved by the first constraint in the optimization problem (5.5). The passivity constraint reduces the fluctuations at frequencies where $\mathrm{Re}\,\mathscr{P} < 0$, however, to add an effective filtering over the entire bandwidth the sum rule constraint with an upper bound γ_u is added.

The right and the left hand sides of (3.4) are estimated using the parallel plate capacitor to $\gamma_\mathrm{e} = 3.65\,\mathrm{cm}^3$ and the parallel plate waveguide to $2.75\,\mathrm{cm}^3$, respectively. The region shown as measurement region in Fig. 7 is used as a subset of the possible polarizabilities. In Fig. 7 the γ_u is swept over a wider range of possible solutions. When minimizing the norm in (5.5) over the range of γ_u (Pareto Search method [19]), the minimum least square in (4.10) becomes constant when the second constraint in (5.5) involving the upper bound on sum rule is inactive.

By increasing the γ_u the value of the low frequency asymptotic (3.2) as well as the integral (3.4) of the optimal solution remains constant ($3.52\,\mathrm{cm}^3$ in this case) which is determined only by the passivity constraint. Decreasing the γ_u has an advantage of filtering the spurious resonances but at the same time losing the fitting to the measured values. The transition region in Fig. 7 is the best interval to choose the γ_u. In this case γ_u is chosen to be $3.4\,\mathrm{cm}^3$ to reduce the noise and at the same time achieve the best fitting for $\mathscr{P}_b$. The input to the optimization problem is in the frequency rage of the measurements, *i.e.*, $[2, 20]$ GHz while the modeling interval extends to $f \approx [0, 21]$ GHz. The optimization has the advantage of neglecting negative parts as σ_tot cannot be less than zero.

Using the optimization solution, the value of the linear slope of the curve is estimated to $\mathscr{P}(\mathrm{j}k)/\mathrm{j}k = 3.4\,\mathrm{cm}^3$ as $k \to 0$ which is in good agreement with the polarizability found from the capacitor $3.65\,\mathrm{cm}^3$. Since the measured capacitance in the capacitor is in the order of picofarads, the difference can stem from small errors in the measurement set-up. The value of the integral (3.4) from 0 to 20 GHz is $2.87\,\mathrm{cm}^3$ which gives 84% of the optimal lower bound ($\gamma_\mathrm{e}^\mathrm{olb} = 3.4\,\mathrm{cm}^3$). The optimal lower bound corresponds to the lowest possible polarizability that is found from measurements. The actual value of the polarizability can be greater than this lower bound. It should be noted that more examples of the forward scattering sum rule for bounded and double resonance structures are discussed in [27].

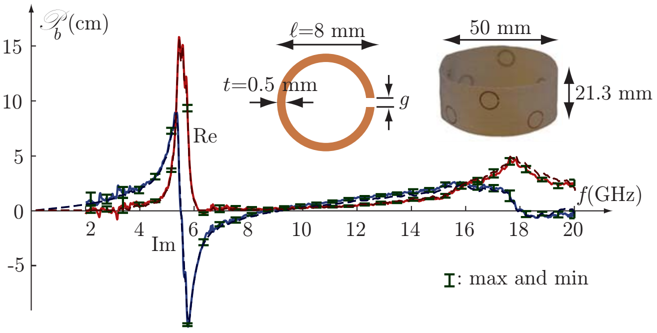

Figure 6: Average of the 10 measurements (solid curves) and the optimal solution (dashed curves) for the forward scattering for an array of circular split rings. Maximum and minimum values over the 10 measurements are illustrated by the bars.

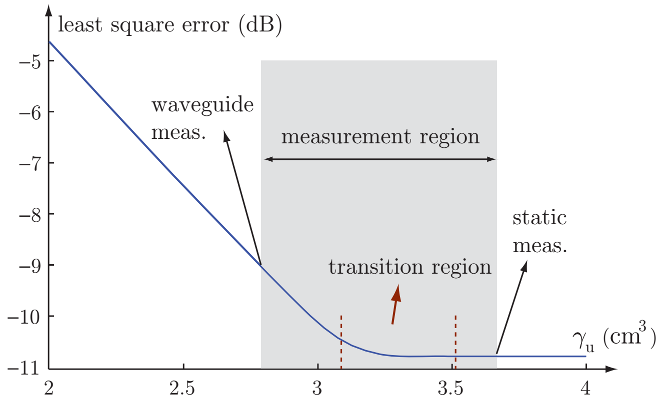

Figure 7: Optimal value of $\left\|\mathscr{P}(\mathrm{j}k)-\mathscr{P}^{(\mathrm{M})}(\mathrm{j}k)\right\|$ (in dB) as a function of the sum rule constraint over the range $\gamma_\mathrm{u}=[2,4]\,\mathrm{cm}^3$. The smallest range for search has to be in a region that is obtained from measurements in the quasi-static (right hand side of sum rule) as well as the waveguide measurement (left hand side of sum rule).

6.2 Planar periodic structure

In order to show the optical theorem for periodic structures discussed in 2.1, we consider a planar periodic structure consisting of 42 in-house fabricated split ring resonators with 2 cm spacing, that are resonant at $f = 9\,\mathrm{GHz}$, attached to a Styrofoam slab as shown in Fig. 8. Using the parallel plate capacitor, the static polarizability is measured over 11, 4, and 2 unit cells separately. All the measured values provide similar results for the polarizability of a unit cell, *i.e.*, $\gamma_{\mathrm{e}} = 0.196 \pm 0.001\,\mathrm{cm}^3$. The solid lines in Fig. 8 show the measured forward scattering of the periodic structure using the expression (2.4). The total cross section has its highest value at the resonance frequency and close to zero over the rest of the frequency band. This is mainly due to the calibration that removes the effect of the Styrofoam. The left hand side of the sum rule (3.4), by integrating the measured σ_{tot}, is estimated to $0.111\,\mathrm{cm}^3$. This value gives a lower bound on the static polarizability that predicts the all spectrum dynamic properties of the object.

In order to improve the estimate of the polarizability the convex optimization (5.5) is applied for this object in the same way as in the previous example. The dashed lines in Fig. 8 are the optimal solution from the convex optimization problem. Choosing an appropriate upper bound on the polarizability, *i.e.*, $\gamma_{\mathrm{u}} = 0.211\,\mathrm{cm}^3$, in (5.5), that is found in the same manner as explained in Section 6.1, the static polarizability per unit cell is estimated to $\mathscr{P}(\mathrm{j}k)/\mathrm{j}k = 0.208\,\mathrm{cm}^3$ as $k \to 0$, which is close to the value assigned to the upper bound of the optimization. The value obtained from the capacitor ($0.196\,\mathrm{cm}^3$) is less than the low frequency asymptotic determined by the convex optimization, however the difference is negligible and can be due to the errors in the waveguide measurement. The left hand side of the sum rule (3.4), by integrating the optimal solution for the forward scattering, is estimated to $0.158\,\mathrm{cm}^3$. This value is 75% of the optimal lower bound on polarizability, $\gamma_{\mathrm{e}}^{\mathrm{olb}} = 0.211\,\mathrm{cm}^3$. The left hand side of (3.4) gives a higher value for the modeled data which is due to the fact that the negative parts of the spurious resonances are ignored by the optimal solution, and in addition to this, the integration is over a wider range of values. The agreement between the measurements and the optimal solution is not as good as the lower frequencies. The reason can be first, the existence of the higher order modes and second, the plane wave approximations lose validity, *i.e.*, the incident field excites the currents on the unit cells with a phase difference which is more significant at higher frequencies. However, the forward scattering in (3.4) is weighted by the frequency square and the inaccuracies at higher frequencies are reduced significantly in the integration.

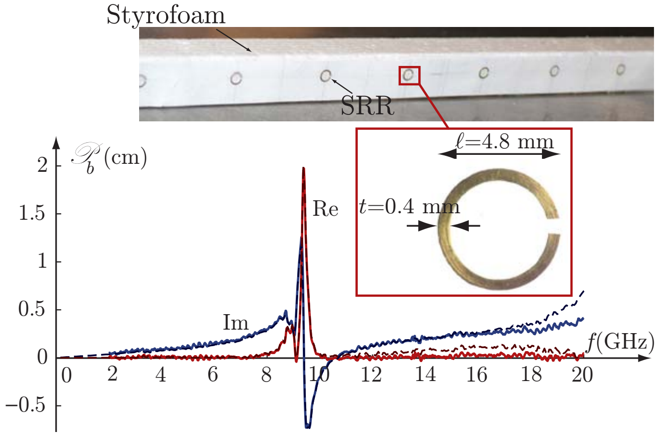

Figure 8: Measured values (solid curves) and the optimal solution (dashed curves) for the forward scattering of an in-house fabricated planar periodic structure of split ring resonators with 20 mm spacing between each two elements.

7 Conclusions

In this paper, a sum rule for parallel plate waveguides is investigated. We have demonstrated that the total interaction between the electromagnetic field and a scatterer, integrated over all frequencies, is bounded by the static polarizability of the object. We show that the optical theorem inside the waveguide is solely related to the zeroth order propagating mode and therefore the problem can be treated as a 2D scattering problem. A parallel plate capacitor has been used to find the static polarizability and a parallel plate waveguide to determine the total cross section and estimate a lower bound on the polarizability of various resonant scattering objects. The accuracy of the measurements is improved by applying a convex optimization problem to identify the passive system. The optimization solution gives an entire spectrum representation of the forward scattering as well as an optimal lower bound on the static polarizability. The left hand side of the sum rule from dynamic measurements is on the average about 80% of the polarizability in the right hand side measured in the parallel plate capacitor.

References

[1] A. Bernland, A. Luger, and M. Gustafsson. Sum rules and constraints on passive systems. *J. Phys. A: Math. Theor.*, **44**(14), 145205, 2011.

[2] S. P. Boyd and L. Vandenberghe. *Convex Optimization.* Cambridge Univ Pr, 2004.

[3] F. Capolino, editor. *Theory and Phenomena of Metamaterials.* CRC Press, 2009.

[4] M. Gustafsson. Time-domain approach to the forward scattering sum rule. *Proc. R. Soc. A*, **466**, 3579–3592, 2010.

[5] M. Gustafsson, M. Cismasu, and S. Nordebo. Absorption efficiency and physical bounds on antennas. *International Journal of Antennas and Propagation*, **2010**(Article ID 946746), 1–7, 2010.

[6] M. Gustafsson, C. Sohl, and G. Kristensson. Physical limitations on antennas of arbitrary shape. *Proc. R. Soc. A*, **463**, 2589–2607, 2007.

[7] M. Gustafsson, C. Sohl, and G. Kristensson. Illustrations of new physical bounds on linearly polarized antennas. *IEEE Trans. Antennas Propagat.*, **57**(5), 1319–1327, May 2009.

[8] M. Gustafsson. Sum rule for the transmission cross section of apertures in thin opaque screens. *Opt. Lett.*, **34**(13), 2003–2005, 2009.

[9] M. Gustafsson and D. Sjöberg. Physical bounds and sum rules for high-impedance surfaces. *IEEE Trans. Antennas Propagat.*, **59**(6), 2196–2204, 2011.

[10] M. Gustafsson, I. Vakili, S. E. B. Keskin, D. Sjöberg, and C. Larsson. Optical theorem and forward scattering sum rule for periodic structures. *IEEE Trans. Antennas Propagat.*, **60**(8), 3818–3826, 2012.

[11] J. D. Jackson. *Classical Electrodynamics.* John Wiley & Sons, New York, third edition, 1999.

[12] S. M. Kay. *Fundamentals of Statistical Signal Processing, Estimation Theory.* Prentice-Hall, Inc., NJ, 1993.

[13] G. Kristensson. The polarizability and the capacitance change of a bounded object in a parallel plate capacitor. *Physica Scripta*, **86**(3), 035405, 2012.

[14] N. Marcuvitz. *Waveguide Handbook.* McGraw-Hill, New York, 1951.

[15] B. Munk. *Frequency Selective Surfaces: Theory and Design.* John Wiley & Sons, New York, 2000.

[16] R. Newton. Optical theorem and beyond. *Am. J. Phys*, **44**, 639–642, 1976.

[17] H. M. Nussenzveig. *Causality and dispersion relations.* Academic Press, London, 1972.

[18] E. M. Purcell. On the absorption and emission of light by interstellar grains. *J. Astrophys.*, **158**, 433–440, 1969.

[19] H. Sawaragi, Y. Nakayama and T. Tanino. *Theory of Multiobjective Optimization.* Elsevier Science & Technology Books, 1985.

[20] D. Sjöberg. Low frequency scattering by passive periodic structures for oblique incidence: low pass case. *J. Phys. A: Math. Theor.*, **42**, 385402, 2009.

[21] D. R. Smith, S. Schultz, P. Markos, and C. M. Soukoulis. Determination of effective permittivity and permeability of metamaterials from reflection and transmission coefficients. *Phys. Rev. B*, **65**, 195104–195108, 2002.

[22] C. Sohl and M. Gustafsson. A priori estimates on the partial realized gain of Ultra-Wideband (UWB) antennas. *Quart. J. Mech. Appl. Math.*, **61**(3), 415–430, 2008.

[23] C. Sohl, M. Gustafsson, and G. Kristensson. Physical limitations on broadband scattering by heterogeneous obstacles. *J. Phys. A: Math. Theor.*, **40**, 11165–11182, 2007.

[24] C. Sohl, C. Larsson, M. Gustafsson, and G. Kristensson. A scattering and absorption identity for metamaterials: experimental results and comparison with theory. *J. Appl. Phys.*, **103**(5), 054906, 2008.

[25] J. W. Strutt. On the light from the sky, its polarization and colour. *Phil. Mag.*, **41**, 107–120 and 274–279, April 1871. Also published in Lord Rayleigh, Scientific Papers, volume I, Cambridge University Press, Cambridge, 1899.

[26] I. Vakili, M. Gustafsson, and D. Sjöberg. Forward scattering properties of periodic metamaterials. In *Antennas and Propagation (EUCAP), 2012 6th European Conference on*, pages 2680–2682. IEEE, 2012.

[27] I. Vakili, M. Gustafsson, D. Sjöberg, R. Seviour, M. Nilsson, and S. Nordebo. Sum rules for parallel plate waveguides: Experimental results and theory. Technical Report LUTEDX/(TEAT-7229)/1–20/(2014), Lund University, Department of Electrical and Information Technology, P.O. Box 118, S-221 00 Lund, Sweden, 2014. http://lup.lub.lu.se.

[28] J. van Bladel. *Electromagnetic Fields.* Hemisphere Publication Corporation, New York, 1986. Revised Printing.

[29] F. Yang and Y. Rahmat-Samii. *Electromagnetic band gap structures in antenna engineering.* Cambridge University Press, 2009.

[30] A. H. Zemanian. *Distribution theory and transform analysis: an introduction to generalized functions, with applications.* McGraw-Hill, New York, 1965.

Optical theorem and forward scattering sum rule for periodic structures

Mats Gustafsson, Iman Vakili, Daniel Sjöberg

Paper V

Published as: M. Gustafsson, I. Vakili, D. Sjöberg, Optical theorem and forward scattering sum rule for periodic structures, *IEEE Transactions on Antennas and Propagation*, Vol. 60, No. 8, pp. 3818-3826, 2012

Abstract

Based on energy conservation, an optical theorem is constructed for a slab having an arbitrary periodic microstructure in a plane. A sum rule for low pass structures is derived using analytic properties of Herglotz functions based on causality and passivity. The sum rule relates the extinction cross section to the static polarizability per unit cell, and quantifies the interaction between the slab and electromagnetic fields possible over all wavelengths. The results are illustrated with several numerical and experimental examples.

1 Introduction

The optical theorem relates the forward scattering from an object to the extinction (or total) cross section [22]. It was first discussed more than a century ago by Rayleigh [36] and later extended to quantum mechanics, acoustics, and elastodynamics. There are also formulations of the optical theorem for inhomogeneous backgrounds [19, 20], waveguides [24], corrugated surfaces [39], and in the time domain [16]. The corresponding forward scattering sum rule shows that the extinction cross section integrated over all wavelengths is proportional to the polarizability of the object. It was introduced for dielectric spheroids by Purcell [27] and generalized to arbitrary objects in [6, 34].

The forward scattering sum rule shows that the all-spectrum interaction between the electromagnetic field and an object is proportional to the (static) polarizability of the object. This identity is useful since the solution of a relatively simple static problem provides physical insight in the dynamic scattering over a bandwidth. It also gives physical limitations on the extinction cross section bandwidth product expressed in the polarizability of the object. The sum rule has recently been used to derive an antenna identity and several physical bounds on antennas [7–9, 33]. It has also been used to show bounds on metamaterial scatterers [35] and extraordinary transmission [10].

In this paper, the optical theorem and the forward scattering sum rule are generalized to periodic structures. This version of the optical theorem shows that the extincted power from an incident plane wave is proportional to $\operatorname{Im} h(k)$, where $h(k) = \mathrm{i}2(1-T(k))A$ is a Herglotz function [1], A denotes the cross section area of the unit cell and T the co-polarized part of the lowest order transmission coefficient. The low-frequency asymptotic expansion of $h(k)$ is used to derive the forward scattering sum rule according to the general procedure in [1]. The derivation is solely based on the assumptions that the periodic structure does not support global currents in the low-frequency limit and that the micro structure is made of linear, passive, and time-translational invariant materials.

Moreover, we show that the forward scattering sum rule for isolated objects is retrieved by extending the unit cell length to infinity. An intermediate forward scattering sum rule for two dimensional objects and objects that are periodic in one dimension by letting the unit cell increase in one direction is also derived. The

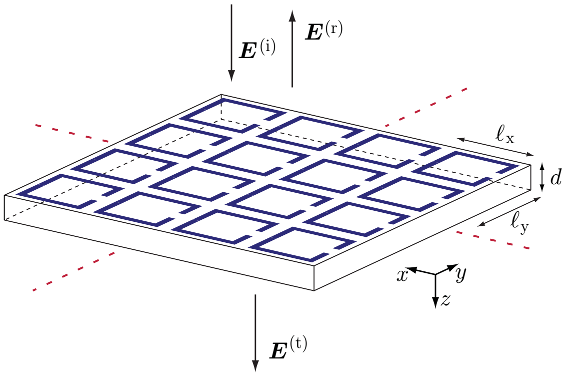

Figure 1: Illustration of a screen with a periodic microstructure. The incident, reflected, and transmitted electric fields are denoted by $\boldsymbol{E}^{(\mathrm{i})}$, $\boldsymbol{E}^{(\mathrm{r})}$, and $\boldsymbol{E}^{(\mathrm{t})}$, respectively. The lattice lengths in the xy-plane are denoted by ℓ_{x} and ℓ_{y}, and d is the thickness of the supporting dielectric substrate. The entire structure is assumed to be in the half space $z \leqslant 0$.

theoretical results are illustrated by numerical simulations and measurements for the scattering of a periodic sheet of split ring resonators (SRR) in free space and for a cylinder of SRRs in a parallel plate waveguide.

The new sum rule is instrumental in the understanding of interaction between electromagnetic field and periodic structures with applications for frequency selective surfaces [21], electromagnetic band gap structures [40], and metamaterials [3, 32]. It also provides new insight about the forward scattering sum rule for finite scatterers [6, 34] and its associated antenna identity [8, 9].

This paper is organized as follows. The optical theorem for periodic structures is presented in Sec. 2. A Herglotz function and its high and low-frequency asymptotic expansions are presented in Sec. 3. The forward scattering sum rule is derived in Sec. 4. In Sec. 5, we present numerical and experimental verifications of the sum rule. The paper is concluded in Sec. 6.

2 Optical theorem for periodic structures

We consider a planar periodic structure in otherwise free space. The material and microstructure are modeled with arbitrary linear and temporally dispersive constitutive relations, restricted to causal and passive dispersion models such as, *e.g.*, the Debye, Lorentz, and Drude models [14]. The array is also assumed to not support currents in the low-frequency limit and be sufficiently large to be modeled as an infinite array [12]. This is, *e.g.*, the case for arrays with disjoint metallic inclusions printed on a bulk material with negligible static conductivity.

The array lattice is described by two basis vectors $\ell_{\mathrm{x}}\hat{\boldsymbol{x}}$ and $\ell_{\mathrm{y}}\hat{\boldsymbol{y}}$, and the entire heterogeneous structure is contained in the interval $-d \leqslant z \leqslant 0$, with a unit cell lying in the xy-plane, see Fig. 1. Consider a time harmonic linearly polarized plane wave impinging at normal incidence on the array, *i.e.*, $\boldsymbol{E}^{(\mathrm{i})}(\boldsymbol{r}) = \boldsymbol{E}_0\mathrm{e}^{\mathrm{i}kz}$, where $\boldsymbol{E}_0 = E_0\hat{\boldsymbol{e}}$, $\hat{\boldsymbol{e}}$ is a real valued unit vector along the polarization direction of the incident field, $\boldsymbol{r} = x\hat{\boldsymbol{x}} + y\hat{\boldsymbol{y}} + z\hat{\boldsymbol{z}} = \boldsymbol{\rho} + z\hat{\boldsymbol{z}}$ is the position vector, k denotes the wavenumber, and time convention $\mathrm{e}^{-\mathrm{i}\omega t}$ is used.

A spectral decomposition of the transmitted field, $\boldsymbol{E}^{(\mathrm{t})}$, in Floquet modes is used outside the array

$$\boldsymbol{E}^{(\mathrm{t})}(k;\boldsymbol{r}) = \sum_{m=-\infty}^{\infty}\sum_{n=-\infty}^{\infty} \boldsymbol{E}_{mn}^{(\mathrm{t})}(k)\mathrm{e}^{\mathrm{i}\boldsymbol{k}_{mn}\cdot\boldsymbol{\rho}}\mathrm{e}^{\mathrm{i}k_{z,mn}z}, \tag{2.1}$$

for $z \geqslant 0$, where $\boldsymbol{k}_{mn} = m2\pi/\ell_{\mathrm{x}}\hat{\boldsymbol{x}} + n2\pi/\ell_{\mathrm{y}}\hat{\boldsymbol{y}}$, and $k_{z,mn} = \sqrt{k^2 - |\boldsymbol{k}_{mn}|^2}$ is the wavenumber in the z direction for the mn mode. For m or n large enough, $k_{z,mn}$ is an imaginary number indicating an evanescent wave. The expansion coefficients are expressed in the electric field behind the structure as

$$\boldsymbol{E}_{mn}^{(\mathrm{t})}(k) = \frac{1}{\ell_{\mathrm{x}}\ell_{\mathrm{y}}}\int_{-\ell_{\mathrm{y}}/2}^{\ell_{\mathrm{y}}/2}\int_{-\ell_{\mathrm{x}}/2}^{\ell_{\mathrm{x}}/2} \boldsymbol{E}^{(\mathrm{t})}(k;x,y,0)\mathrm{e}^{-\mathrm{i}\boldsymbol{k}_{mn}\cdot\boldsymbol{\rho}}\,\mathrm{d}x\,\mathrm{d}y. \tag{2.2}$$

The reflected field, $\boldsymbol{E}^{(\mathrm{r})}(k;\boldsymbol{r})$, is similarly expanded in the region $z \leqslant -d$. The expansion coefficients of the transmitted and reflected fields are related to the incident field via the linear mappings $\boldsymbol{E}_{mn}^{(\mathrm{t})} = \mathbf{T}_{mn}\cdot\boldsymbol{E}_0$ and $\boldsymbol{E}_{mn}^{(\mathrm{r})} = \mathbf{R}_{mn}\cdot\boldsymbol{E}_0$. It is only a finite number of modes that propagate for a fixed frequency, and, specifically, it is only the zeroth order modes ($m = n = 0$) that propagate for frequencies below the first grating lobe [21], *i.e.*, $f < \mathrm{c}_0/\max\{\ell_{\mathrm{x}},\ell_{\mathrm{y}}\}$. In the following we use the short-hand notation $T = \hat{\boldsymbol{e}}\cdot\mathbf{T}_{00}\cdot\hat{\boldsymbol{e}}$ for the co-polarized transmission coefficient T.

We use energy conservation to show an optical theorem for periodic structures, see also [24]. The incident power per unit cell is $P_{\mathrm{i}} = A|E_0|^2/(2\eta_0)$, where $A = \ell_{\mathrm{x}}\ell_{\mathrm{y}}$ is the cross section area of the unit cell. The reflected power, P_{r}, can be written as a square sum of the expansion coefficients. The corresponding transmitted power, $P_{\mathrm{t}} = |T|^2P_{\mathrm{i}} + P_{\mathrm{t1}}$, is decomposed into the contributions from the co-polarized part of the lowest order mode, $|T|^2P_{\mathrm{i}}$, and from the remaining modes, P_{t1}. The absorbed power, P_{a}, is the difference between the incident and the sum of the reflected and transmitted powers, *i.e.*,

$$P_{\mathrm{a}} = P_{\mathrm{i}} - P_{\mathrm{r}} - P_{\mathrm{t}} = P_{\mathrm{i}} - P_{\mathrm{r}} - |T|^2P_{\mathrm{i}} - P_{\mathrm{t1}}. \tag{2.3}$$

The scattered power, P_{s}, is the sum of the reflected power, P_{r}, and the power in the scattered part of the transmitted field. This scattered power consists of the power in the co-polarized forward scattered field, i.e. the difference between the total field and the incident field, $|1-T|^2P_{\mathrm{i}}$, and transmitted power in the remaining modes, P_{t1}, *i.e.*,

$$P_{\mathrm{s}} = P_{\mathrm{r}} + |1-T|^2P_{\mathrm{i}} + P_{\mathrm{t1}}. \tag{2.4}$$

The extincted power is finally the sum of the absorbed and scattered powers

$$P_{\mathrm{ext}} = P_{\mathrm{a}} + P_{\mathrm{s}} = P_{\mathrm{i}} - P_{\mathrm{r}} - |T|^2 P_{\mathrm{i}} - P_{\mathrm{t1}} + P_{\mathrm{r}} + |1-T|^2 P_{\mathrm{i}} + P_{\mathrm{t1}} \\ = 2\,\mathrm{Re}\{1-T\} P_{\mathrm{i}} \quad (2.5)$$

that after normalization with the incident power flux, $|E_0|^2/(2\eta_0)$, gives the extinction cross section

$$\sigma_{\mathrm{ext}} = \sigma_{\mathrm{a}} + \sigma_{\mathrm{s}} = 2\,\mathrm{Re}\{1-T\} A. \quad (2.6)$$

This is the optical theorem for the periodic structure. The derivation is based only on energy conservation and the use of a power orthogonal mode decomposition outside the structure, where one mode is singled out and considered fundamental. This calls for two remarks: 1) Since nothing in the derivation changes if we choose an arbitrary Floquet mode $\boldsymbol{E}_{mn}$ instead of $\boldsymbol{E}_{00}$, the optical theorem (2.6) is valid for any Floquet mode. 2) The optical theorem is valid for any structure where a similar mode decomposition can be made, for instance in a waveguiding system.

3 Low- and high-frequency expansions

We use causality and passivity of $T(k)$ to define a Herglotz function that is used to construct sum rules. The transmission coefficient $T(k)$ is holomorphic in k for $\mathrm{Im}\, k > 0$ due to causality, and bounded in magnitude by unity due to passivity, *i.e.*, $|T| \leqslant 1$. The logarithm [4,12,28], the Cayley transform [5] and many other combinations of T can be used to construct Herglotz functions [1,11]. Here, we follow the extinction cross section (2.6) and use

$$h(k) = \mathrm{i}2\big(1 - T(k)\big)A \quad (3.1)$$

This is a Herglotz function [1,25], *i.e.*, $h(k)$ is holomorphic and $\mathrm{Im}\{h(k)\} \geqslant 0$ for $\mathrm{Im}\, k > 0$.

It is illustrative to use the mode expansion (2.1) and (2.2) in the free space $z \geqslant 0$ and express $h(k)$ in the electromagnetic fields. The expansion coefficients (2.2) simplify for the transmission coefficient, which is given by the average of the electric field behind the structure. This gives the explicit expression

$$h(k) = \mathrm{i}2\left(1 - \frac{\hat{\boldsymbol{e}} \cdot \boldsymbol{E}_{00}^{(\mathrm{t})}(k)}{E_0}\right)\ell_{\mathrm{x}}\ell_{\mathrm{y}} = \frac{-2\mathrm{i}}{E_0}\int_{-\ell_{\mathrm{y}}/2}^{\ell_{\mathrm{y}}/2}\int_{-\ell_{\mathrm{x}}/2}^{\ell_{\mathrm{x}}/2} \hat{\boldsymbol{e}} \cdot \boldsymbol{E}^{(\mathrm{s})}(k;x,y,0)\,\mathrm{d}x\,\mathrm{d}y \\ = \frac{-\mathrm{i}}{E_0}\int_{-\ell_{\mathrm{y}}/2}^{\ell_{\mathrm{y}}/2}\int_{-\ell_{\mathrm{x}}/2}^{\ell_{\mathrm{x}}/2} \hat{\boldsymbol{e}} \cdot \boldsymbol{E}^{(\mathrm{s})}(k;x,y,0) + \eta_0(\hat{\boldsymbol{z}} \times \hat{\boldsymbol{e}}) \cdot \boldsymbol{H}^{(\mathrm{s})}(k;x,y,0)\,\mathrm{d}x\,\mathrm{d}y, \quad (3.2)$$

where the scattered field $\boldsymbol{E}^{(\mathrm{s})} = \boldsymbol{E}^{(\mathrm{t})} - \boldsymbol{E}^{(\mathrm{i})}$ is used. The last line is obtained by using the fact that the zeroth order modes are plane waves propagating in the positive z direction, and all higher modes integrate to zero.

For a low-pass structure, the low-frequency asymptote of T is obtained from the Maxwell equations by an expansion of the fields in powers of k as discussed in [12, 17, 30], *i.e.*,

$$h(k) \sim k\gamma = k\big(\hat{\boldsymbol{e}} \cdot \boldsymbol{\gamma}_{\mathrm{e}} \cdot \hat{\boldsymbol{e}} + (\hat{\boldsymbol{k}} \times \hat{\boldsymbol{e}}) \cdot \boldsymbol{\gamma}_{\mathrm{m}} \cdot (\hat{\boldsymbol{k}} \times \hat{\boldsymbol{e}})\big) \tag{3.3}$$

as $k \to 0$. The electric and magnetic static polarizabilities $\boldsymbol{\gamma}_{\mathrm{e}}$ and $\boldsymbol{\gamma}_{\mathrm{m}}$ provide the induced electric and magnetic dipole moments per unit cell, $\boldsymbol{p} = \epsilon_0 \boldsymbol{\gamma}_{\mathrm{e}} \cdot \boldsymbol{E}$ and $\boldsymbol{m} = \boldsymbol{\gamma}_{\mathrm{m}} \cdot \boldsymbol{H}$, when the structure is subjected to constant electric and magnetic fields $\boldsymbol{E}$ and $\boldsymbol{H}$, respectively. More precisely, $\boldsymbol{\gamma}_{\mathrm{e}}$ is defined as [34, 35]

$$\hat{\boldsymbol{e}} \cdot \boldsymbol{\gamma}_{\mathrm{e}} \cdot \hat{\boldsymbol{e}} = \frac{1}{E_0} \int_{\Omega \times [-d,0]} \hat{\boldsymbol{e}} \cdot (\boldsymbol{\epsilon}(0;\boldsymbol{r})/\epsilon_0 - \mathbf{I}) \cdot \boldsymbol{E}(0;\boldsymbol{r}) \, \mathrm{dV}, \tag{3.4}$$

where the zero-frequency field $\boldsymbol{E}(0;\boldsymbol{r})$ has the prescribed mean value $\hat{\boldsymbol{e}}$ and satisfies the electrostatic equations

$$\nabla \times \boldsymbol{E}(0;\boldsymbol{r}) = \mathbf{0}, \quad \nabla \cdot \big(\boldsymbol{\epsilon}(0;\boldsymbol{r}) \cdot \boldsymbol{E}(0;\boldsymbol{r})\big) = 0, \tag{3.5}$$

in the unit cell $\Omega \times \mathbb{R}$, with periodic boundary conditions in the xy-plane. Here, $\boldsymbol{\epsilon}(0;\boldsymbol{r})$ is the static permittivity dyadic (which is real-valued, symmetric, and positive-definite), and ϵ_0 is the free space permittivity. This system of partial differential equations can be solved using the Finite Element Method, typically by representing the electric field with a scalar potential as $\boldsymbol{E}(0;\boldsymbol{r}) = \hat{\boldsymbol{e}}E_0 - \nabla\varphi(\boldsymbol{r})$ and solving the elliptic equation $\nabla \cdot [\boldsymbol{\epsilon} \cdot (\hat{\boldsymbol{e}}E_0 - \nabla\varphi)] = 0$, where the scalar potential φ is periodic in the plane and decays to zero as $z \to \pm\infty$ if $\hat{\boldsymbol{e}}$ is in the plane. The elliptic nature of the problem means this numerical solution provides an upper bound to the polarizability; solving the problem with a vector potential instead provides a lower bound [31]. Integral equation solvers such as the method of moments (MoM) are sometimes preferred, particularly due to their efficiency in model problems involving only metal structures and no materials.

The static problem (3.5) possesses some variational properties, which can be used to show that the polarizability dyadic is monotone in $\boldsymbol{\epsilon}$ in the respect that if $\boldsymbol{\epsilon}$ is increased anywhere in $\Omega \times [-d, 0]$, then the quadratic form $\hat{\boldsymbol{e}} \cdot \boldsymbol{\gamma}_{\mathrm{e}} \cdot \hat{\boldsymbol{e}}$ (simply referred to as the polarizability throughout this paper) does not decrease [15, 31]. The magnetic polarizability dyadic, $\boldsymbol{\gamma}_{\mathrm{m}}$, is defined analogously, by substituting $(\boldsymbol{E}, \boldsymbol{\epsilon}) \to (\boldsymbol{H}, \boldsymbol{\mu})$.

The high-frequency asymptotic is $h(k) = \mathcal{O}(1)$ as $k \hat{\to} \infty$, where $\hat{\to}$ denotes limits taken inside the upper half complex plane. This follows from passivity $|T(k)| \leqslant 1$ and hence $|h(k)| \leqslant 4A$ for all k.

4 Forward scattering sum rules

Sum rules are equations stating that the sum or integral of a certain quantity has a given value. In particular, a large variety of sum rules can be derived for

Herglotz functions [1], where typically the integrand is the imaginary part of the Herglotz function weighted by some function of frequency k, and the integral is related to the low- and high frequency expansions of the function. In the present case where the Herglotz function is given by the extinction cross section (3.1), the asymptotic expansions are

$$h(k) \sim \begin{cases} k\gamma & \text{as } k \hat{\to} 0 \\ \mathcal{O}(1) & \text{as } k \hat{\to} \infty \end{cases} \tag{4.1}$$

and the relevant sum rule is [1]

$$\frac{2}{\pi}\int_0^\infty \frac{\sigma_{\text{ext}}(k;\hat{\boldsymbol{k}},\hat{\boldsymbol{e}})}{k^2}\,\mathrm{d}k = \hat{\boldsymbol{e}}\cdot\boldsymbol{\gamma}_{\text{e}}\cdot\hat{\boldsymbol{e}} + (\hat{\boldsymbol{k}}\times\hat{\boldsymbol{e}})\cdot\boldsymbol{\gamma}_{\text{m}}\cdot(\hat{\boldsymbol{k}}\times\hat{\boldsymbol{e}}), \tag{4.2}$$

where $\sigma_{\text{ext}} = \operatorname{Im} h$ is used. It is convenient to rewrite the sum rule in the wavelength variable, $\lambda = 2\pi/k$, that transforms (4.2) into

$$\frac{1}{\pi^2}\int_0^\infty \sigma_{\text{ext}}(\lambda;\hat{\boldsymbol{k}},\hat{\boldsymbol{e}})\,\mathrm{d}\lambda = \hat{\boldsymbol{e}}\cdot\boldsymbol{\gamma}_{\text{e}}\cdot\hat{\boldsymbol{e}} + (\hat{\boldsymbol{k}}\times\hat{\boldsymbol{e}})\cdot\boldsymbol{\gamma}_{\text{m}}\cdot(\hat{\boldsymbol{k}}\times\hat{\boldsymbol{e}}), \tag{4.3}$$

where the symbol $\sigma_{\text{ext}}(k;\hat{\boldsymbol{k}},\hat{\boldsymbol{e}})$ is reused as the extinction cross section as a function of the wavelength. We observe that (4.2) is identical to the forward scattering sum rule with σ_{ext} being the extinction cross section for an object in free space [6, 34]. The identity (4.3) is bounded to derive a physical limitation on the product between the bandwidth and extinction cross section

$$\frac{\lambda_2-\lambda_1}{\pi^2}\min_{\lambda\in[\lambda_1,\lambda_2]}\sigma_{\text{ext}}(\lambda) \leqslant \hat{\boldsymbol{e}}\cdot\boldsymbol{\gamma}_{\text{e}}\cdot\hat{\boldsymbol{e}} + (\hat{\boldsymbol{k}}\times\hat{\boldsymbol{e}})\cdot\boldsymbol{\gamma}_{\text{m}}\cdot(\hat{\boldsymbol{k}}\times\hat{\boldsymbol{e}}). \tag{4.4}$$

The sum rule is valid for arbitrary periodic structures that do not support currents in the static limit and is composed by linear and passive materials. In the following, we show that the forward scattering sum rule [6, 34] for isolated objects is obtained by extending the unit cell in two directions, *i.e.*, by letting $\ell_{\text{x}} = \ell_{\text{y}} \to \infty$, see Fig. 2c. We also obtain an intermediate sum rule for two-dimensional objects and for objects that are periodic in one direction, see Fig. 2b.

As $\ell_{\text{x}} = \ell_{\text{y}} = \ell \to \infty$, the low-frequency limit is obtained by replacing Ω with $\mathbb{R}^2$ in (3.4) and (3.5) and observing that the potential $\varphi(\boldsymbol{r})$ vanish as $|\boldsymbol{r}| \to \infty$. The decay of the potential follows from the expression of the potential as a sum over the induced dipole moments, *i.e.*,

$$\varphi(\boldsymbol{r}) = \sum_{m=-\infty}^{\infty}\sum_{n=-\infty}^{\infty}\frac{\boldsymbol{r}-\boldsymbol{r}_{mn}}{4\pi|\boldsymbol{r}-\boldsymbol{r}_{mn}|^3}\cdot\boldsymbol{\gamma}_{\text{e}}\cdot\boldsymbol{E}_0 \tag{4.5}$$

where $\boldsymbol{r}_{mn} = m\ell_{\text{x}}\hat{\boldsymbol{x}} + n\ell_{\text{y}}\hat{\boldsymbol{y}} + \zeta\hat{\boldsymbol{z}}$. Note, that the monopole term vanishes as the objects are uncharged. The sum is convergent for $\boldsymbol{r} \neq \boldsymbol{r}_{mn}$ and it shows that

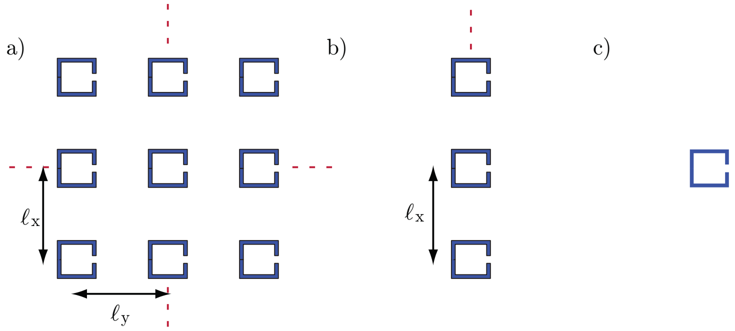

Figure 2: Scattering geometries. a) periodic in two directions. b) periodic in one direction. c) single object.

the potential between the objects decay, *e.g.*, for $\boldsymbol{r} = \boldsymbol{r}_{11}/2$, to zero as $\ell \to \infty$. The polarizability dyadic $\boldsymbol{\gamma}_{\mathrm{e}}$ approximates hence the free space polarizability dyadic [17,34] as $\ell \to \infty$.

The entire periodic structure contributes to the scattered field for a finite unit cell. However, the contributions from the neighboring objects decrease as $\ell \to \infty$. The integral representation (3.2) is used to express h in the fields behind the structure as

$$h(k) \to h_3(k) = \frac{-\mathrm{i}}{E_0}\int_{\mathbb{R}^2} \hat{\boldsymbol{e}}\cdot\boldsymbol{E}^{(\mathrm{s})}(k;x,y,0) + \eta_0(\hat{\boldsymbol{z}}\times\hat{\boldsymbol{e}})\cdot\boldsymbol{H}^{(\mathrm{s})}(k;x,y,0)\,\mathrm{d}x\,\mathrm{d}y \quad (4.6)$$

in the limit $\ell \to \infty$. The right-hand side of (4.6) is recognized as the surface integral representation of the electromagnetic field expressing the far field in the scattered field on the surface $z = 0$, *i.e.*, $h_3(k) = 4\pi \lim_{z\to\infty} z\mathrm{e}^{-\mathrm{i}kz}\hat{\boldsymbol{e}} \cdot \boldsymbol{E}^{(\mathrm{s})}(k, z\hat{\boldsymbol{z}})/(kE_0)$, see [6]. This shows that $\operatorname{Im} h_3(k) = \sigma_{\mathrm{ext}}(k)$, where σ_{ext} denotes the extinction cross section for an object in free space. This forward scattering sum rule has been extensively verified [6,34,35] and is useful in the analysis of small antennas [8,9].

The case with $\ell_{\mathrm{y}} \to \infty$ corresponds to a situation with periodicity in the x-direction, see Fig. 2b. This scattering configuration is found in scattering of elongated objects that can be approximated by two dimensional scattering. Following the analysis above, we let $\ell_{\mathrm{y}} \to \infty$ in (3.2), to get the Herglotz function

$$\begin{aligned} h(k) &= \mathrm{i}2\ell_{\mathrm{x}}\ell_{\mathrm{y}}\big(1 - T(k)\big) \to h_2(k)\ell_{\mathrm{x}} \\ &= \frac{-\mathrm{i}}{E_0}\int_{\mathbb{R}}\int_{-\ell_{\mathrm{x}}/2}^{\ell_{\mathrm{x}}/2} \hat{\boldsymbol{e}}\cdot\boldsymbol{E}^{(\mathrm{s})}(k;x,y,0) + \eta_0(\hat{\boldsymbol{z}}\times\hat{\boldsymbol{e}})\cdot\boldsymbol{H}^{(\mathrm{s})}(k;x,y,0)\,\mathrm{d}x\,\mathrm{d}y \end{aligned} \quad (4.7)$$

After dividing with ℓ_{x}, we recognize the first term in the right-hand side of (4.7) as the mean electric field on the line described by $z = 0$ and $-\infty < y < \infty$, and correspondingly for the magnetic field. The right hand side is then seen to

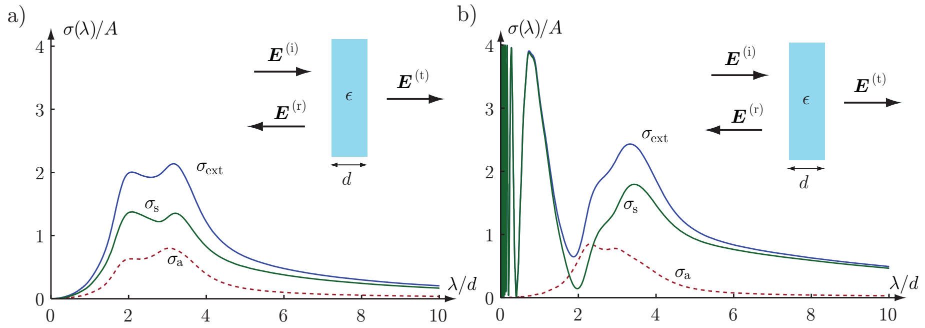

Figure 3: Simulated values for the absorption σ_{a}, scattering σ_{s}, and extinction σ_{ext} cross sections of dielectric slabs with the Lorentz models $\epsilon_{\mathrm{r}}(k) = 1+1/(1-\mathrm{i}0.1k-0.2k^2)$ and $\epsilon_{\mathrm{r}}(k) = 2+1/(1-\mathrm{i}0.1k-0.2k^2)$ in a) and b), respectively.

be the line integral representation of the electromagnetic field expressing the 2D far field in the scattered field at $z = 0$, *i.e.*, $h_2(k) = \lim_{z\to\infty}(\mathrm{i}8\pi kz)^{1/2}\mathrm{e}^{-\mathrm{i}kz}\hat{\boldsymbol{e}}\cdot\boldsymbol{E}^{(\mathrm{s})}(k, z\hat{\boldsymbol{z}})/(kE_0)$, see [2, p. 6] and [29, p. 207]. This shows that $\operatorname{Im} h_2(k) = \sigma_{\mathrm{ext,2D}}(k)$, where $\sigma_{\mathrm{ext,2D}}$ denotes the extinction cross section per unit length of an infinite cylindrical object.

5 Examples

We demonstrate the sum rule (4.3) in four applications: transmission through dielectric slabs, arrays of lossy split ring resonators, perfectly conducting split ring resonators on a dielectric substrate, and a resonant cylinder structure.

5.1 Dielectric slabs

The transmission and reflection coefficients of a homogeneous isotropic slab with thickness d are

$$T = \frac{(1-r_0^2)\mathrm{e}^{\mathrm{i}(n-1)kd}}{1-r_0^2\mathrm{e}^{2\mathrm{i}nkd}} \quad \text{and } R = r_0\frac{1-\mathrm{e}^{2\mathrm{i}nkd}}{1-r_0^2\mathrm{e}^{2\mathrm{i}nkd}}, \tag{5.1}$$

respectively, where $n = \sqrt{\epsilon_{\mathrm{r}}\mu_{\mathrm{r}}}$ is the refractive index, $r_0 = (1-\eta_{\mathrm{r}})/(1+\eta_{\mathrm{r}})$, and $\eta_{\mathrm{r}} = \sqrt{\mu_{\mathrm{r}}/\epsilon_{\mathrm{r}}}$ is the relative impedance. The generalized scattering, absorption, and extinction cross sections are $\sigma_{\mathrm{s}} = A(|R|^2+|1-T|^2)$, $\sigma_{\mathrm{a}} = A(1-|R|^2-|T|^2)$, and $\sigma_{\mathrm{ext}} = 2A\operatorname{Re}\{1-T\}$, respectively, see also the optical theorem (2.6).

Consider a dielectric slab with thickness $d = 1$ and the permittivity modeled by the Lorentz model $\epsilon_{\mathrm{r}}(k) = \epsilon_\infty + (\epsilon_{\mathrm{s}} - \epsilon_\infty)/(1-0.1\mathrm{i}k-0.2k^2)$, where d and k are dimensionless quantities. The absorption, scattering, and extinction cross sections are depicted in Fig. 3 for $\{\epsilon_\infty = 1, \epsilon_{\mathrm{s}} = 2\}$ and $\{\epsilon_\infty = 2, \epsilon_{\mathrm{s}} = 3\}$. The left hand sides of the sum rule (4.3) are determined numerically to A and $2A$.

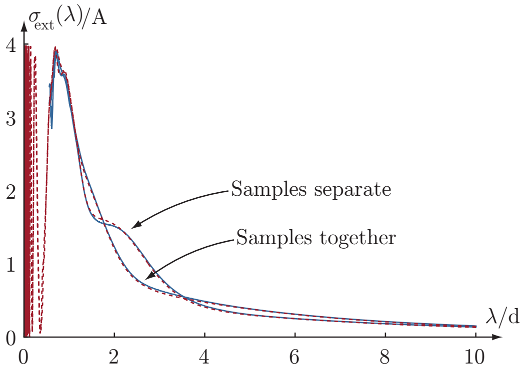

Figure 4: Measured values (solid curves) and simulated values (dashed curves) of extinction cross sections for two different configurations of layered slabs. The length $d = 26.82\,\text{mm}$ is chosen as the total length of configuration 2, *i.e.*, where the two dielectric slabs are separated by air. The theoretical curves are computed using lossless slabs with $\epsilon_{1\text{r}} = 2.1$ and $\epsilon_{2\text{r}} = 2.7$.

This agrees with the polarizability $(\epsilon_{\text{s}} - 1)dA$ and confirms the sum rule (4.3). Note the oscillations at low λ/d for the case $\{\epsilon_\infty = 2, \epsilon_{\text{s}} = 3\}$, corresponding to the positive insertion delay with respect to the background in the high-frequency limit for this case.

An experimental demonstration is obtained as follows. Transmission is measured from 20 MHz to 20 GHz using an Agilent E8363B network analyzer and a coaxial fixture with length 50.81 mm, and inner and outer diameters of 3.05 mm and 6.97 mm, respectively. Two material samples filling the cross section are used, having lengths $d_1 = 9.11\,\text{mm}$ and $d_2 = 8.94\,\text{mm}$, and relative permittivities $\epsilon_{1\text{r}} \approx 2.1 + 0.01\text{i}$ and $\epsilon_{2\text{r}} \approx 2.7 + 0.02\text{i}$ almost constant throughout the band, respectively. The transmission coefficient T is calculated as the insertion loss S_{21} for the fixture with a sample present normalized by the insertion loss for the empty fixture, $T = S_{21}^{(\text{sample})}/S_{21}^{(\text{empty})}$.

Two different configurations are investigated: 1) with the two dielectric samples adjacent to each other, and 2) separated by a distance of 8.77 mm. These two configurations are chosen since they have the same static polarizability per unit area, $\gamma/A = (\epsilon_{1\text{r}} - 1)d_1 + (\epsilon_{2\text{r}} - 1)d_2$, but different frequency dependence due to their different geometric structure. The polarizability for each case is calculated from measurement data by determining the effective permittivity for the two configurations using the Nicolson-Ross-Weir algorithm [23, 38] at 20 MHz, and using $\gamma = (\text{Re}(\epsilon_{\text{eff}}) - 1)Ad$.

The resulting extinction cross sections are depicted in Figure 4, where the measured polarizabilities are $\gamma_1 = 3.14\,\text{cm}^3$ and $\gamma_2 = 3.13\,\text{cm}^3$ for the two configurations, respectively. The left hand side of (4.3) is estimated to $2.98\,\text{cm}^3$ and $2.94\,\text{cm}^3$ respectively for two cases, which shows that the right hand side and the

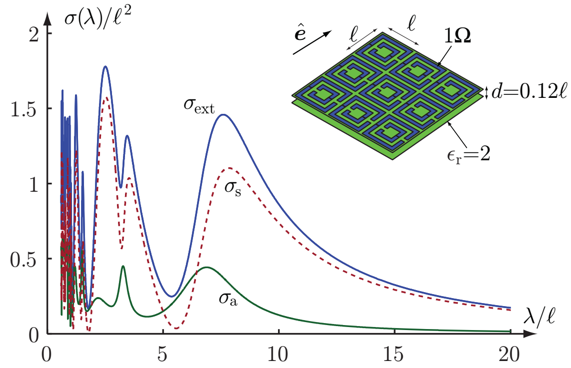

Figure 5: Simulated values for the absorption $\sigma_{\rm a}$, scattering $\sigma_{\rm s}$, and extinction $\sigma_{\rm ext}$ cross sections of an array of $1\,\Omega$ split ring resonators on a dielectric slab with $\epsilon_{\rm r} = 2$ using CST.

left hand side of (4.3) are essentially the same for the two cases.

5.2 Array of lossy split ring resonators

Consider a quadratic split ring resonator (SRR) with unit cell length $\ell = 2.5\,\text{mm}$. The design of the microstructure is similar to the split ring resonators discussed in [32]. The line width and distances in the SRR are $\ell/10$, see also [12] and Sec. 5.3. The SRRs are modeled as a resistive sheet having sheet resistance $R_{\rm s} = 1/(\varsigma d_0) = 1\,\Omega$, where ς and d_0 denote the bulk conductivity and thickness of the SRR [37]. The supporting dielectric structure is $d = 0.3\,\text{mm}$ thick and has the relative permittivity $\epsilon_{\rm r} = 2$.

The transmission and reflection coefficients are simulated using CST Microwave Studio for $0.1\,\text{GHz} \leqslant f \leqslant 200\,\text{GHz}$. The absorption, $\sigma_{\rm a}$, and scattering, $\sigma_{\rm s}$, cross sections are determined from the transmission and reflection coefficients in analogy with (2.3) and (2.4), see Fig. 5. The extinction cross section is determined both as the sum $\sigma_{\rm ext} = \sigma_{\rm a} + \sigma_{\rm s}$ and from the optical theorem (2.6), see Fig. 5.

The integrated extinction (4.3) is determined to $1.6\ell^3$, which is close to the low-frequency limit $\sigma_{\rm ext}(k)/k \approx 1.7\ell^3$ for $k \approx 0$ and the polarizability $\gamma \approx 1.7\ell^3$ as determined using Comsol multiphysics, see also [12].

5.3 Array of split ring resonators on a FR4 substrate

A finite periodic array of split ring resonators composed of 240×240 split ring resonators etched in $18\,\mu\text{m}$ thick copper and supported by a $0.6 \times 0.6\,\text{m}^2$ and $0.3\,\text{mm}$ thick dielectric substrate is used, see Fig. 6b. The experimental setup consists of a pair of wideband ridged horn antennas facing each other at a distance of $0.70\,\text{m}$

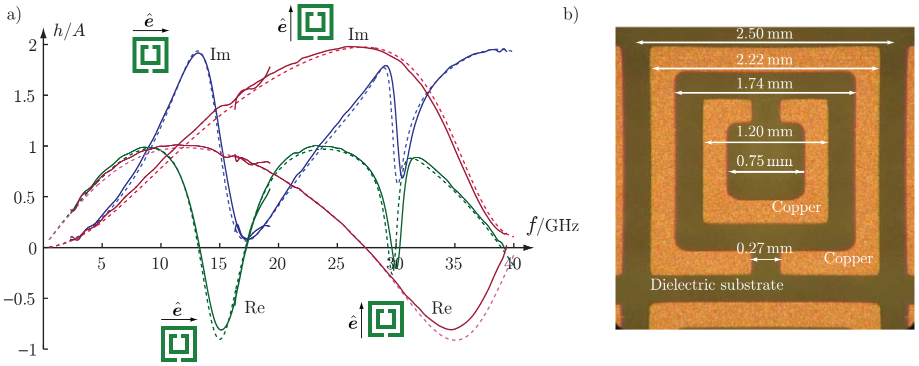

Figure 6: a) Measured values (solid curves) and simulated values (dashed curves) for the forward scattering of an array of split ring resonators on a FR4 substrate. b) Geometry of the split ring resonators on a 0.3mm thick FR4 substrate with $\epsilon_\text{r} = 4.35$.

with the sample placed at the midpoint, see also [12]. The sample measurement is divided into two frequency intervals motivated by the necessity to use two different antenna pairs for the frequency bands $[1, 22]$ GHz and $[16, 40]$ GHz. The sample measurement is normalized with a free space measurement and the resulting transmission coefficient is gated with a 2.3 ns window in the time domain. The size of the window is chosen to minimize the influence of the background, and it reduces the useful frequency range to $[2.5, 38]$ GHz.

The transmission coefficient is also determined numerically using the finite element solver in CST Microwave Studio for the horizontal and vertical polarizations. Since the sheet resistance of the copper layer is very low, $R_\text{s} = 1/(\varsigma d) \approx 1\,\text{m}\Omega$, the copper is modeled as an infinitely thin perfect electric conductor, and the dielectric substrate is modeled with an isotropic temporally dispersive relative permittivity decreasing from 4.45 at 0.1 GHz to 4.30 at 10 GHz. The overall loss factor is 0.02 according to the technical data sheet from the manufacturer. Fig. 6a depicts the real and imaginary parts of $h = \text{i}2A(1 - T)$, and the results from numerical simulations are in good agreement with the measured values.

The polarizability per unit area, $\hat{\boldsymbol{e}} \cdot \boldsymbol{\gamma}_\text{e} \cdot \hat{\boldsymbol{e}}/A$, is estimated by solving (3.4) and (3.5) using the finite element solver from Comsol Multiphysics, where the static relative permittivity $\epsilon_\text{r} = 4.35$ is used. The result is $\hat{\boldsymbol{e}} \cdot \boldsymbol{\gamma}_\text{e} \cdot \hat{\boldsymbol{e}}/A = 7.2\,\text{mm}$ and $\hat{\boldsymbol{e}} \cdot \boldsymbol{\gamma}_\text{e} \cdot \hat{\boldsymbol{e}}/A = 7.1\,\text{mm}$ for the horizontal and vertical polarizations, respectively, see [12]. By numerically integrating the curves in Fig. 6, this integral is estimated to 6.3 mm and 6.0 mm for the horizontal and vertical polarizations, respectively. These values are comparable with the right-hand side of (4.3) normalized by the cross section area of the unit cell. From (4.3) the slope of the real part at low frequencies is the static polarizability.

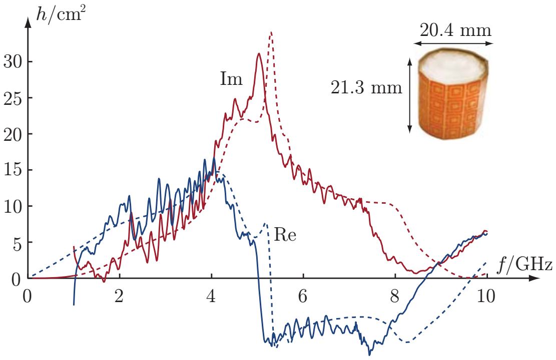

Figure 7: Measured values (solid curves) and simulated values (dashed curves) for the forward scattering of a resonant structure on an ARLON CLTE-XT substrate supported by an expanded polystyrene cylinder.

5.4 Resonant cylinder structure in a parallel plate waveguide

The forward scattering is determined for a set of SRRs on a cylindrical structure in a parallel plate waveguide [18]. The cylindrical structure is constructed by rolling up a $21.3 \times 63.9\,\mathrm{mm}^2$ and 0.51 mm thick Arlon CLTE-XT sheet with 4×12 split ring resonators around an expanded polystyrene cylinder. The SRRs are etched in $18\,\mu\mathrm{m}$ thick copper as in Fig. 6b, but here with a unit cell length of $\ell = 5.32\,\mathrm{mm}$ (the line width and distances are $\ell/10$) giving a resonance frequency around $f = 5\,\mathrm{GHz}$. The outer radius of the cylinder is 10.2 mm. The experimental setup consists of a pair of TEM horn antennas facing each other at a distance 0.98 m with the sample placed in the center of the waveguide [18]. The sample measurement is normalized with a free space measurement [18]. The fluctuations at low frequencies in Fig. 7 are due to noise and interferences introduced in the measurement setup [18]. It is also noted that the setup is too small to use the time gating as used in the free space measurements in Fig. 6.

The forward scattered field is also determined numerically using the finite element solver in CST Microwave Studio as in Sec. 5.3 with the Arlon substrate modeled by the relative permittivity $\epsilon_{\mathrm{r}} = 2.94$ and loss tangent 0.0025. The boundary conditions are modeled with periodic boundaries at the top and bottom of the cylinder and open boundaries for the other directions. It is observed that the numerical results resemble the measured values, see Fig. 7. The right hand side of (4.3) from simulations is calculated to $17.8\,\mathrm{cm}^3$ which is the slope of the real part of the h function at low frequencies and the left hand side is estimated to $13\,\mathrm{cm}^3$ over the frequency range $f = [1 - 10]\,\mathrm{GHz}$. The measurement is noisy at low frequencies and not reliable to calculate the integral value in (4.3). Therefore the left hand side of sum rule is integrated from 2 GHz to 20 GHz and this value is estimated to $13.8\,\mathrm{cm}^3$. The measured values follow the simulated values and the

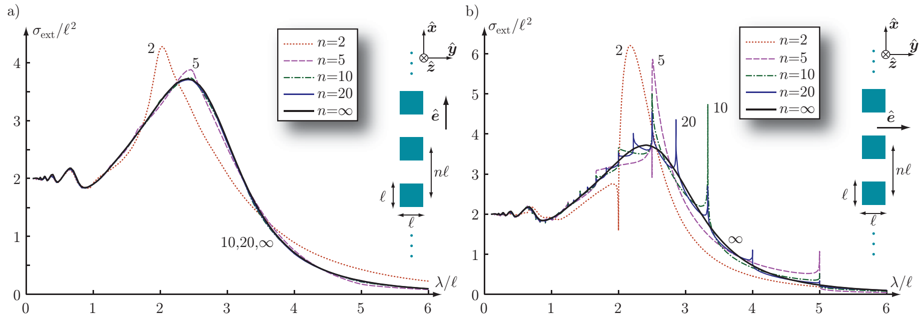

Figure 8: Extinction cross section for one dimensional repetitions of square PEC patches with side lengths ℓ and inter-element distances $n\ell$ for $n = 2, 5, 10, 20$. The incident field is $\boldsymbol{E}^{(\mathrm{i})} = E_0\hat{\boldsymbol{e}}\mathrm{e}^{\mathrm{i}kz}$ with $\lambda = 2\pi/k$. a) polarization $\hat{\boldsymbol{e}} = \hat{\boldsymbol{x}}$. b) polarization $\hat{\boldsymbol{e}} = \hat{\boldsymbol{y}}$.

areas under the $\sigma_{\text{ext}} = \operatorname{Im} h$ curves are almost the same. The difference between the resonance frequencies is probably due to errors in the material modeling.

5.5 Periodicity in one direction

The one-dimensional periodic case in Fig. 2b and its corresponding sum rule is illustrated with the scattering of square PEC patches. The square patches have side lengths ℓ and are repeated periodically in the $\hat{\boldsymbol{x}}$-direction with inter-element distances $\ell_{\mathrm{x}} = n\ell$, for $n = 2, 5, 10, 20$. An in house method of moments (MoM) code is used to compute the forward scattering (4.7) for the incident wave $\boldsymbol{E}^{(\mathrm{i})}(\boldsymbol{r}) = \hat{\boldsymbol{e}}E_0\mathrm{e}^{\mathrm{i}kz}$, see also App. A. The resulting extinction cross sections for the polarizations $\hat{\boldsymbol{e}} = \hat{\boldsymbol{x}}$ and $\hat{\boldsymbol{e}} = \hat{\boldsymbol{y}}$ are depicted in Fig. 8. The extinction cross sections $\sigma_{\text{ext},n}$ for the periodic structures ($n = 2, 5, 10, 20$) are compared with the extinction cross section for a single square patch ($n = \infty$).

The curves for $n = 10, 20, \infty$ are indistinguishable for the copolarized case, $\hat{\boldsymbol{e}} = \hat{\boldsymbol{x}}$, depicted in Fig. 8a illustrating that $\sigma_{\text{ext},n}$ approaches $\sigma_{\text{ext},\infty}$ fast as n increases. This fast convergence follows from the weak mutual coupling due to the null of the scattering pattern from the patches in the $\hat{\boldsymbol{e}} = \hat{\boldsymbol{x}}$-direction. It is also observed that $\sigma_{\text{ext}} \approx 2\ell^2$ for short wavelength in agreement with the extinction paradox [26].

The convergence is much slower for the cross polarized case $\hat{\boldsymbol{e}} = \hat{\boldsymbol{y}}$ as depicted in Fig. 8b, where interference patterns are seen for inter-element distances equal to an integer number of wavelengths, *i.e.*, $n\ell = m\lambda$, $m = 1, 2, \ldots$. This is similar to Wood's anomaly [13] and can be explained by the logarithmic singularity in the one dimensional periodic Green's function, see App. A. However, the influence of the singularities decay with the inter-element distance, $\ell_{\mathrm{x}} = n\ell$, due to the division with ℓ_{x} in (A.2) and therefore $\sigma_{\text{ext},n}$ approaches $\sigma_{\text{ext},\infty}$ as $n \to \infty$.

The sum rule (4.3) is verified using MoM calculations for the electric polarizability dyadic giving $\boldsymbol{\gamma}_{\mathrm{e}} \approx (1.08\hat{\boldsymbol{x}}\hat{\boldsymbol{x}} + 1.00\hat{\boldsymbol{y}}\hat{\boldsymbol{y}})\ell^3$ for $n = 2$, $\boldsymbol{\gamma}_{\mathrm{e}} \approx (1.03\hat{\boldsymbol{x}}\hat{\boldsymbol{x}} + 1.02\hat{\boldsymbol{y}}\hat{\boldsymbol{y}})\ell^3$ for $n = 5$, and $\boldsymbol{\gamma}_{\mathrm{e}} \approx (1.03\hat{\boldsymbol{x}}\hat{\boldsymbol{x}} + 1.03\hat{\boldsymbol{y}}\hat{\boldsymbol{y}})\ell^3$ for $n = 10, 20$. There is no contribution from the magnetic polarizability dyadic in the $\hat{\boldsymbol{z}}$ direction. Numerical integrations of the left-hand side of the sum rule (4.3) over the finite range $\lambda/\ell \in [0.2, 30]$ give approximately 97% of the corresponding right-hand side.

6 Conclusions

We have presented an optical theorem for an arbitrary structure being periodic in a plane, which relates the extinction cross section per unit cell to the co-polarized transmission coefficient. For low pass structures this is used to derive a sum rule, which restricts the integral of the extinction cross section over all wavelengths by the static polarizability per unit cell. Sum rules for scatterers bounded in three and two dimensions (cylinders) are obtained as limits when the unit cell is taken to be very large in both or one directions, respectively. The theoretical results are shown to be in good agreement with numerical and experimental tests.

Acknowledgments

This work was supported in part by Swedish Research Council (VR) and the Swedish Foundation for Strategic Research (SSF).

Appendix A One dimensional periodic Green's functions

The free-space Green's function is $G = \mathrm{e}^{\mathrm{i}kR}/(4\pi R)$, where R denotes the distance between the source and observation point. Consider a one-dimensional periodic array in the $\hat{\boldsymbol{x}}$-direction with inter-element distance ℓ_{x}. Here, we sum over all distances $R_n = ((x - x' - n\ell_{\mathrm{x}})^2 + (y - y')^2 + (z - z')^2)^{1/2}$ for integers n. The distance is asymptotically $R_n \sim |x - x' - n\ell_{\mathrm{x}}|$ and $R_n^{-1} \sim 1/(|n|\ell_{\mathrm{x}})$ as $|n| \to \infty$. Use that

$$\sum_{n=1}^{\infty} \frac{\mathrm{e}^{\mathrm{i}k(n\ell_{\mathrm{x}} + x' - x)}}{n\ell_{\mathrm{x}}} = -\frac{\mathrm{e}^{-\mathrm{i}k(x-x')}}{\ell_{\mathrm{x}}} \ln(1 - \mathrm{e}^{\mathrm{i}k\ell_{\mathrm{x}}}) \tag{A.1}$$

to rewrite the periodic Green's function as

$$G = \frac{\mathrm{e}^{\mathrm{i}kR_0}}{4\pi R_0} - 2\frac{\cos\left(k(x - x')\right)}{4\pi\ell_{\mathrm{x}}} \ln(1 - \mathrm{e}^{\mathrm{i}k\ell_{\mathrm{x}}}) + \sum_{n\neq 0} \left(\frac{\mathrm{e}^{\mathrm{i}kR_n}}{4\pi R_n} - \frac{\mathrm{e}^{\mathrm{i}k|x-x'-n\ell_{\mathrm{x}}|}}{4\pi|n|\ell_{\mathrm{x}}} \right), \tag{A.2}$$

where the logarithmic singularities for $k\ell_{\mathrm{x}} = m2\pi$ or equivalently $\ell_{\mathrm{x}} = m\lambda$, $m = 1, 2, ..$ are observed.

References

[1] A. Bernland, A. Luger, and M. Gustafsson. Sum rules and constraints on passive systems. *J. Phys. A: Math. Theor.*, **44**(14), 145205, 2011.

[2] J. J. Bowman, T. B. A. Senior, and P. L. E. Uslenghi. *Electromagnetic and Acoustic Scattering by Simple Shapes.* North-Holland, Amsterdam, 1969.

[3] F. Capolino, editor. *Theory and Phenomena of Metamaterials.* CRC Press, 2009.

[4] R. M. Fano. Theoretical limitations on the broadband matching of arbitrary impedances. *Journal of the Franklin Institute*, **249**(1,2), 57–83 and 139–154, 1950.

[5] M. Gustafsson. Sum rules for lossless antennas. *IET Microwaves, Antennas & Propagation*, **4**(4), 501–511, 2010.

[6] M. Gustafsson. Time-domain approach to the forward scattering sum rule. *Proc. R. Soc. A*, **466**, 3579–3592, 2010.

[7] M. Gustafsson, M. Cismasu, and S. Nordebo. Absorption efficiency and physical bounds on antennas. *International Journal of Antennas and Propagation*, **2010**(Article ID 946746), 1–7, 2010.

[8] M. Gustafsson, C. Sohl, and G. Kristensson. Physical limitations on antennas of arbitrary shape. *Proc. R. Soc. A*, **463**, 2589–2607, 2007.

[9] M. Gustafsson, C. Sohl, and G. Kristensson. Illustrations of new physical bounds on linearly polarized antennas. *IEEE Trans. Antennas Propagat.*, **57**(5), 1319–1327, May 2009.

[10] M. Gustafsson. Sum rule for the transmission cross section of apertures in thin opaque screens. *Opt. Lett.*, **34**(13), 2003–2005, 2009.

[11] M. Gustafsson and D. Sjöberg. Physical bounds and sum rules for high-impedance surfaces. *IEEE Trans. Antennas Propagat.*, **59**(6), 2196–2204, 2011.

[12] M. Gustafsson, C. Sohl, C. Larsson, and D. Sjöberg. Physical bounds on the all-spectrum transmission through periodic arrays. *EPL Europhysics Letters*, **87**(3), 34002 (6pp), 2009.

[13] A. Hessel and A. A. Oliner. A new theory of Wood's anomalies on optical gratings. *Applied Optics*, **4**(10), 1275–1297, 1965.

[14] J. D. Jackson. *Classical Electrodynamics.* John Wiley & Sons, New York, third edition, 1999.

[15] D. S. Jones. Scattering by inhomogeneous dielectric particles. *Quart. J. Mech. Appl. Math.*, **38**, 135–155, 1985.

[16] A. Karlsson. On the time domain version of the optical theorem. *Am. J. Phys*, **68**(4), 344–349, 2000.

[17] R. E. Kleinman and T. B. A. Senior. Rayleigh scattering. In V. V. Varadan and V. K. Varadan, editors, *Low and high frequency asymptotics*, volume 2 of *Handbook on Acoustic, Electromagnetic and Elastic Wave Scattering*, chapter 1, pages 1–70. Elsevier Science Publishers, Amsterdam, 1986.

[18] C. Larsson, S. E. Bayer, M. Gustafsson, G. Kristensson, D. Sjöberg, C. Sohl, and I. Vakili. Scattering measurements in a parallel plate waveguide – first results. In *Proceedings of the XXXth URSI General Assembly*, page B06.6, 2011.

[19] D. Lytle, P. Carney, J. Schotland, and E. Wolf. Generalized optical theorem for reflection, transmission, and extinction of power for electromagnetic fields. *Phys. Rev. E*, **71**(5), 056610, 2005.

[20] E. A. Marengo. A new theory of the generalized optical cross-section theorem for electromagnetic fields. In *Antennas and Propagation Society International Symposium, 2009. APSURSI'09. IEEE*, pages 1–4. IEEE, 2009.

[21] B. Munk. *Frequency Selective Surfaces: Theory and Design*. John Wiley & Sons, New York, 2000.

[22] R. Newton. Optical theorem and beyond. *Am. J. Phys*, **44**, 639–642, 1976.

[23] A. M. Nicolson and G. F. Ross. Measurement of the intrinsic properties of materials by time-domain techniques. *IEEE Trans. Instrumentation and Measurement*, **19**, 377–382, 1970.

[24] A. Nosich. Radiation conditions, limiting absorption principle, and general relations in open waveguide scattering. *Journal of electromagnetic waves and applications*, **8**(3), 329–353, 1994.

[25] H. M. Nussenzveig. *Causality and dispersion relations*. Academic Press, London, 1972.

[26] R. E. Peierls. *Surprises in Theoretical Physics*. Princeton University Press, 1979.

[27] E. M. Purcell. On the absorption and emission of light by interstellar grains. *J. Astrophys.*, **158**, 433–440, 1969.

[28] K. N. Rozanov. Ultimate thickness to bandwidth ratio of radar absorbers. *IEEE Trans. Antennas Propagat.*, **48**(8), 1230–1234, August 2000.

[29] G. T. Ruck, D. E. Barrick, W. D. Stuart, and C. K. Krichbaum. *Radar Cross-Section Handbook*, volume 1 and 2. Plenum Press, New York, 1970.

[30] D. Sjöberg. Low frequency scattering by passive periodic structures for oblique incidence: low pass case. *J. Phys. A: Math. Theor.*, **42**, 385402, 2009.

[31] D. Sjöberg. Variational principles for the static electric and magnetic polarizabilities of anisotropic media with perfect electric conductor inclusions. *J. Phys. A: Math. Theor.*, **42**, 335403, 2009.

[32] D. R. Smith, S. Schultz, P. Markos, and C. M. Soukoulis. Determination of effective permittivity and permeability of metamaterials from reflection and transmission coefficients. *Phys. Rev. B*, **65**, 195104–195108, 2002.

[33] C. Sohl and M. Gustafsson. A priori estimates on the partial realized gain of Ultra-Wideband (UWB) antennas. *Quart. J. Mech. Appl. Math.*, **61**(3), 415–430, 2008.

[34] C. Sohl, M. Gustafsson, and G. Kristensson. Physical limitations on broadband scattering by heterogeneous obstacles. *J. Phys. A: Math. Theor.*, **40**, 11165–11182, 2007.

[35] C. Sohl, C. Larsson, M. Gustafsson, and G. Kristensson. A scattering and absorption identity for metamaterials: experimental results and comparison with theory. *J. Appl. Phys.*, **103**(5), 054906, 2008.

[36] J. W. Strutt. On the light from the sky, its polarization and colour. *Phil. Mag.*, **41**, 107–120 and 274–279, April 1871. Also published in Lord Rayleigh, Scientific Papers, volume I, Cambridge University Press, Cambridge, 1899.

[37] J. G. Van Bladel. *Electromagnetic Fields.* IEEE Press, Piscataway, NJ, second edition, 2007.

[38] W. B. Weir. Automatic measurement of complex dielectric constant and permeability at microwave frequencies. *Proc. IEEE*, **62**, 33–36, 1974.

[39] H. Xu, D. Huber, and E. Heller. Cross section and optical theorem for defects on a corrugated surface. *The Journal of chemical physics*, **89**, 2550, 1988.

[40] F. Yang and Y. Rahmat-Samii. *Electromagnetic band gap structures in antenna engineering.* Cambridge University Press, 2009.